# A Study of Identified Hadron Fragmentation in $ep$ Collisions at HERA using the H1 Detector

Jonathan Edward Turney *MSci (Hons)*

Department of Physics

Queen Mary

University of London

This thesis is submitted in accordance with regulations

for the Degree of Doctor of Philosophy

in the University of London.

March 2002

## Abstract

Deep inelastic scattering events from $ep$ collisions, recorded in 1996 and 1997 by the H1 detector at HERA, are used to study the fragmentation properties of identified hadrons in the Breit frame of reference. A review of the theory relevant to this analysis is also presented, together with a description of the H1 detector.

Using $\mathrm{d}E/\mathrm{d}x$ information and neutral secondary particle invariant mass spectra, it is possible to identify samples of $\pi^{\pm}$, $K^{\pm}$, protons and antiprotons, $K^0_S$, and $\Lambda$ hadrons in the Breit frame current hemisphere and measure corresponding exclusive fragmentation functions. The evolution of the fragmentation function peak position and width are studied as a function of hadronic mass and four-momentum transfer, $Q$. Comparison is made to published results from $e^+e^-$ experiments, models of the hadronic final state, and to predictions from MLLA/LPHD theory.

The fragmentation properties of identified hadrons in $ep$ data compare well with those in $e^+e^-$ data, giving further evidence for the universality of quark fragmentation. By applying a MLLA/LPHD calculation using parameters derived from fitting H1 data, it is possible to describe the peak evolution in $e^+e^-$ data as a function of energy, hadronic mass, and the parton shower cut-off parameter, $Q_0^h$. However, the MLLA/LPHD calculation is unable to describe the data fully, particularly the $e^+e^-$-derived width evolution. Furthermore, the Monte Carlo models of the hadronic final state are shown to be incompatible with the detailed parameterisation of MLLA/LPHD, but follow the observed trends in $ep$ data well.

# Declaration

No portion of the work referred to in this thesis has been submitted in support of an application for another degree or qualification of this or any other institute of learning.

# Copyright

# Contents

# List of Figures

# List of Tables

# Acknowledgements

The writing of this thesis required constant injections of new inspiration, much of which was drawn from the many places visited and many people encountered over the past three years. As well as relief in finally finishing, I feel immensely satisfied that a childhood ambition has been fulfilled, and would like to thank the people who helped realise it.

I would like to give special thanks to my supervisor, Professor Graham Thompson, for his support and patient guidance throughout my PhD studies, and for his many wise words on life.

Cheers to Dr Keith Donovan for taking me under his wing and showing me the ropes. Thanks to Dr Dave Kant for always finding time to help and advise me. To Dr Paul Dixon for sharing the burden of being an Evertonian, and for constantly trying to out do me with a new musical discovery. Cheers to Dr Mark Williams for the jokes, poems, and philosophies, and best of luck with Surfability Ltd. Best wishes to everyone in the QMUL HEP Group. I really enjoyed my time working alongside you all.

Thank you to the HaQ Working Group members for attending my talks out in Hamburg, and to Dr Dave Milstead for his advice and interest in my work. Also good luck to the H1-UK people, past and present. Thanks for always making me feel welcome and I hope you all do great things in the future.

I acknowledge the Particle Physics and Astronomy Research Council (PPARC) for their financial support, and in particular Andy McKinna for his efforts in keeping my bank balance in credit.

Thanks to all my friends in Liverpool and London, with a special mention for Ed, Beth and Fabian who are always looking out for me. Cheers to Neesh and Clinic for letting me taste the rock'n'roll lifestyle.

An extra special thank you to my family who are the biggest inspiration of all.

**Dedicated to the memory of my Father,**
**and with love to Mum and Carl**

'Holding this book in your hand, sinking back in your soft armchair, you will say to yourself: perhaps it will amuse me. And after you read this story of great misfortunes, you will no doubt dine well, blaming the author for your own insensitivity, accusing him of wild exaggeration and flights of fancy. But rest assured: this tragedy is not a fiction. All is true.'

Honoré de Balzac, *Le Pére Goriot*

# Preface

A description of $ep$ deep inelastic scattering (DIS) is formulated within the Standard Model of particle physics in terms of an exchanged gauge boson resolving the proton and interacting with a quark (or antiquark). The struck quark scatters, and together with the proton remnant, fragments, initiating a parton shower of gluon radiation and quark-antiquark pair ($q\overline{q}$) production, which through hadronisation, leads to an observable final state hadronic jet.

The purpose of this thesis is to measure the fragmentation properties of identified hadrons in the current hemisphere of the Breit frame, allowing comparison with those of a single hemisphere of quark fragmentation in $e^+e^- \rightarrow q\overline{q}$ annihilations. The fragmentation properties are encapsulated in the shape evolution of a scaled momentum spectrum, termed the *fragmentation function*, which is measured at different transverse momentum scales for a number of hadronic species. Comparison is also made to parameterised calculations of the fragmentation function evolution derived using the modified leading logarithmic approximation (MLLA) of perturbative QCD, coupled with the hadronisation prescription of local parton hadron duality (LPHD).

Chapter one of this thesis will give an overview of the $ep$ collider facility at HERA, and describe components of the H1 detector relevant to this analysis.

An introduction to the dominant physics processes observed at HERA is presented in Chapter two, as well as definitions of the kinematic variables used to define event topologies measured by the H1 detector.

Chapter three introduces the theory of QCD, the gauge theory describing the strong interactions between partons, and aspects relevant to this thesis are highlighted. An overview of a selection of Monte Carlo models of the fragmentation process, used to compare with data, is also given.

Neutral current DIS events are of principal interest to this analysis and Chapter four will outline the kinematic cuts designed to reduce unwanted background from such an event sample. A detailed study of the quality of charged tracks and neutral secondary particles ($V^0$) used in this analysis is given, together with a discussion of several methods for reconstructing event kinematics.

This analysis makes use of two particle identification techniques; a measurement of the specific ionisation energy loss ($\mathrm{d}E/\mathrm{d}x$) of charged particles in an ionising medium, and the reconstruction of the $V^0$ invariant mass under different daughter hypotheses. Chapter five will summarise the method used by the H1 experiment to obtain a $\mathrm{d}E/\mathrm{d}x$ measurement together with selection criteria defined to obtain samples of different hadronic species. Invariant mass spectra used for the identification of $K^0_S$ and $\Lambda$ hadrons are also presented.

Chapter six motivates the Breit frame which is a convenient inertial reference frame in which to compare quark fragmentation in $ep$ DIS with that resulting from an $e^+e^- \to q\overline{q}$ annihilation.

Chapter seven summarises the results from a study of the identification efficiencies, resolutions and purities for each of the exclusive hadronic scaled momentum spectra measured. A method for correcting for limited detector acceptance and inefficiencies is also outlined, together with corresponding correction factors.

The properties of exclusive fragmentation functions measured for identified hadrons lying in the Breit frame current hemisphere are presented in Chapter eight as a function of hadronic mass, energy, and the parton shower cut-off parameter, $Q^h_0$. Comparison is made to exclusive fragmentation data measured by $e^+e^-$ experiments and to the QCD models outlined in Chapter 3. A full account of possible sources of systematic error is also given.

# Chapter 1

# HERA and the H1 Experiment

## 1.1 The HERA Collider

The HERA [1] accelerator facility located at the DESY laboratory in Hamburg, Germany, is currently the world's only electron-proton collider. This machine plays an important role in probing the internal structure of the proton and understanding the fundamental interactions of quarks and leptons. HERA consists of two independent rings designed to accelerate and store electrons (or positrons) and protons. The two particle beams circulate in opposite directions approximately 20 m below ground in a tunnel 6.3 km in circumference, and intersect at four interaction points. Figure 1.1 shows the layout of the HERA accelerator together with pre-accelerators.

Before injection into the HERA ring the electrons (positrons) and protons must first be passed through a chain of pre-accelerators. Negatively charged hydrogen ions are accelerated in a 50 MeV linear accelerator and then stripped of their electrons to generate protons which are injected into DESY III. The protons are accelerated to 7.5 GeV before being transferred to PETRA III where they are accelerated to 40 GeV. Injection into the main HERA ring then follows, with a proton current of approximately 80 mA being achieved.

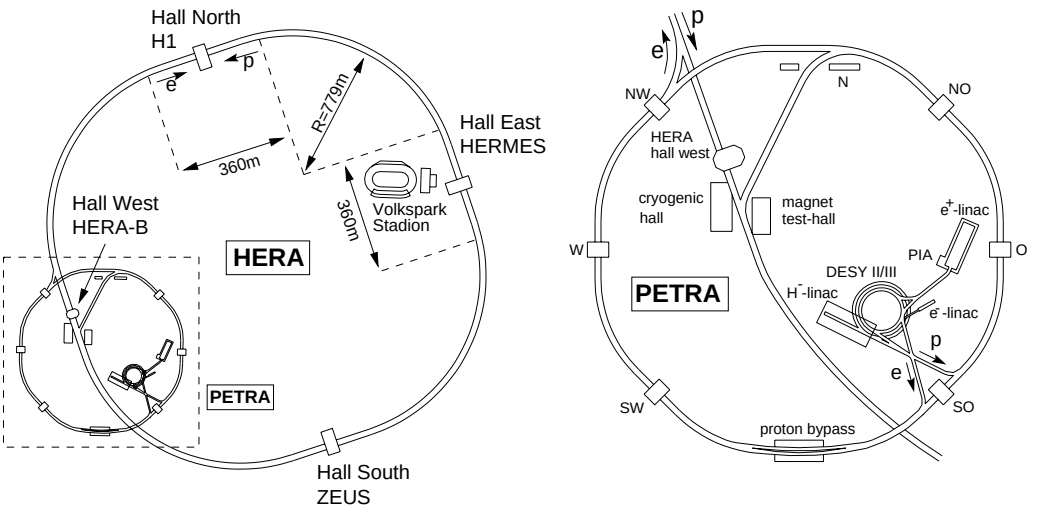


**Figure 1.1**: *Schematic view of the HERA Collider.*

Electrons are injected into a small storage ring after acceleration by a 500 MeV linear accelerator. The electrons are first allowed to accumulate into a single 60 mA bunch before being passed into DESY II, where they are then accelerated to 7 GeV. The accelerated bunch is transferred to the PETRA II ring, with this stage being repeated at a rate of 12.5 Hz until 70 bunches have been filled. The bunches are then injected into the HERA ring. This procedure is carried out three times with a resulting electron current of approximately 30 mA being achieved.

Some bunches are left empty such that a proton or electron bunch may arrive in the detector with no collision partner. These unpaired 'pilot' bunches are used to estimate the rates of background processes such as beam interactions with residual gas in the beam pipe and collisions with the beam wall.

During the 1996 and 1997 running periods, 27.5 GeV positrons were brought into collision with 820 GeV[1] protons, providing a centre-of-mass energy of $\sqrt{s} \approx$ 300 GeV and a time of 96 ns between bunch crossings.

The resulting collision products are measured using two universal, large acceptance detectors, H1 [2] and ZEUS [3], which are situated at the North and South

[1]Since 1998 the HERA accelerator has provided protons of 920 GeV giving a centre-of-mass energy of $\sqrt{s} \approx 318$ GeV

Halls of the HERA ring respectively. The HERMES [4] experiment is situated at the East Hall and studies the internal spin structure of nucleons using a polarised electron beam incident on a polarised gas target. The HERA-B [5] experiment is located at the West Hall and will measure CP symmetry violation in the B-meson system using a proton beam incident on a wire target.

## 1.2 General Description of the H1 Detector

The H1 detector [2] is a general purpose $4\pi$ detector measuring both the scattered electron and the final hadronic state produced by the scattered quark and proton remnant. The H1 co-ordinate system is defined such that the positive $z$-axis is orientated along the direction of the incoming proton, the $y$-axis pointing vertically upwards and the $x$-axis points towards the centre of the HERA ring. A schematic of the H1 detector is shown in Figure 1.2 and highlights the components to be discussed in this section.

Although azimuthally symmetric, the H1 detector is forward-backward asymmetric in design due to the energy imbalance of the colliding particle beams. The forward region of the detector is densely instrumented to measure the large energy flows and particle multiplicities emerging in the proton direction. The backward region is designed to provide an accurate measurement of the scattered electron energy and momentum which are important in determining event kinematics.

Charged particle momenta are determined using the tracking system which is situated, together within the calorimetry, inside a uniform magnetic field of 1.15 T produced by a superconducting solenoid. Tracking in the central region is provided by two concentric jet drift chambers in combination with proportional chambers and $z$ drift chambers. In the forward region there are three radial and three planar drift chamber modules mounted perpendicularly to the beam direction.

The measurement of the hadronic final state and scattered electron energies are

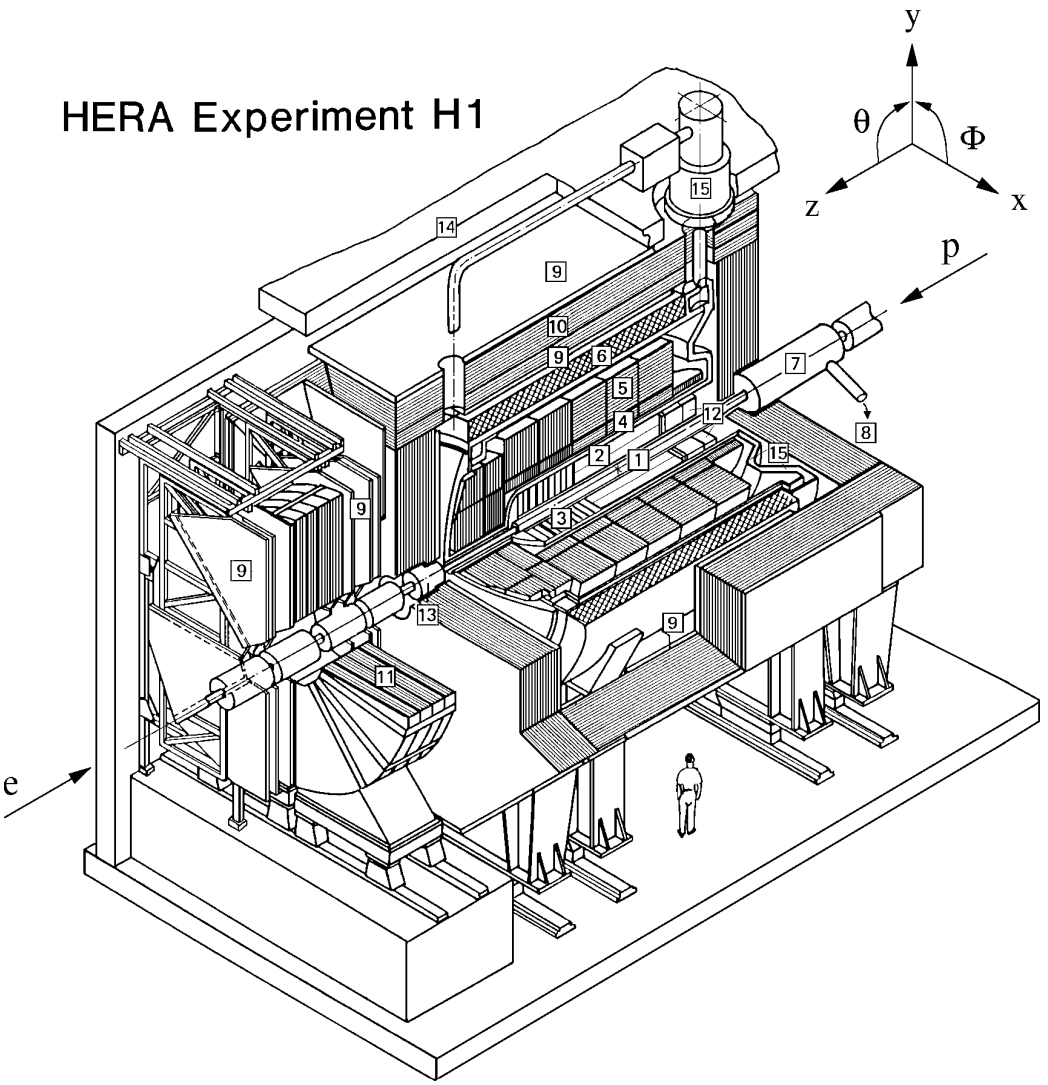


| | | | |
|---|---|---|---|
| 1 | Beam pipe and magnets | 9 | Muon chambers |
| 2 | Central tracking detectors | 10 | Instrumented Iron yoke |
| 3 | Forward tracking detectors | 11 | Forward muon toroid |
| 4 | Electromagnetic LAr calorimeter | 12 | SPACAL and BDC |
| 5 | Hadronic LAr calorimeter | 13 | PLUG calorimeter |
| 6 | Super-conducting coil | 14 | Concrete shielding |
| 7 | Compensating magnet | 15 | LAr cryostat |
| 8 | Liquid Helium supply | | |

**Figure 1.2**: *A 3D view showing the layout of the H1 detector.*

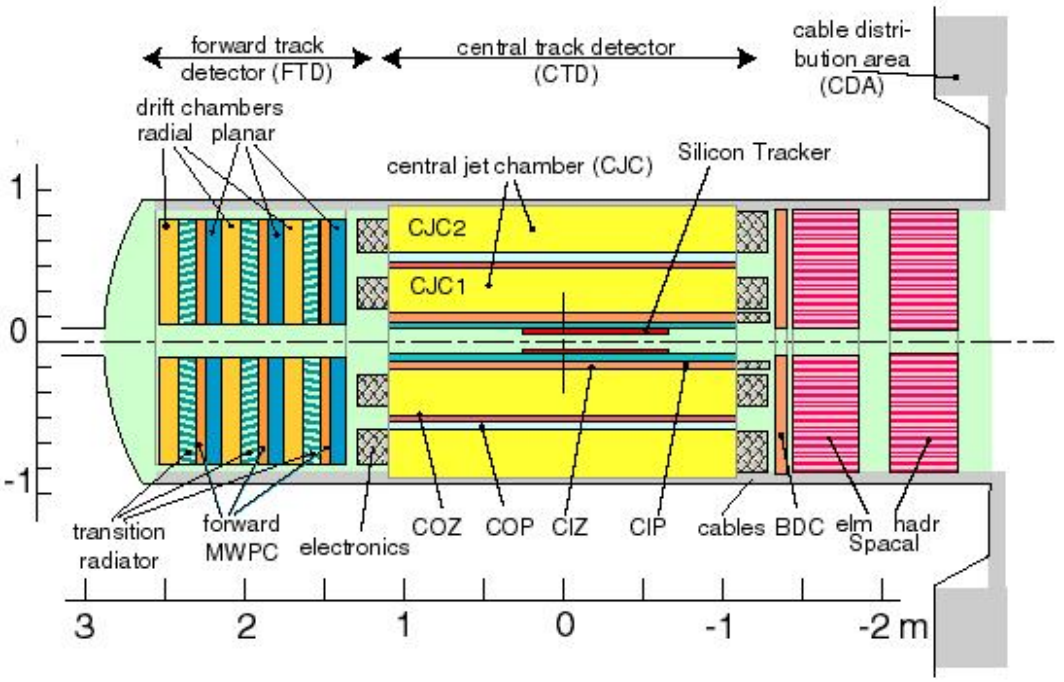


**Figure 1.3**: *The H1 tracking system (r-z view)*

made using the liquid argon calorimeter, the plug calorimeter and the spaghetti calorimeter (SpaCal). These components surround the tracking system and are themselves surrounded by the instrumented iron return yoke, also known as the 'tail catcher', which provides a coarse measurement of the remaining hadronic energy leaking from the main calorimeters.

The luminosity system is comprised of an electron tagger and a photon tagger, located in the electron beam direction 33 m and 103 m from the nominal interaction point respectively. A measure of the luminosity is obtained from the Bethe-Heitler process [6] ($ep \to ep\gamma$) where the cross section can be accurately calculated within QED.

## 1.3 Tracking

The tracking system of H1, shown in Figure 1.3, enables simultaneous track triggering, reconstruction, and particle identification for events produced by $ep$

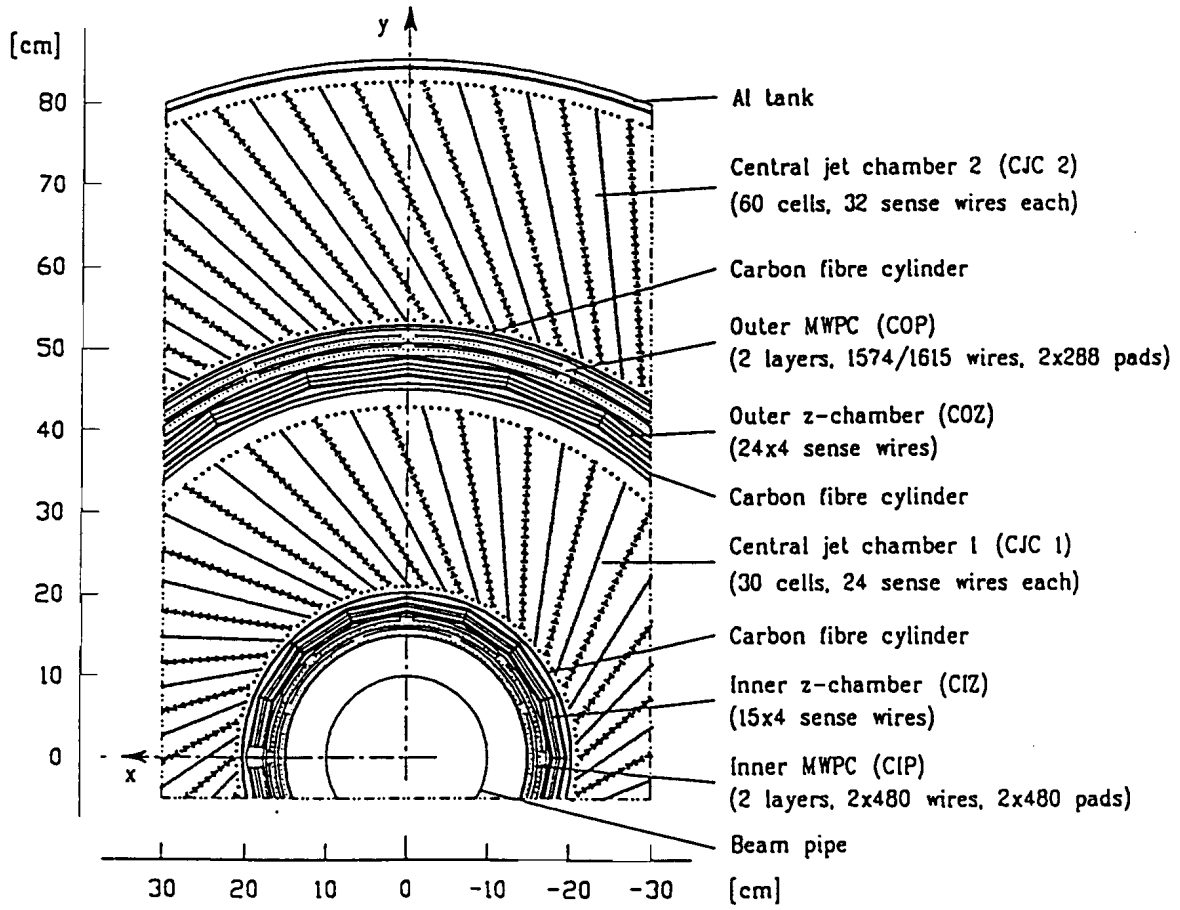


**Figure 1.4**: *Cross section of the central tracking system shown perpendicular to the beam.*

collisions. It has been designed to measure the momentum and angles of charged particles to a precision of $\sigma_p/p^2 \approx 3 \times 10^{-3}$ GeV$^{-1}$ and $\sigma_\theta \approx 1$ mrad respectively, as well as reconstructing jets of high particle density.

The asymmetry between the electron and proton beam energies results in many charged particles being produced at small polar angles relative to the proton (forward) direction. To ensure good efficiency for triggering and reconstruction over the whole solid angle the tracking system is divided into two distinct sections, the central region and the forward region.

### 1.3.1 The Central Tracking Detector

Charged track reconstruction in the central region is based on two large concentric drift chambers, known as central jet chambers (CJC) CJC1 and CJC2, which have wires strung parallel to the beam axis and drift cells inclined with respect to the radial direction in the $r-\phi$ drift plane. The space point resolution in the drift plane is 170 $\mu$m, and by comparing signals read from both wire ends a resolution of 1% of the wire length in $z$ can be achieved. A cross section of the central tracking detector in the $r-\phi$ plane is shown in Figure 1.4.

The measurement of charged track momenta in the central chambers is complemented by two thin drift chambers, the central inner (CIZ) and central outer (COZ) $z$-chambers. The CIZ chamber is located inside CJC1 and the COZ chamber is fitted between CJC1 and CJC2, with the resolutions typically 300 $\mu$m in $z$ and 1-2% of $2\pi$ in $\phi$. The polar angle ranges covered by CIZ and COZ are $16^o < \theta < 169^o$ and $25^o < \theta < 156^o$ respectively.

Central tracker trigger information is obtained from two double layer proportional chambers, the central inner proportional (CIP) chamber, and the central outer proportional chamber (COP), which in combination with forward proportional chambers are used to trigger on tracks coming from a nominal interaction vertex. The CIP chamber is fitted inside CIZ and has an angular coverage of $9^o < \theta < 171^o$. The COP chamber is situated immediately inside CJC2 with an angular coverage of $25^o < \theta < 155^o$. The double layer of chambers in both proportional chambers are rotated by $11.25^o$ in $\phi$ with respect to each other.

### 1.3.2 The Forward Tracking Detector

The forward tracking detector provides an accurate measurement of charged particles for the angular range $5^o < \theta < 30^o$, and is an assembly of three nearly identical 'supermodules'. Each supermodule includes, in increasing $z$, planar wire drift chambers, a multiwire proportional chamber, transition radiators, and

a radial wire drift chamber.

The planar module consists of three drift chambers, each rotated $60^o$ in azimuth with respect to the previous layer and four wires deep in $z$. The wires in each layer are parallel and strung perpendicular to the beam pipe giving an accurate $\theta$ measurement. The high precision enables tracks which pass from the central to the forward tracker to be linked together.

The three forward multiwire proportional chambers (MWPC) are designed to give fast triggering and bunch crossing timing. A chamber has two wire planes interleaved with three cathode planes. The cathode pads are ring shaped, with the inner sixteen rings covering an azimuthal angle of $\pi/8$ and the four outermost rings covering $\pi/16$. A track crossing all or at least two of the three MWPC's must fall into the angular range $6.6^o \leq \theta \leq 18.0^o$ or $5.1^o \leq \theta \leq 21.6^o$ respectively. The timing resolution of such tracks was measured to be 20 ns which is well below the requirement for bunch separation.

The radial wire drift chamber has full azimuthal coverage with 48 separate sectors. Each sector is a drift cell and has wires strung radially outwards providing accurate $r - \phi$ information.

### 1.3.3 The Backward Drift Chamber

The backward drift chamber (BDC) [7] was installed during the 1995 upgrade to improve the measurement of $ep$ events occurring at low $Q^2$ and low $x_{Bj}$. It is mounted in front of the SpaCal calorimeter (see section 1.4.2) and provides an accurate angular measurement of the scattered electron for the interval $153^o < \theta < 177.5^o$. The detector is comprised of four double-layer drift chambers mounted along the $z$-direction with every layer divided into eight sectors in $\phi$, each containing 32 drift cells. Each double-layer is rotated by $11.25^o$ with respect to the previous layer to provide a measurement of the $\phi$ coordinate. The resolution of the BDC for a measurement of the scattered electron polar angle is better than 1 mrad.

### 1.3.4 The Silicon Tracker

The silicon tracker [8] of the H1 detector is positioned between the beam pipe and the central tracker, and has two sections; the central silicon tracker (CST) and the backward silicon tracker (BST). The CST is designed to provide vertex information from precision measurements on charged particle tracks close to the interaction point. The BST allows an accurate measurement of deep inelastic scattering events at small values of $x_{Bj}$ [9].

## 1.4 Calorimetry

To complement the tracking detectors, the H1 calorimeter is designed to measure the energy of neutral particles including photons, distinguish between hadrons and leptons, and measure jets with high particle densities. As the energy of a particle increases the momentum resolution of the tracking detectors deteriorates, since the deflection varies as $1/\sqrt{E}$ in the magnetic field, but the energy resolution of sampling calorimetry improves. Therefore by combining calorimetry with tracking the coverage of a wide range of particle momenta is possible.

The liquid argon calorimeter covers the polar angle range $4^o < \theta < 153^o$, with the calormetric acceptance being in principle completed in the forward direction by the plug calorimeter which is situated between the beam pipe and LAr cryostat.

### 1.4.1 The Liquid Argon Calorimeter

The liquid argon calorimeter is contained within the solenoid magnet giving the advantage of less 'dead' material, and has an inner electromagnetic section (EMC) and an outer hadronic section (HAC). The calorimeter is optimised for the identification and accurate measurement of scattered electrons from high $Q^2$ events. The LAr as a sampling medium has fine granuality and provides stable calibration for hadrons and electrons. Longitudinal and transverse views of the LAr

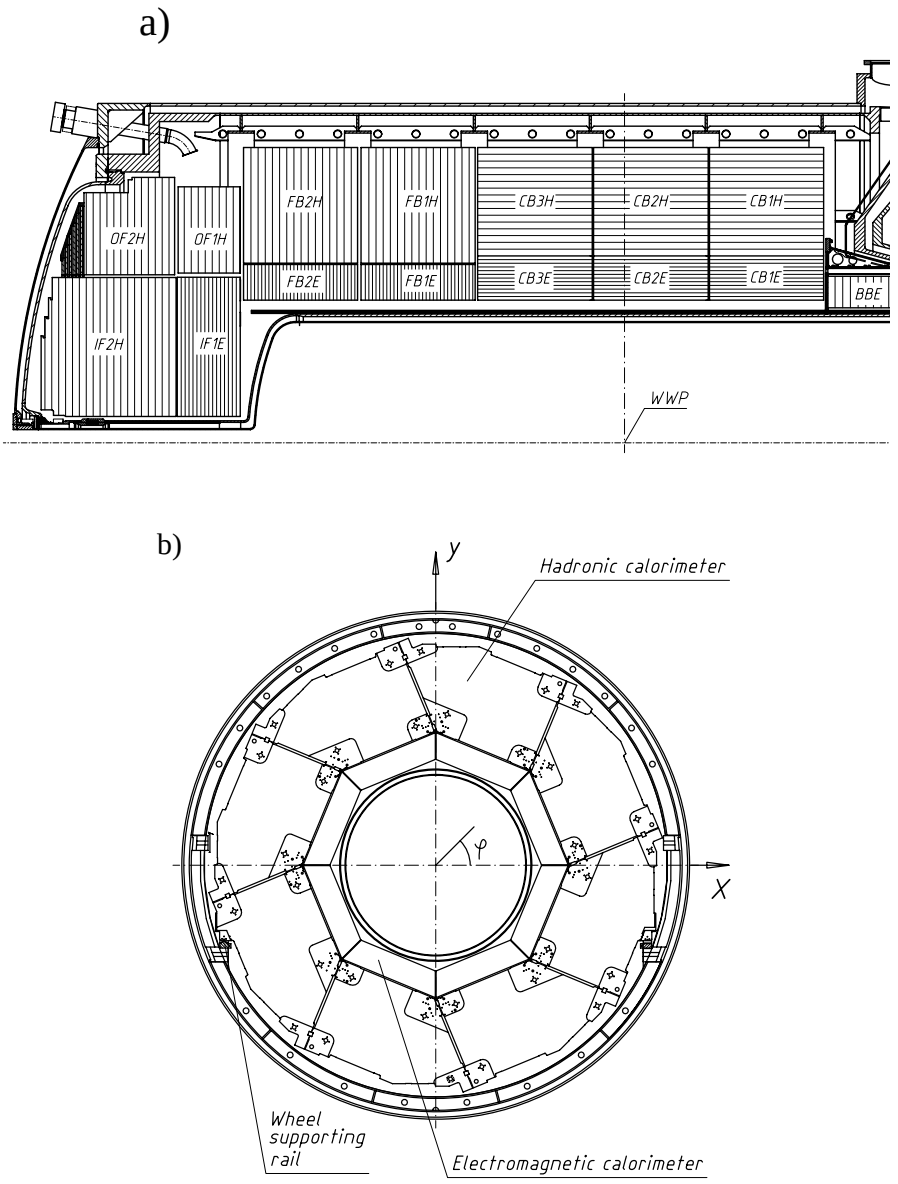


**Figure 1.5**: *a) Longitudinal and b) radial view of the liquid argon (LAr) calorimeter showing the inner electromagnetic and outer hadronic sections.*

calorimeter with respect to the beam axis can be found in Figure 1.5.

The calorimeter is segmented into eight 'wheels' in $z$, each of which is divided into eight identical stacks in $\phi$. The wheel located at the most backward point provides electromagnetic calorimetry only. The electromagnetic cells use lead absorbers 2.4 mm thick together with a 2.35 mm gap filled with LAr. The total showering depth ranges between 20 and 30 radiation lengths ($X_0$). Each hadronic cell consists of a 16 mm stainless steel absorber and a double gap of 2.4 mm containing LAr, with a total depth of 4.5 to 8 interaction lengths ($\lambda$).

The energy resolution for electrons in the EMC is $\sigma(E)/E = 12\%/\sqrt{E} \bigoplus 1\%$, with energy measured in GeV, and for hadrons showering in both the EMC and HAC is $\sigma(E)/E = 50\%/\sqrt{E} \bigoplus 2\%$. The electromagnetic energy scale is known to a precision of 3% and is measured by comparing electron momentum measurements from the tracking system with corresponding electron energy deposits in the LAr calorimeter. The hadronic energy scale is known to a level of 4% and is obtained by studying the transverse momentum balance between scattered electrons and the hadronic final state for high $Q^2$ events.

### 1.4.2 SpaCal

The lead/scintillating-fibre calorimeter [10] or spaghetti calorimeter (SpaCal), shown in Figure 1.6, is designed to give an accurate energy and angular measurement for electrons scattered into the polar interval $153^o < \theta < 177.5^o$. This gives access to a wide range of $Q^2$ and very low values of $x_{Bj}$ ($10^{-5}$) in deep inelastic scattering. The SpaCal has an electromagnetic section (EM) and a hadronic section (HAD), and sufficient timing resolution to assist in the rejection of beam-gas and beam-wall induced backgrounds.

The electromagnetic calorimeter of the SpaCal has a lead to fibre ratio of 2.27:1 and a fibre diameter of 0.5 mm. The basic unit of the EM section has 52 lead plates divided equally into two cells each $40.5 \times 40.5 \times 250$ mm$^3$, corresponding to approximately $27X_0$ and $1\lambda$. The plastic fibres are embedded into the lead

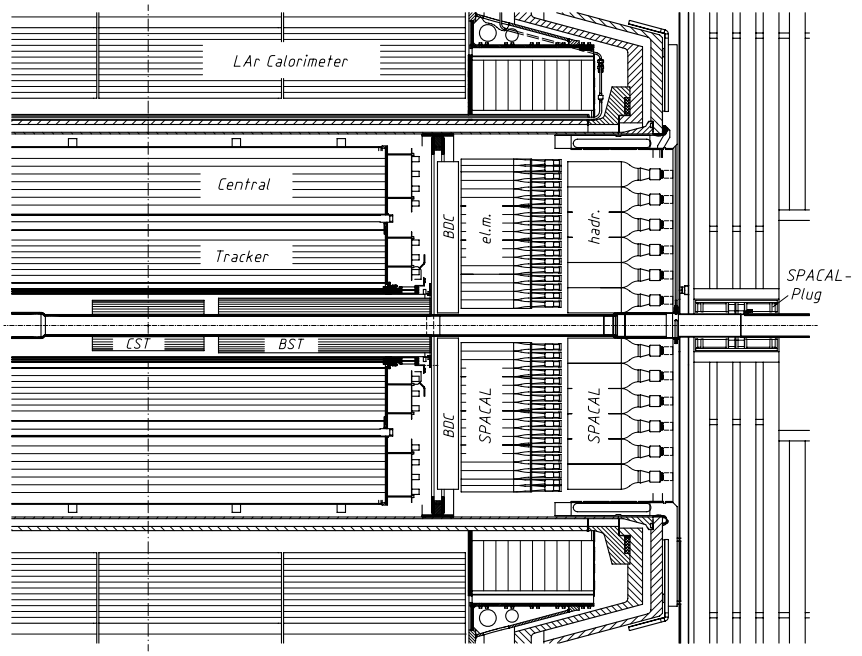


**Figure 1.6**: *Longitudinal view of the H1 detector showing the location of the lead/scintillating-fibre calorimeter (SpaCal).*

absorber matrix and the scintillation light produced is registered by a photomultiplier tube, which has a timing resolution better than 1 ns. The energy resolution is measured as $\sigma_E/E = 7\%/\sqrt{E}$ and the spatial resolution in the transverse plane is 3.4 mm.

The hadronic section has a similar design to the EM section and is used to improve electron-pion separation, thus suppressing photoproduction background events. The lead to fibre ratio is 3.4:1 with a fibre diameter of 1.0 mm. There are 136 cells of cross section $120 \times 120$ mm$^2$, but due to limited space the depth is only $1.2\lambda$ .The combined resolution for a hadronic energy measurement by the HAD and EM sections is $\sigma_E/E = 30\%/\sqrt{E}$.

### 1.4.3 The Plug Calorimeter

The plug calorimeter (PLUG) has been designed to reduce the gap of acceptance for energy flow measurements between the LAr calorimeter ($\theta \approx 4^o$) and the beam pipe ($\theta \approx 0.3^o$). For charged current events there is no observable scattered lepton and therefore event kinematics must be calculated using the hadronic final state. Therefore it is desirable to minimise the loss of transverse momentum due to hadrons emitted close to the beam pipe.

The PLUG consists of nine copper absorber plates interleaved with eight sampling layers of silicon. The PLUG suffers from energy leakage, due to incomplete shower containment, and has coarse sampling resulting in a hadronic energy resolution of $150\%/\sqrt{E}$.

As a result of radiation damage, the PLUG calorimeter is poorly modelled by the detector simulation and is therefore not used at any stage in this analysis.

### 1.4.4 The Tail Catcher

The instrumented iron return yoke, also known as the 'tail catcher', is designed to measure the hadronic energy leaking out of the LAr calorimeter. It is divided into three sections; the forward end cap, the central barrel and the backward end cap, and has a total angular coverage of $6^o < \theta < 172^o$. Each section has eleven out of sixteen limited streamer tubes equipped to measure ionisation for the tail catcher. The instrumented iron energy resolution is measured to be $100\%/\sqrt{E}$. As well as serving as the hadronic tail catcher the instrumented iron can be used to detect muons.

## 1.5 Muon System

### 1.5.1 The Forward Muon Detector

The forward muon detector is designed to measure the momenta of muons in the range between 5 GeV/$c$ and 200 GeV/$c$ for the polar angular interval $3^o \leq \theta \leq 17^o$. The lower limit is determined by the amount of material the muons must penetrate and on the momentum resolution of scattering in the magnet iron. The upper limit is set by the magnetic field of the toroid and the spatial resolution of the drift chambers. Muons with momenta below 5 GeV/$c$ are measured in the forward tracker.

The forward muon detector is comprised of three double-layer drift chambers situated either side of the toroidal magnet. Four planes of drift chambers are orientated to measure the polar angle with the remaining two measuring the azimuthal angle.

## 1.6 Luminosity System

The luminosity is calculated from determining the rate of Bethe-Heitler events $ep \rightarrow ep\gamma$ which have a cross section [6] precisely calculable within QED. The main source of background is bremsstrahlung radiation produced by electrons interacting with residual gas in the beam pipe ($eA \rightarrow eA\gamma$). By using electron 'pilot' bunches this background can be subtracted from the luminosity calculation. The luminosity is then calculated as:

$$L = \frac{R_{tot} - (I_{tot}/I_0)R_0}{\sigma_{vis}}$$

where $R_{tot}$ is the total rate of bremsstrahlung and background events, $R_0$ is the rate in the electron pilot bunches, $I_{tot}$ and $I_0$ are the corresponding electron beam currents, and $\sigma_{vis}$ is the visible part of the $ep \rightarrow ep\gamma$ cross section with the acceptance and trigger efficiency of the luminosity system incorporated.

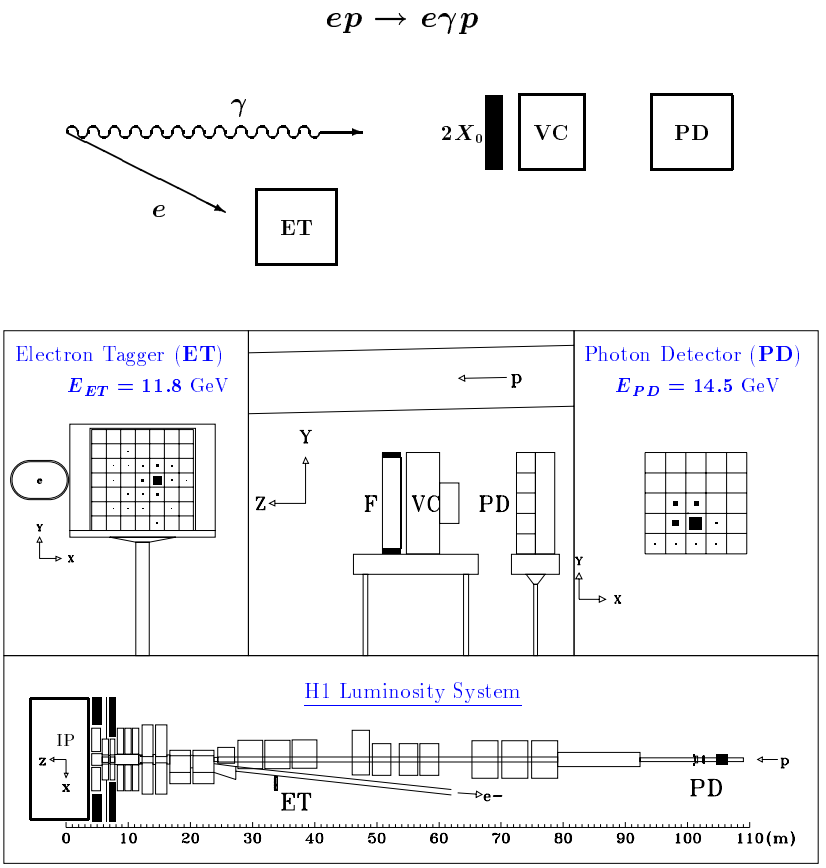


**Figure 1.7**: *Schematic of the H1 luminosity system.*

The layout of the luminosity system is shown in Figure 1.7 and has two main components, the Electron Tagger (ET) and the Photon Detector (PD), located in the backward region close to the beamline and far from the interaction region. This is due to the angular distributions of both the electrons and photons being strongly peaked in the direction of the primary $e$-beam. A set of quadrupoles and a bending magnet located in the region $5.8 < -z < 23.8$ m deflect the scattered electrons into the ET at $z$ = -33.4 m. The photons leave the proton beam pipe through a window at $z$ = -92.3 m and are incident on the PD at $z$ = -102.9 m.

The integrated luminosity delivered by HERA and accumulated by H1 during the 1992-2000 running periods is presented in Figure 1.8 as a function of the day within a given year. A summary of the annual HERA and H1 luminosity performances is given in Table 1.1.

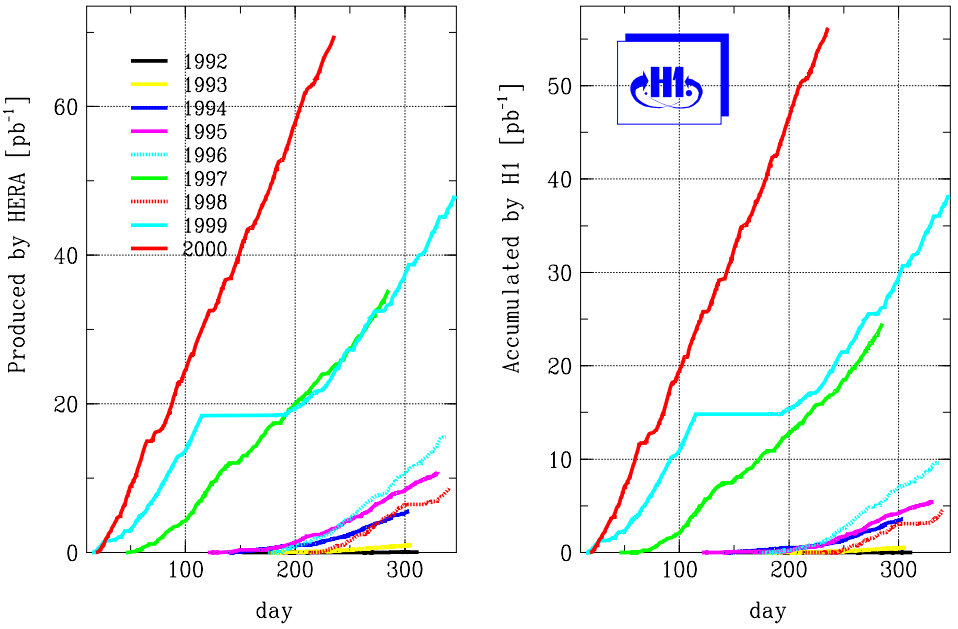


**Figure 1.8**: *Summary of HERA and H1 luminosity performance for 1992-2000.*

| Year | Lumi | HERA L ($pb^{-1}$) | | H1 L ($pb^{-1}$) | | dL (%) |
|---|---|---|---|---|---|---|
| | Runs | Produced | Delivered | On tape | Physics | |
| 2000 | 337 | 70.593 | 67.889 | 60.087 | 56.848 | 1.5 |
| 1999 | 217 | 29.393 | 27.626 | 24.781 | 23.359 | 1.1 |
| 1999 | 169 | 18.316 | 17.419 | 15.726 | 14.812 | 1.1 |
| 1998 | 171 | 8.742 | 8.008 | 6.175 | 4.536 | 1.2 |
| 1997 | 339 | 35.108 | 33.260 | 28.220 | 24.531 | 1.2 |
| 1996 | 228 | 15.603 | 14.460 | 9.887 | 9.605 | 1.3 |
| 1995 | 276 | 10.848 | 9.941 | 6.089 | 5.466 | 1.1 |
| 1994 | 292 | 5.651 | 5.268 | 3.840 | 3.654 | 1.4 |
| 1993 | 214 | 0.999 | 0.890 | 0.558 | 0.520 | 3.4 |
| 1992 | 131 | 0.056 | 0.049 | 0.030 | 0.025 | 6.0 |

**Table 1.1**: *Summary of the HERA and H1 luminosity performances during the 1992-2000 operating periods. The systematic error, dL, does not include a satellite bunch correction. Satellite bunches exist* $\pm 5$ *ns either side of the main proton bunch and consist of escaped protons. The analysis presented in this thesis uses taken during the 1996-1997 running periods.*

## 1.7 Time-of-Flight Counters and the Veto Wall

The time-of-flight (ToF) counters and veto wall are essential components of the H1 detector, being necessary for the rejection of proton beam associated background which occurs at a far higher rate than genuine $ep$ collision events.

The ToF system consists of three scintillators positioned along the beam pipe; the backward ToF at $z = -2.8$ m, the forward ToF at $z = -7.9$ m and the plug ToF at $z = -5.4$ m. Each ToF device has a timing window which enables the separation of particles produced in $ep$ collisions from those particles produced in background processes. The veto wall is formed by two double scintillators positioned at a distance of $z = -6.5$ m and $z = -8.1$ m, respectively upstream from the interaction point. They are designed to detect particle showers known as proton beam halo events, which consist mainly of muons, resulting from inelastic collisions of the proton beam with residual gas in the beam pipe and hardware far upstream from the detector.

## 1.8 Triggering and Data Acquisition

The principal role of the H1 trigger [2] is to select $ep$ interactions of physics interest and to reject background events. Almost every sub-detector used by the H1 experiment has at least one trigger *element*, and these are combined in logical combinations to form the 128 subtriggers (S0 $\rightarrow$ S127) which make up the 'level 1' (L1) trigger. The input rate into L1 is 10.4 MHz, equivalent to a single bunch crossing, and the output rate is 1 kHz. Information from each trigger element must be received within 22 bunch crossings (2.2 $\mu$s) and the central trigger makes a decision on the event quality within a further 2 bunch crossings. To cope with the large bunch crossing rate and to minimise the time the experiment is 'dead' to events in the detector, the trigger system is *pipelined*. This method stores full detector information in memory (pipelining) whilst the trigger information is processed. This introduces no dead-time, ensuring no loss of physics events,

since an event rejected by the central trigger simply falls off the pipeline making room for the next event.

An event is accepted by the central trigger if at least one subtrigger fires, and the pipelines are then rewound by the appropriate 24 bunch crossings, thereby enabling the information for the correct bunch crossing to be read out. The 'L1KEEP' signal is set and the dead-time for the experiment begins as all detectors are disabled. The 'level 2' (L2) trigger receives the same detailed sub-system trigger information and analyses the event in more detail. A further decision whether to keep or reject the event is made within 20 $\mu$s of receiving the 'L1KEEP' signal. If the event is rejected the detector is re-enabled, otherwise the 'L2KEEP' signal is given and full event information is sent to the Central Data Acquisition (CDAQ) system for a 'level 4' (L4) trigger decision. The output rate from L2 is 50 Hz. The 'level 3' (L3) trigger is currently not implemented.

When all event information has been read into the central event builder (CEB) of L4 the dead-time ends. The triggering and reading of an event costs the experiment 1-2 ms of dead-time. The L4 trigger uses approximately 30 parallel processors to run a simplified version of the full event reconstruction routines to examine event topologies. As well as enabling discrimination between different classes of physics events, the bulk of remaining beam-gas and cosmic-ray background events, as well as background from trigger noise, can be rejected. The computing power available at L4 is such that events can be processed at a rate of approximately 45 Hz and events passing L4 filtering are written to tape at a rate of 8 Hz. Approximately 1% of all events rejected are kept for monitoring purposes.

All data passing L4 is written to tape and permanently stored. It is then fully reconstructed using the H1 reconstruction software H1REC [11], and put onto 'production output' (POT) tapes. Software algorithms are used to distinguish the remaining background from events which have topologies of physics interest. Events passing these off-line selections, known as 'level 5' (L5), are classified and stored on data summary tapes (DST).

The physics analysis package H1PHAN [12] is used to convert the real data, stored on the POT's and DST's, or reconstructed Monte Carlo produced from generated physics events passed through the H1 detector simulation program H1SIM [13], into useful 'physics' objects such as four-vectors, calculate event kinematics, reconstruct jets, and provide particle identification.

# Chapter 2

# HERA Physics

## 2.1 Introduction

The $ep$ collider HERA at DESY enables detailed tests of the Standard Model [14] of particle physics, and is unique in its ability to study both QED electron-quark scattering and improve theoretical and phenomenological understanding of the QCD sector, as well as searching for beyond the Standard Model processes such as leptoquark production. The large centre-of-mass energy associated with an electron-proton collider provides access to a vast region of kinematic phase space, with $Q^2$ extending up to $\sim 10^4$ GeV$^2$, equivalent to probing distance scales down to $\sim 10^{-18}$ cm and Bjorken-$x$ down to $10^{-5}$.

This chapter will define the kinematic variables relevant to the analysis presented in this thesis, and give a brief description of the dominant physics processes observed at HERA.

## 2.2 HERA Kinematics

The lowest order diagram for the inclusive lepton-proton deep inelastic scattering (DIS) process $ep \to e' + X$ is shown in Figure 2.1, and defines the relevant four-

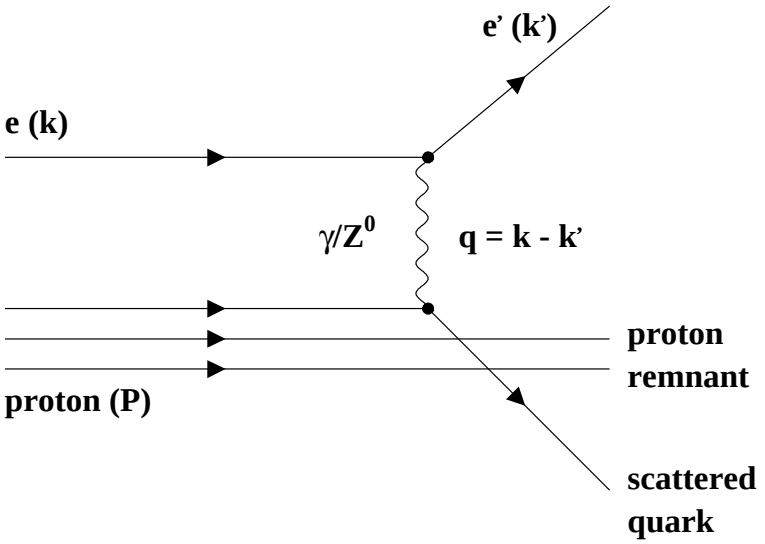


**Figure 2.1**: *Born term QED diagram for lowest order neutral current deep inelastic scattering.*

vectors for its description. The kinematics of DIS at fixed centre-of-mass energy, $\sqrt{s}$, are determined from two independent variables, conventionally chosen from $Q^2$, $W^2$, and the dimensionless scaling quantities $x$ and $y$.

Since the H1 experiment can in principle measure both the scattered electron and the complete hadronic final state, the kinematics of the collision process are over-constrained and thus can be determined from electron variables, hadronic variables or a mixture of both.

The kinematic variables, presented in a Lorentz-invariant form, are defined as:

$$Q^2 = -q^2 = -(k - k')^2 \tag{2.1}$$

$$y = \frac{P \cdot q}{P \cdot k} \tag{2.2}$$

$$x = \frac{Q^2}{2P \cdot q} \tag{2.3}$$

where

- $k$ is the four-momentum of the incident electron,
- $k'$ is the four-momentum of the scattered lepton,
- $P$ is the four-momentum of the incident proton,
- $q$ is the four-momentum of the exchange boson.

$Q^2$ is the negative four-momentum transfer squared between the incident and scattered lepton, $x$ viewed in the infinite momentum frame and using the Quark Parton Model (QPM) is the fraction of the proton momentum carried by the struck parton (Bjorken-$x$), and $y$ calculated in the proton rest frame can be interpreted as the fraction of the initial electron energy transferred to the hadronic system.

Neglecting the proton mass, the invariant mass squared of the hadronic final state, $W^2$, is calculated as:

$$W^2 = (P + q)^2 \approx Q^2 \left(\frac{1 - x}{x}\right) \tag{2.4}$$

The centre-of-mass energy squared, $s$, of the colliding system, neglecting the proton and electron masses, is given as:

$$s = (k + P)^2 \approx 4E_e E_P \tag{2.5}$$

where $E_e$ and $E_P$ are the incoming electron and proton energies respectively. The analysis presented in this thesis studies data taken at $s \approx 90\,200$ GeV$^2$, although

with the proton energy now upgraded to 920 GeV the current HERA $s$ reaches 101 200 GeV$^2$. Equations 2.2, 2.3 and 2.5 imply the very useful relation:

$$Q^2 = sxy \tag{2.6}$$

and given the high centre-of-mass energy, HERA can access $x$ values down to $\sim 10^{-5}$ in the deep inelastic regime ($Q^2 > 10$ GeV$^2$). For small $x$ values, $y$ can be approximated to $\approx W^2/s$ using equations 2.4 and 2.6.

The kinematic variables adopted in this thesis are determined using both the polar angle, $\theta_e$, measured relative to the proton beam ('forward') direction and the energy, $E'_e$, of the scattered electron, through the relations:

$$Q^2 = 4E_e E'_e \cos^2\frac{\theta_e}{2} \tag{2.7}$$

$$y = 1 - \frac{E'_e}{E_e}\sin^2\frac{\theta_e}{2} \tag{2.8}$$

and the variable $x$ is calculated using equation 2.6.

For a large region of the kinematic plane, corresponding approximately to $y < 0.1$, the energy of the scattered electron is close to that of the incident electron beam energy. This results in a Jacobian peak in the scattered electron energy distribution, termed the 'kinematic peak', and enables accurate calibration.

## 2.3 Photoproduction

The dominant contribution to the lepton-proton cross section measured at HERA is from photoproduction processes [15, 16], whereby the incident electron radiates an almost real photon, i.e. $Q^2 \sim 0$, which interacts with the proton. This is a major source of background to DIS studies due to its enormous cross section, and associated final state products can give a false DIS signature.

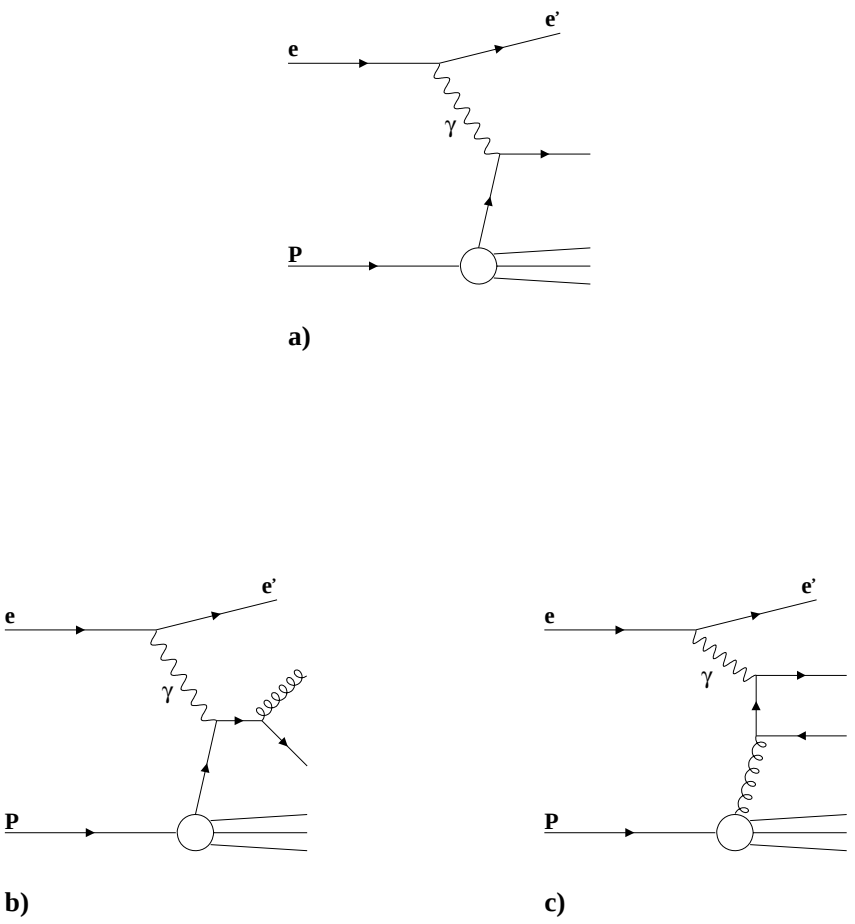


**Figure 2.2**: *Examples of a) zero order and b-c) leading order direct photoproduction processes.*

Photoproduction has a dominant, *soft* component due to the photon fluctuating into a low mass vector meson, described by the Vector Dominance Model (VDM) [17], but hard photon processes (*direct* or *resolved*) can produce measurable high $p_T$ jets [18] of particles, enabling new tests of QCD and measurements of the gluon content of the photon [16]. In direct photoproduction processes the near mass-shell photon couples directly to a charged parton from the proton (see Figure 2.2a-c). Alternatively the photon can develop a hadronic structure through quantum fluctuations, which can be probed by parton-parton collisions known as resolved processes (see Figure 2.3a-b). The quark and gluon content of

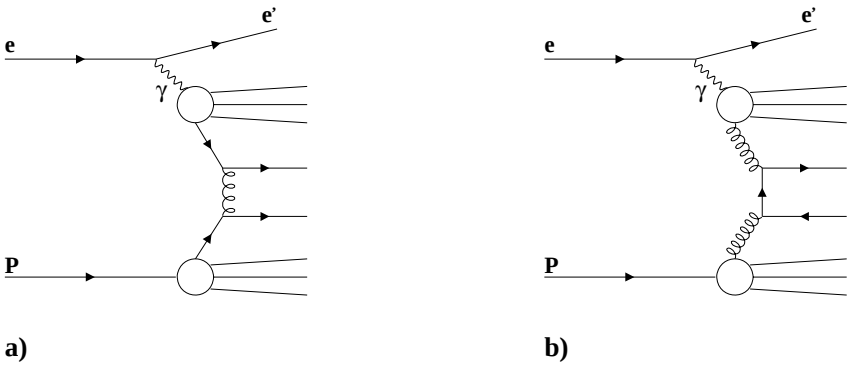


**Figure 2.3**: *Examples of a-b) leading order resolved photoproduction processes.*

the photon is parameterised by the photon structure function $F^{\gamma}$.

## 2.4 Deep Inelastic Scattering

Precise measurements of DIS have proven invaluable in extending the understanding of the partonic substructure of the nucleon. In neutral (charged) current DIS, an incident charged (neutral) lepton exchanges a highly virtual gauge boson, $\gamma^*$ or $Z^0$ ($W^{\pm}$), with a resolved charged parton within the nucleon, which then scatters and separates from the nucleonic remnant. An example of an actual neutral current deep inelastic scattering event detected by H1 is shown in Figure 2.4. By measuring the resultant hadronic final state, information can be gained about the underlying dynamics of the nucleon enabling tests of perturbative QCD.

The theory of QCD is unable to predict the parton densities within the nucleon, but a successful description of their evolution has enabled the calculation of parton density functions from experimental data. The DGLAP (Dokshitzer-Gribov-Lipatov-Altarelli-Parisi) formalism [21] provides a theoretical framework for the description of the $Q^2$ evolution of the nucleonic structure functions. The DGLAP equations are calculated by resumming leading logarithmic contributions to the

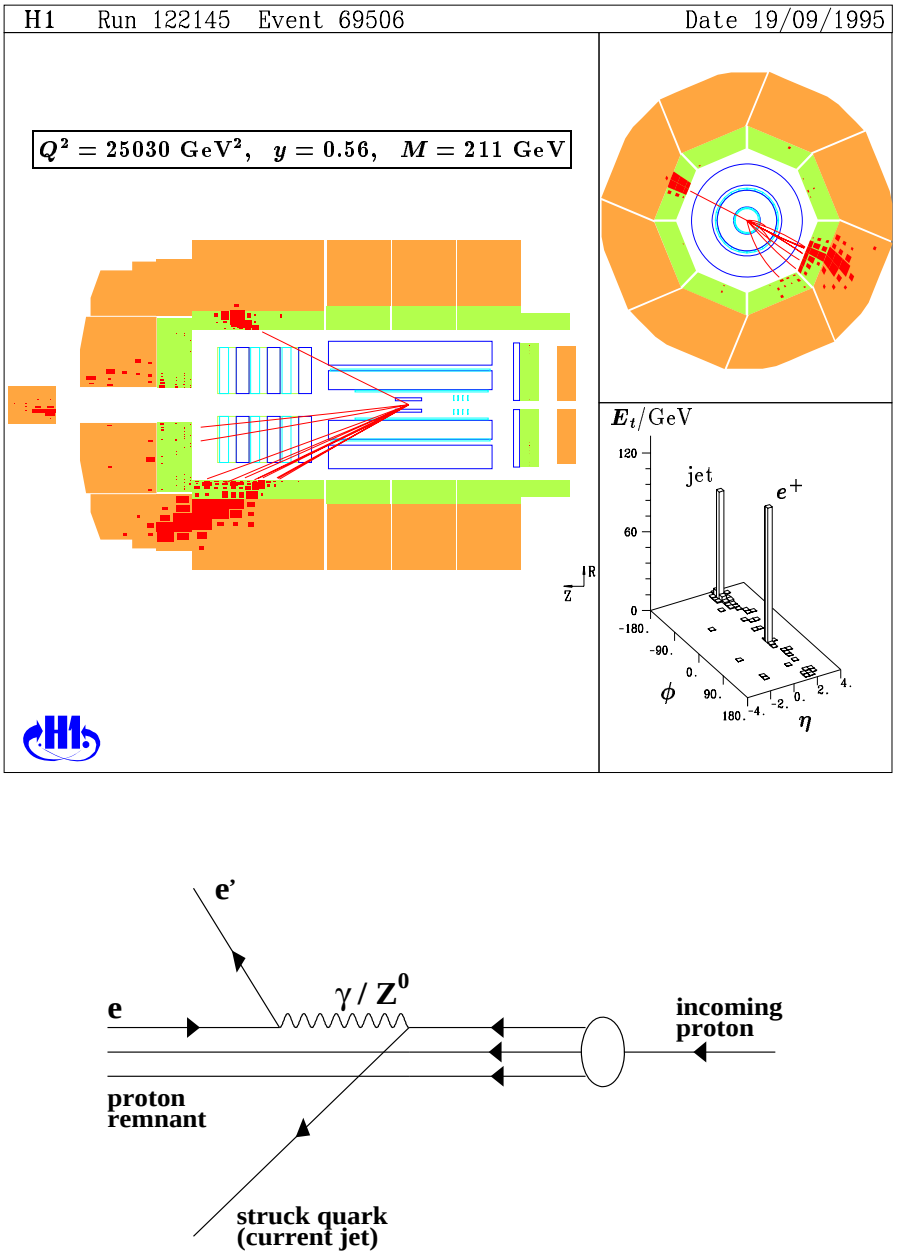


**Figure 2.4**: *Event display of a neutral current deep inelastic scattering event detected in the H1 detector.*

parton evolution of the form $(\alpha_s \ln(Q^2/Q_0^2))^n$, where $\alpha_s$ is the strong coupling, and predict the scaling violation of the structure function $F_2$ seen in Figure 2.5a. However, at small enough $x$ this description is expected to cease to be a good approximation, since the dominant contribution to the evolving parton density will be from terms in $\ln(1/x)$. The BFKL (Balitsky-Fadin-Kuraev-Lipatov) equation [22] sums terms in $(\alpha_s \ln(1/x))^n$, and it is this scheme which is expected to be most applicable in the description of very low $x$ physics.

The double differential cross sections for neutral current (NC) and charged current (CC) DIS interactions at HERA are written in terms of the proton structure functions ($F_2$, $F_L$, $F_3$) [23] as:

$$\frac{\mathrm{d}^2\sigma^{NC}}{\mathrm{d}x\mathrm{d}Q^2} = \frac{4\pi\alpha^2}{xQ^4}\left[\left(1-y+\frac{y^2}{2}\right)F_2(x,Q^2) - \frac{y^2}{2}F_L(Q^2,x) \pm \left(y-\frac{y^2}{2}\right)xF_3(x,Q^2)\right] \tag{2.9}$$

$$\frac{\mathrm{d}^2\sigma^{CC}}{\mathrm{d}x\mathrm{d}Q^2} = \frac{G_F^2}{2\pi x\left(1+\frac{Q^2}{M_W^2}\right)^2}\left[\left(1-y+\frac{y^2}{2}\right)F_2(x,Q^2) - \frac{y^2}{2}F_L(Q^2,x) \pm \left(y-\frac{y^2}{2}\right)xF_3(x,Q^2)\right] \tag{2.10}$$

where $G_F$ is the Fermi coupling constant and the upper (lower) sign applies for electron (positron) proton scattering. Quark and antiquark couplings to the longitudinal component of the exchanged virtual photon are described by the longitudinal structure function $F_L$. The structure function $F_3$ measures parity violating contributions from $Z^0$ and $W^\pm$ exchange, which only become significant when the momentum transfer $Q$ is comparable to or larger than their respective masses. Above the electroweak unification scale ($Q^2 \geq M_W^2 \approx M_Z^2$) the NC and CC cross sections become comparable in magnitude, as seen in Figure 2.6, due to the similar coupling strengths of the electromagnetic and weak interactions.

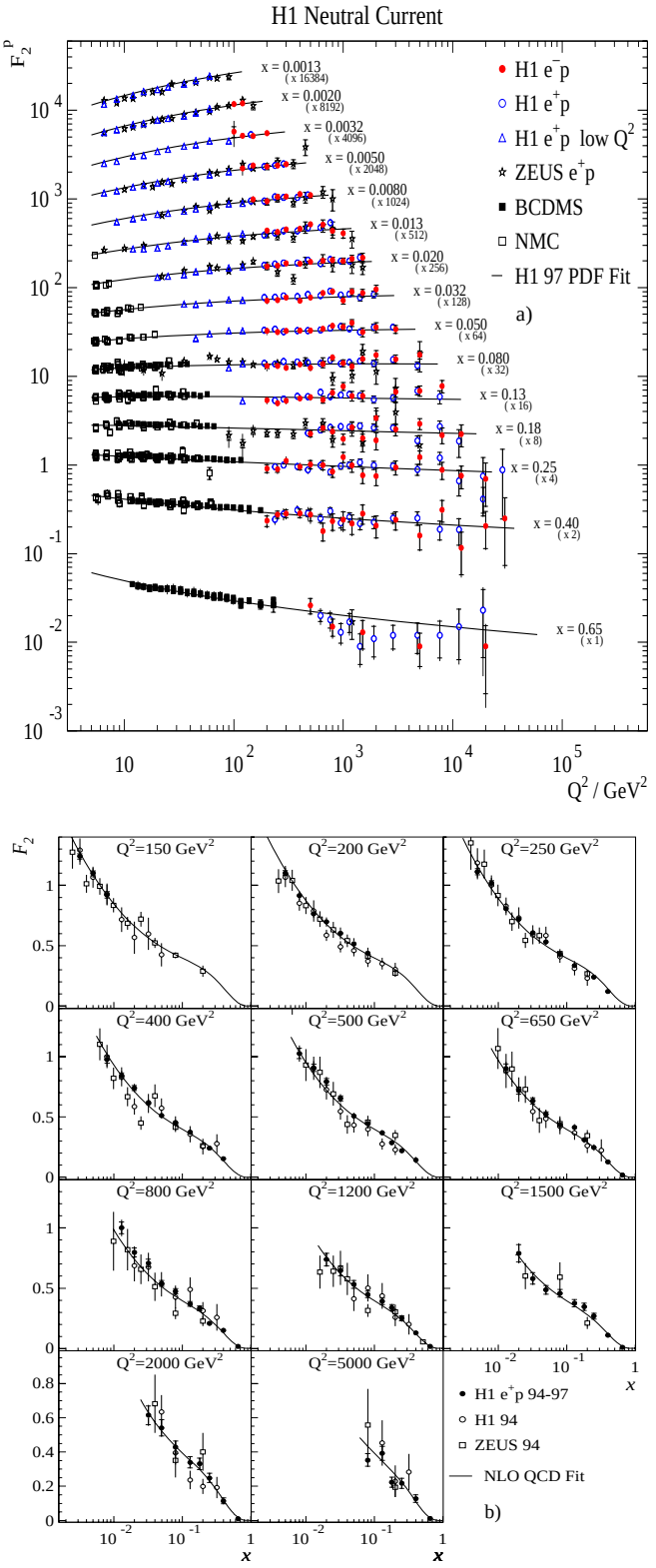


**Figure 2.5**: *The structure function $F_2$ measured a) as a function of $Q^2$, for various values of $x$ [19], and b) as a function of $x$, for various values of $Q^2$ [20]. In each case a NLO QCD fit is overlayed.*

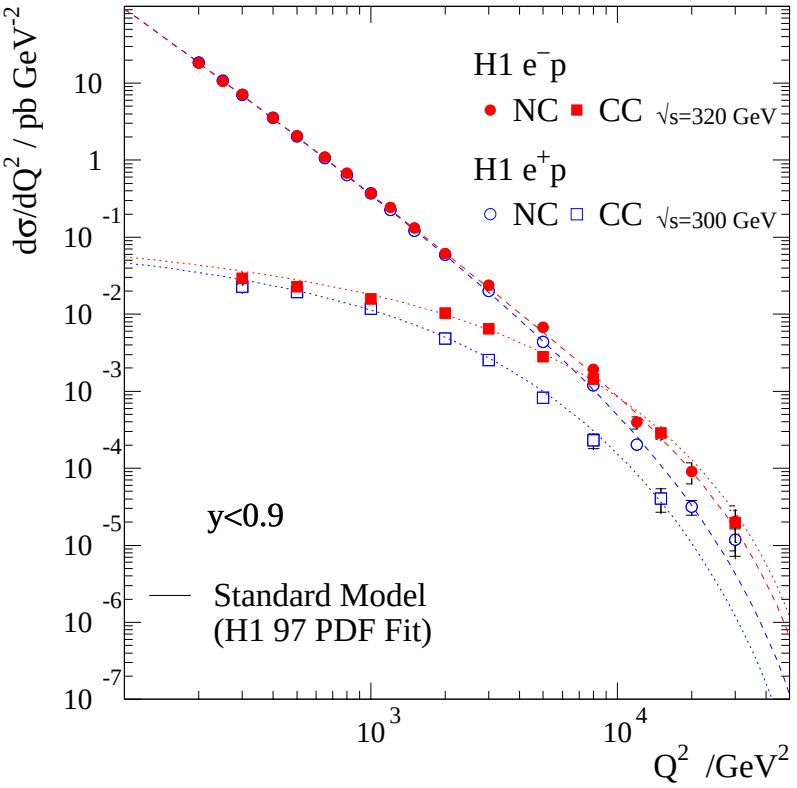


**Figure 2.6**: *The single differential cross section $d\sigma/dQ^2$ for neutral current (circles) and charged current (squares) scattering, as measured by H1 [19] for two different centre-of-mass energies, $\sqrt{s} = 300$ GeV (open symbols) and $\sqrt{s} = 320$ GeV (closed symbols). Overlayed is a theoretical prediction calculated using the Standard Model.*

## 2.5 QCD Parton Dynamics

At very low $x$ the simplistic notion of DIS as a process in which a highly virtual gauge boson interacts with a quasi-free, point-like parton in the proton must be modified. The interacting parton carries such a small fraction of the proton's momentum that the phase space for gluon emission between the photon and proton becomes so large that many partons can be radiated before the hard scatter with the photon. Electron-proton collisions at HERA have given access to new kinematic regions in DIS down to very small values of $x$, making important tests of different parton emission schemes possible. The observed strong rise of the structure function $F_2$ [20, 24] as $x$ decreases (see Figure 2.5b), due to a steeply

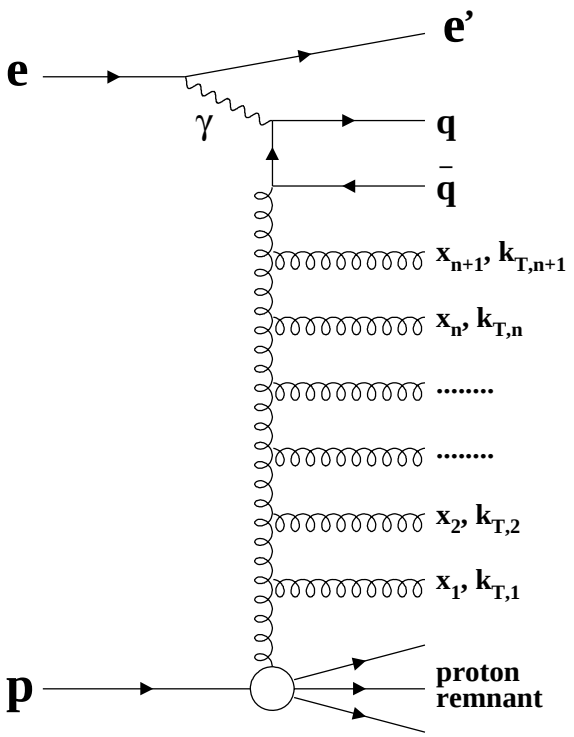


**Figure 2.7**: *Schematic Feynman diagram for ep DIS at low x.*

rising gluon density within the proton, is consistent with both DGLAP and BFKL calculations. However, measurements of charged particle transverse momentum ($p_T$) spectra [25] and transverse energy flows ($E_T$) [26] in the hadronic final state may offer increased sensitivity to the underlying QCD parton dynamics at low $x$.

Figure 2.7 is a schematic representation of a gluon emission ladder extending between the virtual photon and proton in a DIS interaction at low $x$. Within the DGLAP framework, the evolving parton cascade has a strong ordering of parton transverse momenta, $k_T$, ($k_{T1}^2 \ll ... \ll k_{Ti}^2 \ll ...Q^2$) with respect to the incident proton direction. The BFKL parton evolution scheme has a strong ordering in fractional longitudinal momentum ($x_n \ll x_{n-1} \ll ... \ll x_1$), but no ordering in transverse momentum ($k_{Ti}^2 \approx k_{Ti+1}^2$). By the nature of strong ordering in $k_T$,

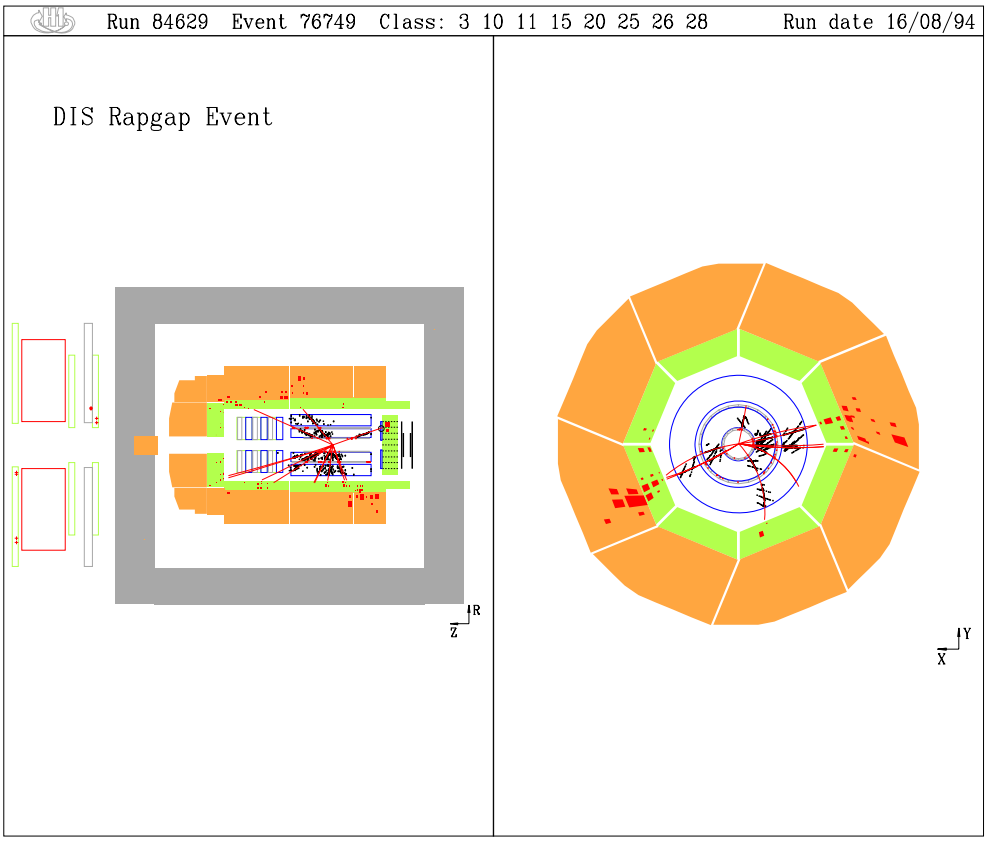


**Figure 2.8**: *Event display of a diffractive dijet deep inelastic scattering event detected by H1 showing a lack of hadronic activity in the forward direction.*

there is a suppression of the available phase space for gluon emission towards the proton, leading to the DGLAP expectation of less $E_T$ and a softer $p_T$ spectrum, as compared to BFKL, in the region between the struck quark and proton remnant.

Also, recent measurements [27] of the inclusive $\pi^0$ cross section are well described by an analytic leading order (LO) calculation based on the BFKL formalism, which is in contrast to a DGLAP inspired model's failure to describe fully the data in the low $x$ region.

## 2.6 Large Rapidity Gap Events

A new class of DIS process, known as *diffraction* [28], has been studied in detail by the H1 and ZEUS experiments, and is characterised by a lack of hadronic activity

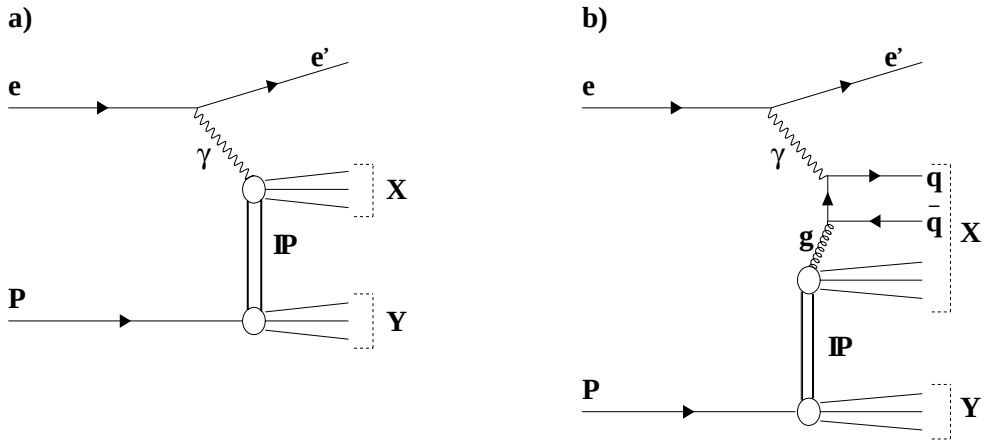


**Figure 2.9**: *a) Illustration of generic process, $ep \to eXY$, in which the largest rapidity gap separates the hadronic sub-systems X and Y. b) An example of a leading order diffractive boson-gluon fusion (BGF) process resulting in diffractive dijet production.*

in the forward region of the detector due to the absence of a gluon emission ladder between the photon and proton. A typical DIS event has energy flow in the direction of the remnant proton, which within the colour string model results from fragmentation of the colour flux tube connecting the scattered quark and remnant proton system. However, it has been shown at HERA [29] that 8-10% of DIS events have a large rapidity gap (LRG) (see Figure 2.8) with no energy flow in-between two hadronic sub-systems. A possible mechanism for diffractive scattering, illustrated in Figure 2.9, is modelled in terms of the virtual photon interacting at the proton vertex with an exchanged colourless object, called a pomeron ($I\!P$), which carries the vacuum quantum numbers.

## 2.7 Physics Beyond the Standard Model

Recent results [30] from HERA have hinted at possible new physics beyond the current Standard Model. An excess of observed number of events above the Standard Model expectation for $Q^2 > 15000$ GeV$^2$ has been reported by the H1 and

ZEUS collaborations. Possible explanations for this high $Q^2$ excess include leptoquark production, supersymmetric squark production, and the interference of Standard Model bosons with a new heavy boson, in contact interactions. The H1 experiment has also reported an excess of events with a high transverse momentum of the hadronic final state, in addition to highly energetic isolated leptons and a large amount of missing transverse momentum, which again hints at possible new physics processes. The scheduled luminosity upgrade [31] at HERA will provide a substantial increase in new data which may help establish the source of these exciting observations.

# Chapter 3

# QCD Models

## 3.1 Introduction

In the late 1960s, observational evidence [32] gathered from electron-nucleon scattering experiments at the Stanford Linear Accelerator Centre (SLAC) suggested that nucleons are composed of pointlike objects. As highlighted in section 2.4, lepton-nucleon cross sections can be parameterised in terms of *structure functions*, and when measured, the structure function $F_2(x, Q^2)$ was found to be approximately independent of the relevant scale, $Q^2$. This behaviour, known as *Bjorken scaling*, was interpreted as the interaction of the electron with a charged, pointlike object, termed a parton [33], via the exchange of a photon. Within the theoretical framework used to describe the observations of hadron spectroscopy, the partons were identified with the quarks postulated by Gell-Mann [34]. Using complementary measurements of $F_2$ from neutrino-nucleon and electron-nucleon scattering experiments, it was further deduced that the quarks carry a fractional electric charge.

This Chapter will introduce the theory of Quantum Chromodynamics (QCD) which is used to describe parton-parton interactions, and highlight aspects relevant to the analysis presented in this thesis.

## 3.2 Quantum Chromodynamics

In the current Standard Model of particle physics the most successful description of the strong interactions of partons is by the gauge theory Quantum Chromodynamics, which under local SU(3) colour transformations is invariant. The six known flavours of quark are each a colour triplet, carrying a colour charge of either red, blue or green. Strong interactions are mediated by the exchange of massless, vector gauge bosons, known as gluons, which exist in a colour octet as a result of the non-Abelian structure of QCD. The self-coupling of the gluon is in contrast to the photon of the electromagnetic interaction, which being electrically neutral does not interact with other photons.

The coupling of the strong interaction, $\alpha_s$, has a 'running' $Q^2$ dependence induced by anti-screening effects associated with gluon-gluon interactions. As the energy scale increases the strength of the coupling decreases, and this property is known as *asymptotic freedom*. At large enough energies, equivalent to very small distance scales, the theory of QCD can be approximated in the form of a perturbative, calculable theory, allowing testable predictions to be made. However, for low energy, large distance, scales the strong coupling grows such that the perturbative approximation breaks down, and quarks and gluons can no longer be treated as quasi-free. This *confinement* of partons leads to the production of hadrons, detectable colour singlet bound-states of quarks and antiquarks, through *fragmentation*, and no quark or gluon has ever been observed in isolation.

To leading order, $\alpha_s$ can be expressed as:

$$\alpha_s = \frac{12\pi}{(33 - N_f)\ln(Q^2/\Lambda^2_{QCD})} \tag{3.1}$$

where $N_f$ is the number of active flavours in QCD, and $\Lambda_{QCD}$ is a free parameter determined from experiment and currently estimated to be $\Lambda_{QCD} \sim$ 200-300 MeV, governing the scale at which perturbative QCD breaks down. In the low energy, non-perturbative regime phenomenological models must be used to describe quark

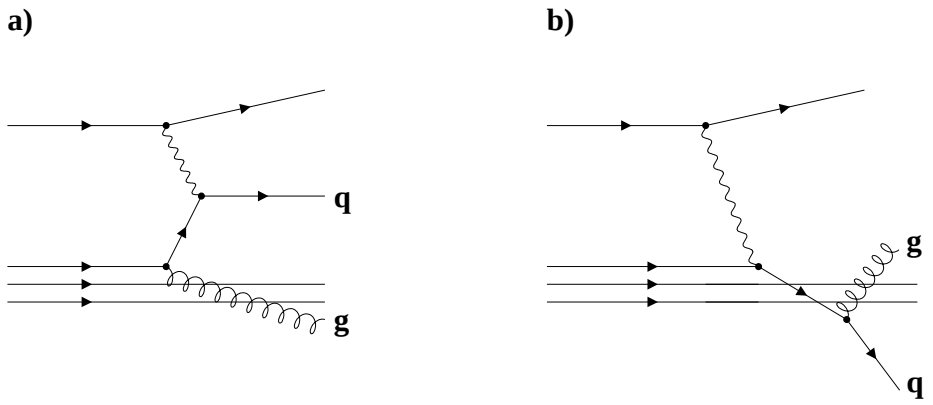


**Figure 3.1**: *First order Feynman diagrams for a) initial state and b) final state QCD Compton scattering.*

and gluon evolution (see section 3.8 for discussion).

## 3.3 The Quark Parton Model

The Quark Parton Model (QPM) is the simplest description of the lepton-parton scattering process, and is essentially a zeroth order approximation of QCD. Since QCD radiation is neglected, the proton is viewed as comprising of three valence quarks $| uud >$ only. Due to the short time-scale of the scattering, the partons of the proton can be considered non-interacting, with the exchanged virtual gauge boson scattering off a 'free' quark carrying a fraction $x$ of the proton's momentum.

In the QPM, the parton only couples to transversely polarised photons due to helicity conservation, and by neglecting contributions from the weak interaction, the neutral current (NC) deep inelastic scattering (DIS) cross section, as defined in equation 2.9, can be simplified to:

$$\frac{\mathrm{d}^2\sigma^{NC}}{\mathrm{d}x\mathrm{d}Q^2} = \frac{4\pi\alpha^2}{xQ^4}[xy^2F_1(x,Q^2) + (1-y)F_2(x,Q^2)] \tag{3.2}$$

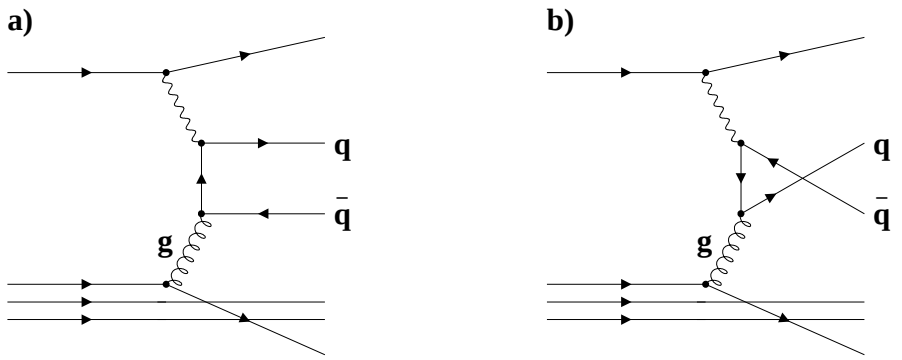


**Figure 3.2**: *First order Feynman diagrams for Boson-Gluon Fusion.*

The structure functions $F_1(x, Q^2)$ and $F_2(x, Q^2)$ are related by the Callan-Gross relation [35]:

$$F_2 = 2xF_1 \tag{3.3}$$

which is a consequence of the quarks having spin-$\frac{1}{2}$ and is well borne out by data.

Within the QPM the structure functions are interpreted as parton momentum distributions weighted by the electric charge squared, and are expressed in terms of the quark and antiquark densities. The structure functions can be written as:

$$F_1(x, Q^2) = \frac{1}{2} \sum_q e_q^2 [q(x, Q^2) + \overline{q}(x, Q^2)] \tag{3.4}$$

$$F_2(x, Q^2) = x \sum_q e_q^2 [q(x, Q^2) + \overline{q}(x, Q^2)] \tag{3.5}$$

The function $q(x, Q^2)\mathrm{d}x$ is the probability of finding a quark of flavour $q$ and electric charge $e_q$, carrying a fraction of the proton's momentum in the range $x$ to $x + \mathrm{d}x$, when probed at a scale $Q^2$. The sums are over all quark flavours.

## 3.4 Leading Order Processes

The simple QPM can be extended to include higher order contributions to the electron-parton cross section. For example, in first order the interacting quark can radiate a gluon before or after interacting with the exchanged gauge boson, $\gamma^* q \rightarrow qg$ (see Figure 3.1). A further leading order (LO) contribution to the DIS cross section is from a gluon within the proton splitting into a $q\overline{q}$ pair (see Figure 3.2), with one of the pair coupling to the exchanged boson, $\gamma^* g \rightarrow q\overline{q}$. These processes, for which the matrix element has been calculated exactly, are known as QCD Compton (QCDC) and Boson-Gluon Fusion (BGF) processes respectively.

## 3.5 Parton Showers

In models of DIS the emission of gluons by the struck quark, both before and after the interaction vertex, gives rise to initial and final state parton showers, producing an observable scaling violation [36, 37] in both the structure functions and fragmentation functions. A near mass-shell parton within the incoming nucleon can initiate a parton cascade (or shower) before the boson vertex by radiating gluons, becoming increasingly space-like ($m^2 < 0$) after each branching. After the exchanged electroweak boson is absorbed, the struck quark either becomes on-shell, or has a time-like virtuality ($m^2 > 0$). In the latter case a final state shower will result, with both the virtuality of the struck quark and the off-shell mass of the radiated gluon decreasing after each successive branching. Any time-like parton produced in an initial shower will have a similar evolution.

The general properties of initial and final state parton showers are described by the DGLAP equations, since both are based on the branching processes $q \rightarrow qg$, $g \rightarrow gg$, and $g \rightarrow q\overline{q}$. The corresponding splitting functions, $\mathcal{P}_{ab}$, are given as [21]:

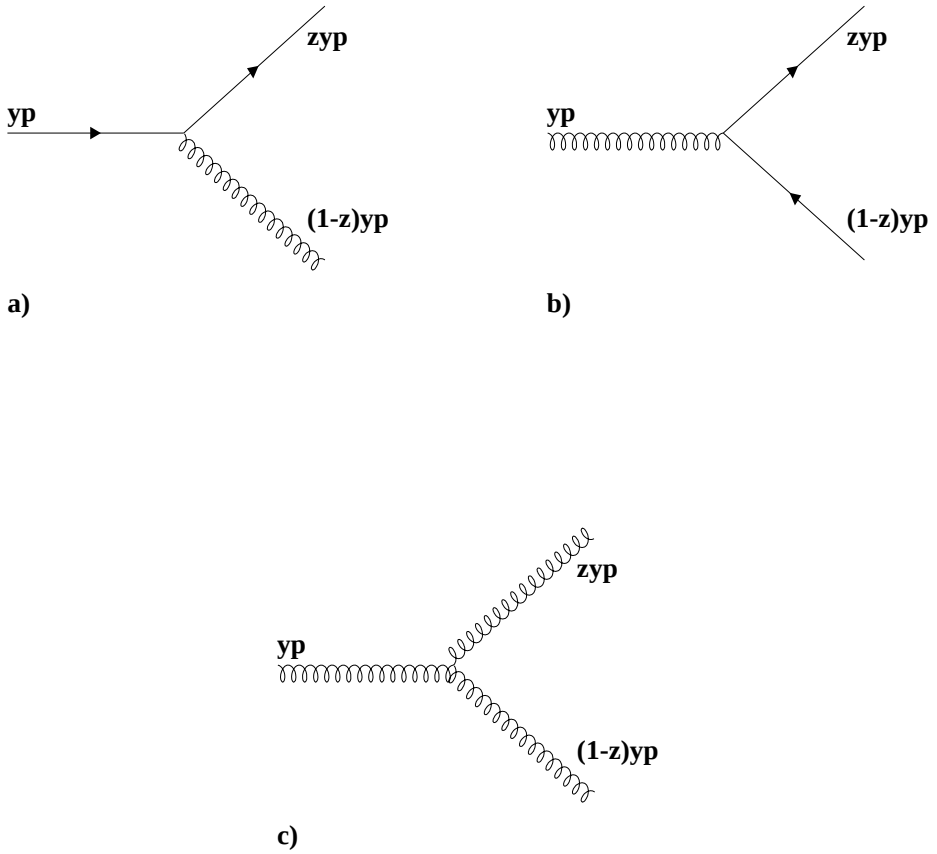


**Figure 3.3**: *Diagrams for QCD splitting functions a) $\mathcal{P}_{qq}$, b) $\mathcal{P}_{qg}$ and, c) $\mathcal{P}_{gg}$.*

$$\mathcal{P}_{qq}(z) = \frac{4}{3}\left[\frac{1+z^2}{1-z}\right] \tag{3.6}$$

$$\mathcal{P}_{qg}(z) = \frac{1}{2}\left[z^2 + (1-z)^2\right] \tag{3.7}$$

$$\mathcal{P}_{gq}(z) = \frac{4}{3}\left[\frac{1+(1-z)^2}{z}\right] \tag{3.8}$$

$$\mathcal{P}_{gg}(z) = 6\left[\frac{(1-z)}{z} + z(1-z) + \frac{z}{(1-z)}\right] \tag{3.9}$$

and interpreted to be the probability of a parton $a$ originating from a parton $b$ carrying a fraction $z$ of its longitudinal momentum.

## 3.6 Expectations from the Modified Leading Logarithmic Approximation

The Modified Leading Logarithmic Approximation (MLLA) [38, 39, 40] to perturbative QCD has provided a successful theoretical framework within which to describe soft and semihard multiparticle production resulting from fragmentation. The formulation of MLLA theory is based upon an expansion of the DGLAP parton evolution equations summed to NLO, and incorporates QCD colour coherence [39], the running of $\alpha_s$, energy-momentum conservation, and uses the exact form of the parton splitting functions. Calculated predictions of partonic final state energy and momentum spectra can be related directly to hadronic final state spectra by applying the hadronisation prescription of Local Parton-Hadron Duality (LPHD)(see section 3.8.1 for discussion). Predictions are dependent upon two free parameters only; the infra-red cut off, $Q_0$, at which the parton evolution is terminated, and a universal effective QCD scale, $\Lambda_{eff}$, which appears in the one-loop expression for the running coupling, but is not directly related to $\Lambda_{QCD}$.

The approximately Gaussian shape (the so-called 'hump-backed plateau') of the inclusive scaled momentum spectrum of the hadronic final state, also known as the fragmentation function, is a well-known prediction of MLLA-LPHD theory, and has been experimentally observed [41, 42] as shown in Figure 3.4. It has been proposed that this depletion of soft partons is due to the phenomena of QCD colour coherence, whereby wide angled, low $p_t$ gluon emission is suppressed due to the inability of long wavelengths gluons to resolve the individual colour charges of partons within the parton cascade.

The analytical form of the inclusive momentum spectrum, $\overline{D}^{lim}(\xi, Y)$ [38, 39, 43], for massless partons radiated from a source of energy $E^*$ is calculated under the

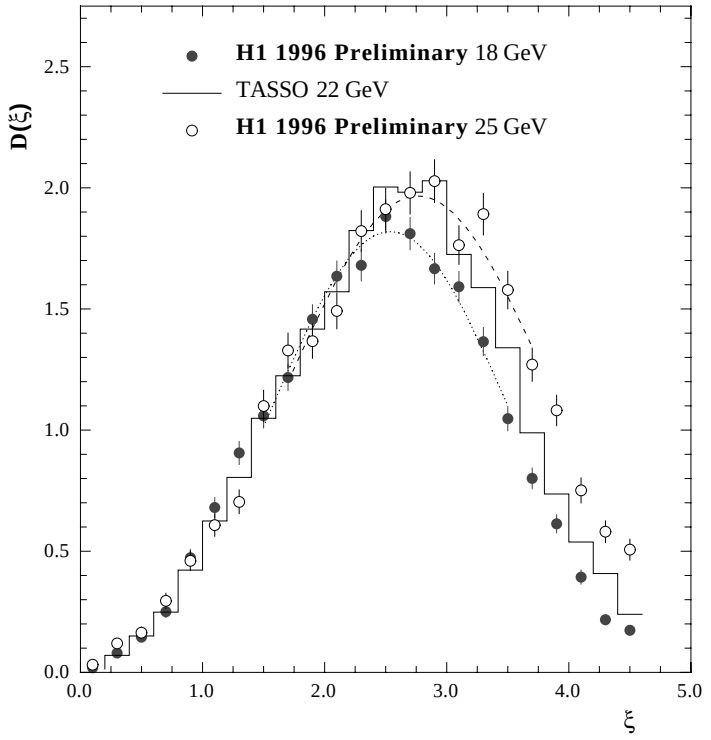


**Figure 3.4**: *H1 results [41] for the fragmentation function $D(\xi)$ measured as function of $\xi$, where $\xi = \ln(1/x_p)$, at 18 GeV (closed circles) and 25 GeV (open circles) in Q compared to TASSO data (histogram) at 22 GeV in $E^*$. The broken line is a simple Gaussian function fitted to H1 data over the interval $\pm$ 1 unit in $\xi$ about the statistical mean.*

premise of the *limiting spectrum*, whereby the parton cascade is evolved down to a limit of $Q_0 = \Lambda_{eff}$. The relevant fragmentation variables are defined to be $\xi = \ln(1/x_p)$, where $x_p$ is the scaled momentum and is related to the hadronic momentum, $p^{hadron}$, through the definition, $x_p = 2p^{hadron}/E^*$, and the dimensionless variable $Y = \ln(E^*/2\Lambda_{eff})$. By introducing a constant of proportionality, $\kappa^{ch}$, and using LPHD, the MLLA calculation can be related directly to the observed inclusive hadronic spectrum, $1/\sigma\ \mathrm{d}\sigma/\mathrm{d}\xi$, where no particle identification is used, such that:

$$\frac{1}{\sigma}\frac{\mathrm{d}\sigma}{\mathrm{d}\xi} = \kappa^{ch}\overline{D}^{lim} \tag{3.10}$$

The shape of the spectrum can be approximated by a Gaussian distribution in the neighbourhood of the peak, and is given by:

$$\frac{1}{\sigma}\frac{\mathrm{d}\sigma}{\mathrm{d}\xi} \approx N(Y)\left(\frac{c_1}{\pi Y^{3/2}}\right)\exp\left(\frac{-c_1[\xi-\xi_{max}]^2}{Y^{3/2}}\right) \tag{3.11}$$

where $c_1 = \sqrt{36N_c/b}$ and $b = 11N_c/3 - 2N_f/3$ are fully determined constants dependent upon the number of active colours, $N_c$, and flavours, $N_f$, in QCD. The average charged particle multiplicity, $N(Y)$, is proportional to the parton multiplicity under the assumption of LPHD.

If the momentum transfer, $Q$, is taken to be equivalent to the scale $E^*$ (see Chapter 6 for discussion), then $Y = \ln(Q/2\Lambda_{eff})$. The energy evolution of the peak position, $\xi_{peak}$, and width, $\xi_{width}$, of the Gaussian distribution has been calculated in the limiting spectrum, assuming gluon coherence, to be:

$$\xi_{peak} = 0.5Y + c_2\sqrt{Y} + \mathcal{O}(1) \tag{3.12}$$

$$\xi_{width} = \sqrt{Y^{3/2}/2c_1} \tag{3.13}$$

where $c_2 = B\sqrt{b/16N_c}$ and $B = (\frac{11}{3}N_c + \frac{2}{3}N_f/N_c^2)/b$. It is dependent upon one free parameter, $\Lambda_{eff}$, and an $\mathcal{O}(1)$ term, assumed to be constant, containing higher order corrections. A simultaneous fit using equations 3.12 and 3.13 to inclusive charged hadron peak and width data measured by H1 [41] ($\Lambda_{eff} = 0.21 \pm 0.02$ GeV, $\mathcal{O}(1) = -0.43 \pm 0.06$) shows very good agreement with results obtained in an analysis [42] of combined $e^+e^-$ data ($\Lambda_{eff} = 0.21 \pm 0.02$ GeV, $\mathcal{O}(1) = -0.32 \pm 0.06$) giving support to the universality of quark fragmentation, i.e. the quark scattered out of the proton in DIS is the same particle that quantum mechanically tunnels out of the vacuum in an $e^+e^- \to q\bar{q}$ annihilation, with the resulting fit presented in Figure 3.5.

By extending the description of fragmentation to include exclusive hadron pro-

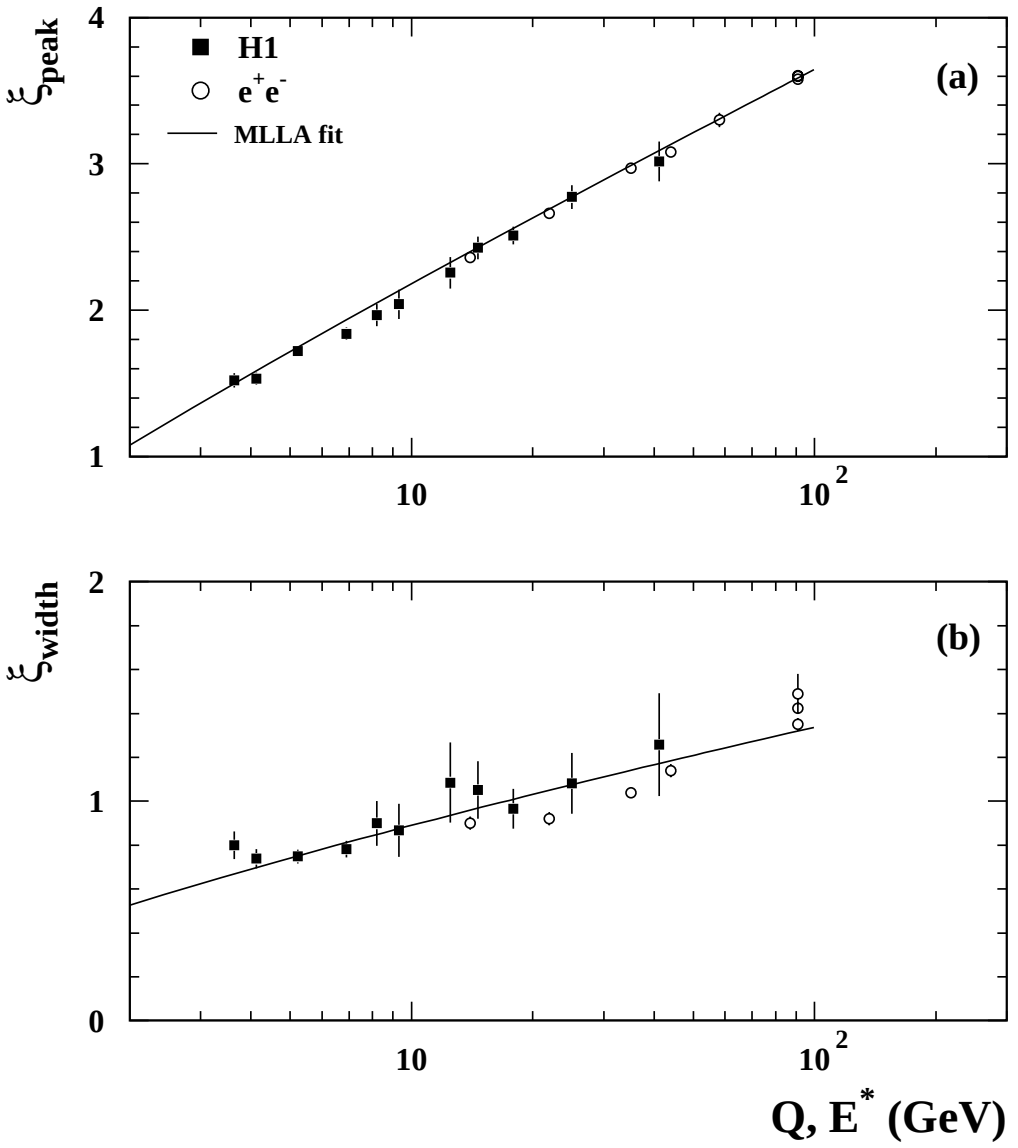


**Figure 3.5**: *H1 results [41] showing the evolution of the fragmentation function a) peak position, $\xi_{peak}$, and b) width, $\xi_{width}$, measured as function of Q compared to $e^+e^-$ results as a function of the $E^*$. The solid line is a simultaneous fit of H1 peak and width data alone to the MLLA/LPHD expectation defined in equations 1.12 and 1.13.*

duction, the approximation of the limiting spectrum can no longer be applied. The cut-off of the parton cascade ($Q_0^h(m_h) > \Lambda_{eff}$) will differ between hadronic species as a result of their range of masses. A high energy approximation for the exclusive peak and width evolution has been calculated as [40]:

$$\xi_{peak}^h = \frac{24N_c c_2}{c_1} + \frac{1}{2}(\tau - \lambda) + c_2(\sqrt{\tau} - \sqrt{\lambda}) \tag{3.14}$$

$$\xi_{width}^h = \left[\frac{1}{2c_1}(\tau^{\frac{3}{2}} - \lambda^{\frac{3}{2}}) - \frac{9}{8c_1^2}(\tau - \lambda)\right]^{\frac{1}{2}} \tag{3.15}$$

where $\tau = \ln(Q/2\Lambda_{eff})$ and $\lambda = \ln(Q_0^h/\Lambda_{eff})$. This perturbative expectation is for a universal energy evolution of the peak position, and a narrowing of the fragmentation function as the mass increases. Within the MLLA/LPHD framework there is no recipe for relating $Q_0^h$ to the quantum numbers or masses of the hadrons produced. A subject of this thesis is to measure the fragmentation properties of identified hadronic species, and to carry out a phenomenological study of the relationship between $Q_0^h$ and hadronic mass.

## 3.7 The Colour Dipole Model

The Colour Dipole Model (CDM) [44] describes the emission of QCD radiation in terms of a colour field generated by a chain of radiating colour dipoles extending between a pair of colour charges. A gluon is emitted from a color dipole between the $q\bar{q}$ pair, forming two independent colour dipoles, one between the gluon and quark, the other between the gluon and antiquark. Further gluons can be radiated, leading to a chain of colour dipoles, where one gluon connects two dipoles, and one dipole connects two gluons. The CDM is considered more BFKL-like than DGLAP-like as the evolving parton cascade has no strong ordering in the transverse momenta, $k_T$.

The CDM has had considerable success in describing data from $e^+e^-$ experi-

ments [45], but two important modifications must be made if the CDM is to be applied successfully to DIS. The quark-antiquark pair produced from $e^+e^-$ annihilation may be treated as point-like, which is in contrast to DIS where only the struck quark can be considered point-like as the proton remnant is an extended structure. This leads to a suppression of gluon radiation with wavelengths greater than the size of the proton remnant. Secondly, the boson-gluon fusion process described in section 3.4 is not present in the CDM, as the possibility of the radiated gluon splitting into a $q\bar{q}$ pair is not included, and must therefore be added on separately.

## 3.8 Hadronisation Models

The process of *hadronisation* [46] converts the partonic final state, resulting from evolving the initial hard scattering process perturbatively through multiple gluon emission, into the observed hadronic final state. This occurs in the low energy, large distance scale regime and is therefore non-perturbative. At present, hadronisation must rely upon phenomenological models for its description, and this section will briefly detail some of them.

### 3.8.1 Local Parton-Hadron Duality

Although not implemented in any Monte Carlo, the most general hadronisation prescription is that of Local Parton-Hadron Duality (LPHD) [43], in which the effects of large distance scales are neglected entirely. According to the hypothesis of LPHD the measurable hadronic spectra are required to be directly proportional to the partonic spectra obtained from perturbative calculations, and are related by an overall normalisation constant determined from experiment.

### 3.8.2 Independent Fragmentation

The Independent Fragmentation Model, first proposed by Field and Feynman in 1978 [47], generates a hadronic final state by treating the fragmentation of each parton independently. A fragmenting quark is combined with an antiquark from a $q\overline{q}$ pair produced from the vacuum, forming a first-generation meson. The leftover quark can be fragmented in an identical manner, and so on, until the remaining energy from the initial parton falls below some cut-off. This scheme can be modified to incorporate baryon production [48], where occasionally a quark will combine with a diquark formed from the vacuum in a $qq - \overline{qq}$ pair, creating a baryon state, $|qqq>$. The remaining antidiquark combines with an antiquark from a $q\overline{q}$ pair, forming an antibaryon state, $|\overline{qqq}>$.

A basic deficiency of the Independent Fragmentation Model is its inability to conserve both energy and longitudinal momentum simultaneously, as the fragmenting parton is assumed to remain on mass shell. Several different schemes for energy and momentum conservation have been devised, see for example [49].

### 3.8.3 String Fragmentation

In the Lund String Model [50] of fragmentation, the separating partonic system loses kinetic energy to a colour flux tube, or colour string, stretching between it. The potential energy stored in the colour string grows linearly with distance of separation between the partonic system, with the string breaking in two when it becomes energetically probable for a $q\overline{q}$ to tunnel out of the vacuum. The two resulting pieces of colour string continue to separate, and if sufficient energy is available further breaking can occur, iteratively generating $q\overline{q}$ pairs until only on mass-shell hadrons remain. An illustration of the Lund String Model is shown in Figure 3.6, and is the principal hadronisation scheme used in this analysis.

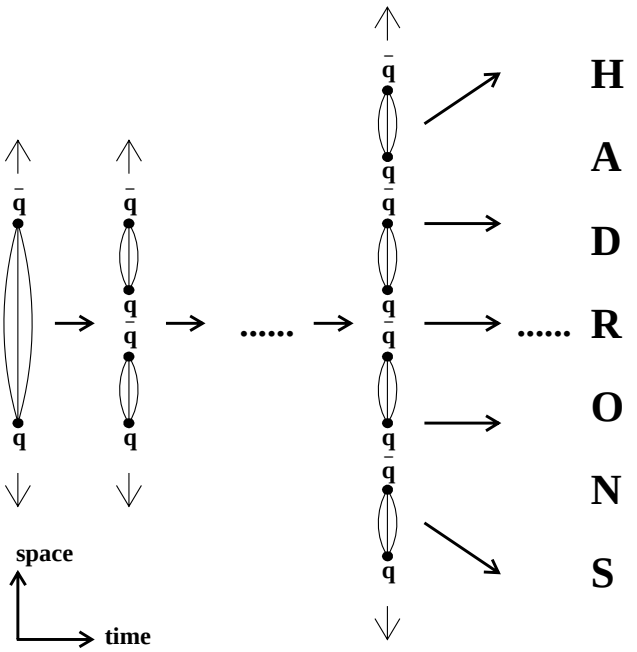


**Figure 3.6**: *Illustration of the Lund String Model of fragmentation. The initial $q\bar{q}$ system separates with a colour string stretching between it, until it becomes energetically favourable for the string to break with a $q\bar{q}$ pair forming out of the vacuum. The two resulting pieces of colour string continue to separate with further breakages occurring, until only on mass-shell hadrons remain.*

### 3.8.4 Cluster Fragmentation

The concept of Cluster Fragmentation [51] models the partonic final state as colour-singlet clusters of partons which decay into the observed hadrons. The simplest method for forming colour-singlet clusters after the termination of the parton cascade is by first splitting gluons non-perturbatively into $q\overline{q}$ pairs, with neighbouring colour connected objects then combining into colour singlets, with further splitting possible until a minimum value of the cluster mass is reached. Each cluster can then decay, producing hadrons according to the available phase space.

## 3.9 QCD Event Generators

Monte Carlo models can be used to simulate lepton-nucleon scattering and the production of the hadronic final state, enabling a comparison of theoretical expectation with experimental data, as well as acceptance, efficiency, and resolution calculations. The hard interaction between an exchanged virtual boson and a parton is calculated using a leading order electroweak cross section, with the inclusion of a first order QCD correction given by exact $\mathcal{O}(\alpha_s)$ matrix elements. Models differ in their treatment of the parton cascade, which simulates higher order QCD corrections needed to generate additional partons, and the hadronisation prescription used.

The Monte Carlo LEPTO [52] generates the electroweak scatter between the incident electron and parton, and can be interfaced with different generators of the parton cascade. For the analysis presented in this thesis, data is compared to a Monte Carlo model in which the parton shower is produced using a QCD cascade generator, ARIADNE [53], based upon the Colour Dipole Model, and will henceforth be referred to as MEAR (**M**atrix **E**lement + **AR**iadne) Monte Carlo. Alternatively, the parton cascade can be described using the leading-log approximation of the DGLAP evolution equations which form the basis of MEPS [54] (**M**atrix **E**lement + **P**arton **S**hower) Monte Carlo. In each case, hadronisation is performed using the Lund String Model as implemented in the program JETSET [55].

HERWIG [56] is a general purpose event generator of high energy hadronic processes. The showering algorithm again uses a leading logarithmic approximation, and includes colour coherence and soft gluon interference. Hadronisation is performed using the Cluster Fragmentation Model.

# Chapter 4

# DIS Event Selection

## 4.1 Introduction

The majority of data recorded using the H1 detector is produced by cosmic ray and beam-gas induced events, and photoproduction processes. Only a small fraction consists of neutral current (NC) deep inelastic scattering (DIS) events which are of interest to the analysis presented in this thesis. This Chapter will define a number of selection cuts designed to obtain a relatively clean sample of NC DIS events, and will discuss several methods for reconstructing the event kinematic variables defined in Chapter 2.

## 4.2 Event Selection

This analysis considers two independent data samples taken during the 1996 and 1997 running periods in which 820 GeV protons were in collision with 27.5 GeV positrons. The integrated luminosities for the 1996 run are calculated as $\sim 5.6$ pb$^{-1}$ and $\sim 7.6$ pb$^{-1}$ for low $Q^2$ and high $Q^2$ events respectively, and similarly, $\sim 9.1$ pb$^{-1}$ and $\sim 9.6$ pb$^{-1}$ for the 1997 run[1].

[1]For the 1997 running period a severe problem was observed in the central jet chamber (CJC) of the H1 detector. The CJC information for sets of consecutive events was corrupted

The H1 trigger divides the data into a subset of low and high $Q^2$ events. The data are then subjected to a number of selection cuts principally designed to reduce unwanted background, thereby providing a high quality sample of NC DIS events. The kinematic cuts used are projected onto the ($x$,$Q^2$) plane, together with a sample of 1996 data, as shown in Figure 4.1, and are discussed in detail below.

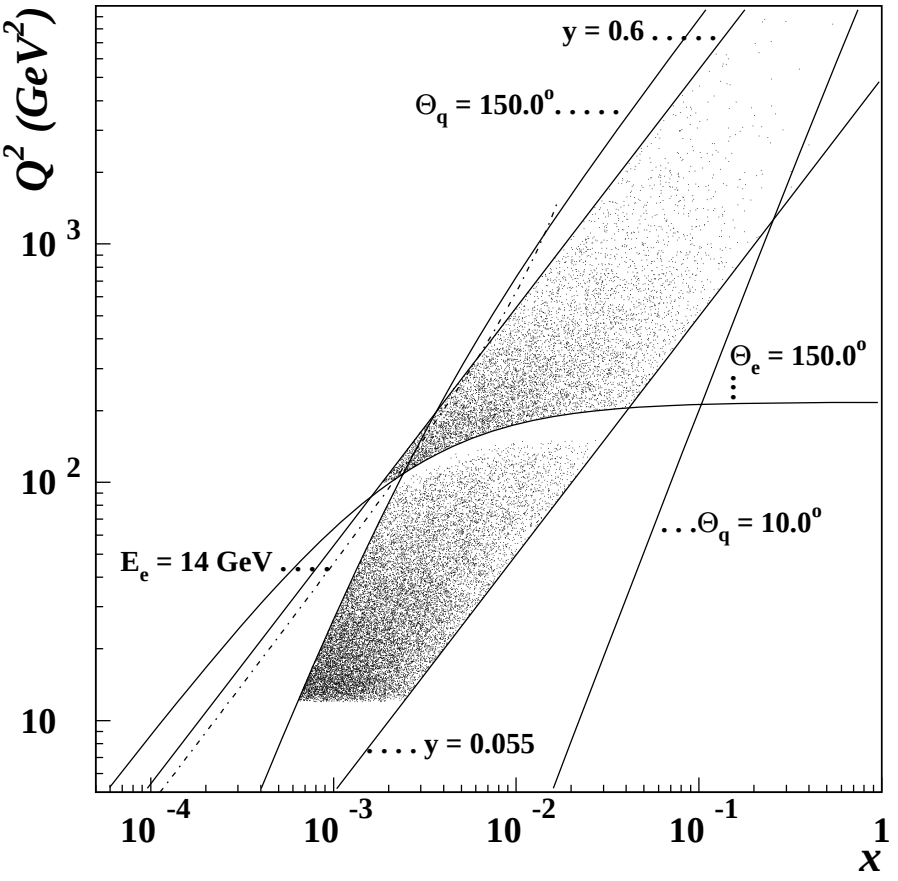


**Figure 4.1**: *Sample of 1996 low and high $Q^2$ data displayed on the ($x$,$Q^2$) plane, showing the phase space region defined by some of the events cuts applied in this analysis. Event kinematics have been calculated using the Electron Only method.*

due to a malfunctioning readout, and the affected events have been removed.

### 4.2.1 Specific Low $Q^2$ NC DIS Event Selection

For an $ep$ interaction to be classified as a low $Q^2$ NC DIS event an electron must be detected in the SpaCal with a corresponding track in the BDC. The scattered electron is required to lie in the polar angular interval $153.0^\circ < \theta_e < 177.5^\circ$ and have an energy $E'_e > 14$ GeV, which corresponds to a $Q^2$ range of $12 < Q^2 < 150$ GeV$^2$. Historically, the requirement of a scattered electron energy above 14 GeV is imposed to explicitly remove low energy electron candidates resulting from the decay of $\pi^0$ hadrons produced in photoproduction events. However, in practice, practically no such events survive this constraint, as the polar angle, $\theta_q$, of a scattering massless quark is selected to lie in the interval $10^\circ < \theta_q < 150^\circ$, ensuring excellent acceptance in the current hemisphere of the Breit frame (see Chapter 6) in a manner independent of the detector.

### 4.2.2 Specific High $Q^2$ NC DIS Event Selection

A NC DIS event is classified as high $Q^2$ if a scattered electron is detected in the LAr calorimeter. The electron must lie in the polar angular range $10^\circ < \theta_e < 150^\circ$, and events have a $Q^2$ in the range $100 < Q^2 < 20\,000$ GeV$^2$.

### 4.2.3 Common NC DIS Event Selection

A number of selection cuts are common to both low and high $Q^2$ data samples.

The inelasticity variable as calculated using both the Electron Only method ($y$) and the Jacquet-Blondel method ($y_{JB}$) (see section 4.6), is required to lie in the interval $0.055 < y, y_{JB} < 0.6$. The sum $\Sigma_i(E_i - p_{z,i})$ over all calorimetric energy deposits can be shown to equal twice the incident electron energy, and events are selected for which $35 < \Sigma_i(E_i - p_{z,i}) < 70$ GeV. Together, these selection cuts minimise the size of necessary initial state QED radiative corrections, and remove photoproduction events which have low values of the sum $\Sigma_i(E^i - p_{z,i})$.

As discussed in section 2.6, approximately 10% of DIS events have little or no energy deposited in the forward region of the detector, and are defined to be diffractive. The generation of diffractive events has not been included in the Monte Carlo models used in this analysis, and therefore a cut is made to remove such events from the data sample. Events are selected which have more than 0.5 GeV of energy deposited in the angular interval $4.4^\circ < \theta < 15.0^\circ$ [29].

The $z$ coordinate of the event vertex is calculated using the H1 tracking system, and is required to be within 35 cm of the nominal interaction point. This ensures the kinematic variables are well determined from the scattered electron's properties, and removes beam-gas induced events occurring upstream from the detector.

The number of events in the 1996 and 1997 data samples passing the selection criteria outlined in sections 4.2.1-4.2.3 is presented in Table 4.1 for each of the $Q^2$ intervals used in this analysis.

### 4.2.4 Comparison Between 1996 Data and MEAR Monte Carlo

In Figures 4.2 to 4.4 comparisons between 1996 data and reconstructed MEAR Monte Carlo are shown, after full event selection, for a number of event variables. Although in general the Monte Carlo gives a very good distribution of the low $Q^2$ data, the $z$-vertex distribution (ZVTX) of the Monte Carlo is shifted by $\sim 2$ cm relative to the data, and fails to describe the scattered electron energy spectrum. Therefore, events in the Monte Carlo are re-weighted using the ratio of the $z$-vertex distribution and, independently, the scattered electron energy spectrum in data to Monte Carlo.

In Figure 4.3, the description of the event variables by Monte Carlo after the above procedure is excellent. The Monte Carlo provides a very good description of the event variables in high $Q^2$ data, as presented in Figure 4.4, and no re-weighting

| $Q^2$ interval ($\mathrm{GeV}^2$) | 1996 | | 1997 | |
|---|---|---|---|---|
| | $< Q >$ (GeV) | Events | $< Q >$ (GeV) | Events |
| $12 \rightarrow 150$ | 5.6 | 95 086 | 5.6 | 150 319 |
| $100 \rightarrow 20\,000$ | 18.2 | 9 711 | 18.2 | 13 347 |
| $12 \rightarrow 15$ | 3.7 | 16 009 | 3.7 | 25 354 |
| $15 \rightarrow 20$ | 4.1 | 18 028 | 4.1 | 28 710 |
| $20 \rightarrow 40$ | 5.3 | 33 334 | 5.3 | 52 559 |
| $40 \rightarrow 60$ | 7.0 | 13 075 | 7.0 | 20 953 |
| $60 \rightarrow 80$ | 8.3 | 7 287 | 8.3 | 11 285 |
| $80 \rightarrow 100$ | 9.4 | 4 332 | 9.4 | 6 450 |
| $100 \rightarrow 150$ | 10.9 | 3 419 | 11.0 | 5 008 |
| $100 \rightarrow 175$ | 12.0 | 1 761 | 12.1 | 2 390 |
| $175 \rightarrow 250$ | 14.4 | 2 830 | 14.5 | 4 010 |
| $250 \rightarrow 450$ | 18.1 | 3 435 | 18.2 | 4 554 |
| $450 \rightarrow 1\,000$ | 25.2 | 1 205 | 25.2 | 1 627 |
| $1\,000 \rightarrow 2\,000$ | 36.5 | 352 | 36.5 | 517 |
| $2\,000 \rightarrow 20\,000$ | 57.4 | 173 | 57.2 | 249 |

**Table 4.1**: *Number of events passing the selection criteria, as defined in section 4.2, for each of the $Q^2$ intervals used in this analysis, together with the average $Q$ value, $< Q >$.*

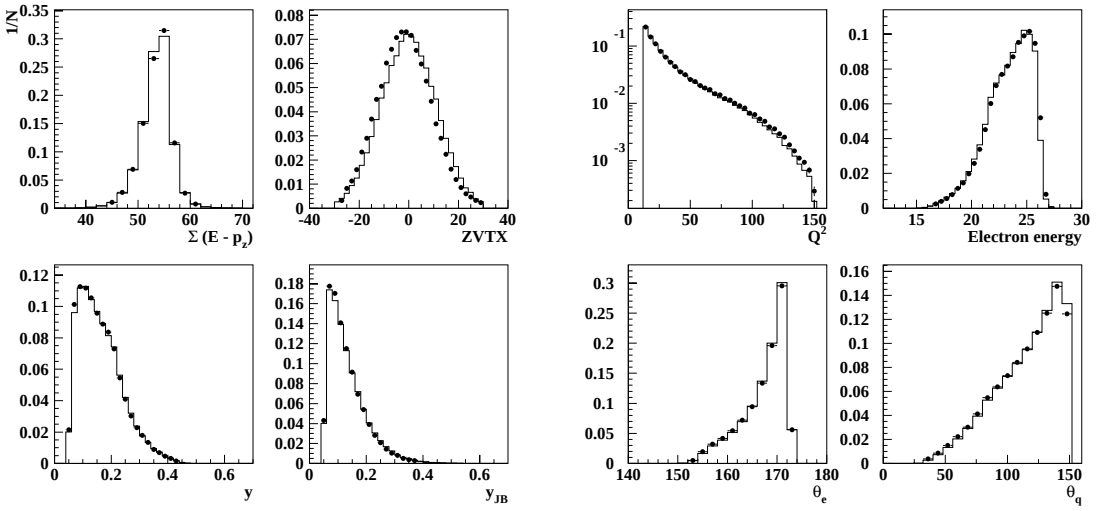


**Figure 4.2**: *Event variables $\Sigma(E-p_z)$, event vertex z coordinate (ZVTX), $Q^2$, scattered electron energy and $\theta_e$, y calculated using two methods, and $\theta_q$, after event selection criteria have been applied, for 1996 low $Q^2$ data (closed circles) and MEAR Monte Carlo (histograms).*

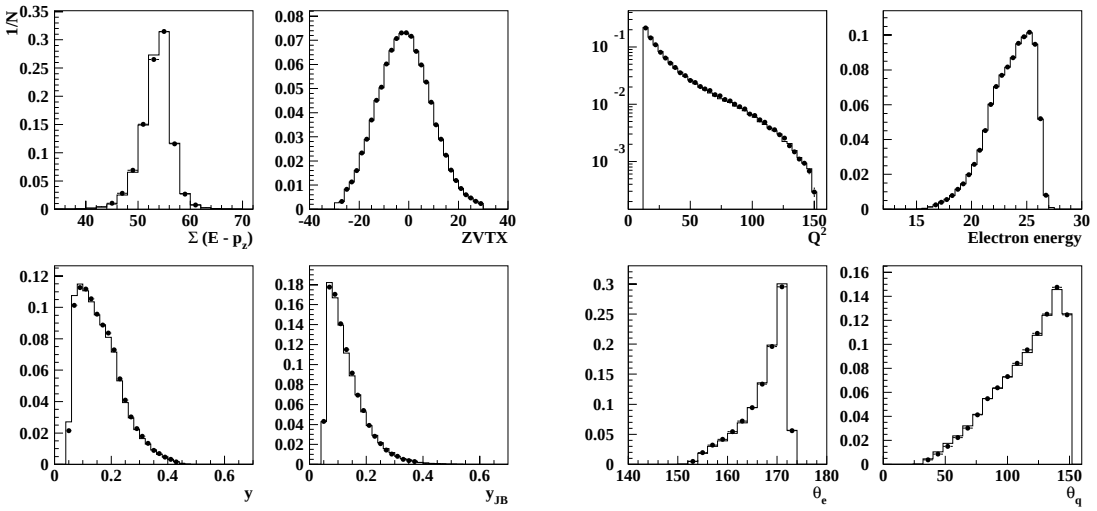


**Figure 4.3**: *The event variables shown in Figure 4.2 after Monte Carlo event reweighting.*

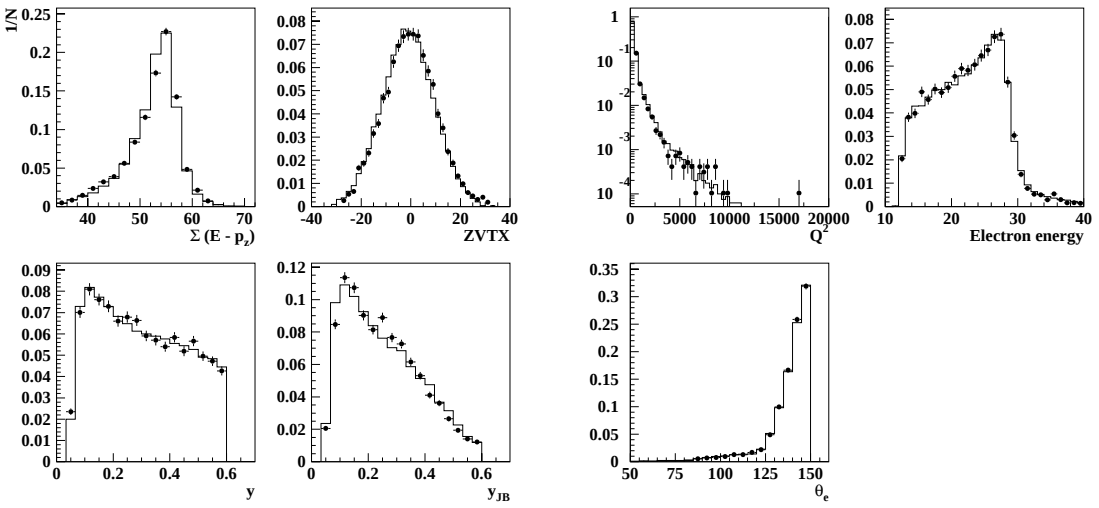


**Figure 4.4**: *Event variables $\Sigma(E - p_z)$, event vertex z coordinate (ZVTX), $Q^2$, scattered electron energy and $\theta_e$, and y calculated using two methods, after event selection criteria have been applied, for 1996 high $Q^2$ data (closed circles) and MEAR Monte Carlo (histograms).*

is applied for any of the event variables.

## 4.3 Track Selection

The H1 tracking system, as detailed in section 1.3, provides good triggering and reconstruction over the full solid angle, and is comprised of two distinct sections; the forward tracker and the central tracker. However, the identification of hadrons through the use of $\mathrm{d}E/\mathrm{d}x$ information and the reconstruction of neutral secondary particles is restricted exclusively to the central tracker. Since this analysis is concerned with the identification of different hadronic species, which is discussed in detail in Chapter 5, this section will only discuss central track and neutral secondary selection criteria.

Tracks which originate from the nominal vertex position are referred to as primary tracks, and tracks that are produced at secondary vertices, for example from neutral secondary decays or background processes, are termed daughter or

secondary tracks.

### 4.3.1 Track Selection for Identified Charged Primary Hadrons

Each primary charged track is subjected to a number of selection requirements designed to ensure only good quality tracks are included in this analysis. These are outlined in detail below. The hadronic type hypothesised for a given primary charged track is assigned after track quality criteria have been satisfied, and according to the identification procedure discussed in section 5.2.4:

1. The transverse momentum, $p_t$, of the primary track must be greater than 150 MeV/$c$. This avoids reconstruction inefficiencies associated with low momentum tracks being unable to penetrate the beam pipe.

2. The primary track polar angle, $\theta_{lab}$, lies between 25° and 160°.

3. The primary track must have a distance of closest approach to the vertex in the $x-y$ plane, $\mid DCA \mid$, of less than 2.0 cm.

4. The radial distance, $R_0$, from the beam line to the innermost hit associated with the primary track must be less than 50.0 cm.

5. In the central jet chamber, the track length, $Trk_{length}$, of primary tracks with $\theta_{lab} < 150°$ must be longer than 10.0 cm, and tracks with $\theta_{lab} > 150°$ must be longer than 5.0 cm.

6. The number of hits, $N_{\mathrm{d}E/\mathrm{d}x}$, associated with a good $\mathrm{d}E/\mathrm{d}x$ measurement must greater than 15.

### 4.3.2 Tracker Inefficiency

Previous studies [57] of inclusive primary charged tracks measured a reasonably flat and well-modelled laboratory azimuthal angle ($\phi_{lab}$) distribution for 1996 data. However in the 1997 data sample a significant dead-region hole is observed

for the azimuthal range $-150^\circ < \phi_{lab} < -80^\circ$. The hole is run-dependent and poorly described for most of the 1997 period. There is also an added complication of a steadily reducing gain in the CJC channels, particularly for $\phi_{lab} > 57^\circ$. A simple algorithm [57] has been successfully devised to degrade the 1997 reconstructed Monte Carlo by removing tracks in a given ($\theta_{lab}$,$\phi_{lab}$) region in a random way. For consistency an identical algorithm is applied to charged tracks included in this analysis, and is performed before any identification is made.

### 4.3.3 Comparison Between Low $Q^2$ 1996 Data and MEAR Monte Carlo

In Figures 4.5 to 4.16 a number of track quality variables are displayed for each hadronic species identified using the $\mathrm{d}E/\mathrm{d}x$ selection criteria defined in section 5.2.4. They are shown separately for positively and negatively charged tracks.

In the comparison between 1996 low $Q^2$ data and reconstructed MEAR Monte Carlo, the most noticeable feature in each set of distributions is the poor description of the $N_{\mathrm{d}E/\mathrm{d}x}$ distribution shape by the Monte Carlo simulation. As a result, each track in the Monte Carlo is re-weighted by the ratio of the $N_{\mathrm{d}E/\mathrm{d}x}$ distribution in data to Monte Carlo, and is performed separately for positively and negatively charged tracks for each identified hadronic species. From the presented figures it is clear that re-weighting $N_{\mathrm{d}E/\mathrm{d}x}$ gives an overall improvement in the description of track quality variables in data by reconstructed Monte Carlo, particularly for $K^+$, $K^-$, protons and antiprotons. An identical re-weighting procedure is applied to 1997 data.

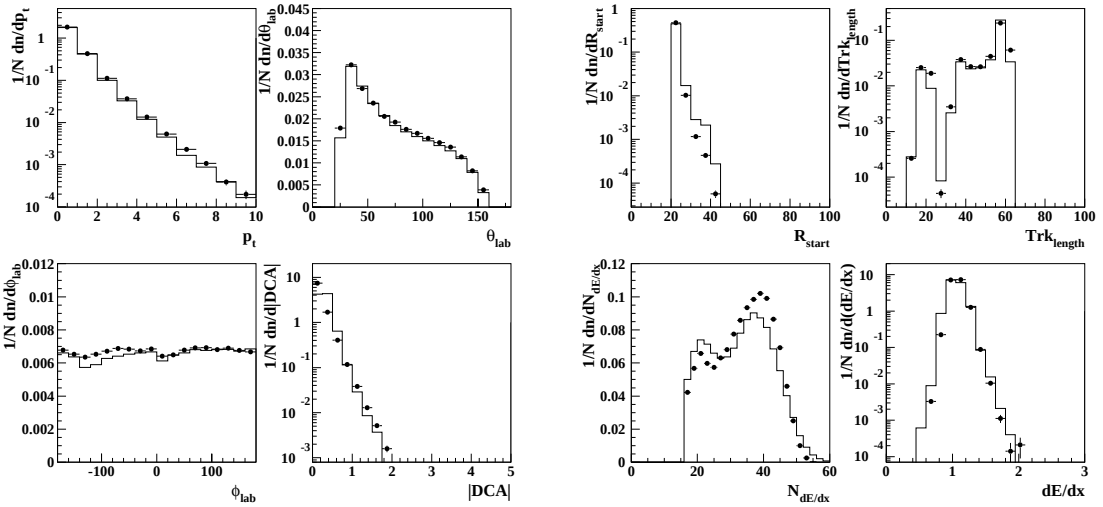


**Figure 4.5**: *Selection of track quality variables shown for 1996 low $Q^2$ data (closed circles) and reconstructed MEAR Monte Carlo (histogram), for $\pi^+$ candidates identified using dE/dx information.*

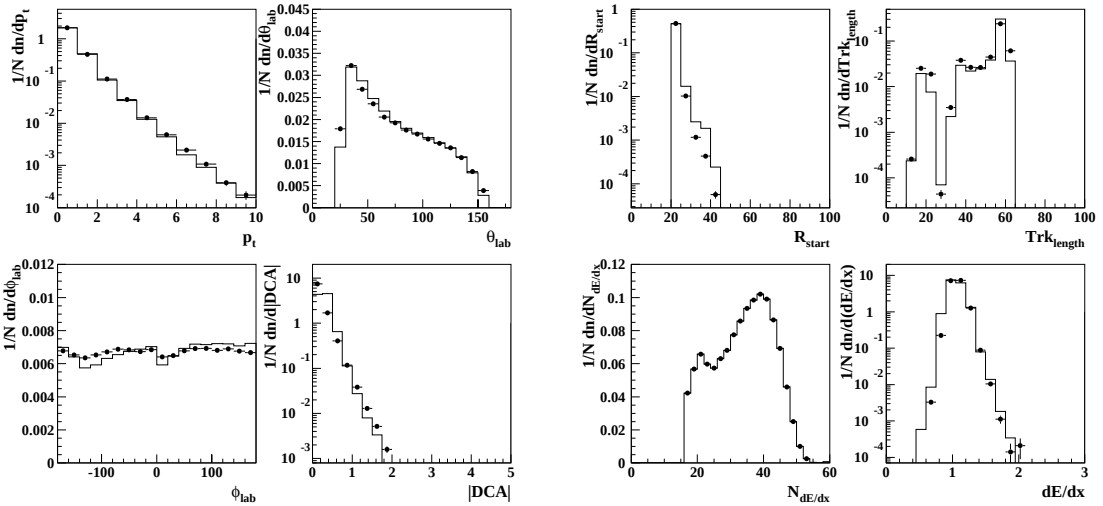


**Figure 4.6**: *Track quality variables shown in Figure 4.5 after Monte Carlo track reweighting.*

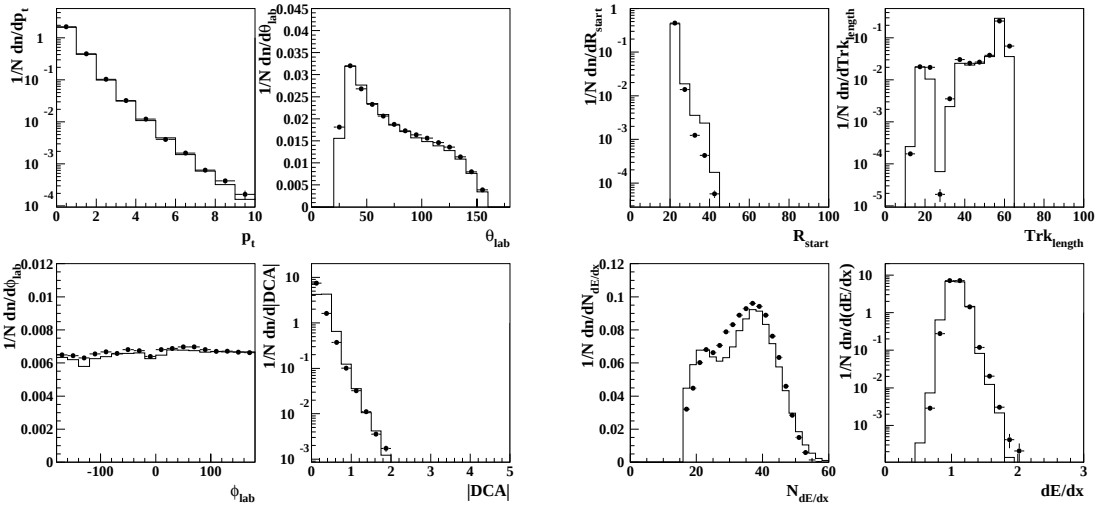


**Figure 4.7**: *Selection of track quality variables shown for 1996 low $Q^2$ data (closed circles) and reconstructed MEAR Monte Carlo (histogram), for $\pi^-$ candidates identified using dE/dx information.*

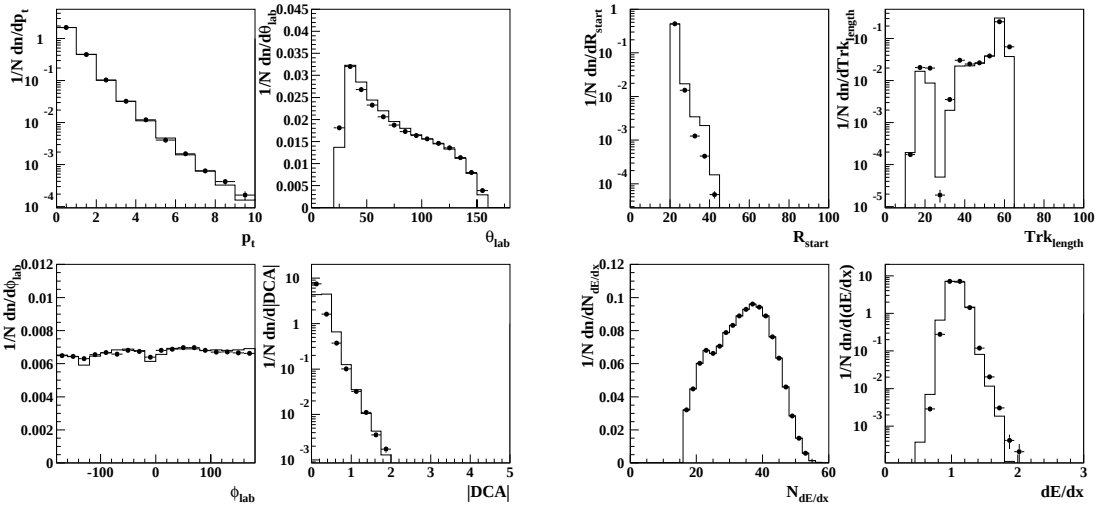


**Figure 4.8**: *Track quality variables shown in Figure 4.7 after Monte Carlo track re-weighting.*

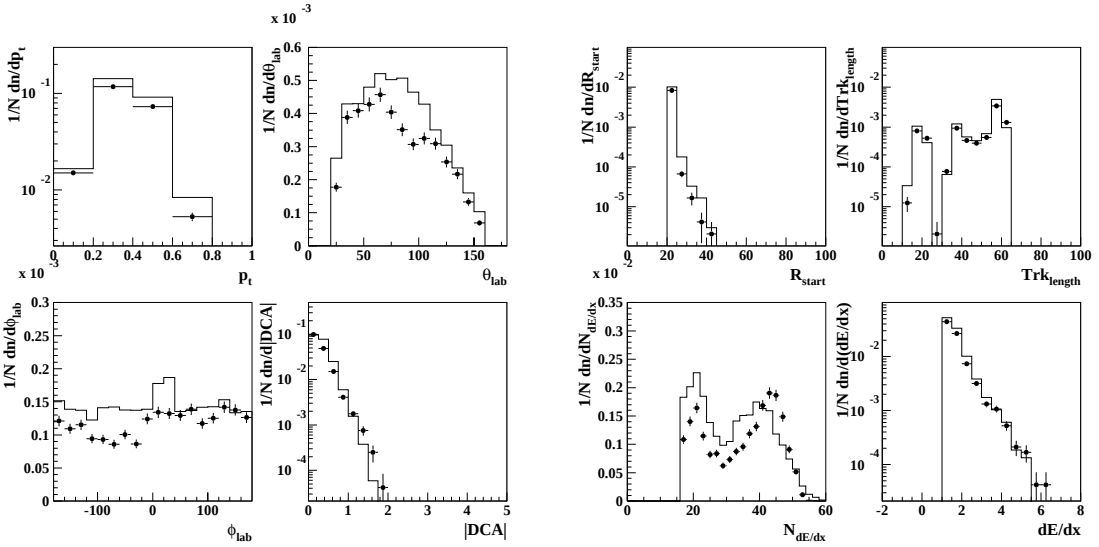


**Figure 4.9**: *Selection of track quality variables shown for 1996 low $Q^2$ data (closed circles) and reconstructed MEAR Monte Carlo (histogram), for $K^+$ candidates identified using dE/dx information.*

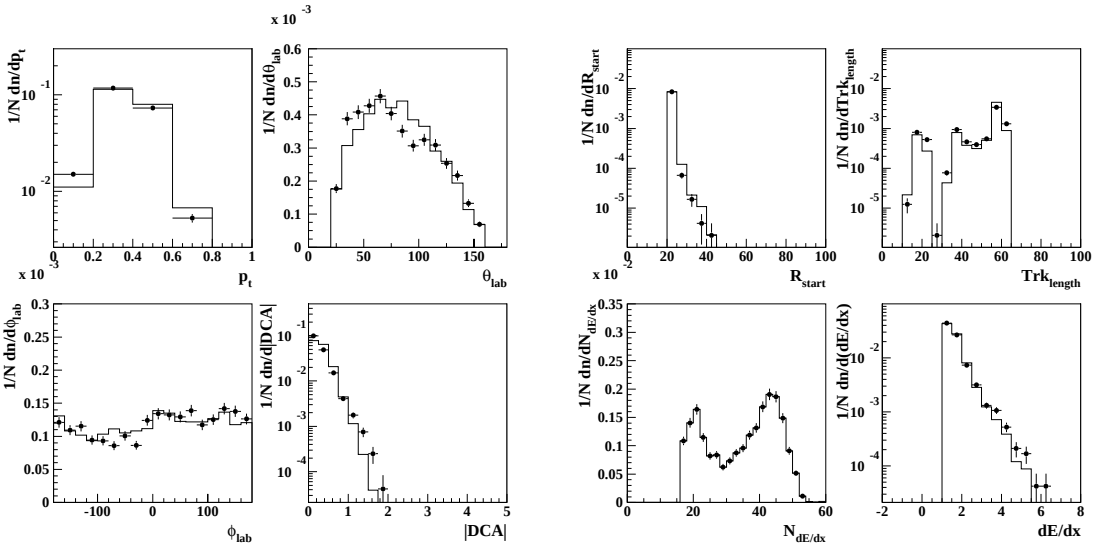


**Figure 4.10**: *Track quality variables shown in Figure 4.9 after Monte Carlo track re-weighting. An improved description of the $p_t$, $\theta_{lab}$, and $\phi_{lab}$ distributions in data by Monte Carlo is obtained.*

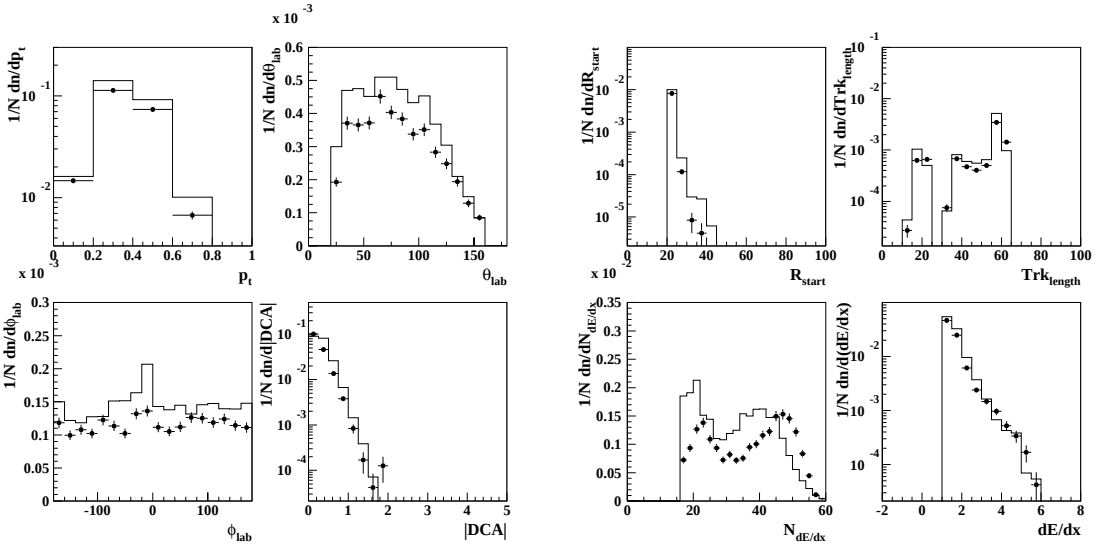


**Figure 4.11**: *Selection of track quality variables shown for 1996 low $Q^2$ data (closed circles) and reconstructed MEAR Monte Carlo (histogram), for $K^-$ candidates identified using dE/dx information.*

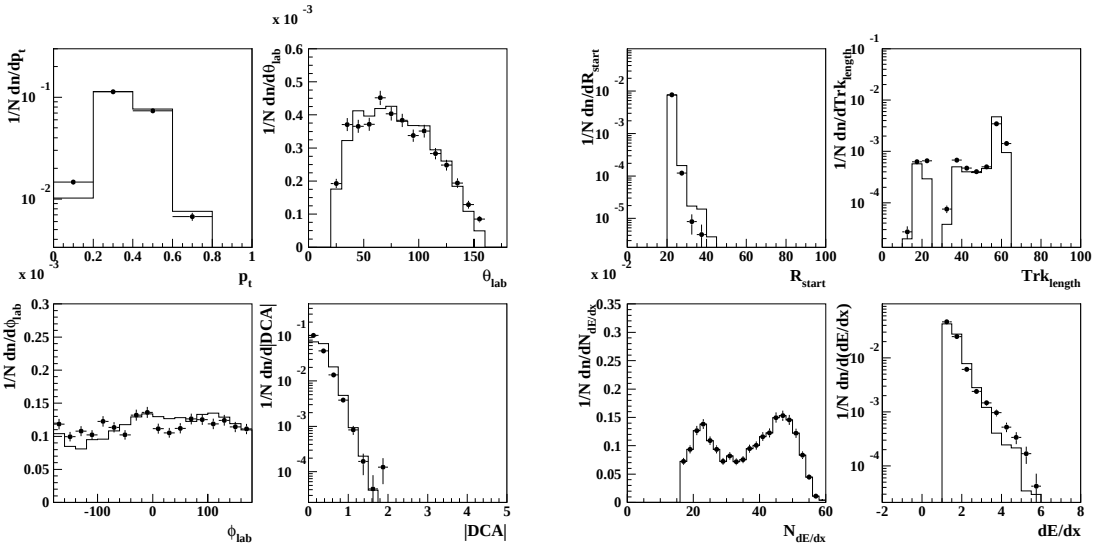


**Figure 4.12**: *Track quality variables shown in Figure 4.11 after Monte Carlo track re-weighting. An improved description of the $p_t$, $\theta_{lab}$, and $\phi_{lab}$ distributions in data by Monte Carlo is obtained.*

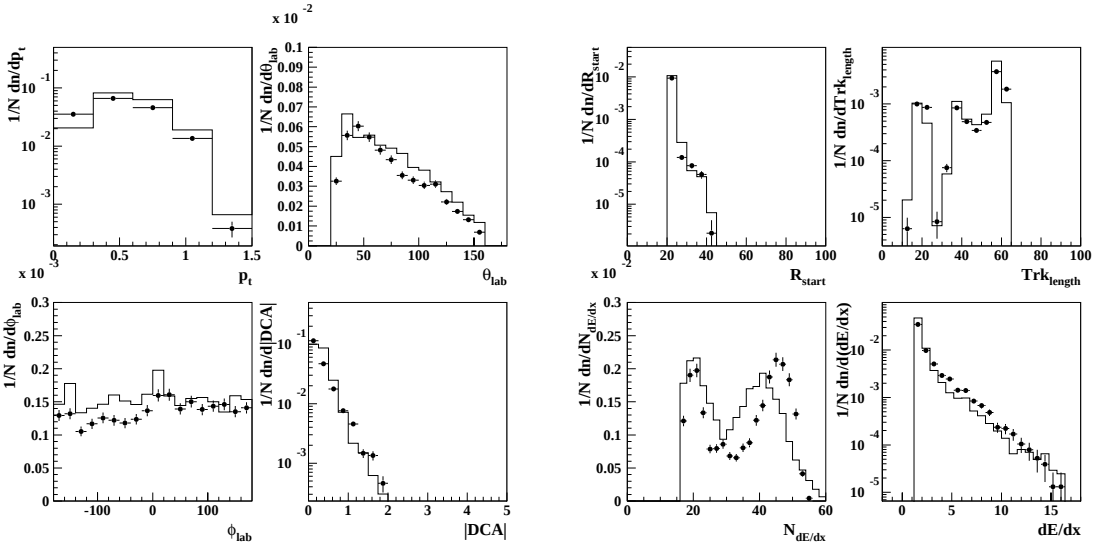


**Figure 4.13**: *Selection of track quality variables shown for 1996 low $Q^2$ data (closed circles) and reconstructed MEAR Monte Carlo (histogram), for proton candidates identified using dE/dx information.*

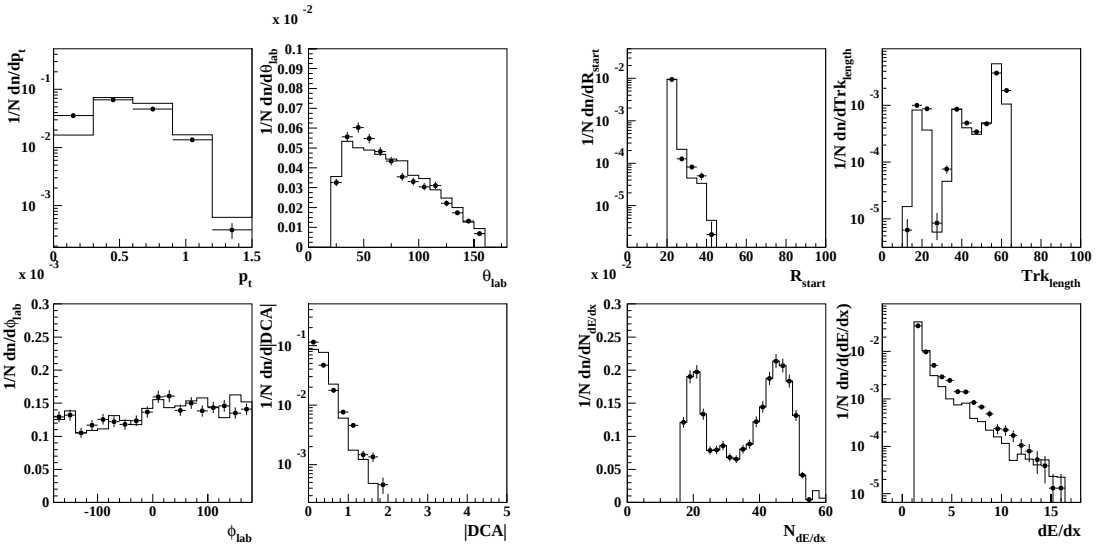


**Figure 4.14**: *Track quality variables shown in Figure 4.13 after Monte Carlo track re-weighting. An improved description of the $p_t$ and $\phi_{lab}$ distributions in data by Monte Carlo is obtained.*

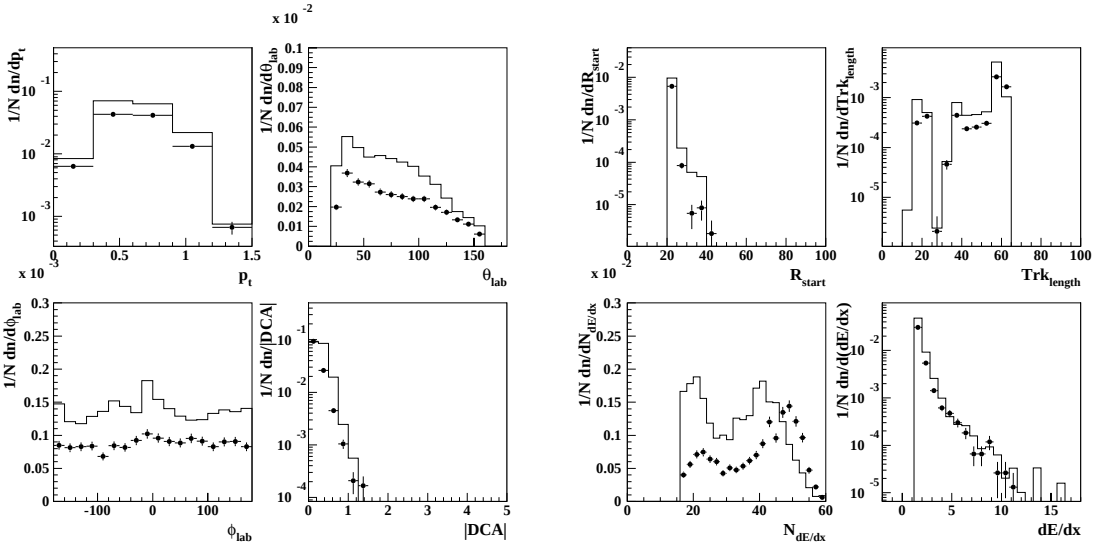


**Figure 4.15**: *Selection of track quality variables shown for 1996 low $Q^2$ data (closed circles) and reconstructed MEAR Monte Carlo (histogram), for antiproton candidates identified using dE/dx information.*

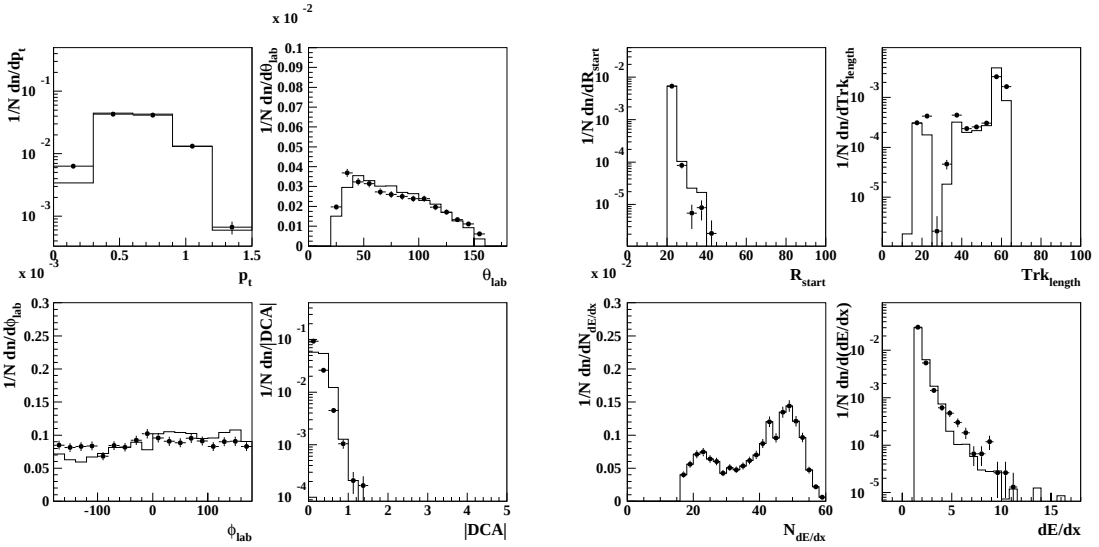


**Figure 4.16**: *Track quality variables shown in Figure 4.15 after Monte Carlo track re-weighting. An improved description of the $p_t$, $\theta_{lab}$, $\phi_{lab}$, and $Trk_{length}$ distributions in data by Monte Carlo is obtained.*

### 4.3.4 Comparison Between High $Q^2$ 1996 Data and MEAR Monte Carlo

In Figures 4.17 to 4.28, a comparison between 1996 data and reconstructed MEAR Monte Carlo at high $Q^2$ is shown for a number of track quality variables measured separately for identified positively and negatively charged hadrons after track quality cuts have been applied.

As observed at low $Q^2$, the $N_{\mathrm{d}E/\mathrm{d}x}$ distribution in data is poorly described by Monte Carlo, particularly for $\pi^{\pm}$ candidates. Again, each track is re-weighted in 1996 and 1997 reconstructed Monte Carlo, as described in section 4.3.3, giving an overall improvement in the description of the data.

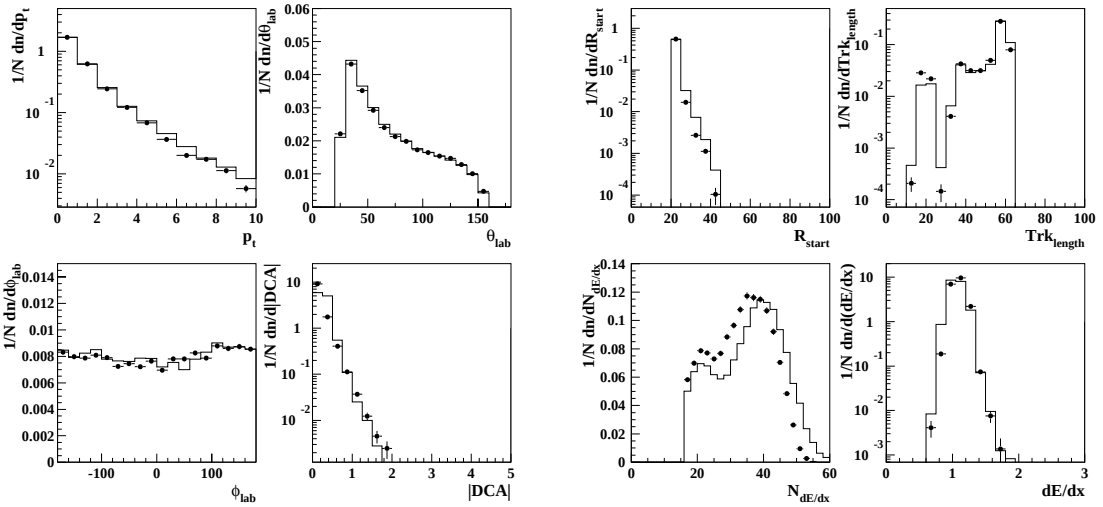


**Figure 4.17**: *Selection of track quality variables shown for 1996 high $Q^2$ data (closed circles) and reconstructed MEAR Monte Carlo (histogram), for $\pi^+$ candidates identified using dE/dx information.*

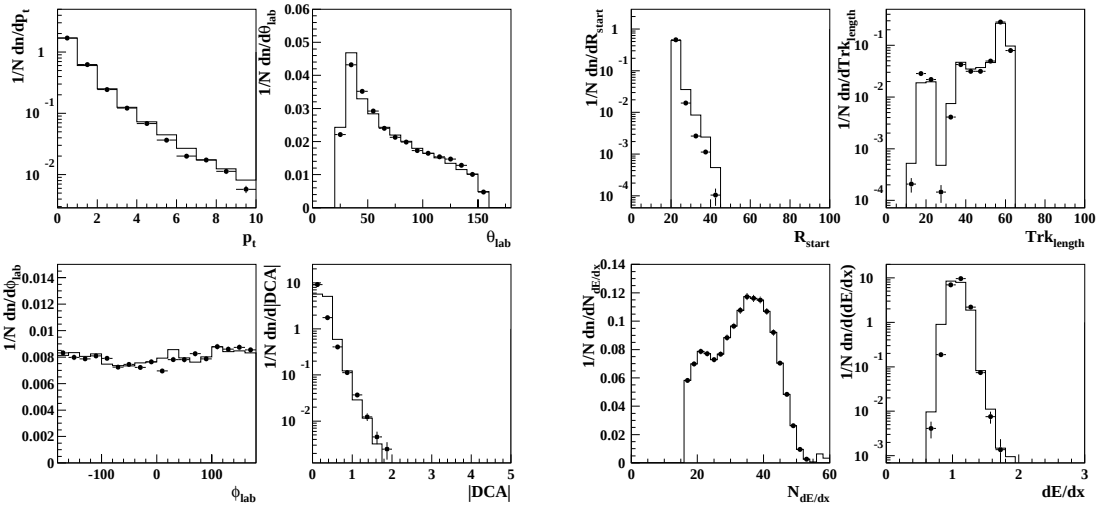


**Figure 4.18**: *Track quality variables shown in Figure 4.17 after Monte Carlo track re-weighting.*

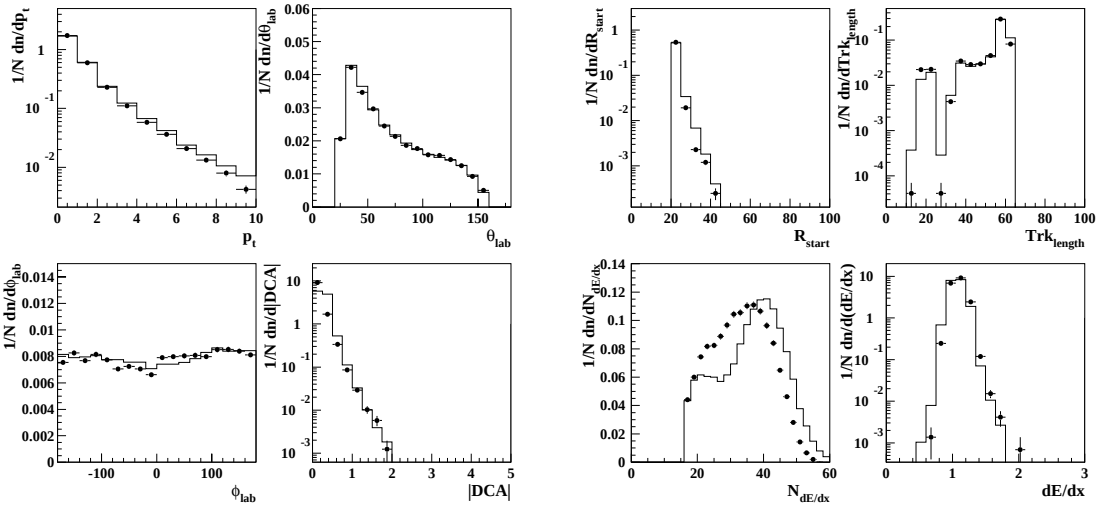


**Figure 4.19**: *Selection of track quality variables shown for 1996 high $Q^2$ data (closed circles) and reconstructed MEAR Monte Carlo (histogram), for $\pi^-$ candidates identified using dE/dx information.*

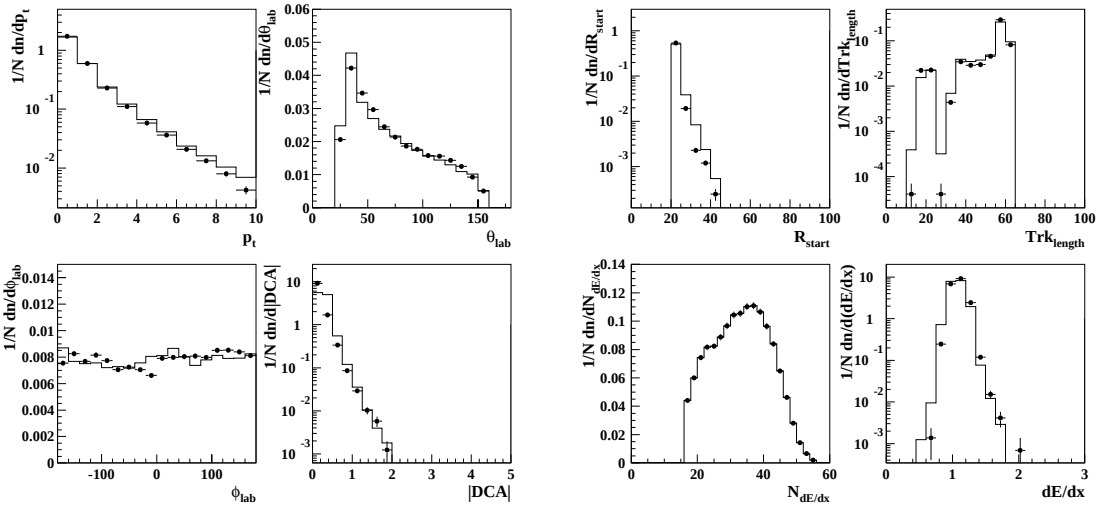


**Figure 4.20**: *Track quality variables shown in Figure 4.19 after Monte Carlo track re-weighting.*

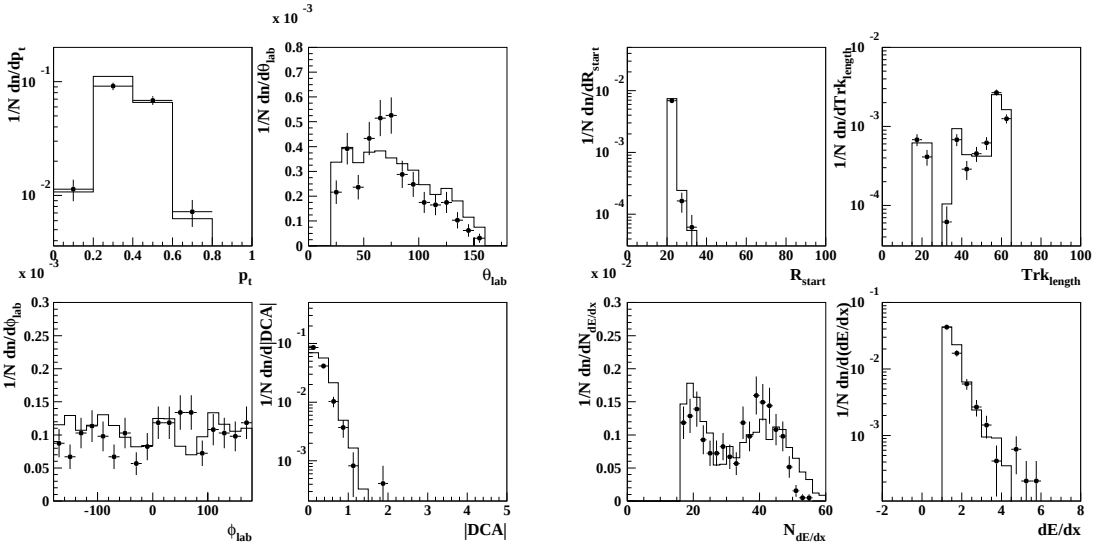


**Figure 4.21**: *Selection of track quality variables shown for 1996 high $Q^2$ data (closed circles) and reconstructed MEAR Monte Carlo (histogram), for $K^+$ candidates identified using dE/dx information.*

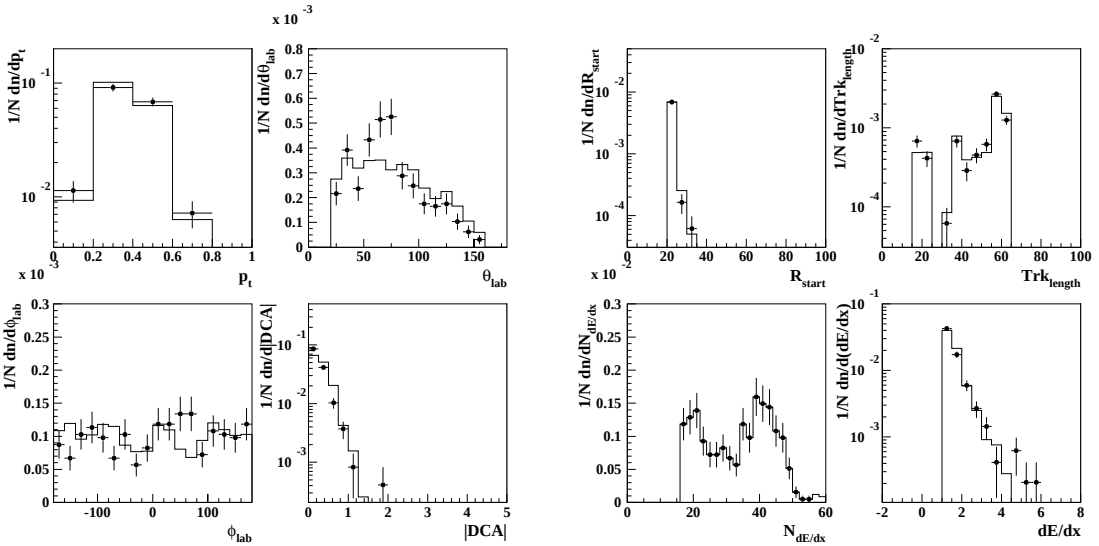


**Figure 4.22**: *Track quality variables shown in Figure 4.21 after Monte Carlo track re-weighting. An improved description of the $p_t$ spectrum in data by Monte Carlo is obtained.*

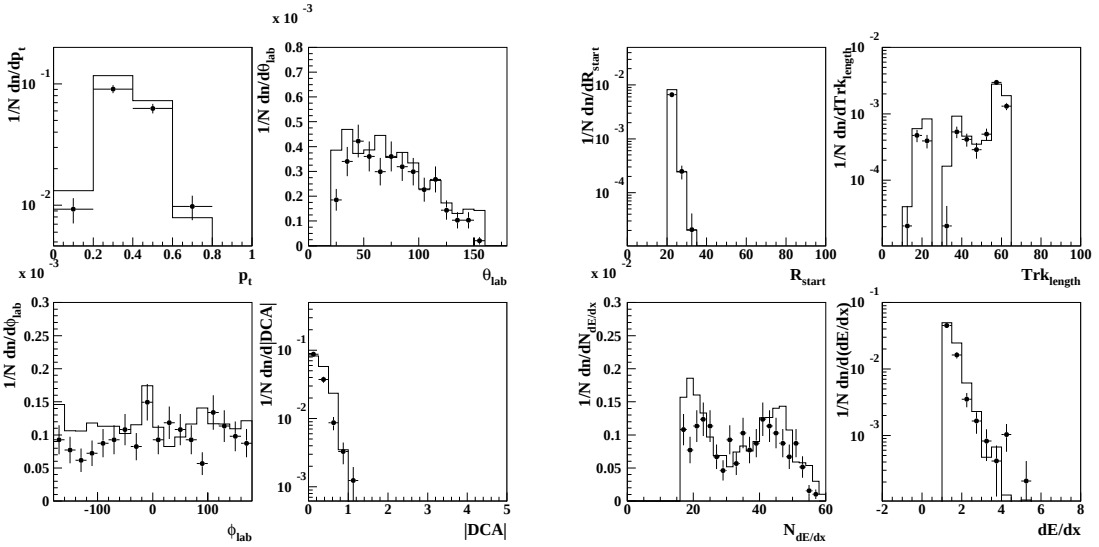


**Figure 4.23**: *Selection of track quality variables shown for 1996 high $Q^2$ data (closed circles) and reconstructed MEAR Monte Carlo (histogram), for $K^-$ candidates identified using dE/dx information.*

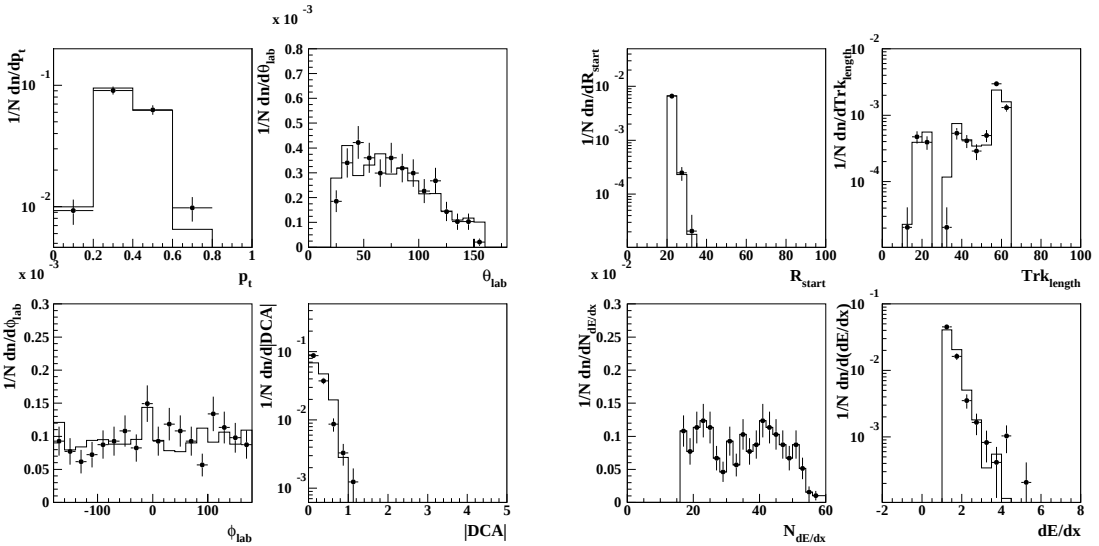


**Figure 4.24**: *Track quality variables shown in Figure 4.23 after Monte Carlo track re-weighting. An improved description of the $p_t$, $\theta_{lab}$, and $\phi_{lab}$ distributions in data by Monte Carlo is obtained.*

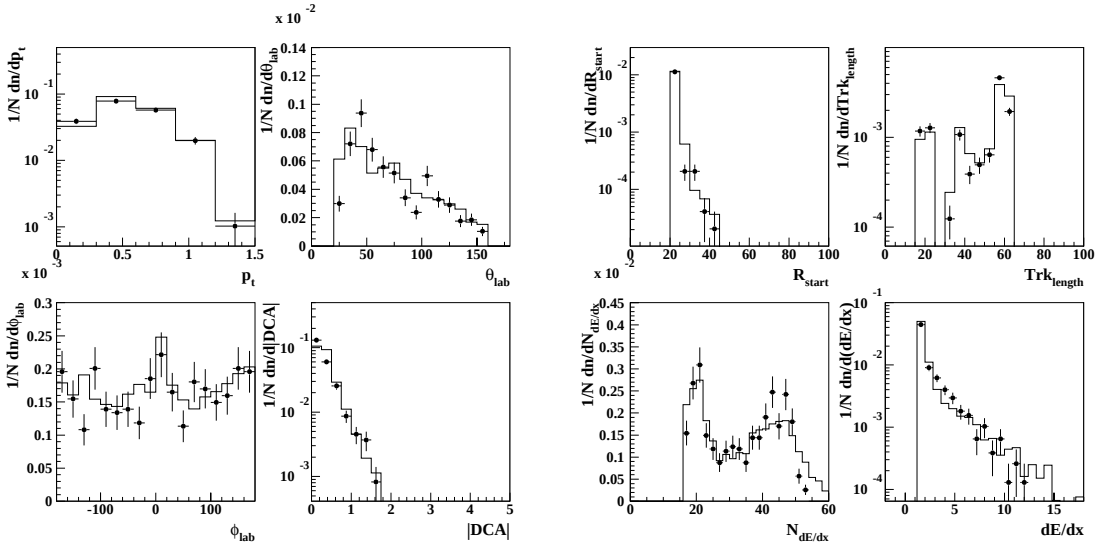


**Figure 4.25**: *Selection of track quality variables shown for 1996 high $Q^2$ data (closed circles) and reconstructed MEAR Monte Carlo (histogram), for proton candidates identified using dE/dx information.*

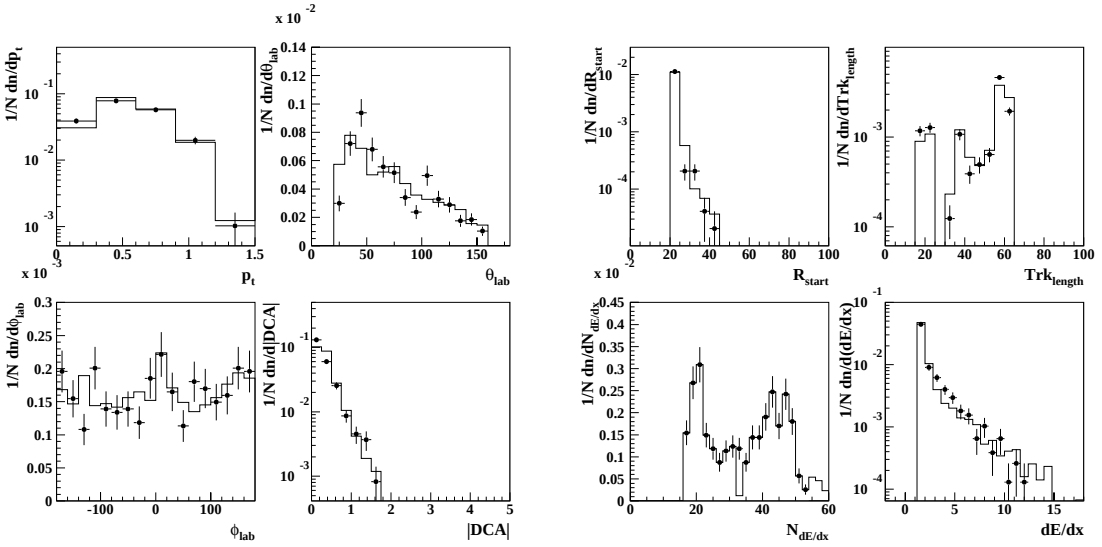


**Figure 4.26**: *Track quality variables shown in Figure 4.25 after Monte Carlo track re-weighting.*

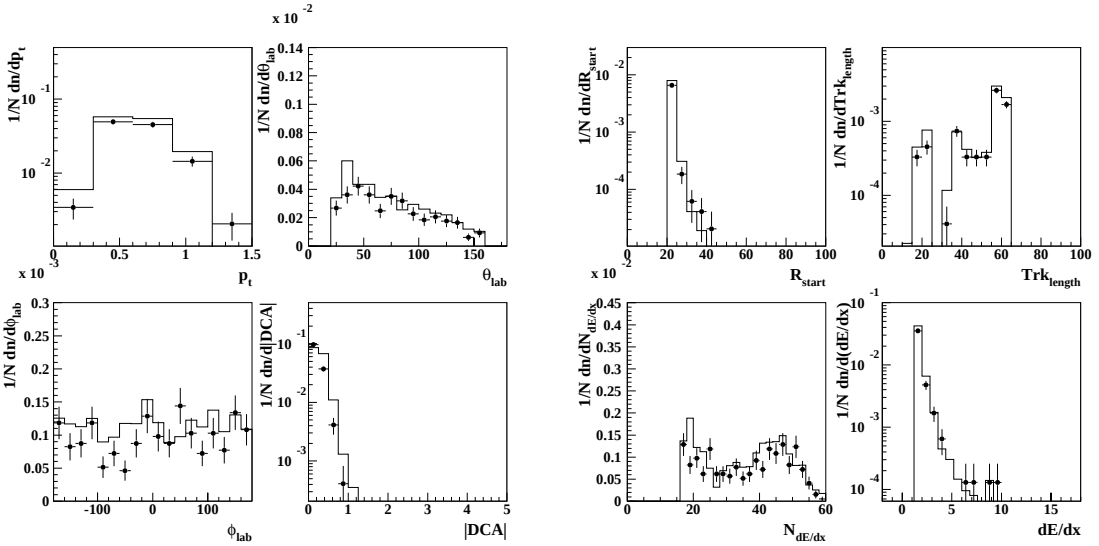


**Figure 4.27**: *Selection of track quality variables shown for 1996 high $Q^2$ data (closed circles) and reconstructed MEAR Monte Carlo (histogram), for antiproton candidates identified using dE/dx information.*

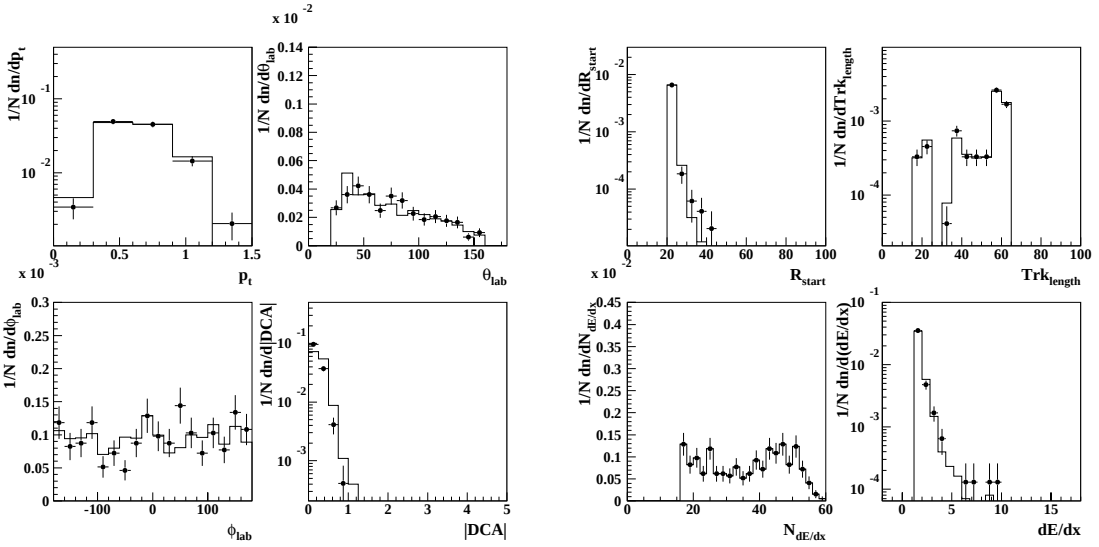


**Figure 4.28**: *Track quality variables shown in Figure 4.27 after Monte Carlo track re-weighting.*

### 4.3.5 Secondary $V^0$ Selection

Neutral secondary particles, hereafter called $V^0$ candidates, are identified through the reconstruction of secondary vertices formed by pairs of oppositely charged tracks, known as daughters, in the CJC [58]. Events with one $V^0$ candidate only are included in this analysis to remove any combinatorial background. Less than 5% of events having at least one $V^0$ candidate have more than one $V^0$, with this loss being included in the bin-by-bin acceptance correction procedure (see Chapter 7). To ensure a good quality $V^0$ candidate and associated pair of daughter tracks, a number of selection cuts are applied:

1. The transverse momentum, $p_t$, of the $V^0$ candidate must be greater than 500 MeV/$c$.
2. The polar angle of the $V^0$ candidate must lie in the range $20° < \theta_{lab} < 160°$.
3. The $\chi^2/ndf$ of the secondary vertex, $\chi^2(vtx)$, must be less than 10.0.
4. The $\Delta \mid DCA \mid$ of the $V^0$ candidate must be greater than 0.5 cm.
5. The decay length of the $V^0$ candidate in the $x$-$y$ plane must be greater than 2 cm, ensuring good separation from the primary vertex and therefore reducing the number of fake vertices.
6. The $p_t$ of the daughter track of the $V^0$ candidate must be greater than 150 MeV/$c$.
7. The track length, $Trk_{length}$, of each daughter must be at least 10.0 cm.
8. The number of CJC hits, $N_{hits}$, associated with each daughter track must be greater than 10.

Displayed in Figures 4.29 to 4.33 are a selection of $V^0$ candidate and daughter track quality variables after the application of the above selection cuts. Overall, MEAR Monte Carlo gives an excellent description of both low and high $Q^2$ data,

although the $V^0$ daughter azimuthal angle distributions for 1997 data, as shown in Figure 4.31, are poorly described.

## 4.4 Comparison Between 1996 and 1997 Data Samples

A detailed comparison between 1996 and 1997 data samples for a selection of event, charged track and $V^0$ quality variables can be found in Appendix A. Consistency is found between the two data samples, and as for 1996, the 1997 reconstructed Monte Carlo is re-weighted event-by-event and track-by-track due to a poor simulation of the $z$-vertex distribution and scattered electron energy spectrum, and $N_{\mathrm{d}E/\mathrm{d}x}$ distribution respectively.

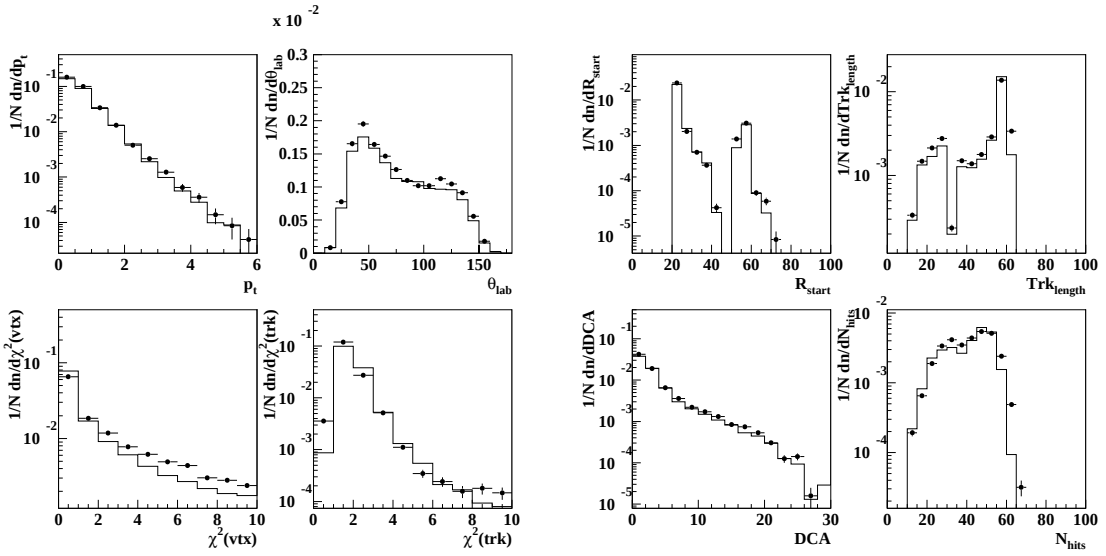


**Figure 4.29**: *Selection of $V^0$ candidate daughter track quality variables for 1996 low $Q^2$ data (closed circles) and reconstructed MEAR Monte Carlo (histogram).*

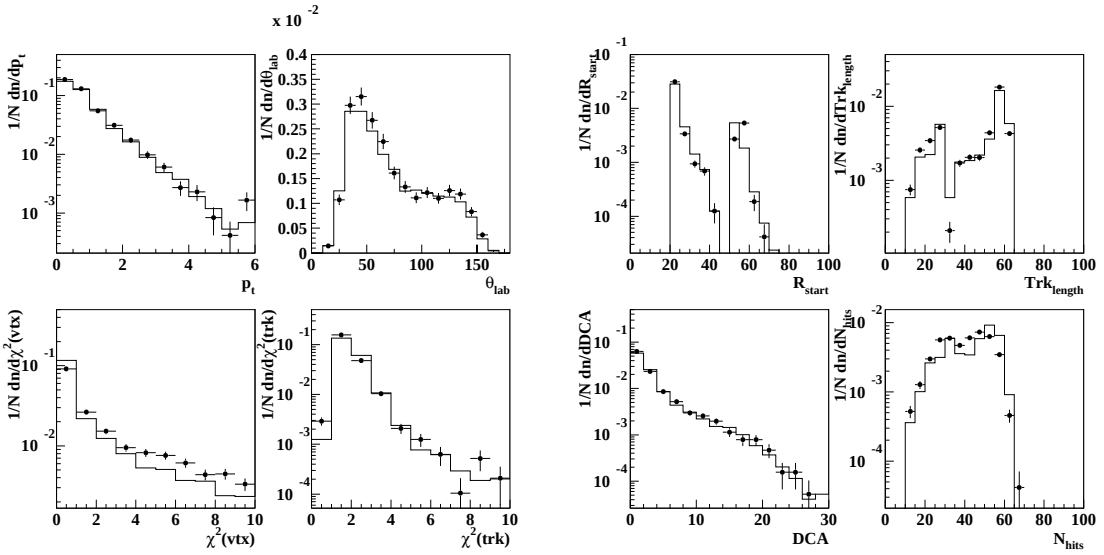


**Figure 4.30**: *Selection of $V^0$ candidate daughter track quality variables for 1996 high $Q^2$ data (closed circles) and reconstructed MEAR Monte Carlo (histogram).*

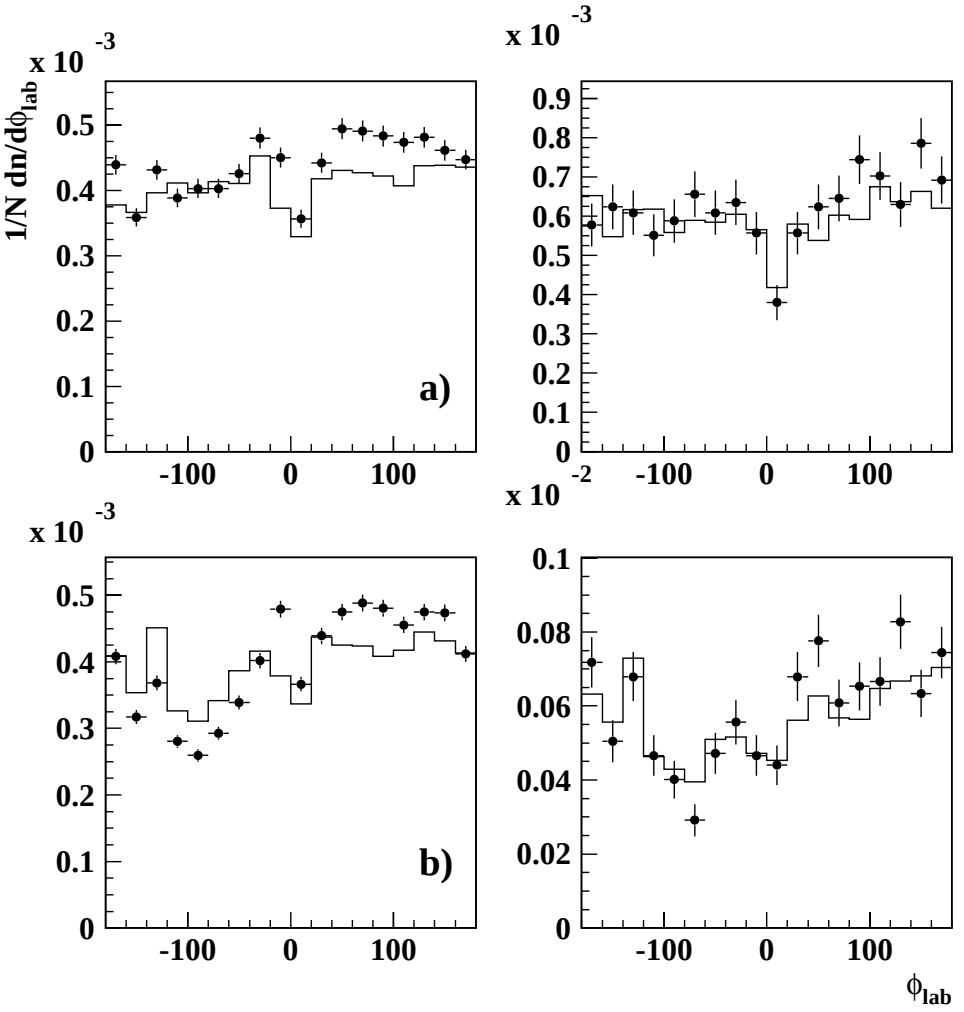


**Figure 4.31**: *$V^0$ daughter laboratory azimuthal angle, $\phi_{lab}$, at left) low and right) high $Q^2$ for a) 1996 and b) 1997 data (closed circles) and reconstructed MEAR Monte Carlo (histogram).*

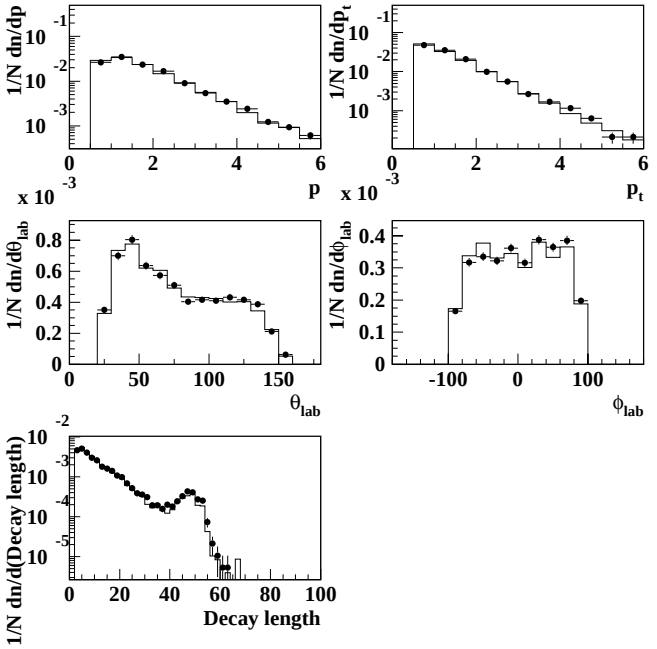


**Figure 4.32**: *Selection of $V^0$ quality variables for 1996 low $Q^2$ data (closed circles) and reconstructed MEAR Monte Carlo (histogram).*

## 4.5 Trigger Efficiency

This section will summarise results from a recent study [23, 59] of the triggering efficiency for selecting low and high $Q^2$ H1 data taken in 1996 and 1997. The study has shown the net efficiency to be in excess of 99% for an unbiased selection of NC DIS events. It is important to note that the fragmentation analysis presented in this thesis does not measure cross sections, being only interested in the shape of event normalised distributions.

### 4.5.1 Low $Q^2$ Trigger Efficiency

The low $Q^2$ data is selected using a cocktail of ORd trigger elements. The dominant triggers are essentially a low threshold calorimetric trigger demanding at least 2 GeV deposited in the SpaCal and a track trigger giving an acceptable multiplicity at the $z$-vertex, together with information from the time-of-flight system

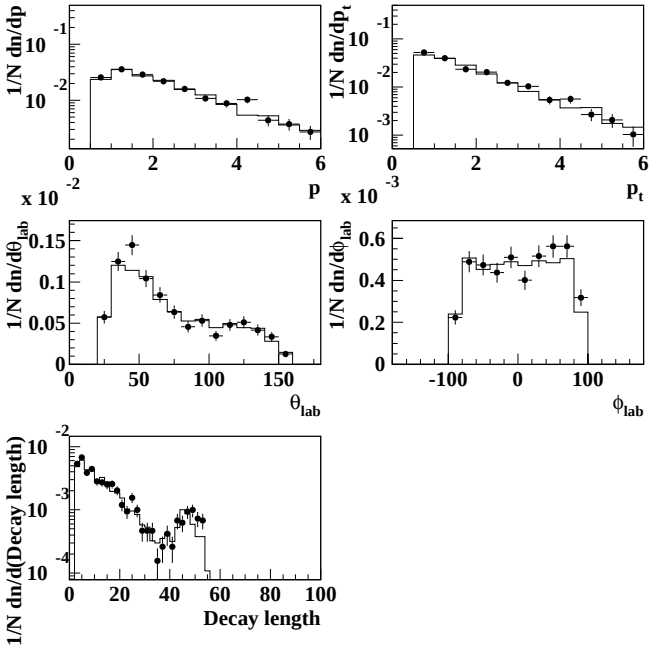


**Figure 4.33**: *Selection of $V^0$ quality variables for 1996 high $Q^2$ data (closed circles) and reconstructed MEAR Monte Carlo (histogram).*

and veto wall. For monitoring, a combination of LAr calorimeter triggers has been chosen. The triggering efficiency for the entire system is estimated using 1996 data and is calculated to be better than 99.99%, with this value falling during 1997 due to the degradation of some $\phi$ regions in the CJC, as discussed in section 4.3.2.

### 4.5.2 High $Q^2$ Trigger Efficiency

The selection of high $Q^2$ NC DIS events is based upon a trigger which demands at least 6 GeV of energy deposited in any trigger tower of the LAr calorimeter. To maintain a high triggering efficiency, regions in the LAr calorimeter containing $\phi$ and $z$ cracks are excluded. The total efficiency for the selection of high $Q^2$ data in 1996 and 1997 is calculated to be 99.0 $\pm$ 1.0%.

## 4.6 Reconstruction of Event Kinematics

In order to calculate the correct Lorentz transformation from the HERA laboratory reference frame to the Breit frame (see discussion in Chapter 6), it is necessary to calculate the variables $Q^2$ and $x$ as accurately as possible to minimise boost uncertainties. The variables are defined in terms of the energies of the incident electron, $E_e$, the scattered electron, $E'_e$, the incident proton, $E_P$, and the hadronic recoil jet, $E_h$, together with the polar angles, $\theta_e$ and $\theta_h$, of the scattered electron and hadronic jet respectively, both of which are measured relative to the proton direction.

### 4.6.1 Electron Only Method (EL)

Within this thesis, the event kinematics are determined using information from the scattered electron only. This ensures that the event-by-event boost to the Breit frame is performed independently of the hadronic final state. Using the electron variables:

$$Q_e^2 = 2E_e E'_e(1 + \cos\theta_e) \tag{4.1}$$

$$y_e = 1 - \frac{E'_e}{2E_e}(1 - \cos\theta_e) \tag{4.2}$$

$$x_e = \frac{E_e E'_e(1 + \cos\theta_e)}{E_P(2E_e - E'_e(1 - \cos\theta_e))} \tag{4.3}$$

where $x_e$ is simply obtained from $Q_e^2 = s x_e y_e$.

### 4.6.2 Jacquet-Blondel Method (JB)

In charged current (CC) DIS events the scattered neutrino remains undetected, and it is therefore necessary to calculate the kinematic variables from the hadronic final state. The Jacquet-Blondel (or hadrons-only) method [60] was developed to determine the event kinematics for CC DIS events, and is based upon energy-momentum conservation between the scattered lepton (electron or neutrino) and the hadronic system. The kinematics are calculated using definitions of $Q^2$ and $y^2$ at the hadronic vertex, which are given as:

$$y_{JB} = \frac{\Sigma_h (E_h - p_{z,h})}{2E_e} \tag{4.4}$$

$$Q^2_{JB} = \frac{(\Sigma_h p_{x,h})^2 + (\Sigma_h p_{y,h})^2}{1 - y_{JB}} \tag{4.5}$$

$$x_{JB} = \frac{Q^2_{JB}}{s y_{JB}} \tag{4.6}$$

where the above summations are performed over all outgoing hadrons.

The angle $\gamma$ characterises the recoil of the hadronic system, and is given as:

$$\cos\gamma = \frac{Q^2_{JB}(1 - y_{JB}) - 4E_e^2 y^2_{JB}}{Q^2_{JB}(1 - y_{JB}) + 4E_e^2 y^2_{JB}} \tag{4.7}$$

Within the QPM, this corresponds to the polar scattering angle of the massless struck quark.

### 4.6.3 Double Angle Method (DA)

The Double Angle method uses the scattered electron polar angle and the inclusive angle of the hadronic final state. By assuming a homogeneous energy

measurement over the full solid angle the event kinematics are independent of any calorimetric energy scale uncertainties:

$$Q^2_{\theta_e\gamma} = 4E_e^2 \frac{\sin\gamma(1+\cos\theta_e)}{\sin\gamma + \sin\theta_e - \sin(\theta_e+\gamma)} \tag{4.8}$$

$$y_{\theta_e\gamma} = \frac{\sin\theta_e(1-\cos\gamma)}{\sin\gamma + \sin\theta_e - \sin(\theta_e+\gamma)} \tag{4.9}$$

$$x_{\theta_e\gamma} = x_o \frac{\sin\gamma + \sin\theta_e + \sin(\theta_e+\gamma)}{\sin\gamma + \sin\theta_e - \sin(\theta_e+\gamma)} \tag{4.10}$$

where $x_o = E_e/E_P$.

### 4.6.4 The $\Sigma$ Method

The $\Sigma$ method enables the calculation of $y$ and $Q^2$ to be independent of initial state QED radiation, and is performed by reconstructing the incident electron energy. Applying energy-momentum conservation and assuming no particles escape detection, the measured quantity $\Delta$ is defined to be twice the electron beam energy:

$$\Delta \equiv \Sigma + E'_e(1-\cos\theta_e) = 2E_e \tag{4.11}$$

where $\Sigma = \Sigma_h(E_h - p_{z,h})$.

By substituting the definition of $\Delta$ into equation 4.4, the following expressions are obtained:

$$y_\Sigma = \frac{\Sigma}{\Sigma + E'_e(1-\cos\theta_e)} \tag{4.12}$$

$$Q^2_\Sigma = \frac{E'^2_e \sin^2\theta_e}{1-y_\Sigma} \tag{4.13}$$

$$x_\Sigma = \frac{E_e'^2 \sin^2\theta_e}{s y_\Sigma (1 - y_\Sigma)} \tag{4.14}$$

### 4.6.5 Mixed Method (MI)

The Mixed method combines the $y$ measurement from the Jacquet-Blondel method and $Q^2$ determined from the Electron Only method, such that:

$$x_{MI} = \frac{Q_e^2}{s y_{JB}} \tag{4.15}$$

The Mixed method allows the extension of $F_2$ measurements performed using the Double-Angle or Electron Only methods towards lower values of $y$.

## 4.7 $Q^2$ and $x$ Resolution

The resolutions on $x$ and $Q^2$ for the different reconstruction methods can be estimated by subjecting the reconstructed Monte Carlo to the same kinematic cuts applied to the real data. The resolutions are measured in terms of the fractions $\Delta x$ and $\Delta Q^2$, which are defined through the relations:

$$\frac{\Delta x}{x_T} = \frac{x_R - x_T}{x_T} \tag{4.16}$$

$$\frac{\Delta Q^2}{Q_T^2} = \frac{Q_R^2 - Q_T^2}{Q_T^2} \tag{4.17}$$

where $x_T$ and $Q_T^2$ are the generated (true) values of the kinematic variables $x$ and $Q^2$, and $x_R$ and $Q_R^2$ are the reconstructed values.

| $Q^2$ interval | $\Delta x/x_T$ | | | | | $\Delta Q^2/Q_T^2$ | | | |
|---|---|---|---|---|---|---|---|---|---|
| ($\mathrm{GeV}^2$) | EL | DA | $\Sigma$ | JB | MI | EL | DA | $\Sigma$ | JB |
| $12 \rightarrow 15$ | 0.214 | 0.488 | 0.270 | 0.412 | 0.356 | 0.038 | 0.091 | 0.068 | 0.248 |
| $15 \rightarrow 20$ | 0.212 | 0.488 | 0.254 | 0.497 | 0.344 | 0.036 | 0.099 | 0.070 | 0.279 |
| $20 \rightarrow 40$ | 0.215 | 0.429 | 0.239 | 0.623 | 0.355 | 0.034 | 0.098 | 0.068 | 0.273 |
| $40 \rightarrow 60$ | 0.219 | 0.355 | 0.226 | 0.663 | 0.309 | 0.034 | 0.095 | 0.075 | 0.266 |
| $60 \rightarrow 80$ | 0.224 | 0.320 | 0.235 | 0.625 | 0.297 | 0.035 | 0.090 | 0.098 | 0.262 |
| $80 \rightarrow 100$ | 0.247 | 0.282 | 0.228 | 0.619 | 0.284 | 0.036 | 0.089 | 0.112 | 0.257 |
| $100 \rightarrow 150$ | 0.282 | 0.275 | 0.234 | 0.591 | 0.270 | 0.041 | 0.090 | 0.115 | 0.224 |
| $100 \rightarrow 175$ | 0.206 | 0.301 | 0.253 | 0.268 | 0.345 | 0.055 | 0.117 | 0.137 | 0.190 |
| $175 \rightarrow 250$ | 0.266 | 0.279 | 0.259 | 0.305 | 0.302 | 0.055 | 0.087 | 0.116 | 0.220 |
| $250 \rightarrow 450$ | 0.263 | 0.256 | 0.253 | 0.360 | 0.284 | 0.044 | 0.083 | 0.109 | 0.236 |
| $450 \rightarrow 1000$ | 0.236 | 0.236 | 0.226 | 0.397 | 0.273 | 0.041 | 0.084 | 0.103 | 0.224 |
| $1000 \rightarrow 2000$ | 0.199 | 0.243 | 0.196 | 0.359 | 0.278 | 0.042 | 0.086 | 0.099 | 0.205 |
| $2000 \rightarrow 8000$ | 0.175 | 0.313 | 0.175 | 0.264 | 0.305 | 0.041 | 0.086 | 0.093 | 0.192 |
| $8000 \rightarrow 20000$ | 0.141 | 0.559 | 0.129 | 0.202 | 0.289 | 0.042 | 0.082 | 0.083 | 0.177 |

**Table 4.2**: *Summary of the fractional error in $x$ and $Q^2$, calculated as the root-mean-square (rms) of the $\Delta x/x_T$ and $\Delta Q^2/Q_T^2$ distributions respectively, for the $Q^2$ intervals used in this analysis, and calculated for each of the methods of kinematic reconstruction [61].*

### 4.7.1 Summary

The $x$ and $Q^2$ resolutions are calculated as the root-mean-square (rms) of the $\Delta x/x_T$ and $\Delta Q^2/Q_T^2$ distributions and the values obtained are summarised in Table 4.2 [61] for each method, with the distributions being shown in Figures 4.34 to 4.37 for the Electron Only method. The $\Sigma$ method and Electron Only method are the most competitive techniques for calculating $x$, with the Electron Only method producing the best results in the lowest five $Q^2$ bins, and the $\Sigma$ method most successful in the highest six $Q^2$ bins. In calculating $Q^2$, the Electron Only method consistently achieves the best resolution in all $Q^2$ intervals, although the Double Angle method and the $\Sigma$ method perform reasonably well. In comparison, the Jacquet-Blondel method has a relatively poor resolution in all low and high $Q^2$ bins.

From this study, the Electron Only method has been chosen to the reconstruct the event variables $x$ and $Q^2$ in this analysis and furthermore, enables $Q^2$ and $x$ to be determined without constraining the hadronic system.

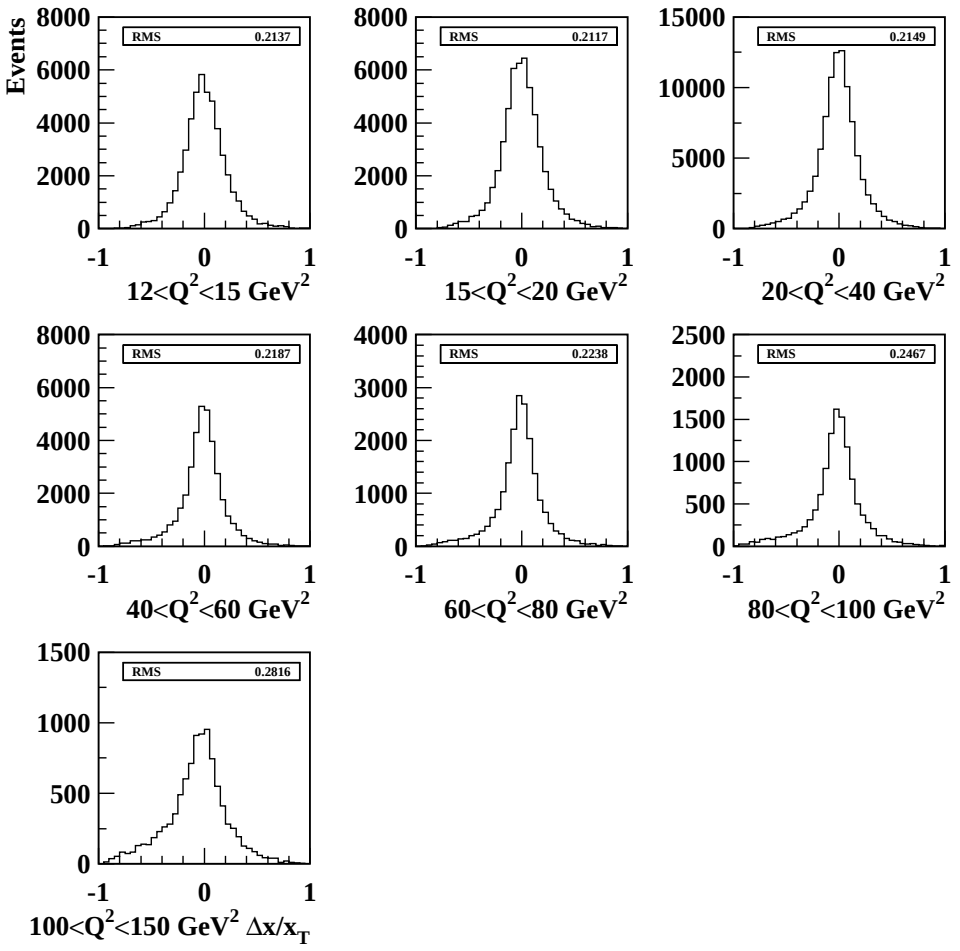


**Figure 4.34**: *$\Delta x/x_T$ calculated from 1996 low $Q^2$ reconstructed MEAR Monte Carlo using the Electron Only method.*

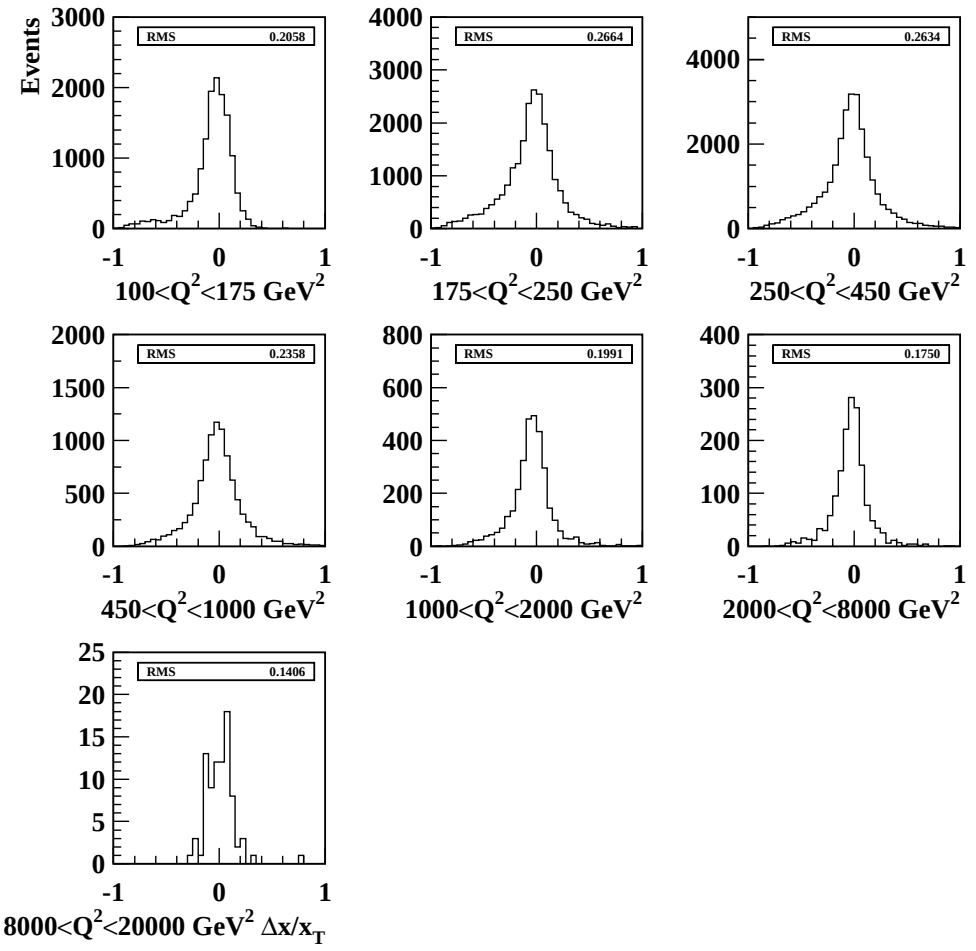


**Figure 4.35**: *$\Delta x/x_T$ calculated from 1996 high $Q^2$ reconstructed MEAR Monte Carlo using the Electron Only method.*

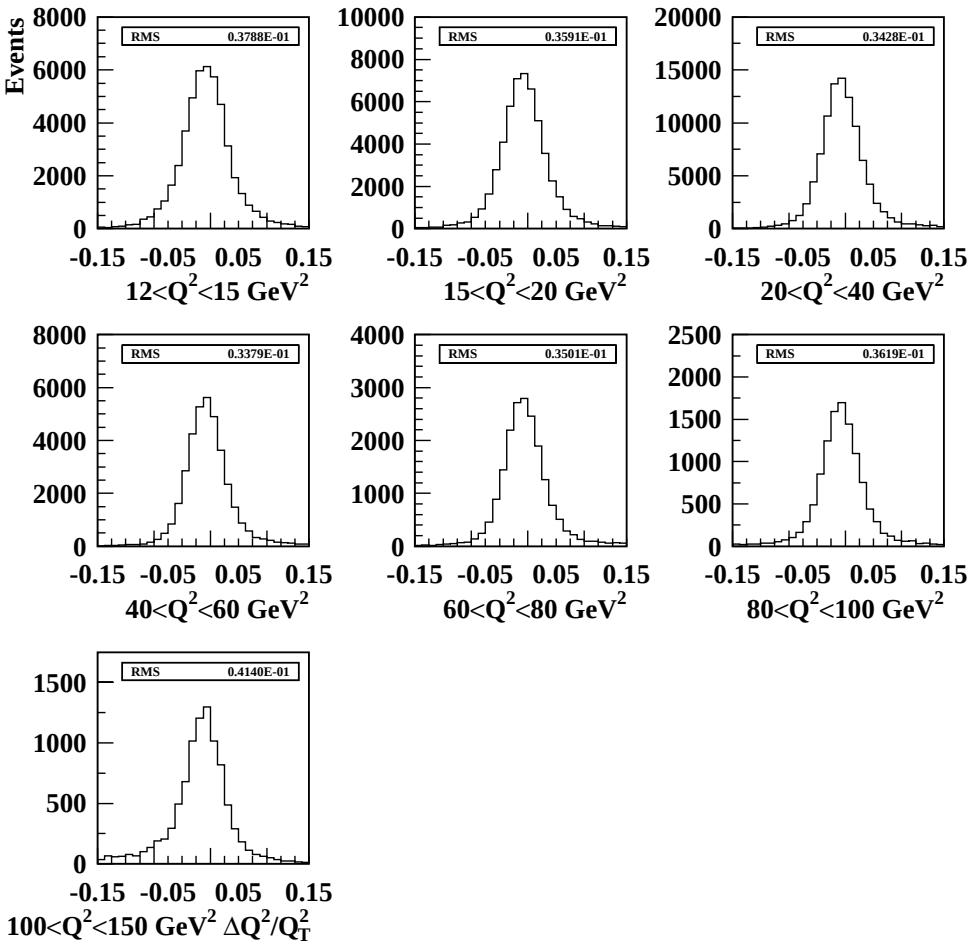


**Figure 4.36**: *$\Delta Q^2/Q_T^2$ calculated from 1996 low $Q^2$ reconstructed MEAR Monte Carlo using the Electron Only method.*

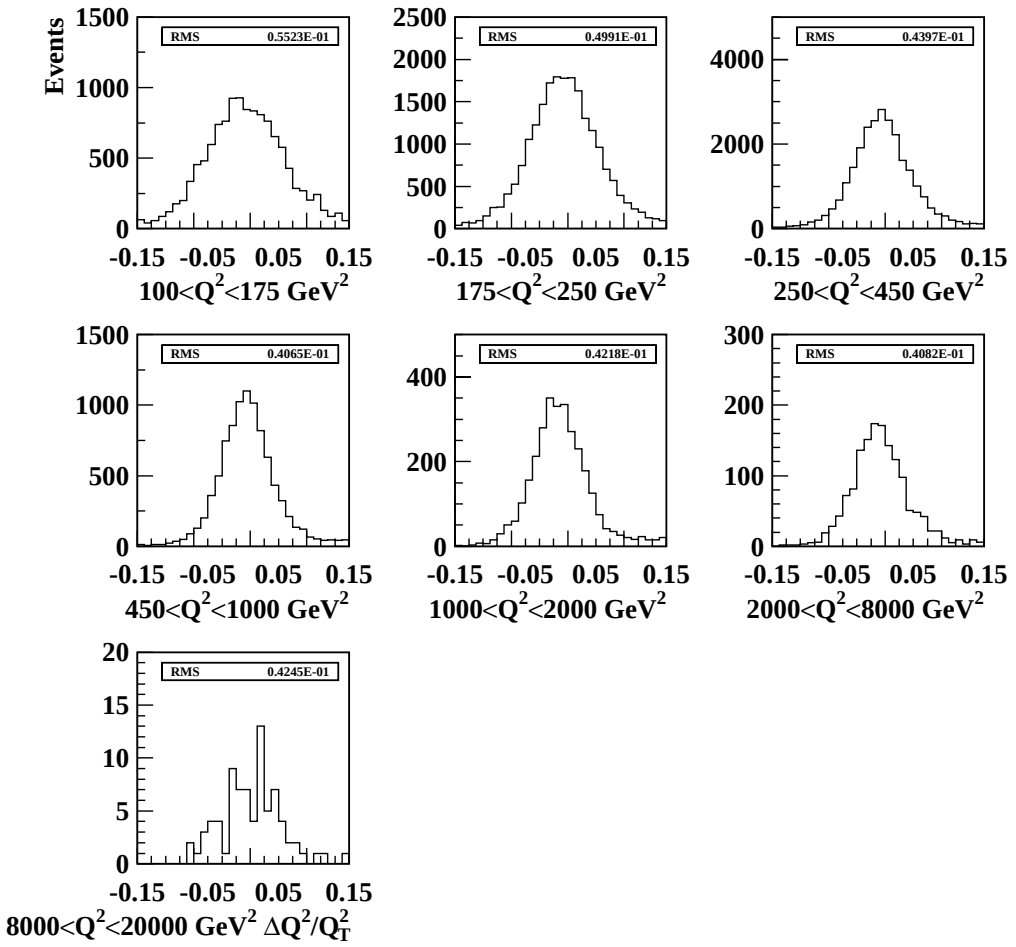


**Figure 4.37**: *$\Delta Q^2/Q_T^2$ calculated from 1996 high $Q^2$ reconstructed MEAR Monte Carlo using the Electron Only method.*

# Chapter 5

# Particle Identification

## 5.1 Introduction

This thesis is concerned with the identification of different hadronic species, and the measurement of corresponding scaled momentum spectra. This Chapter will discuss in detail two particular particle identification techniques; one based upon a measurement of the specific ionisation energy loss of primary charged particles passing through an ionising medium, and a second which reconstructs the $V^0$ invariant mass under different daughter hypotheses.

## 5.2 Particle Identification using $\mathrm{d}E/\mathrm{d}x$

By carrying out a simultaneous measurement of the momentum, $p$, and specific ionisation energy loss, $\mathrm{d}E/\mathrm{d}x$, of a charged track in the central tracking system, it is possible to identify charged pions ($\pi^{\pm}$), charged kaons ($K^{\pm}$), protons ($p$) and antiprotons ($\bar{p}$), and in principle deuterons (d). This section will outline the $\mathrm{d}E/\mathrm{d}x$ measurement performed at H1 and the selection criteria defined to obtain samples of different charged hadronic species. A more detailed discussion of the $\mathrm{d}E/\mathrm{d}x$ analysis technique can be found elsewhere [62, 63].

### 5.2.1 Measurement of Track Momentum

The momentum of a charged particle can be determined by measuring its curvature in a magnetic field. The trajectory of a particle with momentum $p$ (GeV/c) and charge $z$e, passing through a uniform magnetic field of strength $B$ (Tesla), is helical, with a radius of curvature $R$ (metres) and pitch angle $\lambda$. The relationship between $p$ and $R$ is given by:

$$p\cos\lambda = 0.3zBR \tag{5.1}$$

The distribution of curvature measurements, $k(\equiv 1/R)$, is approximately Gaussian. For a large number of uniformly spaced measurements of the particle trajectory the curvature error $\delta k$ can be estimated as:

$$(\delta k)^2 = (\delta k_{res})^2 + (\delta k_{ms})^2 \tag{5.2}$$

where $\delta k_{res}$ is the curvature error due to a finite measurement resolution and $\delta k_{ms}$ is the curvature error resulting from multiple scattering.

### 5.2.2 Specific Ionisation Energy Loss $\mathrm{d}E/\mathrm{d}x$

Moderately relativistic charged particles traversing a medium will lose energy primarily through ionisation. The mean rate of energy loss for a specific medium is given by the Bethe-Bloch equation [64]:

$$-\frac{\mathrm{d}E}{\mathrm{d}x} = 4\pi N_0 r_e^2 m_e c^2 z^2 \frac{Z}{A}\frac{1}{\beta^2}\left[\ln\left(\frac{2m_e c^2\gamma^2\beta^2}{I}\right) - \frac{\delta}{2}\right] \tag{5.3}$$

where $N_0$ is Avogadro's number, $Z$ and $A$ are the atomic number and weight of the atoms in the ionising medium respectively, $m_e$ is the orbital electron mass, $r_e$ is the classical radius of the electron, and $I$ is the mean excitation energy. The constant factor $4\pi N_0 r_e^2 m_e c^2/A$ is equal to 0.307 MeV g$^{-1}$ mol$^{-1}$ for $A = 1$ g mol$^{-1}$.

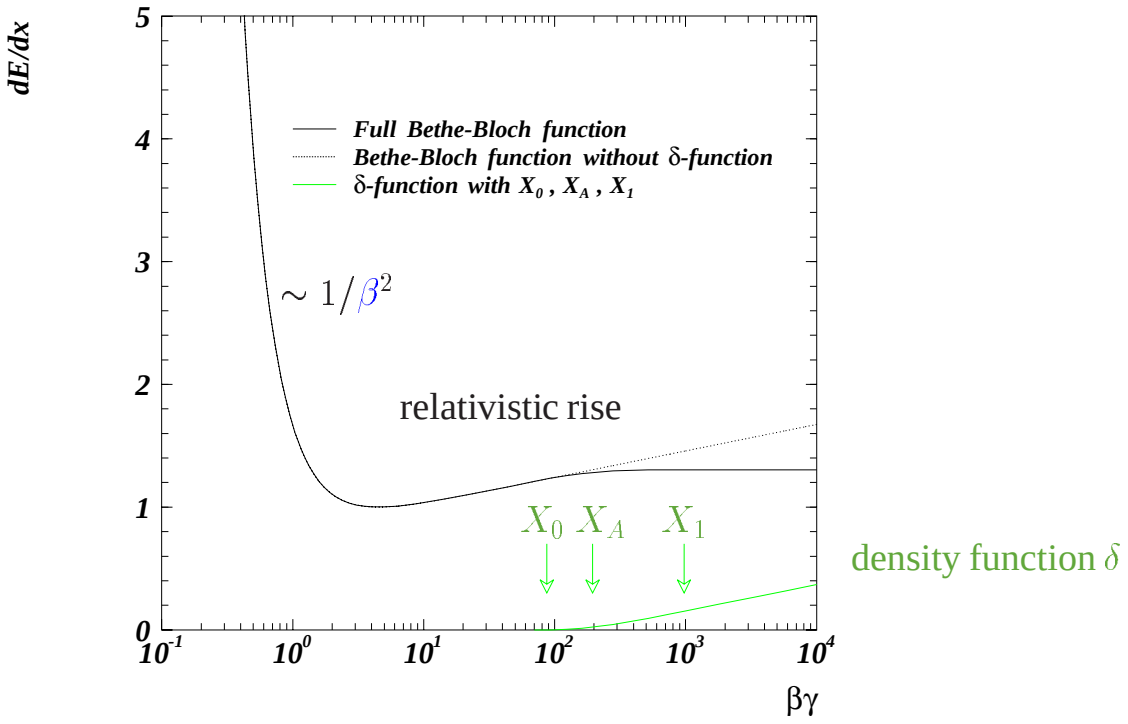


**Figure 5.1**: *The Bethe-Bloch equation as function of $\beta\gamma$, taken from [62]. See section 5.2.3 for definitions of $X_0$, $X_1$ and $X_A$.*

The density effect correction, $\delta$, modifies the growth of energy loss for charged particles at very high energies.

In Figure 5.1, a form of the Bethe-Bloch equation is plotted as a function of $\beta\gamma$[1]. At low momenta the mean rate of energy loss decreases as $\beta\gamma$ increases, with $|\mathrm{d}E/\mathrm{d}x| \propto \beta^{-5/3}$ (although traditionally this fall off is approximated to be $\propto \beta^{-2}$), until reaching a broad minimum at $\beta\gamma \approx 3.0$-$3.5$. This fall in $\mathrm{d}E/\mathrm{d}x$ with increasing particle momentum is attributed to a decreasing interaction time between the traversing particle and ionising medium. As the energy of the particle increases further, its electric field flattens and extends, ionising distant atoms from the particle's trajectory, leading to $|\mathrm{d}E/\mathrm{d}x|$ increasing as $\ln\beta\gamma$. At very high energies the density effect correction modifies the rise of $|\mathrm{d}E/\mathrm{d}x|$ which grows as $\ln\beta\gamma$ rather than $\ln\beta^2\gamma^2$.

[1]The boost variable $\vec{\beta}$ is defined in terms of the particle velocity, $\vec{v}$, as $\vec{\beta} = \vec{v}/c$, and is related to the Lorentz factor, $\gamma$, through the relationship $\gamma = 1/\sqrt{1-\beta^2}$. Note $\vec{p} = m\vec{\beta}\gamma c$.

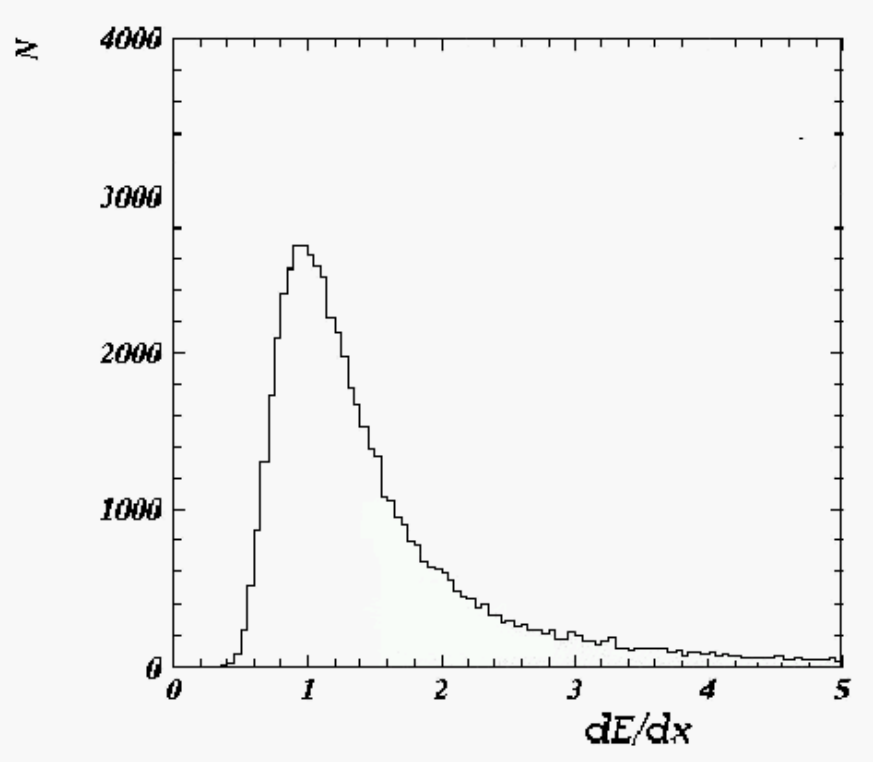


**Figure 5.2**: *The Landau distribution as observed for specific ionisation energy loss.*

The Bethe-Bloch equation is a universal function of $\beta\gamma = p/m$ for all charged particles, where $m$ is the traversing particle mass. For low and intermediate $p$, the rate of energy loss through ionisation in a specific medium thus increases with $m$. Therefore, the simultaneous measurement of momentum and $\mathrm{d}E/\mathrm{d}x$ enables good separation and identification of different particle species, particularly at low momenta.

### 5.2.3 Measurement of $\mathrm{d}E/\mathrm{d}x$ at H1

The measurement of $\mathrm{d}E/\mathrm{d}x$ for a charged particle passing through the H1 detector is made using the sense wires of the central jet chamber (CJC) (see section 1.3.1). Each sense wire has an associated value of energy loss, $\mathrm{d}E/\mathrm{d}x_i$, and the final energy loss assigned to a track comprises of $N_{\mathrm{d}E/\mathrm{d}x}$ such measurements or 'hits'. The values of $\mathrm{d}E/\mathrm{d}x_i$ have a Landau distribution [65], as presented in Figure 5.2, which is asymmetric and has a high energy loss tail extending asymptotically

to infinity. The method used by the H1 experiment [66] to determine the mean $\mathrm{d}E/\mathrm{d}x$ of a track is to calculate the average of a transformed distribution where tail contributions are suppressed, and is given by:

$$-\frac{\mathrm{d}E}{\mathrm{d}x} = \left( \frac{1}{N_{\mathrm{d}E/\mathrm{d}x}} \sum_{i=1}^{N_{\mathrm{d}E/\mathrm{d}x}} \frac{1}{\sqrt{\mathrm{d}E/\mathrm{d}x_i}} \right)^{-2} \tag{5.4}$$

The precision of the $\mathrm{d}E/d$x measurement is given by [62]:

$$\sigma_{\mathrm{d}E/\mathrm{d}x} = p_1 \frac{1}{N_{\mathrm{d}E/\mathrm{d}x}} + p_2 + p_3 N_{\mathrm{d}E/\mathrm{d}x} \tag{5.5}$$

where parameters $p_i (i = 1, .., 3)$ are associated with the properties of the CJC, and have different values for different data taking periods. To ensure a good quality measurement, a minimum of 5 hits are required for the online reconstruction of the track $\mathrm{d}E/\mathrm{d}x$ value, although a higher minimum value of 15 is used in this analysis.

The online measurement of the specific ionisation energy loss, $\mathrm{d}E/\mathrm{d}x_{meas}$, must be calibrated to take into account important dependencies on atmospheric pressure, lepton beam current, and the high voltage settings (HV) of the CJC. It has been shown [62] that increased atmospheric pressure and a higher effective HV of the sense wires as the lepton beam current decreases, give rise to higher values of $\mathrm{d}E/\mathrm{d}x$. Calibration constants $ddx_1$ and $ddx_2$ are calculated separately for CJC1 and CJC2, and stored during online reconstruction. The calibration is performed using minimum ionising $\pi^{\pm}$ with $0.3 \leq p \leq 0.7$ GeV/$c$ and $N_{\mathrm{d}E/\mathrm{d}x} \geq 10$. The calibrated measurement, $\mathrm{d}E/\mathrm{d}x_{cal}$, is calculated as:

$$\mathrm{d}E/\mathrm{d}x_{cal} = \frac{\mathrm{d}E/\mathrm{d}x_{meas}}{ddx1,2} \tag{5.6}$$

Due to problems with the online $\mathrm{d}E/\mathrm{d}x_{cal}$ calibration, the resulting values of $\mathrm{d}E/\mathrm{d}x$ were in poor agreement with a quasi-empirical Bethe-Bloch formula of the form:

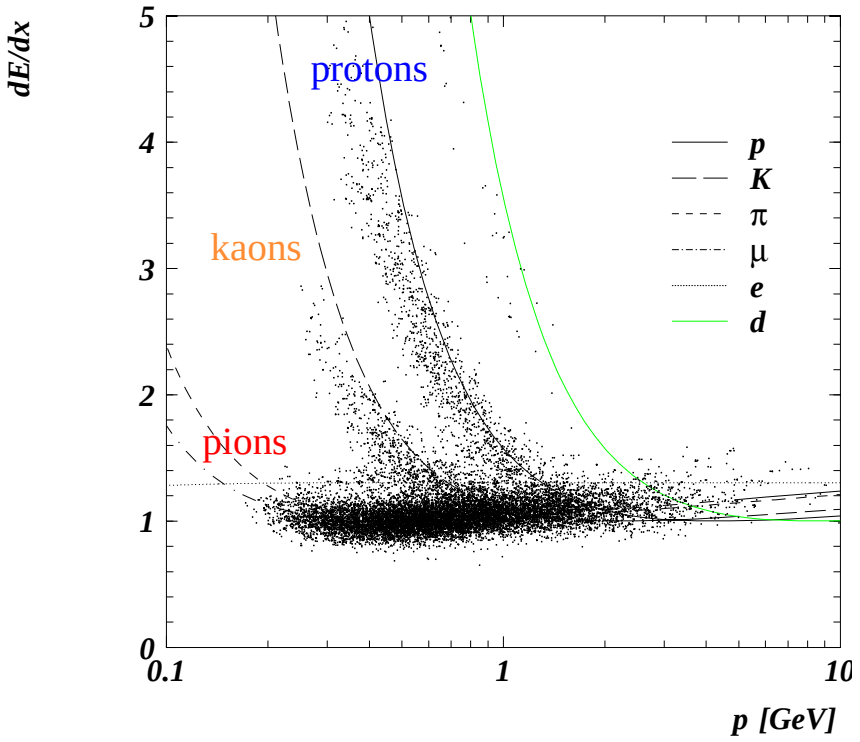


**Figure 5.3**: *Calibrated dE/dx in data as a function of laboratory momentum, p, together with the expectation for protons and antiprotons (p), charged kaons (K), charged pions (π), muons (μ), electrons (e), and deuterons (d), as calculated from equation 5.7, taken from [62].*

$$-\frac{\mathrm{d}E}{\mathrm{d}x} = \xi z^2 \frac{1}{\beta^2}[K + \ln(\beta^2\gamma^2) - \beta^2 - \delta(\beta, X_A, a)] \tag{5.7}$$

where $\delta(\beta, X_A, a)$ is the Sternheimer and Peierls parameterisation for the density effect correction [67]:

$$\delta(\beta, X_A, a) = \begin{cases} 0 & : X < X_0 \\ b(X - X_A) + a(X_1 - X)^m & : X_0 \leq X < X_1 \\ b(X - X_A) & : X_1 \leq X \end{cases}$$

with $X = \log(\beta\gamma)$, $b = 2\ln 10$, $m = 3$. The values of parameters $a$, $X_A$, $K$, and $\xi$ are determined from fitting H1 data and are given as $a = 1.40043$, $X_A = 2.28957$, $K = 18.2684$, and $\xi = 0.05721$ (see [62]). The functions $X_0$ and $X_1$ are parameterised as:

$$X_1 - X_0 = (\frac{b}{ma})^{\frac{1}{m-1}} \tag{5.8}$$

$$X_0 = X_A - \frac{a(X_1 - X_0)^m}{b} \tag{5.9}$$

In Figure 5.3 the calibrated values of $\mathrm{d}E/\mathrm{d}x$ are shown as function of laboratory momentum, with low momentum $K^{\pm}$ and $p/\bar{p}$ having a tendency to lie below the expectation calculated using equation 5.7. A new off-line correction procedure has been developed [62] and re-calibrates the $\mathrm{d}E/\mathrm{d}x$ measurement according to dependencies upon several different parameters:

- particle polar angle, $\theta$
- uncorrected ionisation, $\mathrm{d}E/\mathrm{d}x_{uncorr}$
- particle charge, $q$
- particle azimuthal angle, $\phi$
- particle momentum, $p$
- high voltage settings for a given run range

The new procedure uses a single parameterisation of $\mathrm{d}E/\mathrm{d}x$, taking the form:

$$f_{\mathrm{d}E/\mathrm{d}x} = p_1 \frac{1}{\beta^{p_2}} \left[1.0 + p_3(\exp\{-p_4 \log(0.25 + \beta\gamma)\})\right] \tag{5.10}$$

and can be used for all charged particles. The four parameters $p_i(i{=}1,..,4)$ are determined[2] from fits to data points of muons, $K^{\pm}$, and $p/\bar{p}$, where input values are always taken at $\theta = 90°$. The raw $\mathrm{d}E/\mathrm{d}x$ values are corrected in a similar way as that described by equation 5.6, with the generation of a new correction function:

[2]The values obtained for parameters $p_i(i{=}1,..,4)$ are [62]: $p_1$=1.4139, $p_2$=1.6504, $p_3$=-0.4610, and $p_4$=0.56924

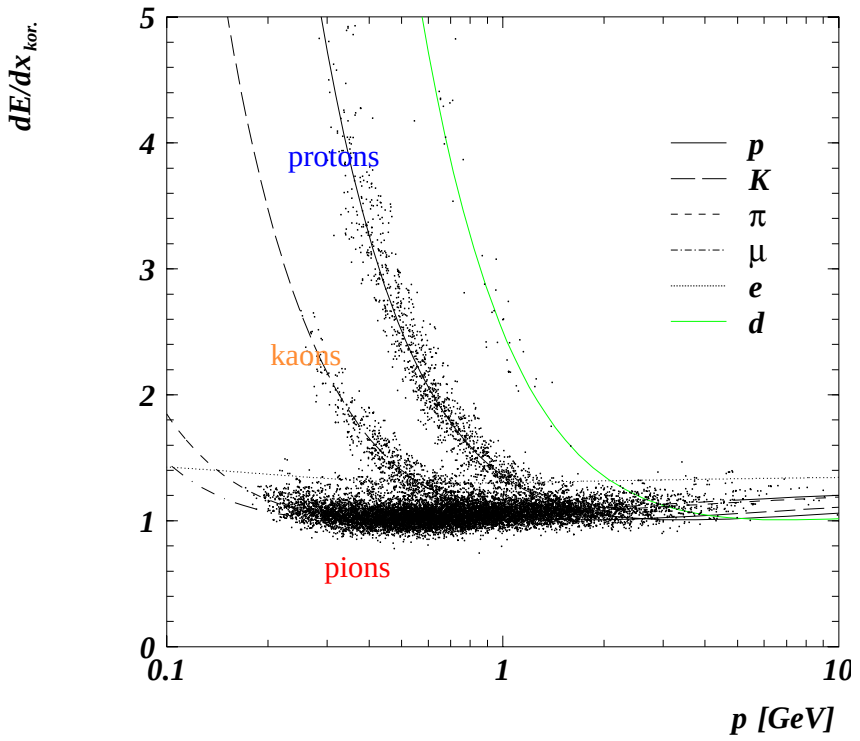


**Figure 5.4**: *Re-calibrated dE/dx in data as a function of laboratory momentum, p, together with expectations for protons and antiprotons (p), charged kaons (K), charged pions (π), muons (μ), electrons (e), and deuterons (d), as calculated from equation 5.10, taken from [62].*

$$\mathrm{d}E/\mathrm{d}x \equiv f_{cor}(\theta, \mathrm{d}E/\mathrm{d}x_{uncorr}, p, q, \phi, run) \tag{5.11}$$

which incorporates the $\theta$ dependency and a small correction for particles with very low momenta. This is done depending upon $q$, $\phi$, and in several run ranges corresponding to different CJC HV settings. The raw values are corrected to the reference function, $f_{\mathrm{d}E/\mathrm{d}x}$, defined in equation 5.10, and by removing any $\theta$ or $\phi$ dependencies an overall improvement in the agreement with expectation (equation 5.10) is obtained, as is clearly seen in Figure 5.4.

The $\mathrm{d}E/\mathrm{d}x$ value of a charged track simulated in the Monte Carlo is calculated by inserting the particle momentum and mass into equation 5.3, and smearing resulting values using a Landau distribution. The correction functions are produced with respect to the reference function $f_{\mathrm{d}E/\mathrm{d}x}$.

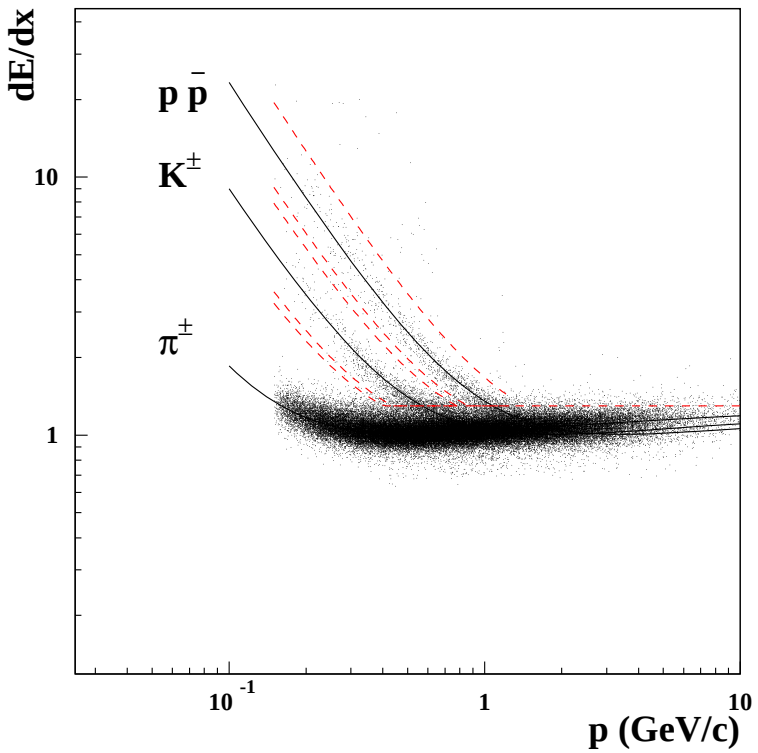


**Figure 5.5**: *Distribution of* $\mathrm{d}E/\mathrm{d}x$ *versus laboratory momentum,* $p$*, for a sample of primary charged tracks selected from 1996 H1 data. The dashed lines define particle identification windows. See section 5.2.4 for discussion.*

### 5.2.4 Particle Identification

A series of identification 'windows' for each particle species can be defined using $f_{\mathrm{d}E/\mathrm{d}x}(m_{win}\ \mathrm{GeV}/c^2)$ with suitable mass limits $m_{win}$ substituted. These are shown as dashed lines on Figure 5.5. A $\pi^{\pm}$ particle hypothesis is automatically applied for tracks with $\mathrm{d}E/\mathrm{d}x < 1.3$, and for tracks with $\mathrm{d}E/\mathrm{d}x < f_{\mathrm{d}E/\mathrm{d}x}(0.35)$ if $\mathrm{d}E/\mathrm{d}x > 1.3$. For tracks with $p < 0.7$ GeV/$c$, and satisfying $f_{\mathrm{d}E/\mathrm{d}x}(0.38) < \mathrm{d}E/\mathrm{d}x < f_{\mathrm{d}E/\mathrm{d}x}(0.68)$ and $\mathrm{d}E/\mathrm{d}x > 1.3$, a $K^{\pm}$ particle hypothesis is applied. A $p/\bar{p}$ hypothesis is applied for tracks with $p < 1.25$ GeV/$c$ and satisfying $f_{\mathrm{d}E/\mathrm{d}x}(0.75) < \mathrm{d}E/\mathrm{d}x < f_{\mathrm{d}E/\mathrm{d}x}(1.25)$ and $\mathrm{d}E/\mathrm{d}x > 1.3$. These windows are non-overlapping and are chosen to optimise identification efficiencies.

An alternative selection procedure [62] based upon a log-likelihood method can be

used as a systematic check of the geometric method outlined above. By defining a $\chi^2$ statistic using data and a theoretical expectation, it is possible to form a log-likelihood probability [65] by integrating the $\chi^2$ distribution for 1 degree of freedom:

$$LH_i = \frac{1}{\sqrt{2}\Gamma(1/2)} \int_{\chi_i^2}^{\infty} e^{-t/2} \frac{1}{\sqrt{2}} dt \tag{5.12}$$

$$\chi_i^2 = \frac{[\mathrm{d}E/\mathrm{d}x - f_{\mathrm{d}E/\mathrm{d}x,i}]^2}{\sigma^2} \tag{5.13}$$

Here, $LH_i$ is the log-likelihood probability of particle hypothesis $i$ for a data point with specific ionisation energy loss $\mathrm{d}E/\mathrm{d}x$. The term $\Gamma(1/2)$ is the gamma function for 1 degree of freedom, $f_{\mathrm{d}E/\mathrm{d}x,i}$ is the reference function with the mass of particle $i$ substituted, and $\sigma$ is the error on the $\mathrm{d}E/\mathrm{d}x$ data measurement calculated using equation 5.5.

The log-likelihood probabilities of different particle hypotheses ($\pi^{\pm}$, $K^{\pm}$, $p/\bar{p}$, deuteron, muon, and electron) can be normalised to give a normalised log-likelihood probability:

$$LN_i = \frac{LH_i}{\sum_{j=1}^{6} LH_j} \tag{5.14}$$

A selection criteria can then be devised based upon a cut on the normalised log-likelihood value. For this analysis, a given particle hypothesis is applied for tracks with $LN_i > 0.1$.

## 5.3 Reconstruction of $V^0$ Particles

### 5.3.1 Introduction

By applying the $V^0$ selection criteria outlined in section 4.3.5, it is possible to identify $K^0_S$ mesons and $\Lambda$ baryons for the decay channels:

$$K^0_S \rightarrow \pi^+\pi^-$$

$$\Lambda\ (\overline{\Lambda}) \rightarrow p\pi^-\ (\bar{\mathrm{p}}\pi^+)$$

by calculating the invariant mass of the $V^0$ candidate assuming the daughter particles are a pair of oppositely charged pions ($\pi\pi$) for $K^0_S$ candidates, and a charged pion and proton ($p\pi$) for $\Lambda$ candidates. To remove combinatorial difficulties with $\Lambda$ ($\overline{\Lambda}$) identification the daughter carrying the largest momentum is taken to be the baryon; no signal is observed if this procedure is reversed. Background contamination from $e^+e^-$ pairs produced in photon conversion ($\gamma \rightarrow e^+e^-$) is reduced by rejecting $V^0$ candidates which have an invariant mass less than 50 MeV/$c^2$ when both daughters are hypothesised to be electrons. Contamination from $\Lambda$ decays in the $K^0_S$ sample is reduced by excluding those $K^0_S$ candidates which have a $p\pi$ invariant mass in the $\Lambda$ selection window, and vice versa.

### 5.3.2 $V^0$ Invariant Mass Spectra

In Figures 5.6 and 5.7, the $V^0$ invariant mass spectra $m(\pi\pi)$ and $m(p\pi)$ are shown, as calculated using a $\pi\pi$ daughter hypothesis and a $p\pi$ daughter hypothesis respectively, for the current and target regions of the Breit frame (see Chapter 6) combined. In Figure 5.6, the $K^0_S$ signal is fitted in each case using a superposition of two Gaussian functions (having a common peak) with a linear background, and the $\Lambda$ signal is described by a single Gaussian function with a flat background. In Tables 5.1 and 5.2 a summary of the mean mass and weighted mean width of

| $K^0_S \to \pi^+\pi^-$ | | Data Sample | |
|---|---|---|---|
| low $Q^2$ | | 1996 | 1997 |
| mean | data | 497.2 ± 0.2 | 496.6 ± 0.2 |
| (MeV/$c^2$) | Monte Carlo | 498.6 ± 0.1 | 498.4 ± 0.1 |
| width | data | 13.9 ± 3.2 | 14.2 ± 1.8 |
| (MeV/$c^2$) | Monte Carlo | 9.4 ± 2.1 | 10.2 ± 1.2 |
| $\tau_0$ ($10^{-10}s$) | data | 0.83 ± 0.04 | 0.90 ± 0.04 |
| high $Q^2$ | | 1996 | 1997 |
| mean | data | 496.7 ± 0.5 | 496.9 ± 1.0 |
| (MeV/$c^2$) | Monte Carlo | 498.5 ± 0.2 | 499.2 ± 0.2 |
| width | data | 15.3 ± 4.8 | 15.0 ± 1.2 |
| (MeV/$c^2$) | Monte Carlo | 13.0 ± 1.8 | 9.1 ± 0.2 |
| $\tau_0$ ($10^{-10}s$) | data | 0.67 ± 0.09 | 0.72 ± 0.12 |

**Table 5.1**: *A comparison of the mean mass and weighted mean width of the $K^0_S$ signal extracted from a fit, of the form described in the text, to the $m(\pi\pi)$ invariant mass spectrum for data and reconstructed Monte Carlo. Also shown is the mean proper lifetime, $\tau_0$. Results are shown separately for low and high $Q^2$ data samples. Statistical errors only are shown.*

| $\Lambda \rightarrow p\pi$ | | Data Sample | |
|---|---|---|---|
| low $Q^2$ | | 1996 | 1997 |
| mean | data | 1115.8 ± 0.4 | 1115.1 ± 0.2 |
| (MeV/$c^2$) | Monte Carlo | 1115.9 ± 1.0 | 1116.0 ± 0.1 |
| width | data | 3.0 ± 0.4 | 3.2 ± 0.2 |
| (MeV/$c^2$) | Monte Carlo | 2.2 ± 0.1 | 2.6 ± 0.1 |
| $\tau_0$ ($10^{-10}s$) | data | 3.1 ± 1.4 | 2.1 ± 0.5 |
| high $Q^2$ | | 1996 | 1997 |
| mean | data | 1116.4 ± 0.6 | 1115.0 ± 2.7 |
| (MeV/$c^2$) | Monte Carlo | 1115.7 ± 0.2 | 1116.1 ± 0.2 |
| width | data | 3.8 ± 0.8 | 10.6 ± 3.0 |
| (MeV/$c^2$) | Monte Carlo | 2.4 ± 0.1 | 2.2 ± 0.1 |
| $\tau_0$ ($10^{-10}s$) | data | - | - |

**Table 5.2**: *A comparison of the mean mass and width of the* $\Lambda$ *signal extracted from a fit, of the form described in the text, to the* $m(p\pi)$ *invariant mass spectrum for data and reconstructed MEAR Monte Carlo. Also shown is the mean proper lifetime,* $\tau_0$*. Results are shown separately for low and high* $Q^2$ *data samples. Statistical errors only are shown.*

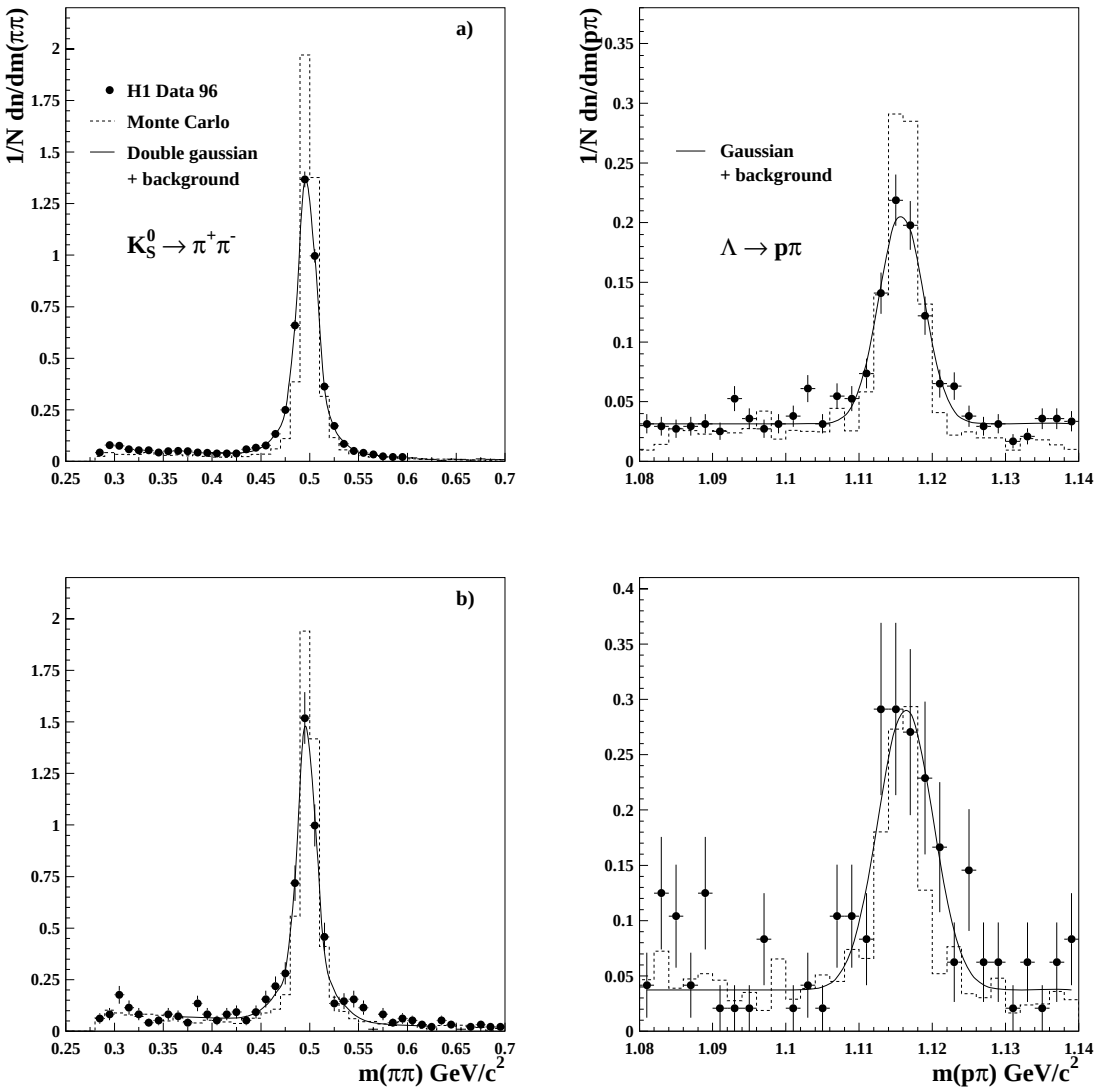


**Figure 5.6**: *Comparison of 1996 a) low $Q^2$ and b) high $Q^2$ data (closed circles) with reconstructed MERA Monte Carlo (dashed histogram) for left) $m(\pi\pi)$ and right) $m(p\pi)$ invariant mass spectra. In each case, the solid line is a fit to the data of a form described in the text. Statistical errors only are shown.*

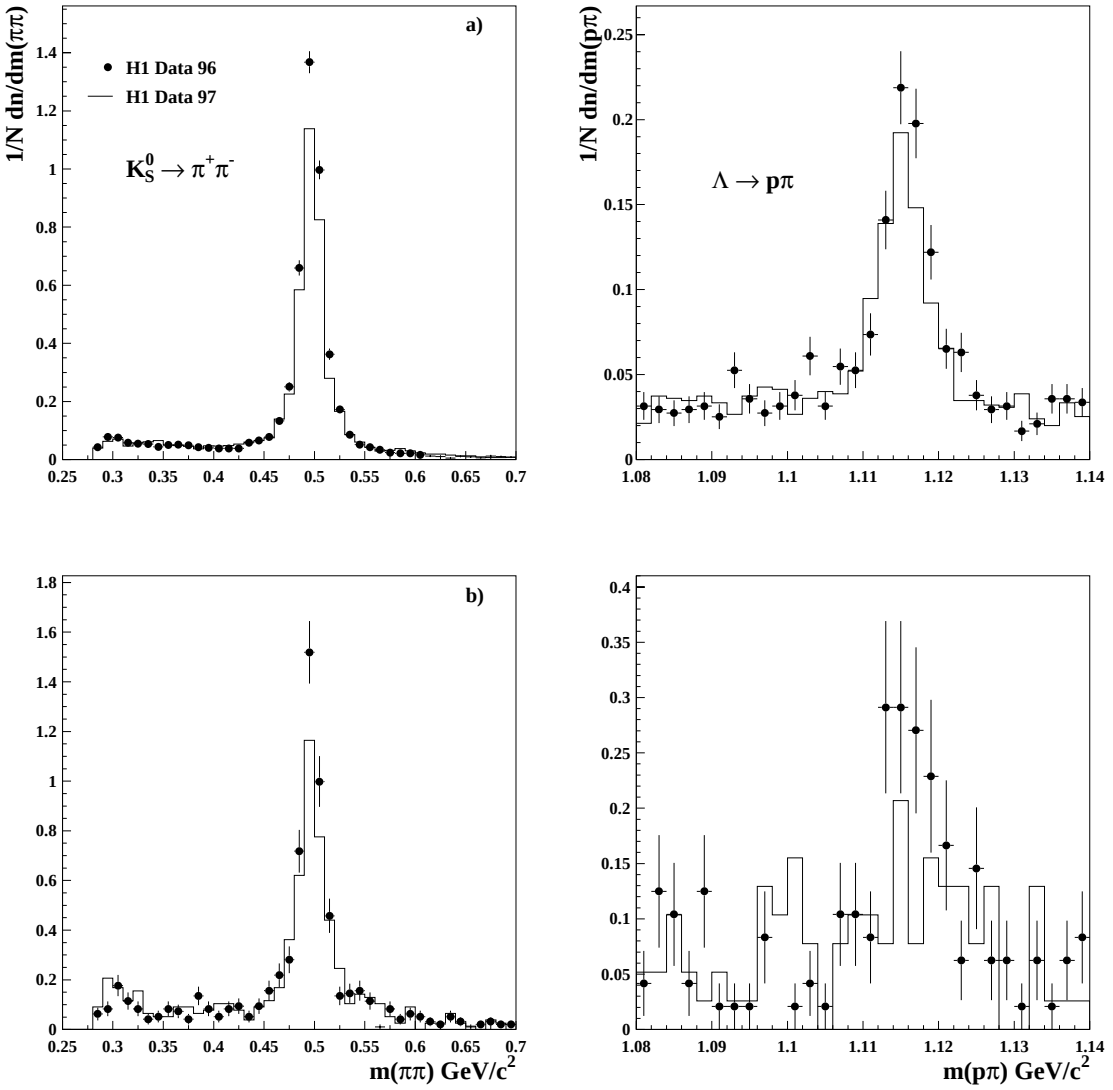


**Figure 5.7**: *Comparison of 1996 a) low $Q^2$ and b) high $Q^2$ (closed circles) and 1997 (histogram) data samples for left) $m(\pi\pi)$ and right) $m(p\pi)$ invariant mass spectra. Statistical errors only are shown.*

| Particle | Year | Sample | Current | Target |
|---|---|---|---|---|
| $K^0_S$ | 1996 | low $Q^2$ | 1581 ± 41 | 2180 ± 51 |
| $K^0_S$ | 1996 | high $Q^2$ | 246 ± 41 | 165 ± 14 |
| $\Lambda$ | 1996 | low $Q^2$ | 16 ± 5 | 108 ± 13 |
| $\Lambda$ | 1996 | high $Q^2$ | 8 ± 4 | 12 ± 4 |
| $K^0_S$ | 1997 | low $Q^2$ | 2038 ± 50 | 2058 ± 66 |
| $K^0_S$ | 1997 | high $Q^2$ | 193 ± 15 | 124 ± 13 |
| $\Lambda$ | 1997 | low $Q^2$ | 23 ± 6 | 144 ± 16 |
| $\Lambda$ | 1997 | high $Q^2$ | 2 ± 2 | 3 ± 3 |

**Table 5.3**: *Uncorrected numbers of $K^0_S$ and $\Lambda$ candidates in the current and target hemispheres of the Breit frame of reference (see Chapter 6 for definition) for 1996 and 1997 low and high $Q^2$ data samples. Errors include a dominant poissonian statistical error added in quadrature to a binomial error from the background subtraction.*

the $K^0_S$ and $\Lambda$ signals is presented. From Figure 5.6 it can be seen that invariant mass spectra shapes in data are well-modelled by the Monte Carlo, although the mean mass position tends to be higher in Monte Carlo, particularly for the $K^0_S$ signal, and the width of both the $K^0_S$ and $\Lambda$ signals in Monte Carlo are narrower than in data. The comparison between 1996 and 1997 data samples presented in Figure 5.7 shows a tendency for 1996 data to lie above 1997 data, and may be due to known CJC inefficiencies. However, the fitted mean mass and width of the $K^0_S$ and $\Lambda$ signals show consistency between data samples, and with published PDG [64] values.

The uncorrected numbers of $K^0_S$ and $\Lambda$ candidates are calculated separately for the current and target regions, with results summarised in Table 5.3. The number of candidates for a given particle species is calculated by subtracting the integrated background from the area under the Gaussian peak over the mass interval $0.45 < m(\pi\pi) < 0.55$ GeV/$c^2$ for $K^0_S$ candidates, and $1.107 < m(p\pi) < 1.124$ GeV/$c^2$ for $\Lambda$ candidates. The errors quoted in Table 5.3 comprise of a dominant poissonian statistical error added in quadrature to a binomial error. The guard bands 0.41

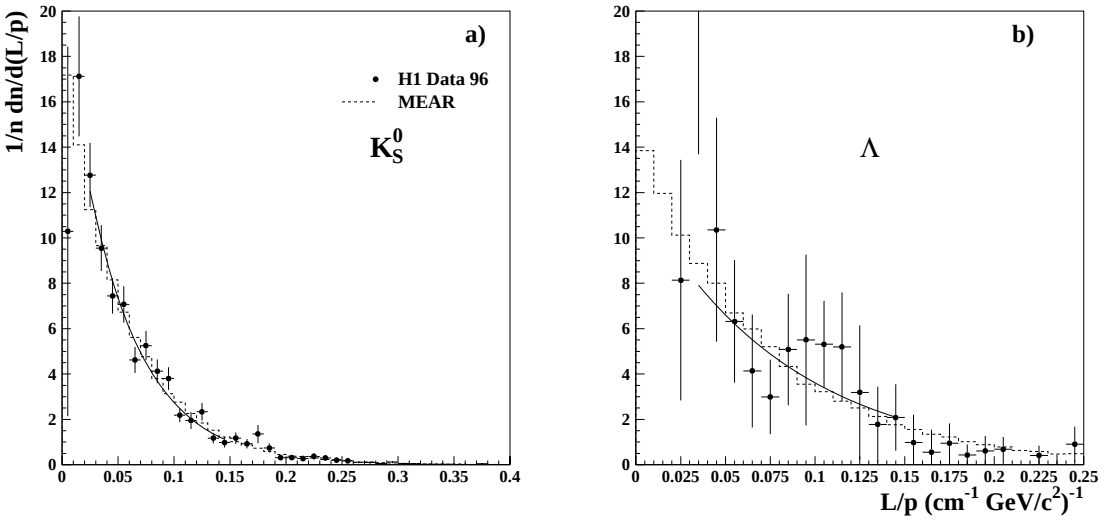


**Figure 5.8**: *The (L/p) distribution for a) $K^0_S$ and b) $\Lambda$ in 1996 low $Q^2$ data (closed circles) and generated MEAR Monte Carlo (histogram), where L and p are the decay length and laboratory momentum of the hadron respectively. Statistical errors only are shown. The solid line is a fit to the data using the functional form defined in equation 5.16.*

$< m(\pi\pi) \leq 0.45$ GeV/$c^2$ and $0.55 \leq m(\pi\pi) < 0.61$ GeV/$c^2$ are defined such that an approximate 10% non-resonant background in the $K^0_S$ selection window can be removed. Likewise, the guard bands $1.099 < m(p\pi) \leq 1.107$ GeV/$c^2$ and $1.124 \leq m(p\pi) < 1.132$ GeV/$c^2$ are defined to remove an approximate 29% non-resonant background from the $\Lambda$ selection window. At no stage in the reconstruction of the $V^0$ invariant mass is $\mathrm{d}E/\mathrm{d}x$ information used. Although there would be a slight improvement in the signal-to-background (S:B) ratio, the increase in the number of $K^0_S$ and $\Lambda$ particles is negligible.

### 5.3.3 $K^0_S$ and $\Lambda$ Lifetimes

By measuring the decay length, $L$, of $K^0_S$ and $\Lambda$ candidates, it is possible to estimate the corresponding mean proper lifetime, $\tau_0$. The number of $V^0$ candidates, $N(L)$, remaining at a time $\Delta t$ after travelling a distance $L$ from the primary vertex decreases exponentially as a function of $(L/p)$:

$$N(L) = N_0 \exp\left[-\frac{(\Delta t/\gamma)}{\tau_0}\right] = N_0 \exp\left[-\left(\frac{m_0}{c\tau_0}\right)\left(\frac{L}{p}\right)\right] \tag{5.15}$$

where $m_0$ and $p$ are the mean mass and laboratory momentum of the candidate respectively, and $N_0$ is the initial number of candidates produced at the primary vertex ($L = 0$). It follows from equation 5.15 that a corrected measured $(L/p)$ distribution normalised to the total number of *observed* particles, $n$, will have the form:

$$\frac{1}{n}\frac{\mathrm{d}n}{\mathrm{d}(L/p)} = \left(\frac{m_0}{c\tau_0}\right) \exp\left[-\left(\frac{m_0}{c\tau_0}\right)\left(\frac{L}{p}\right)\right] \tag{5.16}$$

Hence, by fitting $1/n\ \mathrm{d}n/\mathrm{d}(L/p)$, as measured for $K^0_S$ and $\Lambda$ candidates, using the functional form presented in equation 5.16, it is possible to extract $\tau_0$ for each particle species.

In Figure 5.8, the results of such fits are shown for samples of $K^0_S$ and $\Lambda$ candidates in 1996 low $Q^2$ data. In each case, the $1/n\ \mathrm{d}n/\mathrm{d}(L/p)$ distribution is corrected bin-by-bin (see section 7.6) for acceptance losses resulting from $V^0$ candidates decaying before reaching a minimum decay length of 2.0 cm in the $x$-$y$ plane, and from other $V^0$ quality requirements. Since no generated value of the decay length is available, the correction is performed using an equivalent distribution in which each generated $K^0_S$ and $\Lambda$ particle is assigned a value of $(L/p)$ as calculated from:

$$\left(\frac{L}{p}\right) = -\left(\frac{c\tau_0}{m_0}\right)\ln(1-r) \tag{5.17}$$

where $r$ is a uniformly distributed random number, and $m_0$ and $c\tau_0$ are substituted with corresponding values for $K^0_S$ and $\Lambda$ hadrons as published by the PDG [64].

The fitting interval is over an intermediate range of $(L/p)$ where bin-by-bin correction factors, $cf$, lie in the interval $0.5 < cf < 2.0$. The values of $\tau_0$ determined from 1996 and 1997 data samples are summarised in Tables 5.1 and 5.2, with $\tau_0$ in each case being in close agreement with those values published by the PDG [64].

Due to very low statistics it has not been possible to measure the $\Lambda$ mean proper lifetime using the high $Q^2$ data samples.

# Chapter 6

# The Breit Frame

## 6.1 Introduction

A convenient inertial reference frame for the study of quark fragmentation is the Breit frame [68]. The definition of the Breit frame is such that the fragmentation properties of $ep$ collisions can be compared to a single hemisphere of $e^+e^- \rightarrow \mathrm{q\bar{q}}$ scattering, thus simplifying tests of the universality of quark fragmentation. In this Chapter, the properties of the Breit frame will be discussed, as well as the effect of higher order processes not present in $e^+e^-$ interactions.

## 6.2 The Breit Frame of Reference

To reach the Breit frame of reference the HERA laboratory frame is first Lorentz boosted to the hadronic centre-of-mass frame (HCM), followed by a longitudinal boost along a common $z$ direction. This ensures that the exchanged virtual gauge boson is entirely space-like, having zero energy, zero transverse momentum and longitudinal momentum $-Q$. As in the laboratory frame of reference, the positive $z$-axis is chosen to be along the direction of the incoming proton.

Within the Quark Parton Model (QPM), the gauge boson collides with an incom-

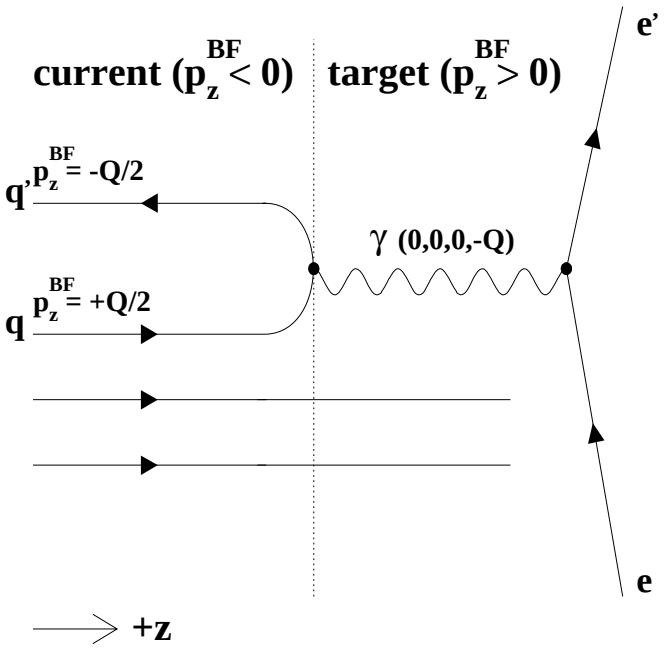


**Figure 6.1**: *A schematic representation of lowest order QED electron-quark scattering as viewed in the Breit frame. The current and target regions are defined by the negative and positive z-axis respectively.*

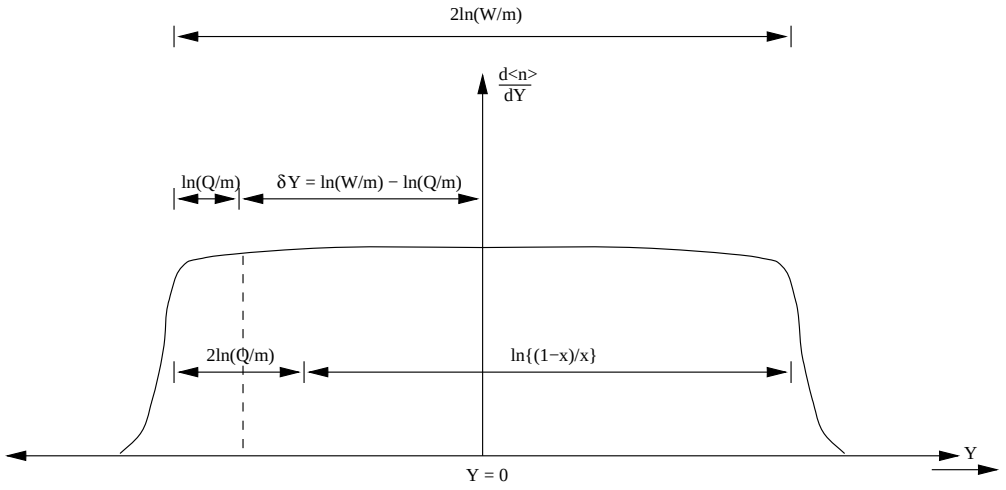


**Figure 6.2**: *A diagram of the rapidity plateau as viewed in the hadronic centre-of-mass system. The dashed line indicates the origin in the Breit frame.*

ing massless quark of four-momentum ($Q/2$,0,0,$Q/2$), as illustrated in Figure 6.1. After absorbing the boson, the struck quark backscatters into the *current* hemisphere, as defined by the negative $z$-axis, with four-momentum ($Q/2$,0,0,$-Q/2$), and the remnant diquark of the proton fragments into the *target* hemisphere defined by the positive $z$-axis. The phase space for current region fragmentation is equal to a single hemisphere of quark fragmentation resulting from an $e^+e^- \rightarrow \mathrm{q\bar{q}}$ annihilation. Thus, the $e^+e^-$ centre-of-mass energy, $E^*$, is taken to be equivalent to the energy scale $Q$.

## 6.3 Properties of the Breit Frame

A previous study [69] has shown that current hemisphere particle multiplicities in the Breit frame are $Q$ dependent, as opposed to the HCM where multiplicities depend upon a scale set by the invariant mass, $W$, of the hadronic final state. Furthermore, the average charged track multiplicity in the current hemisphere of the Breit frame is roughly equal to half the average charged hadronic multiplicity of an $e^+e^-$ interaction at an energy $E^* = Q$, and the multiplicity in the current

hemisphere of the HCM with half the hadronic multiplicity of an $e^+e^-$ interaction at an energy $E^* = W$ which can be shown to result from Feynman scaling [47].

The rapidity, $Y$, of a particle with energy $E$ and longitudinal momentum $p_z$ can be defined in a Lorentz invariant form as:

$$Y = \frac{1}{2} \ln \left( \frac{E + p_z}{E - p_z} \right) \tag{6.1}$$

Feynman argues that due to the relativistic contraction of a target in the beam direction the rapidity distribution will have a flat plateau. For particles of mass $m$ produced at a centre-of-mass energy $W$ the rapidity distribution expected as a result of limited transverse momentum ($p_t$) interactions has a total width of $\Delta Y = 2\ln(W/m)$. Using the expression $W^2 = Q^2((1-x)/x)$, as derived in Chapter 2 with the proton mass neglected, the width $\Delta Y$ can be re-expressed as:

$$2\ln(W/m) = 2\ln(Q/m) + \ln((1-x)/x) \tag{6.2}$$

A somewhat simplified rapidity distribution made up of these partitions is illustrated in Figure 6.2. Within this picture, the averaged charged multiplicity in one hemisphere of the HCM is given by the area to the left (or right) of the origin $Y = 0$. The simplified version described here has the same average multiplicity in each hemisphere.

Given such a flat plateau, the ratio of the multiplicity in the rapidity interval $\ln(W/m)$ to that in a rapidity interval of $\ln(Q/m)$ is trivially $\ln(W/m)/\ln(Q/m)$, which is what would be expected for the ratio of the multiplicities of hadronic $e^+e^-$ interactions at two different energies (assuming a simple logarithmic dependence on $E^*$). It can be shown that if the $Y = 0$ point in the Breit frame is shifted from $Y = 0$ in the HCM by the amount $\delta Y = \ln W - \ln Q = \ln(W/m) - \ln(Q/m)$, then to first order, Breit frame current hemisphere multiplicities agree with $e^+e^-$ data at $E^* = Q$, and HCM current hemisphere multiplicities with $e^+e^-$ data at $E^* = W$.

The HCM and Breit frame are collinear inertial reference frames related by a Lorentz boost along the $z$-axis. The frames are expected to have the same rapidity distribution shifted by a constant amount, $\delta Y$:

$$\delta Y = \frac{1}{2}\ln\frac{(E^* + p_z^*)}{(E^* - p_z^*)} - \frac{1}{2}\ln\frac{(E^B + p_z^B)}{(E^B - p_z^B)} \tag{6.3}$$

where $E^B$ and $p_z^B$ are the Breit frame Lorentz boosted energy and momenta from the equivalent HCM variables $E^*$ and $p_z^*$. For a boost vector of magnitude $\beta^B$ and choosing $p_z^* = 0$ ($Y = 0$ in the HCM), and by substituting $E^B = \gamma(E^* + \beta^B 0)$ and $p_z^B = \gamma(0 + \beta^B E^*)$, $\delta Y$ may be written as:

$$\delta Y = -\frac{1}{2}\ln\frac{(1+\beta^B)}{(1-\beta^B)} \tag{6.4}$$

This expression may be further simplified by using the result $\beta^B = 1 - 2x$ and the relation $W^2 = Q^2((1-x)/x)$ to give:

$$\delta Y = -\frac{1}{2}\ln\frac{W^2}{Q^2} \tag{6.5}$$

This final result may be interpreted as a shift in the Breit frame origin relative to the HCM origin by an amount $(\ln(W/m) - \ln(Q/m))$ in the negative $Y$ direction, as required.

A further advantage of both the Breit and HCM frames is that low $p_t$ tracks can be studied. In these frames the $p_t$ arising from the electroweak recoil of the hadronic system against the scattered lepton is removed, facilitating the observation of QCD effects. In the laboratory frame of reference, low $p_t$ tracks have poor acceptance and are removed below 150 MeV/$c$ to improve the simulation efficiency. A strong correlation of average $p_t$ exists between the laboratory and Breit frames, but event-to-event variable boosts give sufficient acceptance for the study of low $p_t$ tracks in the Breit frame. This important property also enables the measurement of high momenta $K^{\pm}$, protons, and antiprotons in the Breit

frame even though their identification using $\mathrm{d}E/\mathrm{d}x$ information is restricted to a very narrow interval of low laboratory momentum, since low momenta tracks in the laboratory frame can occasionally be boosted to higher momenta in the Breit frame.

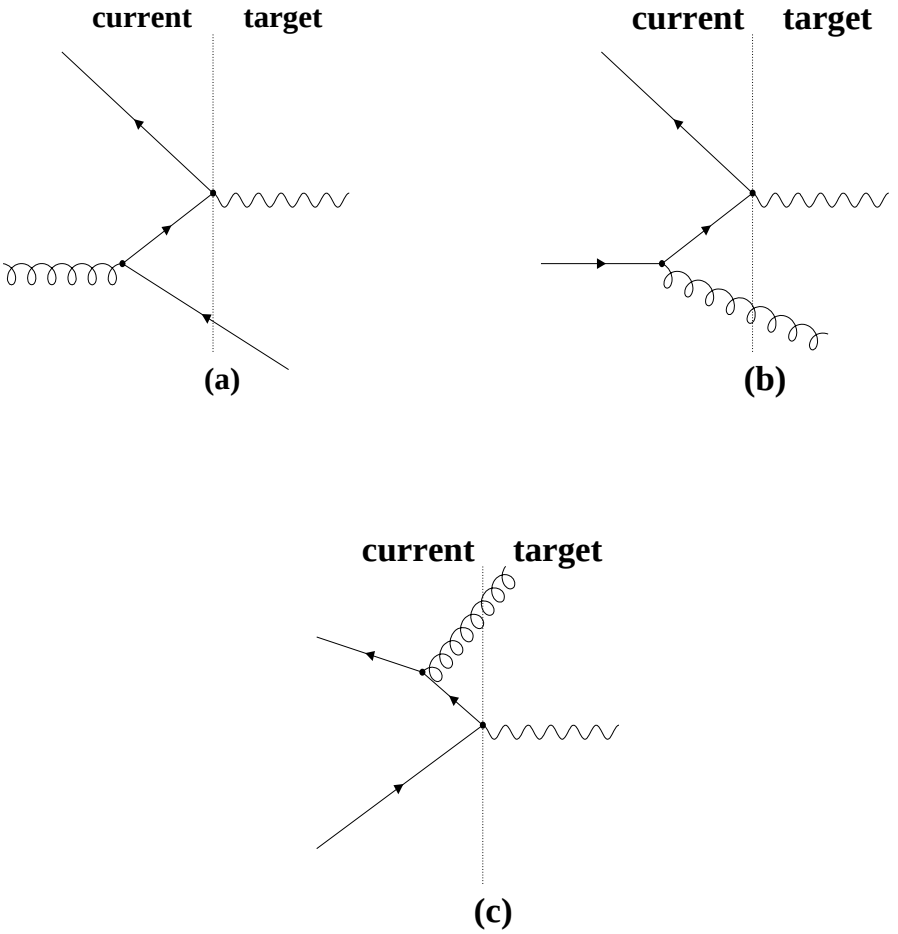


**Figure 6.3**: *Examples of leading order QCD processes as viewed in the Breit frame of reference. a) Boson-gluon fusion and b) initial state QCD Compton radiation processes in DIS have no equivalent in $e^+e^-$. However, c) final state QCD Compton radiation can occur in both DIS and $e^+e^-$.*

## 6.4 Higher Order Processes in the Breit Frame

Necessary $\mathcal{O}(\alpha_s)$ QCD corrections modify the simplistic QPM of scattering in the Breit frame by introducing higher order QCD processes, some of which are displayed in Figure 6.3. Boson-gluon fusion (BGF) and initial state QCD Compton (QCDC) radiation have no analogue in $e^+e^-$ interactions, but contribute to the $ep$ cross section. These processes, in addition to final state QCDC which does occur in hadronic $e^+e^-$ interactions, can de-populate the current region of the Breit frame, even leading to a current hemisphere which is empty [68]. Empty current hemisphere events are included in this analysis for normalisation purposes.

# Chapter 7

# Resolutions and Data Corrections

## 7.1 Introduction

This analysis is concerned with measuring the Breit frame current hemisphere fragmentation function, $D^h(\xi_p) = 1/N \mathrm{d}n/\mathrm{d}\xi_p$, for a number of different hadronic species. The relevant fragmentation variable is the scaled momentum, $\xi_p = \ln(1/x_p)$, where $x_p = 2p/Q$ for a hadron with momentum $p$ in the Breit frame. All particle distributions have been normalised to the number of events, $N$, since the absolute number of hadrons is unimportant. The shape of the distribution is, however, critical and corrections must be applied to account for limited detector acceptance and inefficiencies. Several correction procedures are available, with the *bin-by-bin* method being adopted throughout this analysis. For reliability, this method is dependent upon the reconstructed Monte Carlo successfully describing the shape of equivalent uncorrected distributions in data, and a bin width larger than the corresponding physics variable resolution.

This Chapter will present particle identification efficiencies and purities in $\xi_p$ for each particle species identified, as well as estimates of the resolution for $\xi_p$, as calculated using Monte Carlo.

## 7.2 Hadron Identification Efficiency

The identification *efficiency* for a given hadronic species, $h$, is estimated using MEAR Monte Carlo events. It is defined as the ratio of the Monte Carlo reconstructed hadronic spectrum for hadrons generated of type $h$ to the equivalent spectrum for hadrons hypothesised as $h$ under the corresponding identification criteria. The results are summarised in Figures 7.1 and 7.2, and are presented as a function of $\xi_p^{rpre}$, the value of $\xi_p$ calculated for a *reconstructed* particle boosted to the Breit frame using kinematics determined from the *reconstructed* electron.

The identification efficiency for $\pi^{\pm}$ selection is overall very high, although in the low $\xi_p$ region this is reduced by $\sim 20\%$ due to the merging of the $\pi^{\pm}$, $K^{\pm}$, proton ($p$) and antiproton ($\bar{p}$) $\mathrm{d}E/\mathrm{d}x$ bands. The identification efficiency is in general very good for $K^{\pm}$ identification, being over 70% in most $\xi_p$ bins. The efficiency for $p/\bar{p}$ identification in the low $Q^2$ sample is adequate, but falls below 50% in a number of $\xi_p$ bins in the high $Q^2$ sample. The dominant source of background in the $K^{\pm}$ and $p/\bar{p}$ samples is from $\pi^{\pm}$ contamination. Although corrections based on Monte Carlo are made, to some extent the identification efficiency has been compromised to allow a measurement of the fragmentation function peak region, which necessarily includes high momentum charged tracks from a region where the $K^{\pm}$ and $p/\bar{p}$ $\mathrm{d}E/\mathrm{d}x$ bands begin to merge with the $\pi^{\pm}$ dominated band.

The efficiencies for $K_S^0$ and $\Lambda$ identification are presented in Figure 7.2. Over the whole scaled momentum distribution, for both low and high $Q^2$ samples, the efficiency for $K_S^0$ identification is excellent. However, the $\Lambda$ sample suffers from $\sim 29\%$ $K_S^0$ contamination, and is reliant upon the guard band subtraction technique outlined in section 5.3.2 for its removal.

## 7.3 Hadron Identification Purity

In order to estimate the *quality* of hadron identification independently of the finite boost and track reconstruction resolution, a hadron identification *purity* is

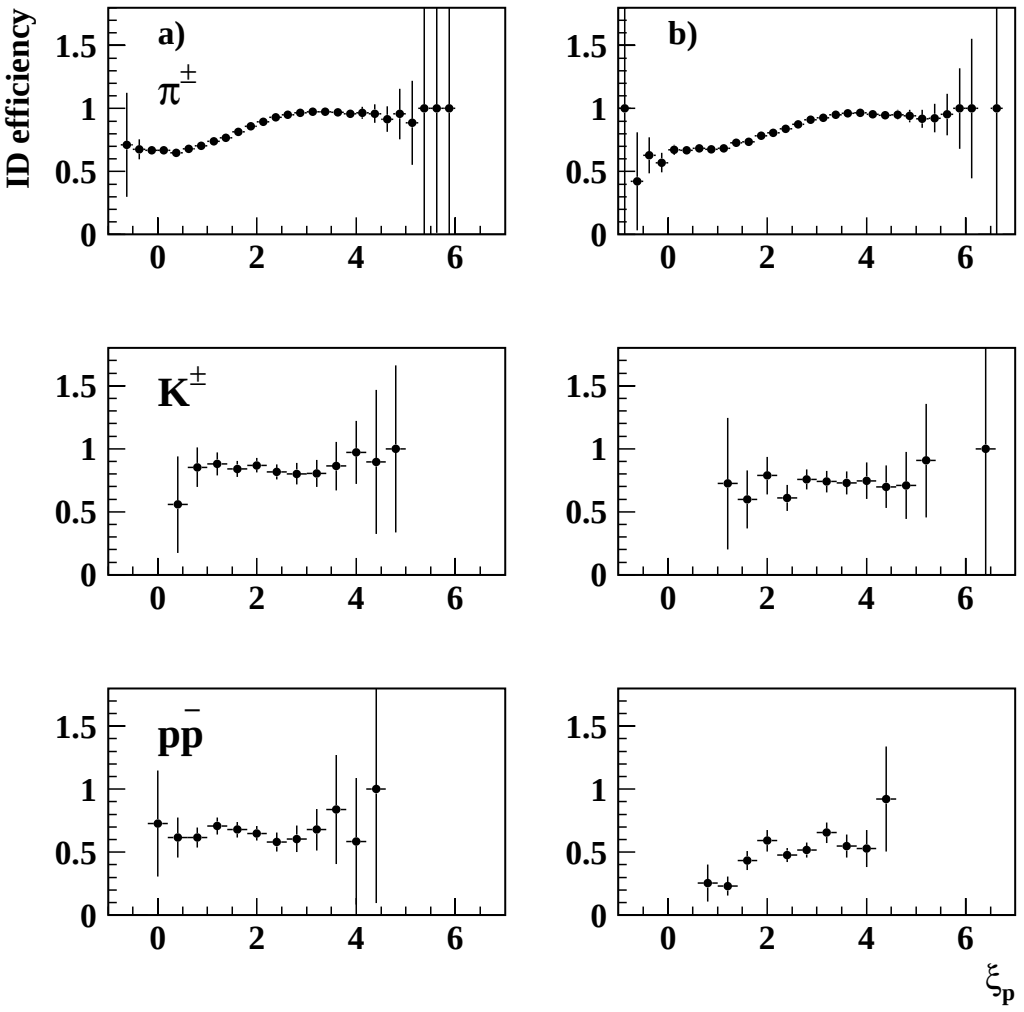


**Figure 7.1**: *Identification efficiency as a function of $\xi_p$ for $\pi^{\pm}$, $K^{\pm}$, and proton/antiproton ($p/\bar{p}$) identification using the dE/dx selection criteria defined in section 5.2.4, as estimated using 1996 a) low $Q^2$ ($12 < Q^2 < 150$ GeV$^2$) and b) high $Q^2$ ($100 < Q^2 < 20\,000$ GeV$^2$) reconstructed MEAR Monte Carlo events. The value of $\xi_p$ is calculated for a reconstructed particle boosted to the Breit frame using kinematics determined from the reconstructed electron.*

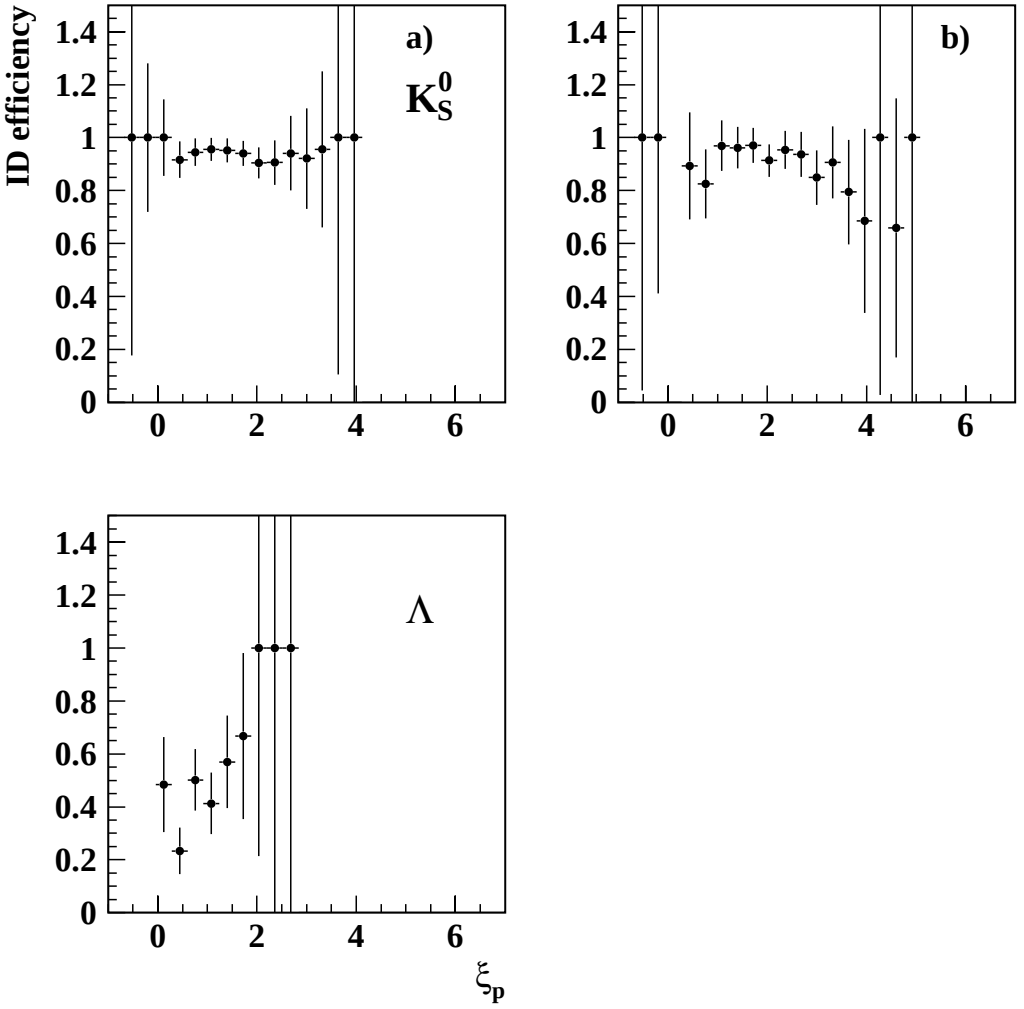


**Figure 7.2**: *Identification efficiency as a function of $\xi_p$ for $K^0_S$ and $\Lambda$ identification using the $V^0$ daughter hypothesis technique discussed in section 5.3, as estimated using 1996 a) low $Q^2$ ($12 < Q^2 < 150\ GeV^2$) and b) high $Q^2$ ($100 < Q^2 < 20\,000\ GeV^2$) reconstructed MEAR Monte Carlo events. The value of $\xi_p$ is calculated for a reconstructed particle boosted to the Breit frame using kinematics determined from the reconstructed electron.*

calculated for each sample of identified hadrons. It is determined in an identical manner to the hadron identification efficiency (see section 7.2), but is presented as a function of $\xi_p^{gpge}$, the value of $\xi_p$ calculated for a *generated* particle boosted to the Breit frame using the *generated* electron, thereby assuming perfect $\xi_p$ resolution. For a given $\xi_p$ bin, differences are expected between the identification efficiency and purity, since for example, the identification efficiency can be reduced by hadrons not of type $h$ migrating into that bin.

The identification purities for primary hadrons are summarised in Figure 7.3. As observed in section 7.2, the identification purity for $\pi^{\pm}$ selection is high, being over 75% in the majority of $\xi_p$ bins, but falls slightly at low $\xi_p$ as the $\pi^{\pm}$, $K^{\pm}$ and $p/\overline{p}$ bands merge. For identified $K^{\pm}$, the identification purity is above 60% in all $\xi_p$ bins but is lower in the central region of the scaled momentum distribution than the equivalent identification efficiency. In general, the $p/\overline{p}$ identification purity is above 50%, but as observed for $K^{\pm}$, falls in the central region of the scaled momentum distribution.

The identification purities for $K_S^0$ and $\Lambda$ hadrons are presented in Figure 7.4. The $K_S^0$ identification purity is overall very high, being over 85% in all regions of the scaled momentum distribution. The $\Lambda$ identification purity is above 40% in the majority of $\xi_p$ bins but suffers from a large $K_S^0$ background as discussed in section 7.2.

## 7.4 Resolution in $\xi_p$

The total resolution of the variable $\xi_p$ is comprised of a dominant boost error due to the measurement resolution on the kinematic quantities $x$ and $Q^2$, and an error due to track reconstruction. Using MEAR Monte Carlo, the total resolution is estimated from the root-mean-square (RMS) of the distribution $(\xi_p^{gpge} - \xi^{rpre})$.

The resolution of $\xi_p$ has been estimated separately for each identified hadronic species, and results are summarised in Tables 7.1 and 7.2 for each $Q^2$ interval. In

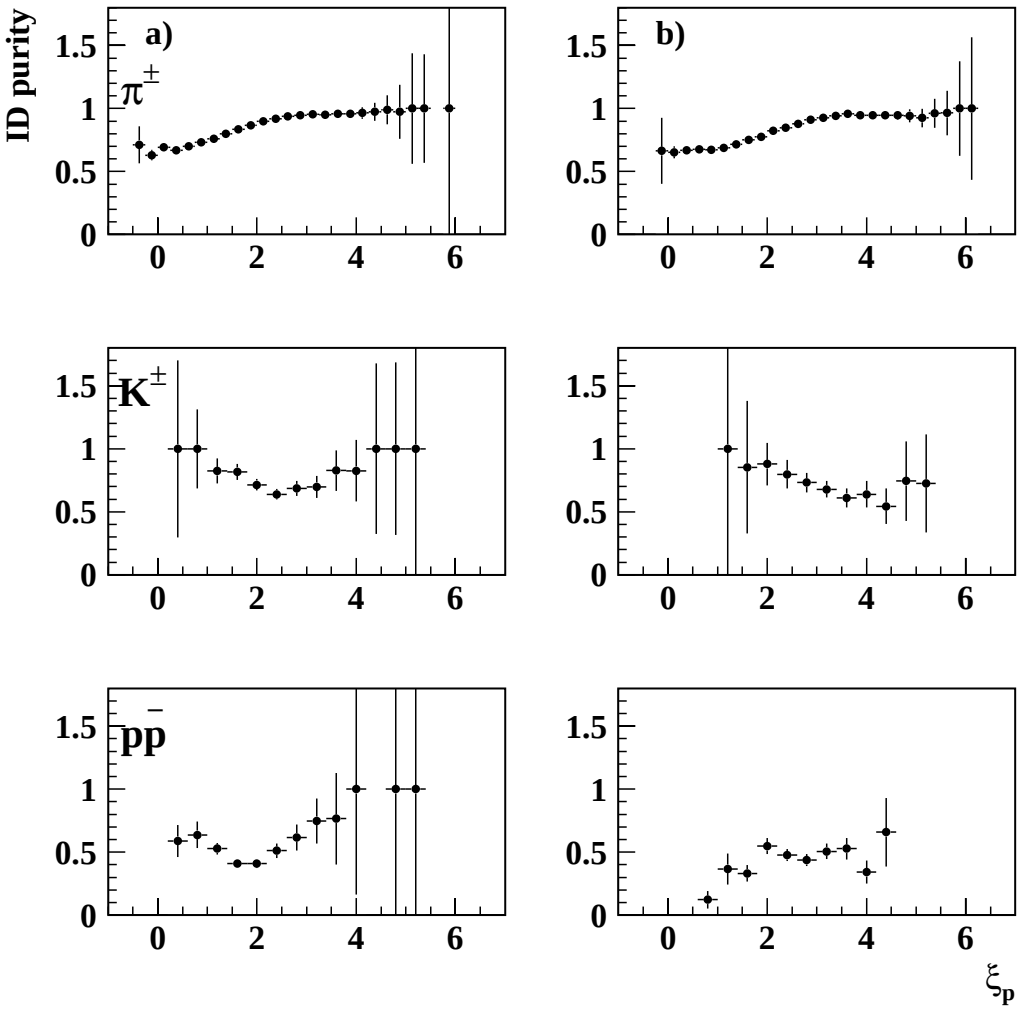


**Figure 7.3**: *Identification purity as a function of $\xi_p$ for $\pi^{\pm}$, $K^{\pm}$, and proton/antiproton ($p/\bar{p}$) identification using the dE/dx selection criteria defined in section 5.2.4, as estimated using 1996 a) low $Q^2$ ($12 < Q^2 < 150$ GeV$^2$) and b) high $Q^2$ ($100 < Q^2 < 20\,000$ GeV$^2$) reconstructed MEAR Monte Carlo events. The value of $\xi_p$ is calculated for a generated particle boosted to the Breit frame using kinematics determined from the generated electron.*

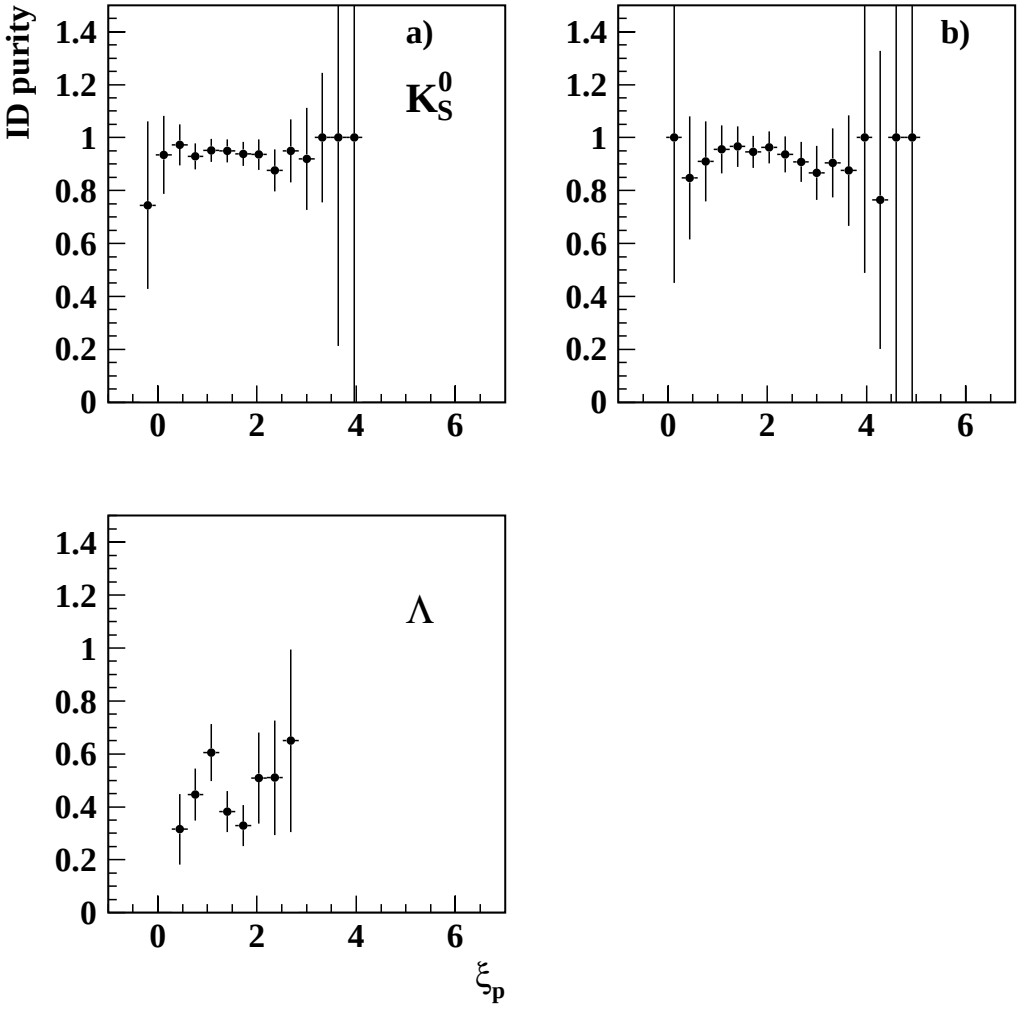


**Figure 7.4**: *Identification efficiency as a function of $\xi_p$ for $K^0_S$ and $\Lambda$ identification using the $V^0$ daughter hypothesis technique discussed in section 5.3, as estimated using 1996 a) low $Q^2$ ($12 < Q^2 < 150\ GeV^2$) and b) high $Q^2$ ($100 < Q^2 < 20\,000\ GeV^2$) reconstructed MEAR Monte Carlo events. The value of $\xi_p$ is calculated for a generated particle boosted to the Breit frame using kinematics determined from the generated electron.*

general, the resolution is found to improve as $Q^2$ increases, but is poorer for $K^{\pm}$ and $p/\bar{p}$ as the measured fragmentation function is dominated by low momenta tracks boosted to low momenta in the Breit frame.

The bin widths selected for the scaled momentum spectra are chosen such that they are wider than the corresponding resolution, but narrow enough for sensitivity to any interesting physics properties.

## 7.5 Purity

In order to estimate the level of migrations between bins of a given physics distribution as a result of a finite boost and measurement resolution, an additional quantity, termed the *purity*, is calculated. This is defined as the fraction of particles reconstructed in a given bin that were generated within that bin. Presented in Figures 7.5 and 7.6 are the purities in $\xi_p$ estimated using low and high $Q^2$ MEAR Monte Carlo for $\pi^{\pm}$, $K^{\pm}$, $p/\bar{p}$, $K^0_S$, and $\Lambda$ samples. Overall the purities are satisfactory, being above 40% in the central region of the fragmentation function for each hadronic species, although in the low and high $\xi_p$ regions the purity falls below 35%.

## 7.6 Data Corrections

In Chapter 4, the MEAR Monte Carlo is shown to describe the energy flow measurements well, and is used to make acceptance corrections to the data throughout this analysis. Corrections are made by repeating the analysis on reconstructed Monte Carlo events with identical event, track, and particle identification selection criteria applied, and then comparing these results with spectra at the generated event level. The bin-by-bin correction factors applied to the data are calculated from the ratio of generated to reconstructed spectra.

In Figures 7.7 to 7.11, a comparison of uncorrected fragmentation functions in

| $Q^2$ Interval | $\xi_p$ resolution | | |
|---|---|---|---|
| ($\mathrm{GeV}^2$) | $\pi^\pm$ | $K^\pm$ | $\mathrm{p}/\bar{\mathrm{p}}$ |
| $12 \rightarrow 150$ | $0.144 \pm 0.001$ | $0.233 \pm 0.012$ | $0.234 \pm 0.015$ |
| $100 \rightarrow 20\,000$ | $0.140 \pm 0.001$ | $0.189 \pm 0.016$ | $0.230 \pm 0.018$ |
| $12 \rightarrow 15$ | $0.148 \pm 0.002$ | | |
| $15 \rightarrow 20$ | $0.147 \pm 0.002$ | | |
| $20 \rightarrow 40$ | $0.143 \pm 0.001$ | | |
| $40 \rightarrow 60$ | $0.139 \pm 0.002$ | | |
| $60 \rightarrow 80$ | $0.138 \pm 0.002$ | | |
| $80 \rightarrow 100$ | $0.140 \pm 0.002$ | | |
| $100 \rightarrow 150$ | $0.158 \pm 0.003$ | | |
| $100 \rightarrow 175$ | $0.105 \pm 0.002$ | | |
| $175 \rightarrow 250$ | $0.145 \pm 0.002$ | | |
| $250 \rightarrow 450$ | $0.148 \pm 0.001$ | | |
| $450 \rightarrow 1\,000$ | $0.143 \pm 0.002$ | | |
| $1\,000 \rightarrow 2000$ | $0.123 \pm 0.003$ | | |
| $2\,000 \rightarrow 20\,000$ | $0.120 \pm 0.004$ | | |

**Table 7.1**: *Total resolution for $\xi_p$, as a function of $Q^2$ for $\pi^\pm$, $K^\pm$, and protons and antiprotons ($p/\bar{p}$). Resolutions are estimated using reconstructed MEAR Monte Carlo and concerned with the current region of the Breit frame only. The resolutions are smaller than the fragmentation function bin widths, which are taken to be 0.25 ($\pi^\pm$) and 0.4 ($K^\pm$, $p/\bar{p}$) in this analysis. Note that the statistics on $K^\pm$ and $p\overline{p}$ do not allow fine subdivisions in $Q^2$.*

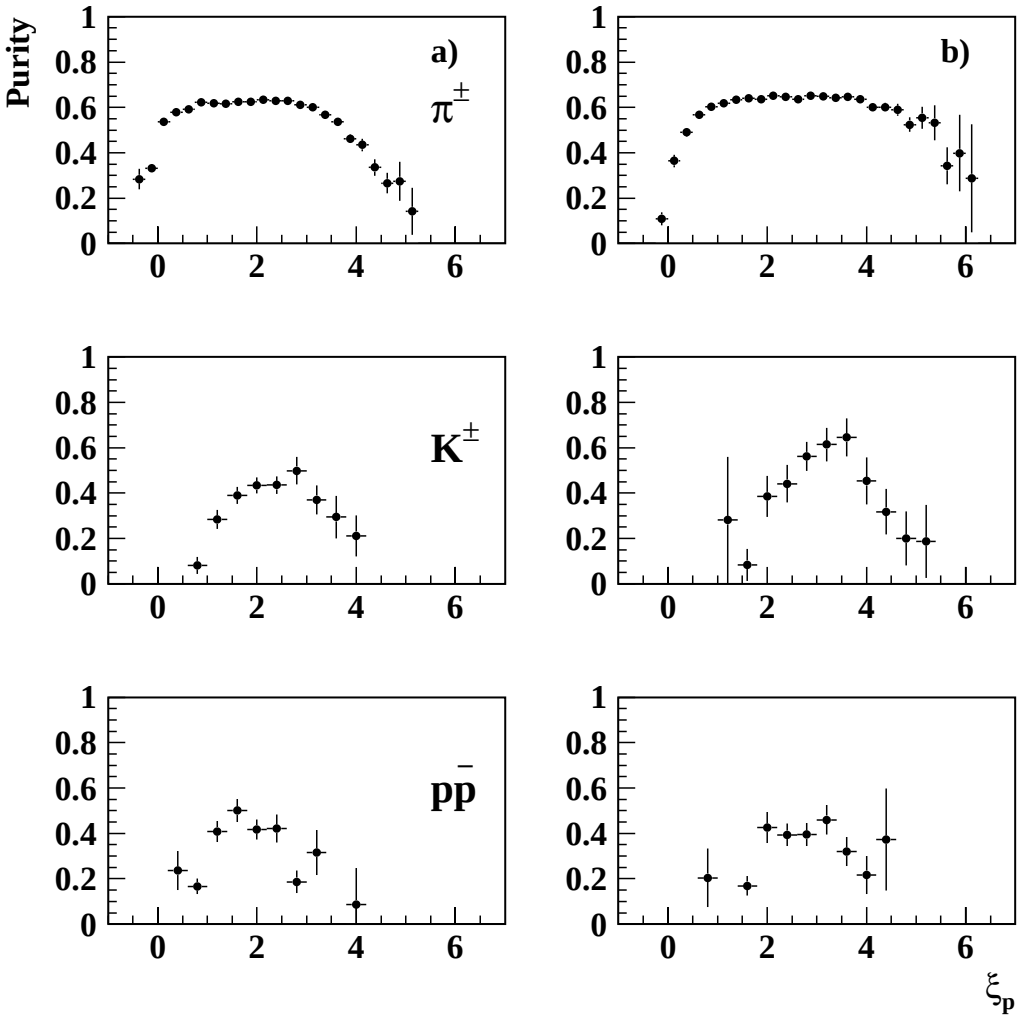


**Figure 7.5**: *Purity as a function of $\xi_p$ for $\pi^{\pm}$, $K^{\pm}$, and proton/antiproton ($p/\bar{p}$) selected using dE/dx information, as estimated using 1996 a) low $Q^2$ ($12 < Q^2 < 150$ GeV$^2$) and b) high $Q^2$ ($100 < Q^2 < 20\,000$ GeV$^2$) reconstructed MEAR Monte Carlo.*

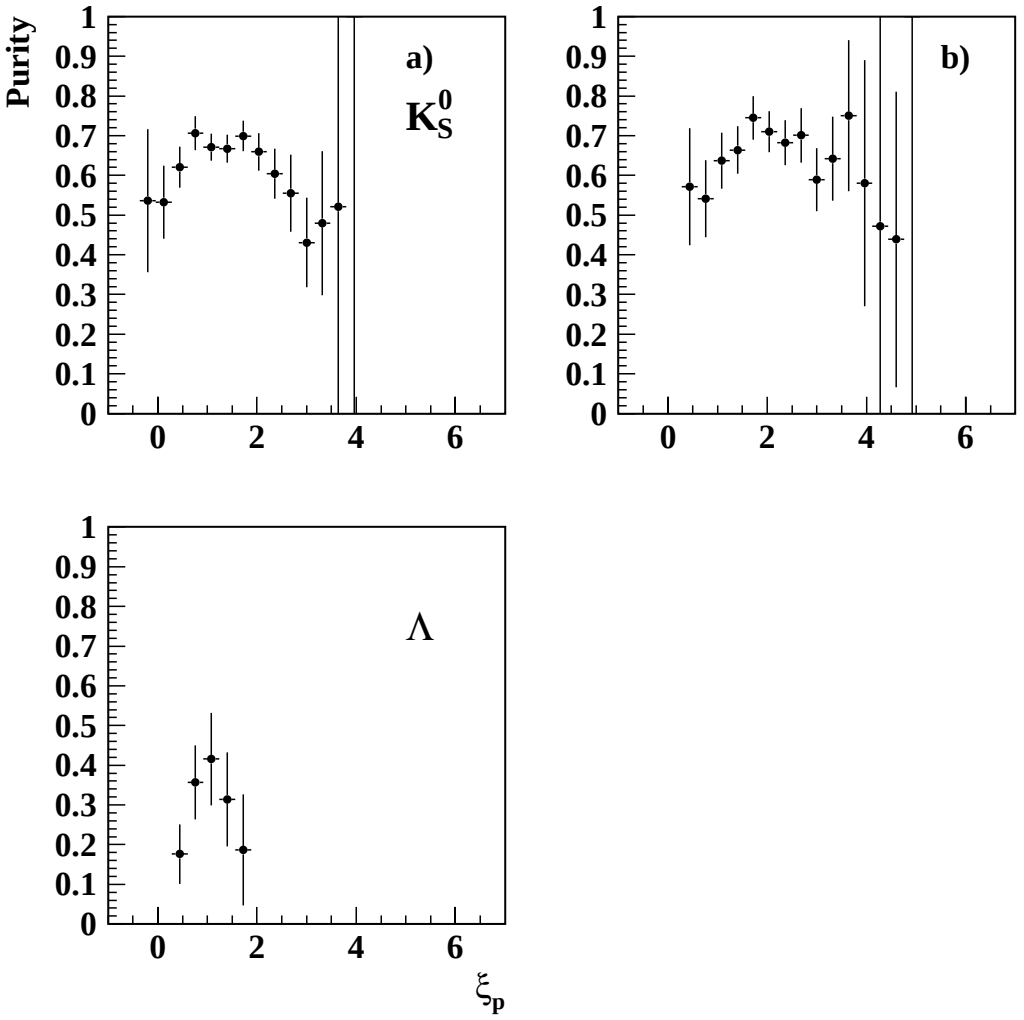


**Figure 7.6**: *Purity as a function of $\xi_p$ for $K_S^0$ and $\Lambda$, as estimated using 1996 a) low $Q^2$ ($12 < Q^2 < 150$ GeV$^2$) and b) high $Q^2$ ($100 < Q^2 < 20\,000$ GeV$^2$) reconstructed MEAR Monte Carlo.*

| $Q^2$ Interval (GeV$^2$) | $\xi_p$ resolution | |
|---|---|---|
| | $K^0_S$ | $\Lambda$ |
| $12 \rightarrow 150$ | $0.146 \pm 0.006$ | $0.198 \pm 0.039$ |
| $12 \rightarrow 20$ | $0.153 \pm 0.012$ | |
| $20 \rightarrow 40$ | $0.146 \pm 0.010$ | |
| $40 \rightarrow 60$ | $0.139 \pm 0.013$ | |
| $60 \rightarrow 80$ | $0.133 \pm 0.016$ | |
| $80 \rightarrow 150$ | $0.152 \pm 0.015$ | |
| $100 \rightarrow 20\,000$ | $0.139 \pm 0.008$ | |

**Table 7.2**: *Total resolution for $\xi_p$, as a function of $Q^2$ for $K^0_S$ and $\Lambda$. Resolutions are estimated using reconstructed MEAR Monte Carlo and concerned with the current region of the Breit frame only. The resolutions are smaller than the fragmentation function bin widths, which are taken to be 0.32 ($K^0_S$, $\Lambda$) in this analysis.*

1996 data with equivalent reconstructed MEAR Monte Carlo is shown, being measured for each of the hadronic species identified in this analysis, together with the corresponding bin-by-bin correction factors. At low $Q^2$, $\pi^\pm$ ($K^0_S$) statistics are sufficiently high for the fragmentation function to be measured in 7 (5) $Q^2$ intervals respectively. At high $Q^2$, the $\pi^\pm$ fragmentation function has been measured for 6 $Q^2$ intervals.

As may be seen in the figures for $\pi^\pm$, the fragmentation function correction factors over the interval of $\xi_p$ from which a peak position and width are measured, range from 0.8 to 1.2 at low $Q^2$, and 0.8 to 1.3 at high $Q^2$. At large values of $\xi_p$, correction factors rapidly increase as a result of the requirement for each charged track to have a transverse momentum greater than 150 MeV/$c$ (see section 4.3).

Unambiguous $K^\pm$ and $p/\bar{p}$ identification from d$E$/d$x$ information is limited to a low laboratory momentum interval. However, by boosting to the Breit frame a measurement of the fragmentation function over a wide range of $\xi_p$ values is still possible, although as well as the above problems at high $\xi_p$, the corrected fragmentation function is dependent upon extremely large correction factors at

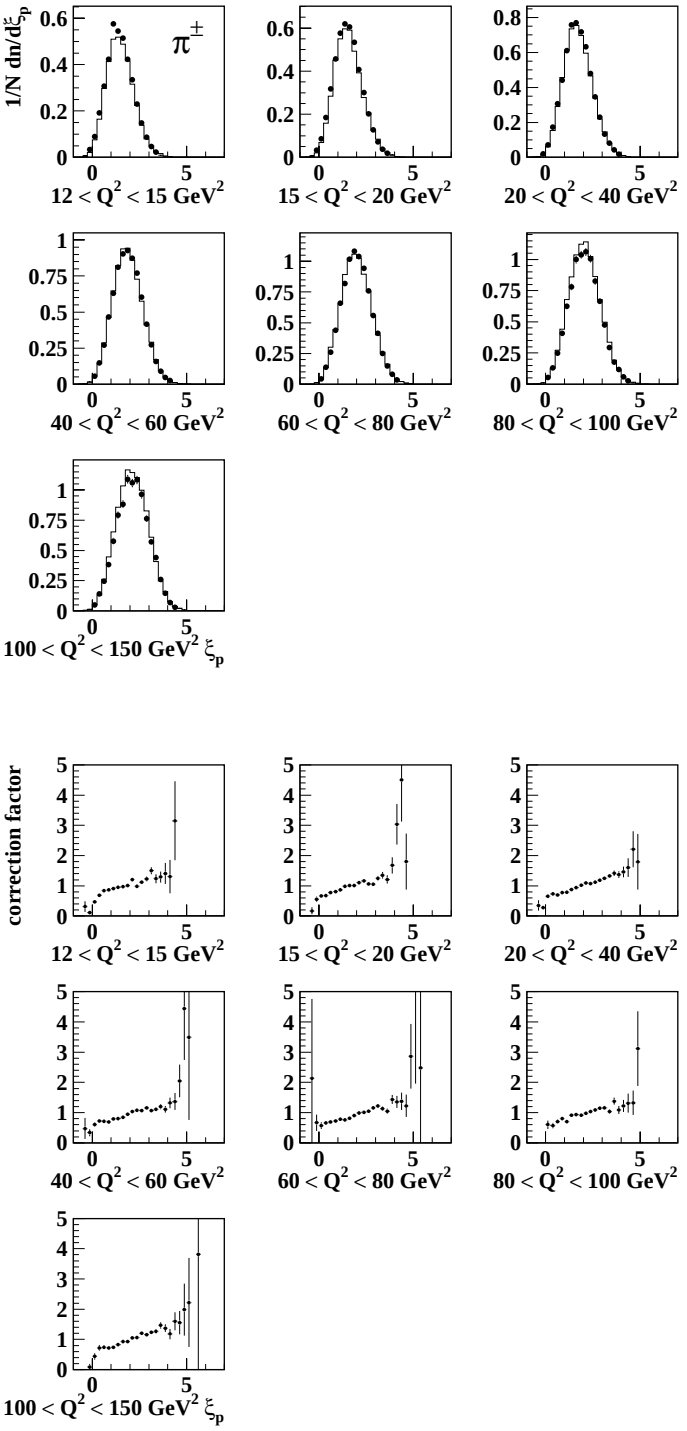


**Figure 7.7**: *Right) Uncorrected event normalised scaled momentum distributions for $\pi^{\pm}$ in 1996 low $Q^2$ data (closed circles) and reconstructed MEAR Monte Carlo (histogram), subdivided into 7 $Q^2$ intervals. Bottom) Correction factors calculated from the ratio of generated to reconstructed Monte Carlo $\xi_p$ distributions.*

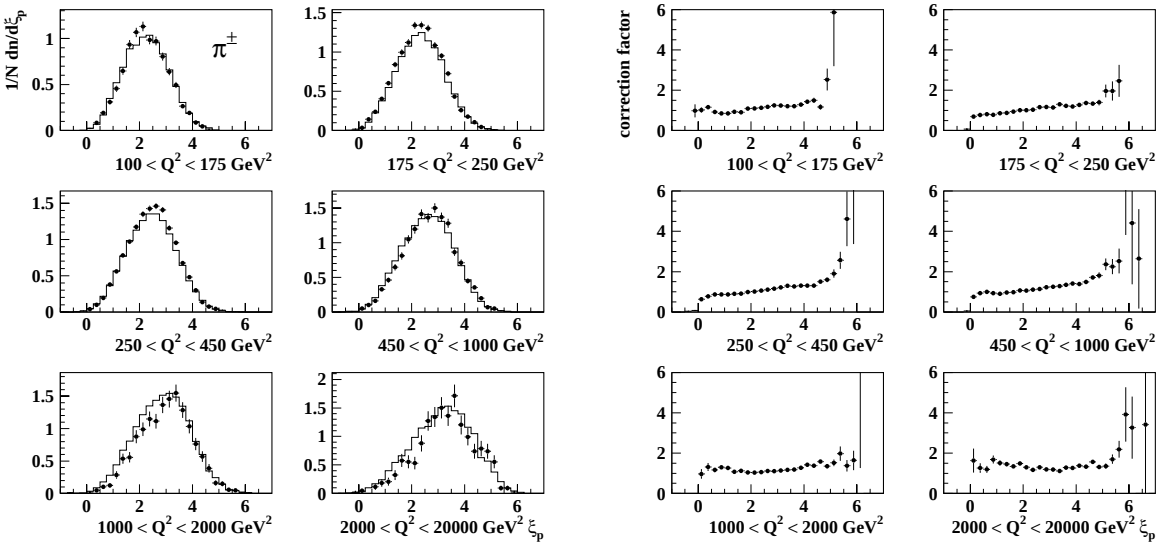


**Figure 7.8**: *Left) Uncorrected event normalised scaled momentum distributions for $\pi^{\pm}$ in 1996 high $Q^2$ data (closed circles) and reconstructed MEAR Monte Carlo (histogram), subdivided into 6 $Q^2$ intervals. Right) Correction factors calculated from the ratio of generated to reconstructed Monte Carlo $\xi_p$ distributions.*

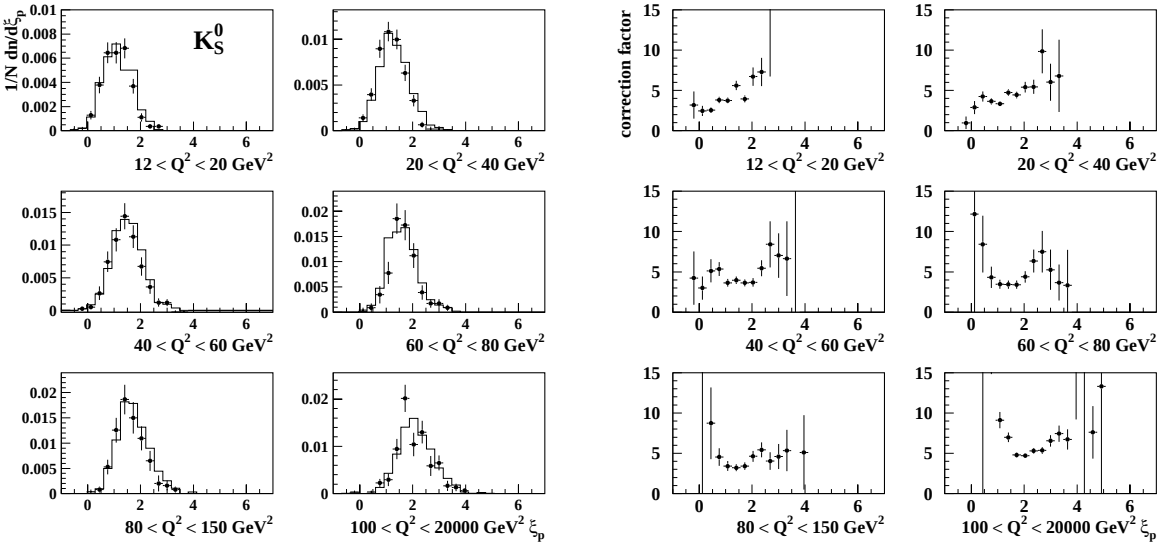


**Figure 7.9**: *Left) Uncorrected event normalised scaled momentum distributions for $K^0_S$ in 1996 data (closed circles) and reconstructed MEAR Monte Carlo (histogram), subdivided into 5 low $Q^2$ and 1 high $Q^2$ interval. Right) Correction factors calculated from the ratio of generated to reconstructed Monte Carlo $\xi_p$ distributions.*

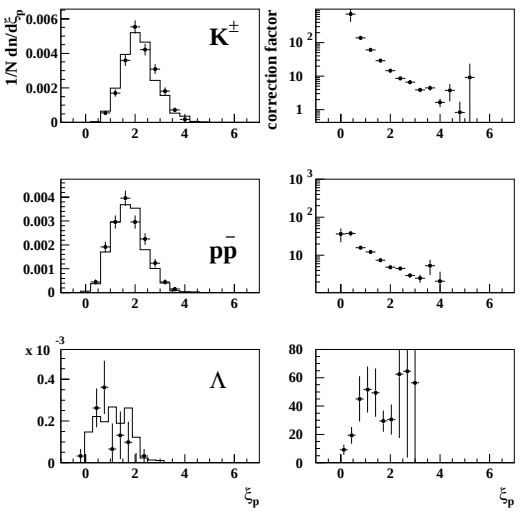


**Figure 7.10**: *Left) Uncorrected event normalised scaled momentum distributions for $K^{\pm}$, proton/antiproton ($p\bar{p}$), and $\Lambda$ in 1996 low $Q^2$ ($12 < Q^2 < 150\ GeV^2$) data (closed circles) and reconstructed MEAR Monte Carlo (histogram). Right) Correction factors calculated from the ratio of generated to reconstructed Monte Carlo $\xi_p$ distributions.*

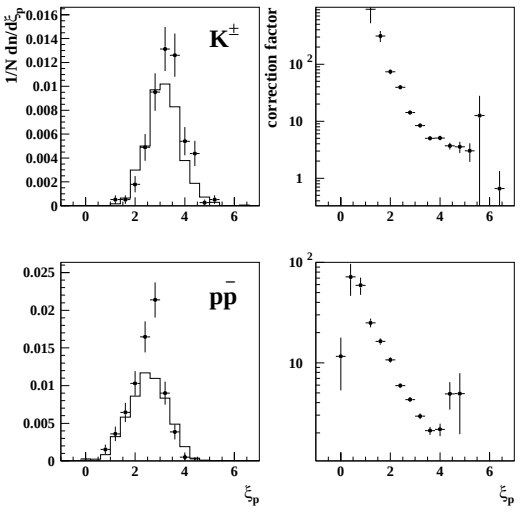


**Figure 7.11**: *Left) Uncorrected event normalised scaled momentum distributions for $K^{\pm}$ and proton/antiproton ($p\bar{p}$) in 1996 high $Q^2$ ($100 < Q^2 < 20\,000\ GeV^2$) data (closed circles) and reconstructed MEAR Monte Carlo (histogram). Right) Correction factors calculated from the ratio of generated to reconstructed Monte Carlo $\xi_p$ distributions.*

low and intermediate values of $\xi_p$. For a given bin, the correction applied is dominated by two components; one resulting from limited laboratory momentum acceptance for particle identification, and a second from the requirement of a high quality $\mathrm{d}E/\mathrm{d}x$ measurement. In Figure 7.12, the generator level laboratory momentum spectra of Breit frame current hemisphere $K^{\pm}$ and $p/\bar{p}$ hadrons are shown, with only $\sim$10% ($\sim$5%) of $K^{\pm}$, and $\sim$15% ($\sim$7%) of $p/\bar{p}$ lying in the laboratory momentum intervals for which identification is possible, as defined in section 5.2.4, at low (high) $Q^2$. This corresponds to correction factors of $\sim 10$ ($\sim 20$) and $\sim 7$ ($\sim 14$) respectively. Of those $p\overline{p}$ reconstructed and identified using $\mathrm{d}E/\mathrm{d}x$ information, the second correction factor component is of the order of one at low and high $Q^2$, and slightly higher for $K^{\pm}$.

Presented in Figure 7.13 are the generator level laboratory momentum spectra for Breit frame current hemisphere $K^0_S$ and $\Lambda$ hadrons, with $\sim$ 70% of $K^0_S$ and $\sim$ 84% of $\Lambda$ particles decaying after a minimum decay length of 2.0 cm in the $x$-$y$ plane. For $K^0_S$ and $\Lambda$ scaled momentum distributions, studies show the dominant contribution to the correction factors results from $V^0$ reconstruction inefficiencies in the central jet chamber (CJC), with only a small contribution from $V^0$ quality requirements. For $K^0_S$ candidates decaying after the minimum decay length and via the channel $K^0_S \to \pi^+\pi^-$, the efficiency for reconstruction ranges from 29% to 41% at low $Q^2$, and 6% to 27% at high $Q^2$, in the peak region of the fragmentation function. For $\Lambda$ candidates identified in the low $Q^2$ data sample using the decay channel $\Lambda \to p\pi$, the equivalent reconstruction efficiency is very low and ranges from 3% to 9% over the peak region. Although only necessary for normalisation rather than shape fragmentation properties relevant to this analysis, and not shown in Figures 7.9 and 7.10, a second, well-determined, correction factor is applied to $K^0_S$ and $\Lambda$ scaled momentum spectra to correct for unmeasured decay channels [64] (e.g. $K^0_S \to \pi^0\pi^0$, $\Lambda \to n\pi^0$).

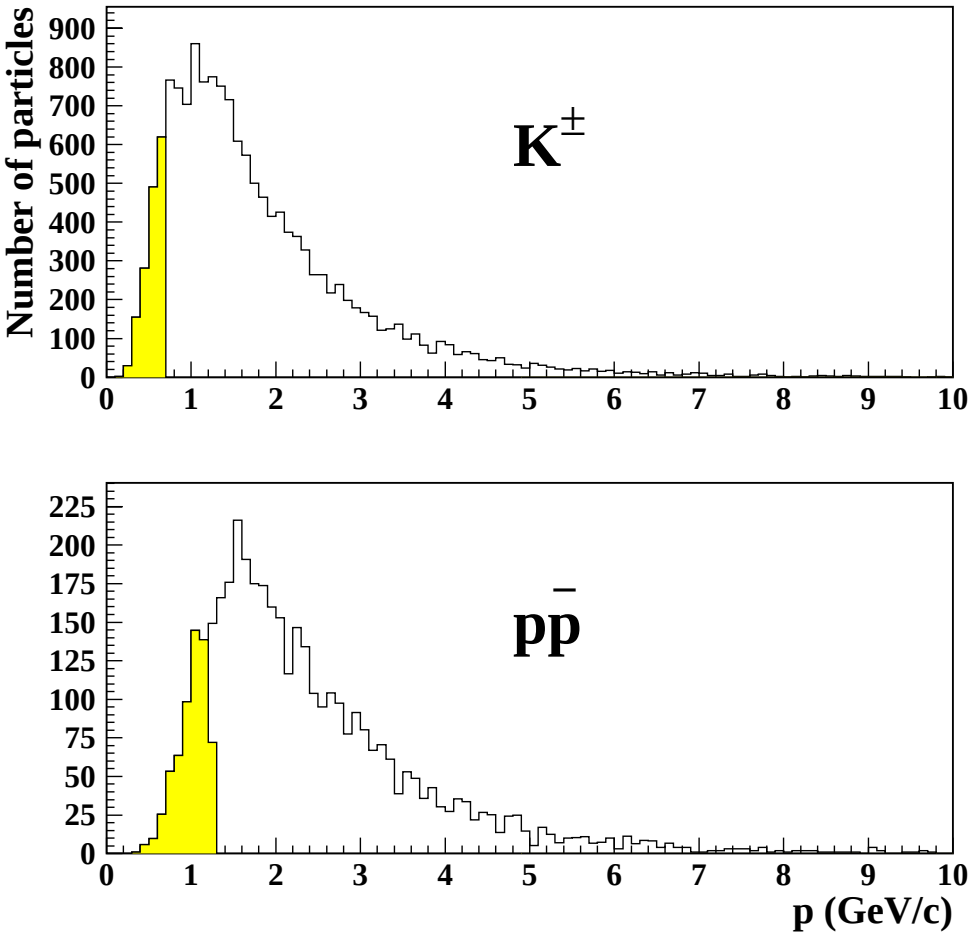


**Figure 7.12**: *Momentum, p, in the laboratory reference frame shown for current hemisphere $K^{\pm}$ and protons/antiprotons ($p/\bar{p}$) in low $Q^2$ generated MEAR Monte Carlo. The shaded region corresponds to the respective momentum intervals, 0.15< p <0.7 GeV/c for $K^{\pm}$ and 0.15< p <1.25 GeV/c for $p/\bar{p}$ respectively, in which dE/dx identification is possible.*

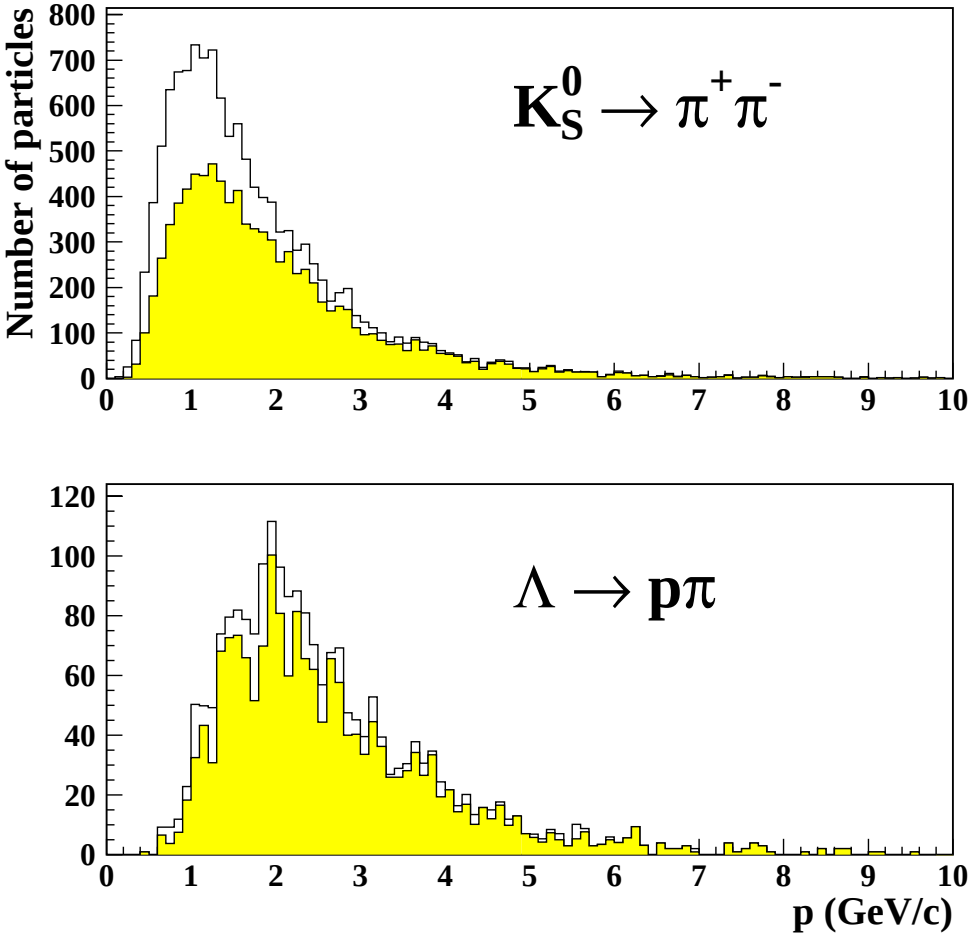


**Figure 7.13**: *Momentum, p, in the laboratory reference frame for current hemisphere $K^0_S$ and $\Lambda$ in low $Q^2$ generated MEAR Monte Carlo. The shaded region corresponds to the momentum spectrum of those particles decaying after a minimum decay length of 2.0 cm in the x-y plane.*

## 7.7 Merging Data Samples

After performing the relevant bin-by-bin Monte Carlo corrections, the scaled momentum spectra measured using 1996 and 1997 data samples are merged together following the method outlined by the PDG [64]. The merged distribution $C(k)$ with error $\mathrm{d}C(k)$ is formed from two statistically independent distributions $A(k)$ and $B(k)$ with errors $\mathrm{d}A(k)$ and $\mathrm{d}B(k)$ according to:

$$C(k) = \frac{wa(k) * A(k) + wb(k) * B(k)}{wa(k) + wb(k)} \tag{7.1}$$

$$\mathrm{d}C(k) = \frac{1}{\sqrt{(wa(k) + wb(k))}} \tag{7.2}$$

where the weights $wa(k)$ and $wb(k)$ are the inverse variances $1.0/\mathrm{d}A(k)^2$ and $1.0/\mathrm{d}B(k)^2$ respectively.

## 7.8 Summary

This Chapter has shown particle identification efficiencies and purities, and the resolution of the fragmentation variable, $\xi_p$, is estimated to be less than the fragmentation function bin widths selected. Furthermore, the Monte Carlo successfully describes both the shape and normalisation of the uncorrected exclusive fragmentation functions in data. However, the bin-by-by correction factors applied to $K^{\pm}$ and proton/antiproton scaled momentum spectra are extremely large, due principally to limited momentum acceptance for $K^{\pm}$, proton and antiproton identification.

# Chapter 8

# Identified Hadron Fragmentation

## 8.1 Introduction

This Chapter will present corrected event normalised exclusive scaled momentum spectra, known hereafter as fragmentation functions, measured for a number of different identified hadronic species identified in $ep$ data. The fragmentation properties are summarised in terms of the mass and energy evolution of the fragmentation function peak position and peak width. The evolution in $ep$ data will be shown to follow that of $e^+e^-$ data and to be consistent with Monte Carlo models of the hadronic final state. A parameterised MLLA/LPHD calculation is shown to describe successfully the peak position evolution with mass, energy, and parton shower cut-off parameter, but unable to describe the width evolution in $e^+e^-$ data, and is shown to be incompatible with the Monte Carlo models used.

The fragmentation properties of identified hadrons are studied in the current hemisphere of the Breit frame. Throughout this analysis, particles are assigned to the current region if they have a negative longitudinal component of momentum ($p_z < 0$) as measured in the Breit frame. Comparison is made to published $e^+e^-$ data by taking the centre-of-mass energy, $E^*$, to be equivalent to the energy scale, $Q$, of the Breit frame.

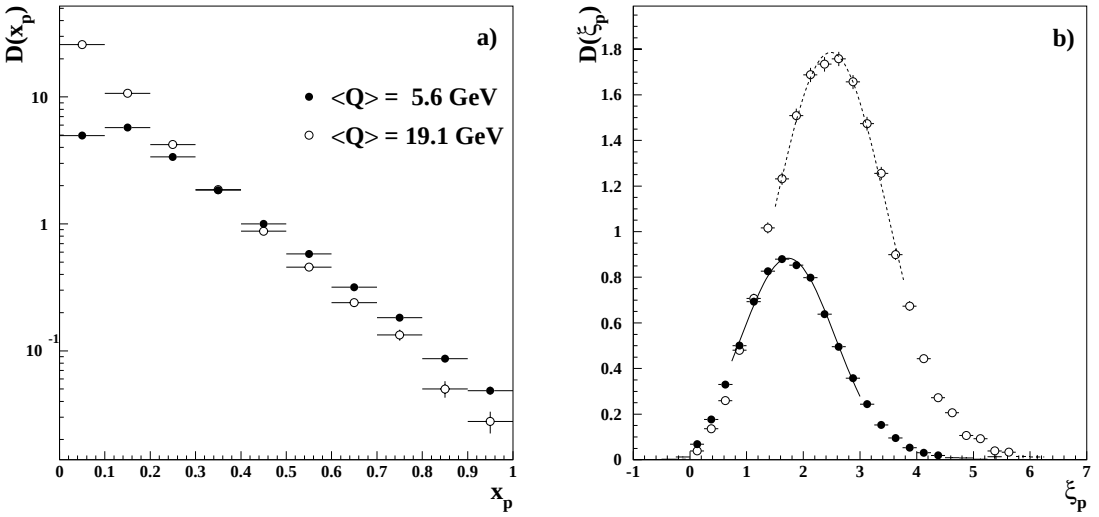


**Figure 8.1**: *Inclusive fragmentation functions a) $D(x_p)$ and b) $D(\xi_p)$ measured for charged tracks in 1996 low $Q^2$ (closed circles) and high $Q^2$ (open circles) data, where $< Q > = 5.6$ GeV and $< Q > = 19.1$ GeV respectively. The solid and dashed lines are simple Gaussian fits to the data for a fitting interval $\pm$ 1.0 unit in $\xi_p$ about the statistical mean. Statistical errors only are shown.*

## 8.2 Fragmentation Functions

The process of fragmentation, in which the initial scattered partonic system evolves perturbatively through gluon emission, before hadronising non-perturbatively into a measurable hadronic final state, can be characterised by a fragmentation function, defined as:

$$D(x_p) = \frac{1}{N}\frac{\mathrm{d}n}{\mathrm{d}x_p} \tag{8.1}$$

This event normalised distribution is cast in terms of a scaled momentum, $x_p = 2p/Q$ $(= 2p/E^*)$, where $p$ is the momentum of a given hadron and $Q/2$ is the scattered quark momentum in the Breit frame. However, a full treatment of hadron production from emitted quarks in deep inelastic scattering (DIS) would require a fragmentation function, $D_q^h(x_{Bj}, Q^2)$, which describes the production of hadronic species $h$ from quark species $q$ at given values of Bjorken-x, $x_{Bj}$, and

four-momentum transfer squared, $Q^2$.

Displayed in Figure 8.1a is an inclusive fragmentation function, $D(x_p)$, measured for all charged tracks with no attempt made to identify individual hadronic species. The boost to the Breit frame is performed under the assumption that all tracks are charged pions. The fragmentation function is *soft*, peaking at $x_p \approx 0$, and exhibits a scaling violation [37, 70] by softening as $Q^2$ increases due to an increased probability for a given hadron to have a smaller fraction of the parent quark's momentum. The turn-over region can be expanded by recasting the fragmentation function in terms of the variable $\xi_p = \ln(1/x_p)$, as shown in Figure 8.1b, whereupon MLLA theory coupled with the hypothesis of LPHD predicts a Gaussian shape in the neighbourhood of the peak region of $D(\xi_p)$ [39, 71].

Previous H1 studies [72, 73] show the insensitivity of fragmentation function properties to $x_{Bj}$, and to the loss of hadronic fragments to the target region through QCD radiation. The evolution of the peak position, $\xi_p^*$, and width, $\sigma_p$, as function of $Q$ is successfully described within the MLLA/LPHD framework and is consistent with published inclusive $e^+e^-$ data [42, 74, 78], where the relevant evolution variable is $E^*$. The energy dependence of the average charged multiplicity, $< n >$, calculated from the area under the fragmentation function has also been investigated [37]. Although there is very good agreement between $ep$ analyses and those of $e^+e^-$ at high $Q(E^*)$, it has been shown that there are significantly smaller average charged multiplicities in DIS events at low $Q(E^*)$. These differences have been attributed to leading and higher order processes (see section 6.4) present in $ep$ interactions but absent in $e^+e^-$ scattering, giving a depletion of the Breit frame current hemisphere.

## 8.3 Identified Hadron Fragmentation Functions

In Figures 8.2 to 8.6, corrected exclusive fragmentation functions, $D^h(\xi_p)$, are presented for $\pi^\pm$, $K^\pm$, protons/antiprotons ($p/\overline{p}$), $K_S^0$, and $\Lambda$ hadrons measured in a merged 1996-97 H1 data sample. The fragmentation function $D^{\pi^\pm}(\xi_p)$ is

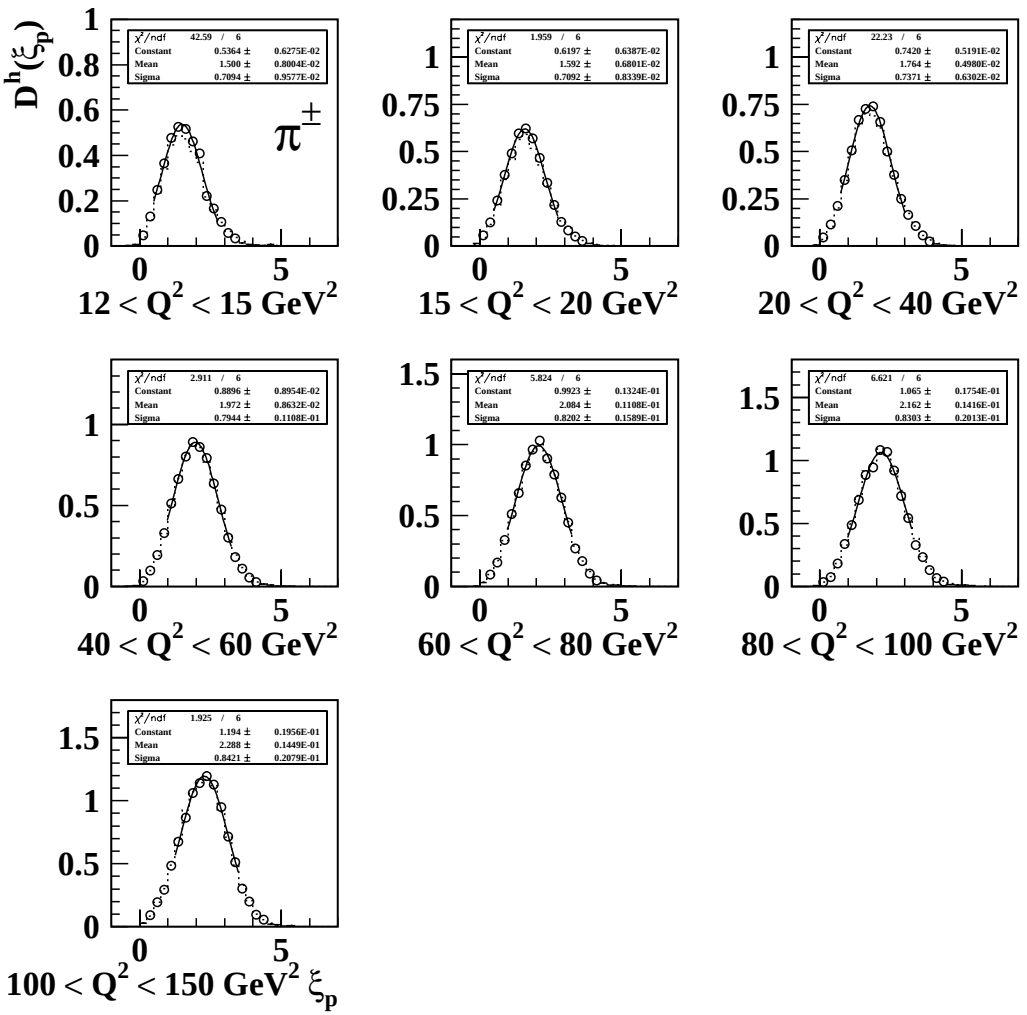


**Figure 8.2**: *Corrected fragmentation function, $D^h(\xi_p)$, for $\pi^{\pm}$ measured in low $Q^2$ 1996-97 data (closed circles) in comparison with generated MEAR Monte Carlo (dashed histogram), for 7 $Q^2$ intervals. Each distribution is normalised to the number of events, $N$. The solid line is a simple Gaussian fit to the data for a fitting interval ± 1.0 unit in $\xi_p$ about the statistical mean.*

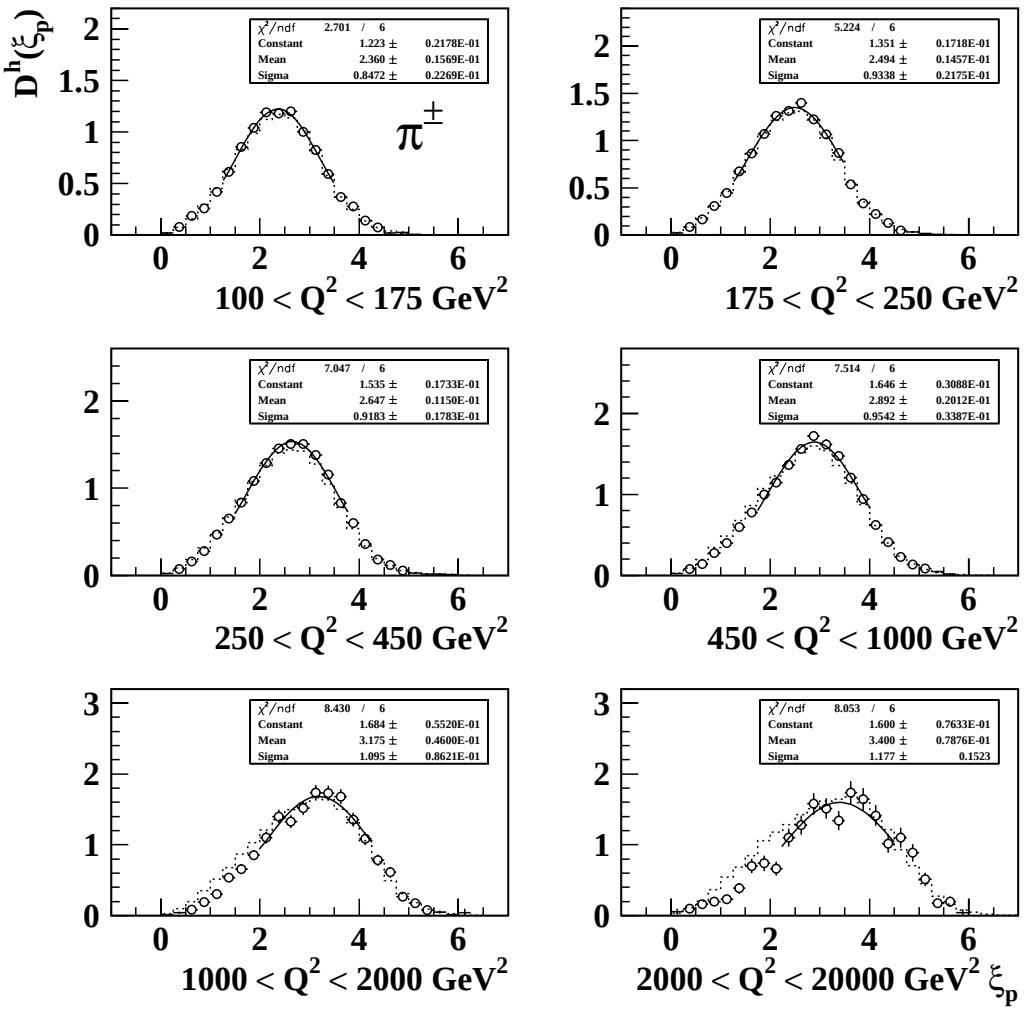


**Figure 8.3**: *Corrected fragmentation function, $D^h(\xi_p)$, for $\pi^{\pm}$ measured in high $Q^2$ 1996-97 data (closed circles) with comparison made to generated MEAR Monte Carlo (dashed histogram), for 6 $Q^2$ intervals. Each distribution is normalised to the number of events, $N$. The solid line is a simple Gaussian fit to the data for a fitting interval $\pm$ 1.0 unit in $\xi_p$ about the statistical mean.*

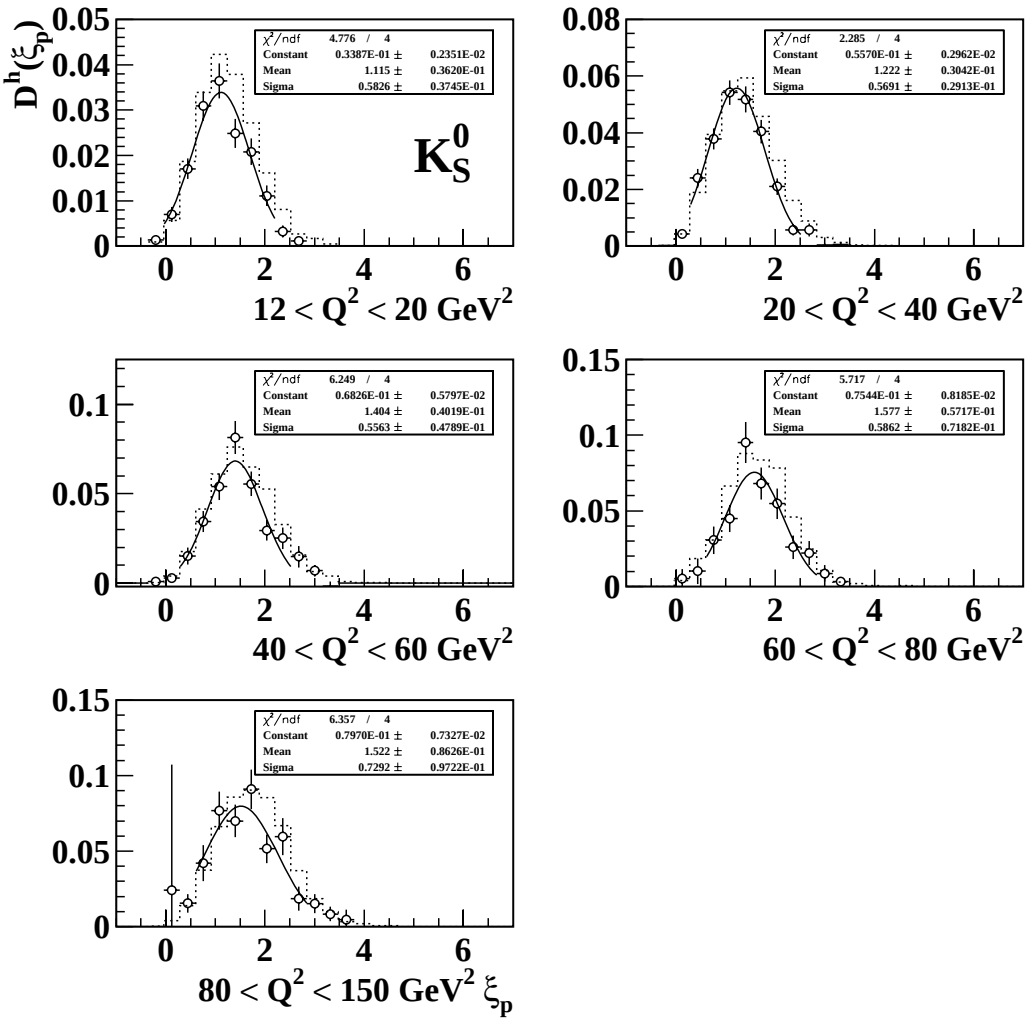


**Figure 8.4**: *Corrected fragmentation function, $D^h(\xi_p)$, for $K^0_S$ measured in low $Q^2$ 1996-97 data (closed circles) with comparison made to generated MEAR Monte Carlo (dashed histogram), for 5 $Q^2$ intervals. Each distribution is normalised to the number of events, $N$. The solid line is a simple Gaussian fit to the data for a fitting interval $\pm$ 1.0 unit in $\xi_p$ about the statistical mean.*

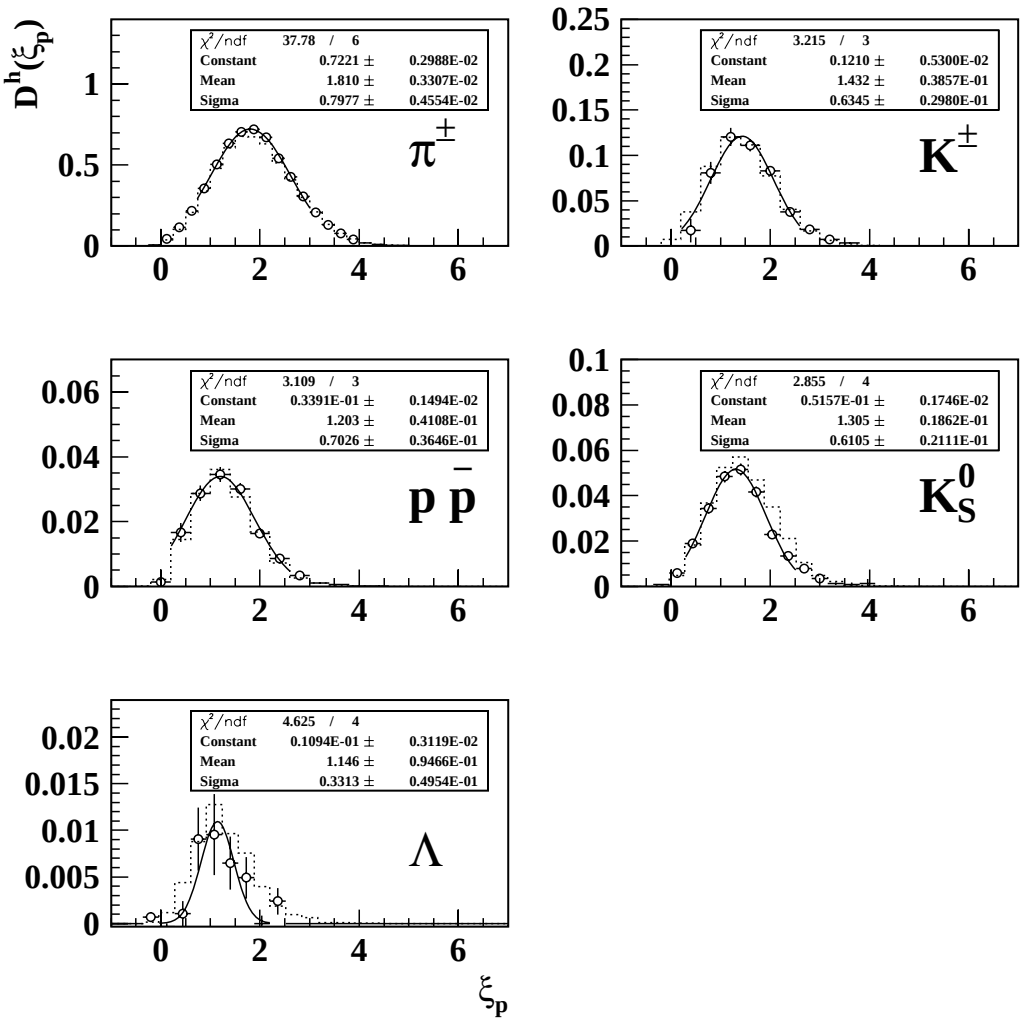


**Figure 8.5**: *Corrected fragmentation function, $D^h(\xi_p)$, for $\pi^{\pm}$, $K^{\pm}$, protons/antiprotons ($p/\bar{p}$), $K^0_S$, and $\Lambda$ measured in low $Q^2$ ($12 < Q^2 < 150\ GeV^2$) 1996-97 data (closed circles) with comparison made to generated MEAR Monte Carlo (dashed histogram). Each distribution is normalised to the number of events, $N$. The solid line is a simple Gaussian fit to the data for a fitting interval ± 1.0 unit in $\xi_p$ about the statistical mean.*

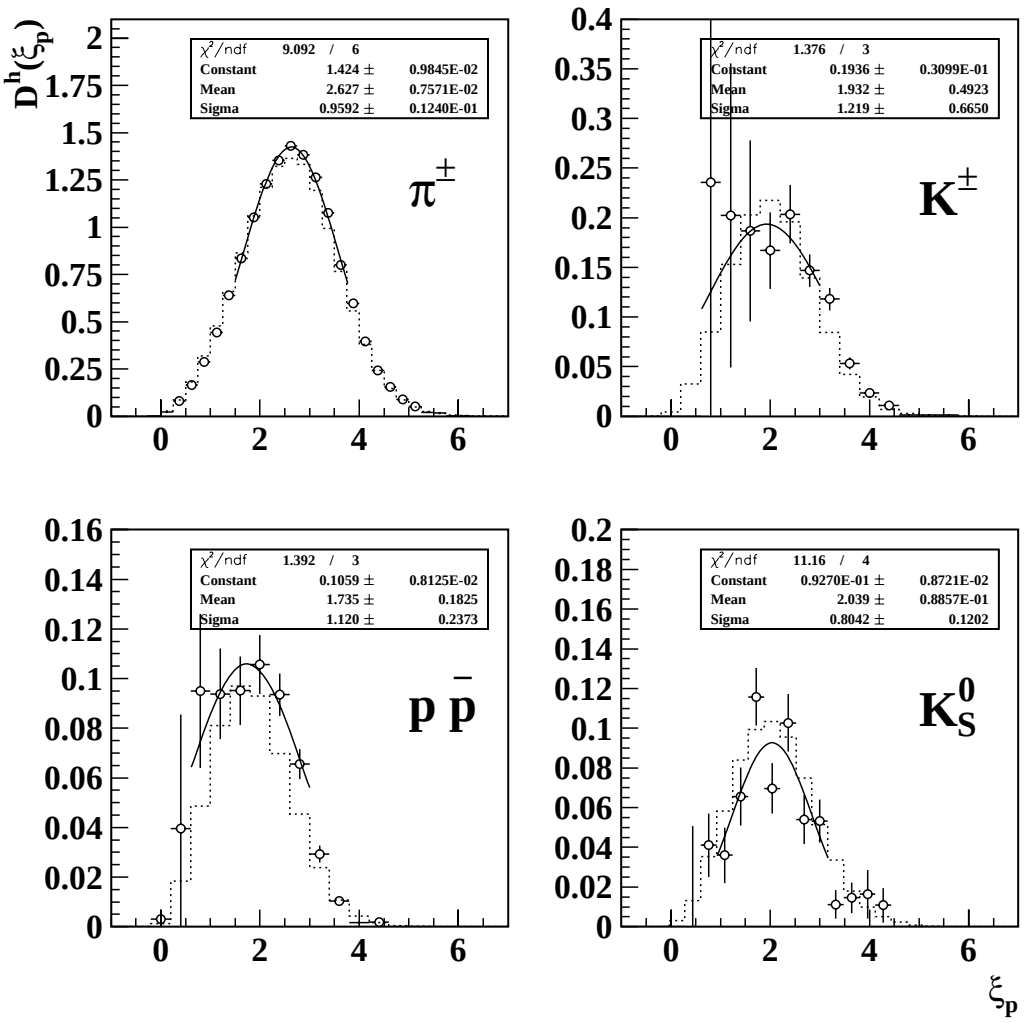


**Figure 8.6**: *Corrected fragmentation function, $D^h(\xi_p)$, for $\pi^\pm$, $K^\pm$, protons/antiprotons ($p/\bar{p}$), $K^0_S$, and $\Lambda$ measured in high $Q^2$ ($100 < Q^2 < 20\,000$ GeV$^2$) 1996-97 data (closed circles) with comparison made to generated MEAR Monte Carlo (dashed histogram). Each distribution is normalised to the number of events, $N$. The solid line is a simple Gaussian fit to the data for a fitting interval ± 1.0 unit in $\xi_p$ about the statistical mean.*

measured in thirteen $Q^2$ intervals, and the fragmentation function $D^{K^0_S}(\xi_p)$ is measured in six $Q^2$ intervals. Due to limited statistics, it is only possible to measure $D^{K^\pm}(\xi_p)$ and $D^{p\overline{p}}(\xi_p)$ for two $Q^2$ intervals, and $D^{\Lambda}(\xi_p)$ for a single $Q^2$ interval.

For consistency with previously published H1 results, $D^h(\xi_p)$ is fitted with a simple Gaussian function in a limited interval of $\pm$ 1.0 unit in $\xi_p$ about the statistical mean, from which a peak position, $\xi_p^{*h}$, and width, $\sigma_p^h$ can be extracted. The results from applying such a fitting procedure are presented in Tables 8.3 and 8.4. A selection of exclusive fragmentation function spectra published by CLEO [76], TASSO [77], TOPAZ [78], ALEPH [79], L3 [80], and OPAL [81] are re-fitted using a procedure identical to that applied to H1 data, with results given in Tables 8.5 and 8.6, thereby enabling a comparison of the fragmentation properties in DIS to those in an $e^+e^-$ annihilation. A systematic error due to the fitting interval selected is added in quadrature to the statistical error.

In order to measure the turn-over region of $K^\pm$ and $p/\overline{p}$ fragmentation functions, extremely large bin-by-bin correction factors must be applied (see section 7.6). Due to the unreliability of such a measurement, extracted values of $\xi_p^{*h}$ and $\sigma_p^h$ will be displayed only, and will not be included in any calculations or fitting.

## 8.4 Systematic Errors

To test the sensitivity of the results presented in this thesis to analysis procedures, a number of possible sources of systematic error are outlined below and investigated. The analysis is repeated with variation of each source, and the corresponding change in the fragmentation function peak position and width is calculated:

- **Scattered Electron Reconstruction and Hadronic Energy Scale**
  The systematic uncertainty in the reconstruction of the scattered electron is studied by varying the energy scales of the SpaCal and LAr calorimeters by

$\pm 1\%$ and $\pm 3\%$ respectively, and the scattered electron polar and azimuthal angles by $\pm 2$ mrad and $\pm 3$ mrad respectively. The hadronic energy scale is varied by $\pm 4\%$.

- **Scattered Electron Energy** The systematic effect of requiring the scattered electron energy to be greater than 14 GeV is studied by increasing this requirement to 20 GeV.

- **Event re-weighting** The systematic effect of event-by-event re-weighting in the reconstructed Monte Carlo due to a poor simulation of the scattered electron energy spectrum and the $z$ vertex distribution, is investigated by comparing results before and after re-weighting. This study shows the change to be very small compared to other sources of systematic error, and is therefore not included in an overall estimate for the total systematic error.

- **Track Quality Criteria** Track quality criteria (such as transverse momentum and track length requirements) are varied independently to estimate the systematic uncertainty related to an imperfect simulation of the Central Tracker acceptance and efficiency. For primary charged tracks identified using $\mathrm{d}E/\mathrm{d}x$ information, the minimum number of $\mathrm{d}E/\mathrm{d}x$ hits is increased from 15 to 20.

- **Track re-weighting** The systematic effect of track-by-track re-weighting in the reconstructed Monte Carlo as a result of a poor $N_{\mathrm{d}E/\mathrm{d}x}$ simulation, is investigated by comparing results before and after re-weighting. The change is small, being less than the statistical error, and is not included in the systematic error.

- **$\mathrm{d}E/\mathrm{d}x$ Selection Procedure** The systematic effect of using a geometric identification window for charged primary hadron identification is studied using an alternative selection procedure based upon a log-likelihood technique, as discussed in section 5.2.4.

- **$V^0$ Mass Windows** To estimate the systematic effect of the mass windows from within which $K^0_S$ and $\Lambda$ candidates are selected, the mass windows were

changed to $0.475 < m_{\pi\pi} < 0.525$ GeV/$c^2$ and $1.113 < m_{p\pi} < 1.119$ GeV/$c^2$ respectively.

- **Model Dependence of Correction Factors** The fragmentation functions measured in this analysis are corrected using MEAR Monte Carlo which is based upon the Colour Dipole Model of the parton cascade. To test the effect of the parton evolution scheme on the corrected fragmentation function, the analysis is repeated utilizes MEPS Monte Carlo which uses the parton shower model.

- **Fitting Interval** The systematic effect of the fitting range over which $\xi_p^{*h}$ and $\sigma_p^h$ are extracted, is estimated by varying the fitting interval, as calculated from the statistical mean, by $\pm 1$ bin.

Although not included as a systematic error, the analysis is repeated using the Double Angle method to reconstruct event kinematics, and as a crosscheck, $\xi_p^{*h}$ and $\sigma_p^h$ values are compared to those determined with the Electron Only method. Overall, the results obtained using the two methods are in close agreement, with differences being of the order of the statistical error.

As highlighted in section 8.3, for a given hadronic species the fragmentation function is measured in a number of $Q^2$ intervals, where the range and number of intervals is constrained by the available statistics. A corresponding $\xi_p^{*h}$ and $\sigma_p^h$ value is determined for each $Q^2$ bin, and Tables 8.1 and 8.2 indicate the range of uncertainties in these peak position and width values for each hadronic species identified and error source investigated.

| Source of systematic error | Systematic effect (%) | | | | |
|---|---|---|---|---|---|
| | $\pi^{\pm}$ | $K^{\pm}$ | $p/\bar{p}$ | $K^0_S$ | $\Lambda$ |
| Scattered electron reconstruction | $\leq 1$ | 8→15 | 8→17 | 1→10 | 10 |
| Hadronic energy scale | $< 1$ | $< 3$ | $< 1$ | $< 1$ | $< 10$ |
| Scattered electron energy | $< 1$ | $< 1$ | $< 1$ | $< 1$ | $< 1$ |
| Track quality criteria | $\leq 2$ | 1→10 | 2→7 | 3→10 | 6 |
| Variation of $N_{\mathrm{d}E/\mathrm{d}x}$ cut | 1→10 | $\leq 6$ | $\leq 18$ | - | - |
| $\mathrm{d}E/\mathrm{d}x$ selection criteria | $\leq 5$ | 1→4 | 1→4 | - | - |
| $V^0$ mass windows | - | - | - | 1→12 | 6 |
| Model dependence of correction factors | 1→9 | $\leq 10$ | 4→6 | 1→15 | 6 |
| Fitting interval | 1→32 | $\leq 3$ | 4→8 | 1→6 | 15 |
| Total Effect | 2→34 | 17→31 | 12→29 | 7→22 | 23 |
| Statistical | <3 | 3→25 | 3→11 | 2→6 | 44 |

**Table 8.1**: *Summary of the range of uncertainties in $\xi_p^{*h}$ for the $Q^2$ intervals defined in this analysis, expressed as a percentage of $\xi_p^{*h}$, for a number of sources of systematic error. Also shown is the corresponding range of percentage statistical errors calculated from a simple Gaussian fit to each fragmentation function.*

| Source of systematic error | Systematic effect (%) | | | | |
|---|---|---|---|---|---|
| | $\pi^{\pm}$ | $K^{\pm}$ | $p/\bar{p}$ | $K^0_S$ | $\Lambda$ |
| Scattered electron reconstruction | $\leq 17$ | 5→15 | 1→3 | 1→10 | 15 |
| Hadronic energy scale | $< 1$ | <4 | $< 1$ | $< 15$ | $< 5$ |
| Scattered electron energy | $\leq 5$ | $< 1$ | 1→3 | $< 1$ | $< 1$ |
| Track quality criteria | 1→5 | 15 | 3→10 | 1→20 | 15 |
| Variation of $N_{\mathrm{d}E/\mathrm{d}x}$ cut | 1→20 | 4→15 | 1→30 | - | - |
| $\mathrm{d}E/\mathrm{d}x$ selection criteria | 1→10 | $< 7$ | $< 5$ | - | - |
| $V^0$ mass windows | - | - | - | 3→25 | 4 |
| Model dependence of correction factors | 1→22 | 1→15 | 1→8 | 2→30 | 6 |
| Fitting interval | 1→25 | 11→20 | 1→10 | 1→15 | 30 |
| Total Effect | 3→40 | 26→52 | 14→42 | 12→49 | 42 |
| Statistical | 1→13 | 5→55 | 5→21 | 5→15 | 15 |

**Table 8.2**: *Summary of the range of uncertainties in $\sigma_p^{*h}$ for the $Q^2$ intervals defined in this analysis, expressed as a percentage of $\sigma_p^{*h}$, for a number of sources of systematic error. Also shown is the corresponding range of percentage statistical errors calculated from a simple Gaussian fit to each fragmentation function.*

## 8.5 Evolution of the Fragmentation Function

Section 8.3 indicated that the fragmentation function can be successfully approximated by a Gaussian distribution. This in turn may be specified by an average charged multiplicity, $< n^h >$, peak position, $\xi_p^{*h}$, and width, $\sigma_p^h$. The full description of the evolution of all fragmentation functions then demands a description of the dependence of these variables on both $Q$ and hadronic type, $h$. In practice, available statistics, systematic errors, and the small kinematic range for positive identification limit the ability, as yet, to report confidently on values of $< n^h >$ and on fine kinematic subdivision for the other variables. Nevertheless, it is still possible to study the mass and $Q$ dependence of $\xi_p^{*h}$ and $\sigma_p^h$ for a number of different hadronic species, and compare with a perturbative QCD calculation.

| Peak Position $\xi_p^{*h}$ | | | | | |
|---|---|---|---|---|---|
| $< Q >$ (GeV) | Identified Hadron | | | | |
| | $\pi^{\pm}$ | $K^{\pm}$ | $K_S^0$ | $p\overline{p}$ | $\Lambda$ |
| 3.7 | 1.500±0.008±0.045 | - | - | - | - |
| 3.9 | - | - | 1.115±0.036±0.100 | - | - |
| 4.1 | 1.592±0.007±0.048 | - | - | - | - |
| 5.3 | 1.764±0.005±0.053 | - | 1.222±0.030±0.086 | - | - |
| 5.6 | 1.809±0.003±0.054 | 1.431±0.039±0.243 | 1.305±0.019±0.091 | 1.203±0.041±0.144 | 1.146±0.095±0.264 |
| 7.0 | 1.972±0.009±0.059 | - | 1.404±0.040±0.140 | - | - |
| 8.3 | 2.084±0.011±0.063 | - | 1.577±0.057±0.126 | - | - |
| 9.4 | 2.162±0.014±0.065 | - | - | - | - |
| 10.2 | - | - | 1.522±0.086±0.304 | - | - |
| 10.9 | 2.228±0.014±0.092 | - | - | - | - |
| 12.0 | 2.360±0.016±0.118 | - | - | - | - |
| 14.5 | 2.494±0.015±0.125 | - | - | - | - |
| 18.1 | 2.647±0.011±0.132 | - | - | - | - |
| 19.1 | 2.627±0.008±0.105 | 1.932±0.492±0.599 | 2.039±0.089±0.367 | 1.735±0.183±0.503 | - |
| 25.2 | 2.892±0.020±0.145 | - | - | - | - |
| 36.5 | 3.175±0.046±0.222 | - | - | - | - |
| 56.6 | 3.400±0.079±0.680 | - | - | - | - |

**Table 8.3**: *The peak position, $\xi_p^{*h}$, determined from $D^h(\xi_p)$ measured at different values of $< Q >$ using H1 data. The first error shown is the statistical (fit) error and the second error is the total systematic error.*

| Width $\sigma_p^h$ | | | | | |
|---|---|---|---|---|---|
| $< Q >$ (GeV) | Identified Hadron | | | | |
| | $\pi^{\pm}$ | $K^{\pm}$ | $K_S^0$ | $p\overline{p}$ | $\Lambda$ |
| 3.7 | 0.709±0.010±0.035 | - | - | - | - |
| 3.9 | - | - | 0.583±0.037±0.070 | - | - |
| 4.1 | 0.709±0.008±0.035 | - | - | - | - |
| 5.3 | 0.737±0.006±0.037 | - | 0.569±0.029±0.091 | - | - |
| 5.6 | 0.797±0.005±0.024 | 0.634±0.030±0.165 | 0.610±0.021±0.073 | 0.703±0.036±0.098 | 0.331±0.050±0.139 |
| 7.0 | 0.794±0.011±0.040 | - | 0.556±0.048±0.139 | - | - |
| 8.3 | 0.820±0.016±0.041 | - | 0.586±0.072±0.147 | - | - |
| 9.4 | 0.830±0.020±0.058 | - | - | - | - |
| 10.2 | - | - | 0.729±0.097±0.255 | - | - |
| 10.9 | 0.842±0.021±0.067 | - | - | - | - |
| 12.0 | 0.847±0.023±0.059 | - | - | - | - |
| 14.5 | 0.934±0.022±0.093 | - | - | - | - |
| 18.1 | 0.918±0.018±0.064 | - | - | - | - |
| 19.1 | 0.959±0.012±0.067 | 1.219±0.665±0.634 | 0.804±0.120±0.322 | 1.121±0.237±0.471 | - |
| 25.2 | 0.954±0.034±0.181 | - | - | - | - |
| 36.5 | 1.095±0.086±0.296 | - | - | - | - |
| 56.6 | 1.177±0.152±0.471 | - | - | - | - |

**Table 8.4**: *The width, $\sigma_p^h$, determined from $D^h(\xi_p)$ measured at different values of $< Q >$ using H1 data. The first error shown is the statistical (fit) error and the second error is the total systematic error.*

| Peak Position $\xi_p^{*h}$ | | | | | | | | | | |
|---|---|---|---|---|---|---|---|---|---|---|
| $e^+e^-$ | $E^*$ | Identified Hadron | | | | | | | | |
| Experiment | (GeV) | $\pi^\pm$ | $\pi^0$ | $K^0$ | $K^\pm$ | $\eta$ | $K^{*0}$ | $p\overline{p}$ | $\Lambda$ | $\Xi^-$ |
| CLEO | 10.49 | 2.29±0.06 | - | 1.58±0.07 | - | - | - | - | - | - |
| TASSO | 14.0 | 2.70±0.10 | - | 1.71±0.16 | - | - | - | - | - | - |
| TASSO | 22.0 | 3.09±0.13 | - | 2.17±0.15 | - | - | - | - | - | - |
| TASSO | 30.0 | 3.58±0.64 | - | - | - | - | - | - | - | - |
| TASSO | 34.0 | 3.21±0.07 | - | 2.25±0.15 | - | - | - | - | - | - |
| TASSO | 44.0 | 3.39±0.16 | - | - | - | - | - | - | - | - |
| TOPAZ | 58.0 | 3.42±0.11 | - | 2.49±0.24 | 2.45±0.13 | - | - | 2.61±0.38 | - | - |
| OPAL | 91.2 | - | - | - | - | - | 2.31±0.27 | - | 2.75±0.15 | 2.75±0.28 |
| ALEPH | 91.2 | 3.71±0.06 | - | 2.67±0.13 | 2.61±0.45 | - | - | 2.83±0.07 | - | - |
| L3 | 91.2 | - | 3.86±0.07 | - | - | 2.15±0.40 | - | - | - | - |

**Table 8.5**: *The peak position, $\xi_p^{*h}$, determined from a simple Gaussian fit to $D^h(\xi_p)$ measured at different centre-of-mass energies, $E^*$, by a number of $e^+e^-$ experiments [76-81]. The errors presented include a systematic error due to the fitting interval, added in quadrature to the statistical (fit) error.*

| Width $\sigma_p^h$ | | | | | | | | | | |
|---|---|---|---|---|---|---|---|---|---|---|
| $e^+e^-$ | $E^*$ | Identified Hadron | | | | | | | | |
| Experiment | (GeV) | $\pi^\pm$ | $\pi^0$ | $K^0$ | $K^\pm$ | $\eta$ | $K^{*0}$ | $p\overline{p}$ | $\Lambda$ | $\Xi^-$ |
| CLEO | 10.49 | 0.85±0.09 | - | 0.53±0.14 | - | - | - | - | - | - |
| TASSO | 14.0 | 0.91±0.09 | - | 0.60±0.18 | - | - | - | - | - | - |
| TASSO | 22.0 | 1.10±0.18 | - | 0.79±0.09 | - | - | - | - | - | - |
| TASSO | 30.0 | 1.09±0.42 | - | - | - | - | - | - | - | - |
| TASSO | 34.0 | 1.14±0.06 | - | 0.83±0.22 | - | - | - | - | - | - |
| TASSO | 44.0 | 1.07±0.13 | - | - | - | - | - | - | - | - |
| TOPAZ | 58.0 | 1.08±0.11 | - | 1.29±0.50 | 1.29±0.14 | - | - | 1.37±0.39 | - | - |
| OPAL | 91.2 | - | - | - | - | - | 1.08±0.24 | - | 1.31±0.07 | 1.10±0.12 |
| ALEPH | 91.2 | 1.18±0.20 | - | 1.37±0.23 | 1.30±0.09 | - | - | 1.20±0.13 | - | - |
| L3 | 91.2 | - | 1.21±0.12 | - | - | 1.27±0.23 | - | - | - | - |

**Table 8.6**: *The width, $\sigma_p^h$, determined from a simple Gaussian fit to $D^h(\xi_p)$ measured at different centre-of-mass energies, $E^*$, by a number of $e^+e^-$ experiments [76-81]. The errors presented include a systematic error due to the fitting interval, added in quadrature to the statistical (fit) error.*

| Particle | Dataset | Gradient | Intercept | $\chi^2/ndf$ |
|---|---|---|---|---|
| mesons | $e^+e^-$ | -0.86±0.03 | 2.06±0.15 | 0.81 |
| baryons | $e^+e^-$ | -0.98±0.66 | 2.81±0.06 | 0.03 |
| all hadrons | H1 96-97 | -0.38±0.02 | 1.07±0.12 | 0.25 |
| | $e^+e^-$ | -0.53±0.04 | 2.70±0.06 | 3.30 |

**Table 8.7**: *Results of separate fits to both H1 ($< Q > = 5.6$ GeV) and $e^+e^-$ ($E^* = 91.2$ GeV) data for mesons and baryons, separately and combined, using $\xi_p^{*h} \propto -ln(m^h)$.*

### 8.5.1 Mass Evolution of the Fragmentation Function

In Figure 8.7, the values of $\xi_p^{*h}$ extracted from fragmentation functions measured for $\pi^\pm$, $K^\pm$, $K_S^0$, $p/\bar{p}$, and $\Lambda$ in 1996-97 low $Q^2$ ($< Q >= 5.6$ GeV) H1 data are displayed as a function of hadronic mass, $m^h$ (GeV/$c^2$). Also shown is a selection of $\xi_p^{*h}$ values obtained from re-fitted $e^+e^-$ data at a centre-of-mass energy $E^* = 91.2$ GeV.

The mesonic and baryonic peak positions are fitted separately for $e^+e^-$ data using the functional form $\xi_p^{*h} \propto -\ln(m^h)$, as motivated by MLLA/LPHD [82]. For reasons discussed in section 8.3, it is not possible at this stage to perform separate fits to H1 mesonic and baryonic data. A simultaneous fit of the above form is performed using H1 $\pi^\pm$, $K_S^0$, and $\Lambda$ fragmentation function peak positions, with all results summarised in Table 8.7. The H1 data supports the MLLA/LPHD expectation that as the hadronic mass increases the fragmentation function peak position decreases. The $e^+e^-$ observation [83] of a different intercept for mesons and baryons is incompatible with a universal evolution for mesons and baryons, as seen in Table 8.7. The H1 data has less discriminating power and is compatible with either behaviour.

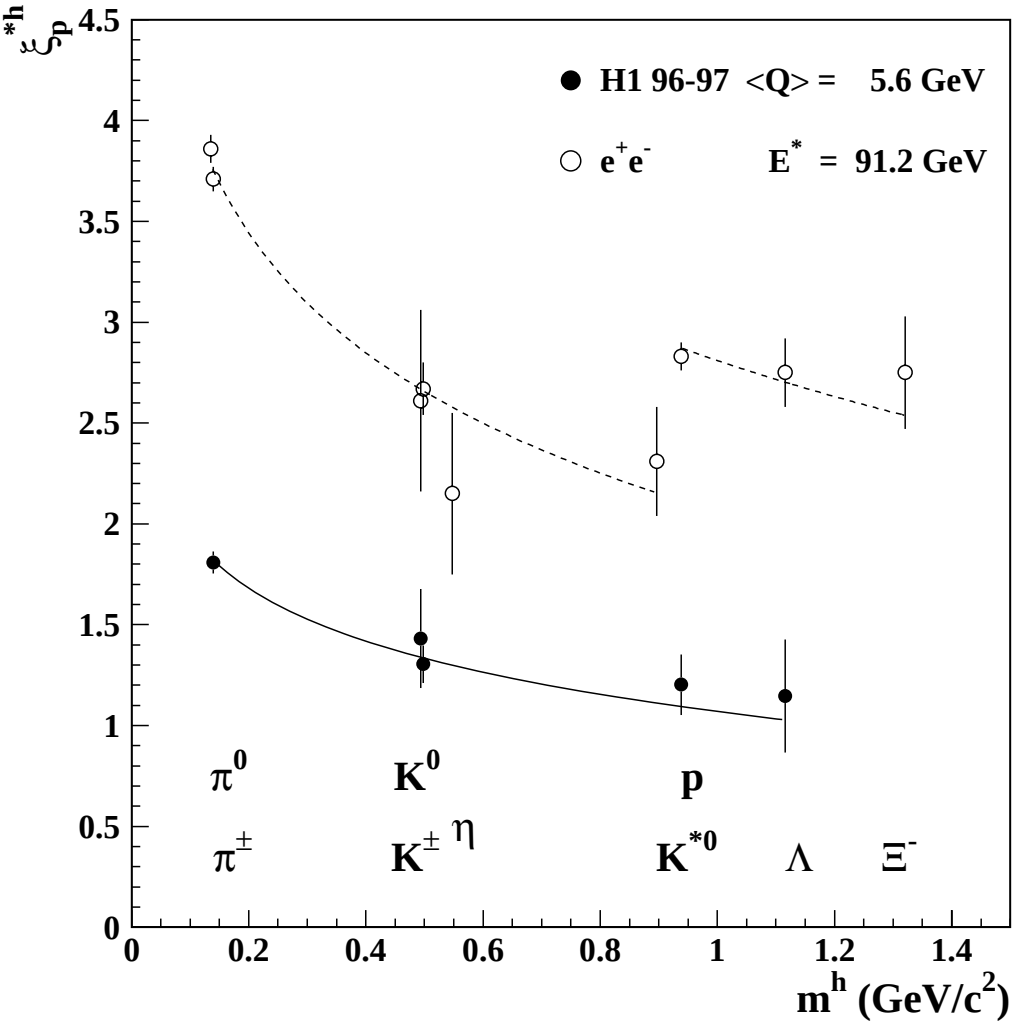


**Figure 8.7**: *The peak position $\xi_p^{*h}$ of the distribution $D^h(\xi_p)$ as a function of hadronic mass, $m^h$. The solid line is a fit to the form $\xi_p^{*h} \propto -ln(m^h)$ using peak positions of $\pi^\pm$, $K_S^0$, and $\Lambda$ in H1 data (closed circles) at $< Q >= 5.6$ GeV, with corresponding $K^\pm$ and $p\overline{p}$ points displayed only. The dashed lines are separate fits to the same functional form using mesonic and baryonic points extracted from re-fitted $e^+e^-$ data [76-81] (open circles) at $E^*$=91.2 GeV.*

| Particle | Dataset | Gradient (a) | Intercept (b) | $\chi^2/ndf$ |
|---|---|---|---|---|
| $\pi^{\pm}$ | H1 96-97 | 0.71±0.04 | 0.58±0.08 | 0.03 |
| $\pi^{\pm}$ | $e^+e^-$ | 0.64±0.01 | 0.91±0.13 | 2.1 |
| $K^0_S$ | H1 96-97 | 0.59 ± 0.03 | 0.27 ± 0.29 | 0.11 |
| $K^0$ | $e^+e^-$ | 0.52 ± 0.02 | 0.38 ± 0.19 | 0.48 |

**Table 8.8**: *Result of separate straight line fits to fragmentation function peak positions for $\pi^{\pm}$ and $K^0$ in H1 data and re-fitted $e^+e^-$ data.*

### 8.5.2 Simple Parameterisation of Energy Evolution

The peak evolution of $D^{\pi^{\pm}}$ and $D^{K^0_S}/D^{K^0}$ are presented in Figure 8.8 as a function of $Q$ and $E^*$ for H1 data and re-fitted $e^+e^-$ data respectively. For both H1 and $e^+e^-$ data, the peak position can be successfully described using a simple linear dependence on the energy scale:

$$\xi_p^{*h} = a \ln Q + b \tag{8.2}$$

The gradient and intercept from resulting fits are summarised in Table 8.8. The higher gradient and lower intercept for $\pi^{\pm}$ and $K^0$ evolution in $ep$ data indicates a steeper evolution as compared to $e^+e^-$ data, which may be due to the $ep$ data extending to lower energies. However, with current errors the gradients measured for H1 and $e^+e^-$ data are compatible, but suggest a different fragmentation function energy evolution for different particle species. As first hinted at with $e^+e^-$ data [84], and here confirmed, the evolving $K^0_S$ peak position has a flatter, diverging, gradient compared with that for $\pi^{\pm}$. This is contrary to the MLLA/LPHD expectation of a universal evolution, as well as the assumed decreasing importance of mass scales at asymptotic energies.

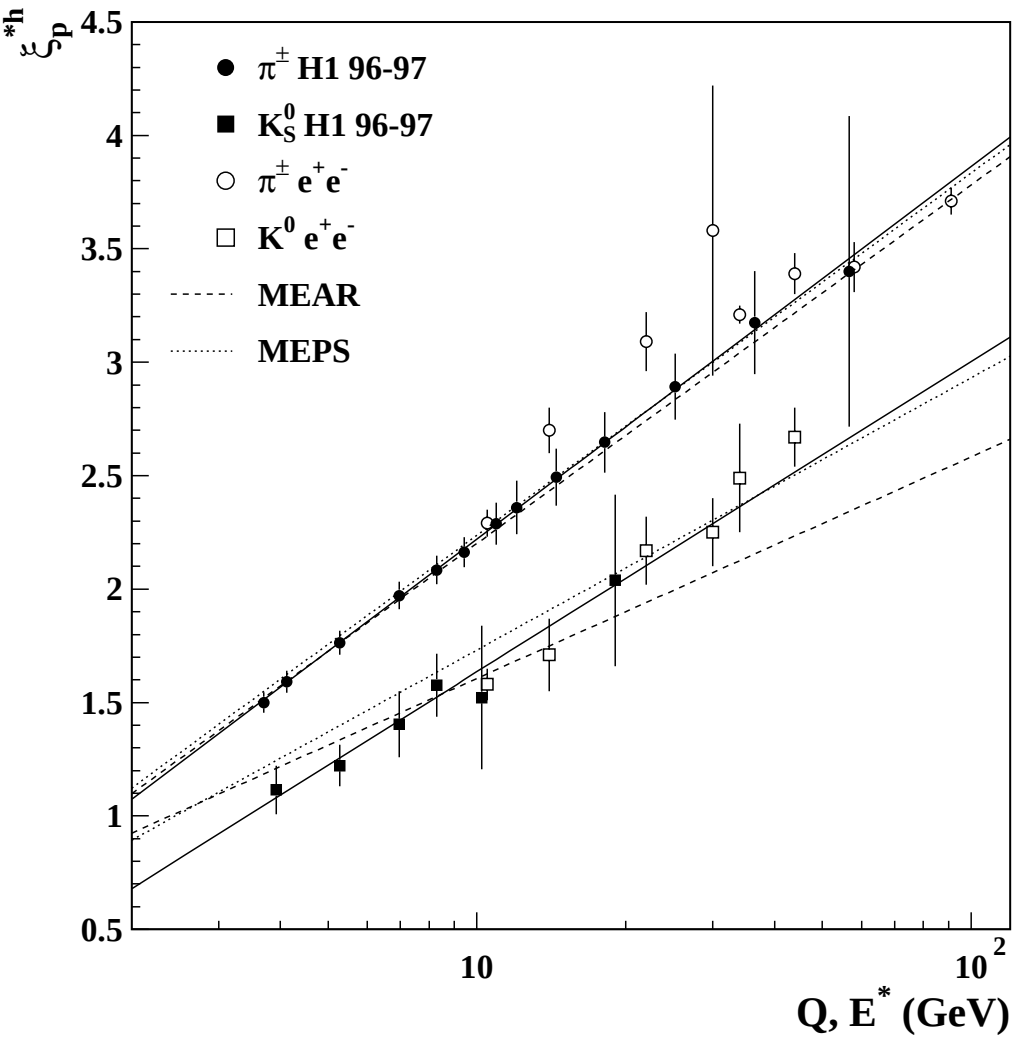


**Figure 8.8**: *Evolution of the peak position, $\xi_p^{*h}$, of the distribution $D^h(\xi_p)$ as a function of four-momentum transfer, $Q$, and centre-of-mass energy, $E^*$, for $\pi^{\pm}$ (circles) and $K^0$ (squares) in H1 (closed points) and re-fitted $e^+e^-$ [76-81] (open points) data. The solid line is a simple linear lnQ fit to H1 data, and the dashed (dotted) line is an equivalent fit to generated MEAR [53] (MEPS [54]) Monte Carlo (see section 8.5.4 for discussion).*

### 8.5.3 MLLA/LPHD Description of Energy Evolution

As highlighted in section 3.6, the MLLA/LPHD calculation for the limiting spectrum assuming gluon coherence provides an excellent description of the energy evolution of the inclusive pion dominated fragmentation function. A natural extension to this work is to attempt to describe the evolution of identified hadron fragmentation within the MLLA/LPHD framework. The limiting spectrum is derived by the premise of a shower cut-off parameter, $Q_0$, tending to a universal effective QCD scale parameter, $\Lambda_{eff}$. The approximation of $Q_0 = \Lambda_{eff}$ is no longer valid since the cut-off of the parton cascade will differ between hadronic species as a result of their differing masses. By assuming that a jet of hadrons contains one species only of hadronic type $h$ and mass $m^h$, with the parton shower terminating at a scale $Q_0^h$, the predicted MLLA/LPHD behaviour for the exclusive fragmentation function peak and width evolution, as shown in section 3.6, is [40]:

$$\xi_p^{*h} = \frac{24N_c c_2}{c_1} + \frac{1}{2}(\tau - \lambda) + c_2(\sqrt{\tau} - \sqrt{\lambda}) \tag{8.3}$$

$$\sigma_p^h = \left[\frac{1}{2c_1}(\tau^{\frac{3}{2}} - \lambda^{\frac{3}{2}}) - \frac{9}{8c_1^2}(\tau - \lambda)\right]^{\frac{1}{2}} \tag{8.4}$$

where $\lambda = \ln(Q_0^h/\Lambda_{eff})$, and constants $c_1$ and $c_2$ are fully determined and dependent only on the number of active flavours, $N_f$, and colours, $N_c$, in QCD.

This section will present simultaneous fits to the $\xi_p^{*h}$ and $\sigma_p^h$ values of hadronic species $h$ using equations 8.3 and 8.4 for H1 data, and will compare with results from equivalent fits to $e^+e^-$ data. In each case, the fit is dependent upon two free parameters, $\Lambda_{eff}$ and $Q_0^h$, and a correlation coefficient is calculated. For each hadronic species, the error on each data point is the square root of the quadratic sum of the statistical error and the total systematic error. The fit assumes that each data point is independent and the errors are uncorrelated, since the points are extracted from exclusive fragmentation functions measured in a merged sam-

ple of 1996 and 1997 data. Furthermore, the current hemisphere jet measured in H1 data contains a mix of hadronic species, and therefore the application of equations 8.3 and 8.4 to describe the fragmentation function evolution of identified hadrons in data is intended only as an approximation. That is, in a given jet this analysis identifies at least one hadron of type $h$, with the remaining jet being a mix of species which are therefore excluded from the study of $h$ fragmentation.

A simultaneous fit to H1 $\pi^{\pm}$ peak and width data using equations 8.3 and 8.4, assuming three colours and four active flavours, yields parameter values $\Lambda_{eff} = 0.058 \pm 0.008$ GeV and $Q_0^{\pi^{\pm}} = 0.316 \pm 0.009$ GeV, with a correlation coefficient of 0.31 and a $\chi^2/ndf = 0.34$. A good quality fit to H1 $K_S^0$ peak and width data is achieved, with $\Lambda_{eff} = 0.092 \pm 0.056$ GeV, $Q_0^{K_S^0} = 0.691 \pm 0.054$ GeV, with a correlation coefficient of 0.25 and a $\chi^2/ndf = 0.23$. As expected, a positive correlation exists between $\Lambda_{eff}$ and $Q_0^h$, indicating that as $\Lambda_{eff}$ increases, the scale at which the parton shower terminates increases leading to a harder momentum spectrum, and vice versa.

These results can be compared to equivalent fits to $\pi^{\pm}$ and $K^0$ data taken by $e^+e^-$ experiments [76-81], which yield parameter values $\Lambda_{eff} = 0.076 \pm 0.022$ GeV and $Q_0^{\pi^{\pm}} = 0.249 \pm 0.015$ GeV, and $\Lambda_{eff} = 0.189 \pm 0.109$ GeV and $Q_0^{K_S^0} = 0.943 \pm 0.082$ GeV respectively. Although there is some disagreement between $Q_0^h$ values, there is agreement with the MLLA/LPHD expectation of a universal energy scale, and therefore fragmentation function evolution, with the momentum spectrum narrowing and hardening as the hadronic mass increases. The value of $\Lambda_{eff}$ is significantly smaller than that obtained from the earlier inclusive fits (see section 3.6) which presume limiting spectrum conditions.

An alternative approach for describing massive hadron fragmentation within MLLA/LPHD theory has been presented in [78, 85], whereby the $\Lambda_{eff}$ and $Q_0^h$ values are determined by fitting a MLLA calculation over the whole exclusive fragmentation function, with a typical fitting range of $1.0 < \xi_p < 4.0$. The values of $Q_0^{\pi^{\pm}}$ and $Q_0^{K_S^0}$ obtained are in good agreement with those calculated from fitting H1 data, although the values of $\Lambda_{eff}$ (100-300 MeV) are slightly higher.

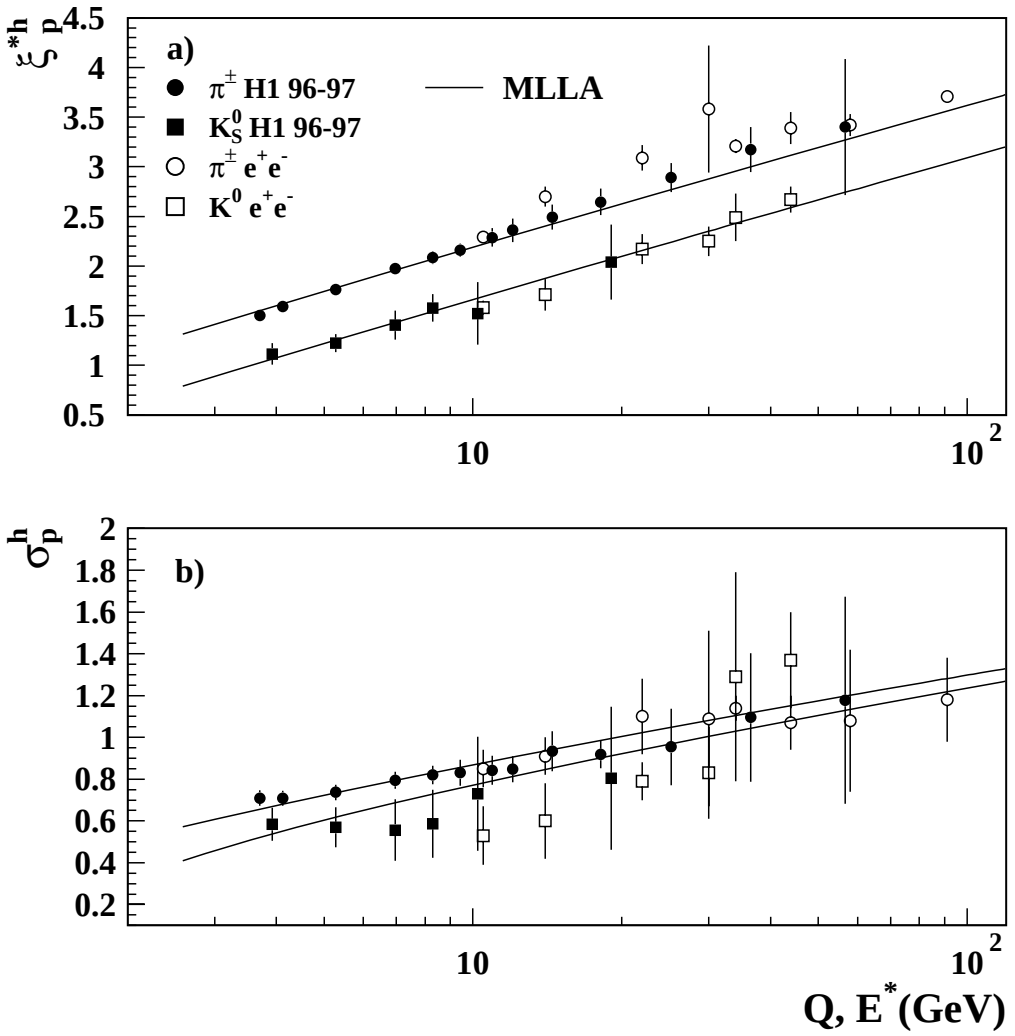


**Figure 8.9**: *Energy evolution of a) the peak position, $\xi_p^{*h}$, and b) the width, $\sigma_p^h$, of $D^h(\xi_p)$ for $\pi^{\pm}$ (circles) and $K_S^0/K^0$ (squares). The solid line is a simultaneous fit to H1 data (closed points) using a MLLA/LPHD calculation, as defined in equation 8.3 and 8.4, together with equation 8.5. Also shown is a selection of re-fitted $e^+e^-$ data [76-81] (open points).*

A totally empirical attempt has been made to relate the cut-off parameter, $Q_0^h$, to the hadronic mass, $m^h$. Repeating the MLLA/LPHD fit using all $\pi^{\pm}$, $K_S^0$, and $\Lambda$ H1 peak and width data shows consistency with the form:

$$Q_0^{h_{bary}^{mes}} = km^h \pm C \tag{8.5}$$

where a common parameter, $C$, is added to or subtracted from the mesonic (mes) or baryonic (bary) mass respectively. The parameter $k$ is consistent with 1.0 and is set to unity in the fit. The fit then has parameter values $\Lambda_{eff} = 0.060 \pm 0.008$ GeV, $C = 0.178 \pm 0.009$ GeV, and a $\chi^2/ndf = 0.35$. An equivalent fit to the $e^+e^-$ data presented in Tables 8.5 and 8.6 yields the parameter values $\Lambda_{eff} = 0.060 \pm 0.014$ GeV, $C = 0.106 \pm 0.008$ GeV, with a $\chi^2/ndf = 1.8$. The differing relationship between hadronic mass and $Q_0^h$ for mesons and baryons is sufficient to account for the observed difference in mass evolution at fixed energy discussed in section 8.5.1, and is shown in Figure 8.10a. Furthermore, if this evolution is expressed in terms of $Q_0^h$, universal behaviour for all hadrons is observed, as seen in Figure 8.10b. The results are summarised in Table 8.9, which also shows the effect of differing assumptions on the number of active flavours. At present there is no theoretical basis to the relationship between hadronic mass and $Q_0^h$. It is simply an observed simplification that may be applied to the MLLA/LPHD parameterisation.

The values of $\Lambda_{eff}$ and $C$ calculated from H1 data, and substituted into equations 8.3-8.5, can describe the evolution of all presented $e^+e^-$ peak position data as a function of $E^*$, $Q_0^h$, and hadronic mass, as seen in Figures 8.9 to 8.11. At high energy both the H1 and $e^+e^-$ $\pi^{\pm}$ $\xi_p^{*h}$ values presented in Figure 8.9a lie above the MLLA/LPHD calculation. The gradient can be steepened above an approximate 10 GeV threshold by increasing the number of active flavours to five, although this is insufficient to account fully for the observed difference.

In Figure 8.12, the evolution of $\sigma_p^h$ is presented as a function of mass and $Q_0^h$. The data supports the MLLA/LPHD expectation of a narrowing fragmentation func-

| Experiment | Number of active flavours | | |
|---|---|---|---|
| | 3 | 4 | 5 |
| **H1** | | | |
| $\Lambda_{eff}$(GeV) | 0.067±0.009 | 0.060±0.008 | 0.052±0.008 |
| $C$ (GeV) | 0.173±0.009 | 0.178±0.009 | 0.182±0.009 |
| $\chi^2/ndf$ | 0.37 | 0.35 | 0.33 |
| $\mathbf{e^+e^-}$ | | | |
| $\Lambda_{eff}$(GeV) | 0.073±0.016 | 0.060±0.014 | 0.047±0.012 |
| $C$ (GeV) | 0.103±0.008 | 0.106±0.008 | 0.109±0.008 |
| $\chi^2/ndf$ | 1.7 | 1.8 | 1.9 |

**Table 8.9**: *Results of a simultaneous fit to the peak position, $\xi_p^{*h}$, and width, $\sigma_p^h$, using the MLLA/LPHD calculation defined in equations 8.3 and 8.4, together with equation 8.5, assuming three colours and three or more active quark flavours.*

tion with increasing mass, but the $e^+e^-$ data lies below the H1 parameterisation of MLLA/LPHD.

### 8.5.4 Comparisons with Monte Carlo Models

Properties of the hadronic final state observed in data can be compared to QCD models parameterised in the form of a Monte Carlo event generator. This analysis compares data with two different models:

- **MEAR**: The electroweak scatter is calculated using a first-order matrix element calculation as implemented in LEPTO 6.5, which is then interfaced with ARIADNE 4.08 to generate the QCD parton cascade. Hadronisation is performed using JETSET 7.407.
- **MEPS**: As with MEAR, the initial electroweak scatter is generated using LEPTO 6.5, and the QCD parton cascade is simulated by the parton shower model. Hadronisation is again performed using JETSET 7.407.

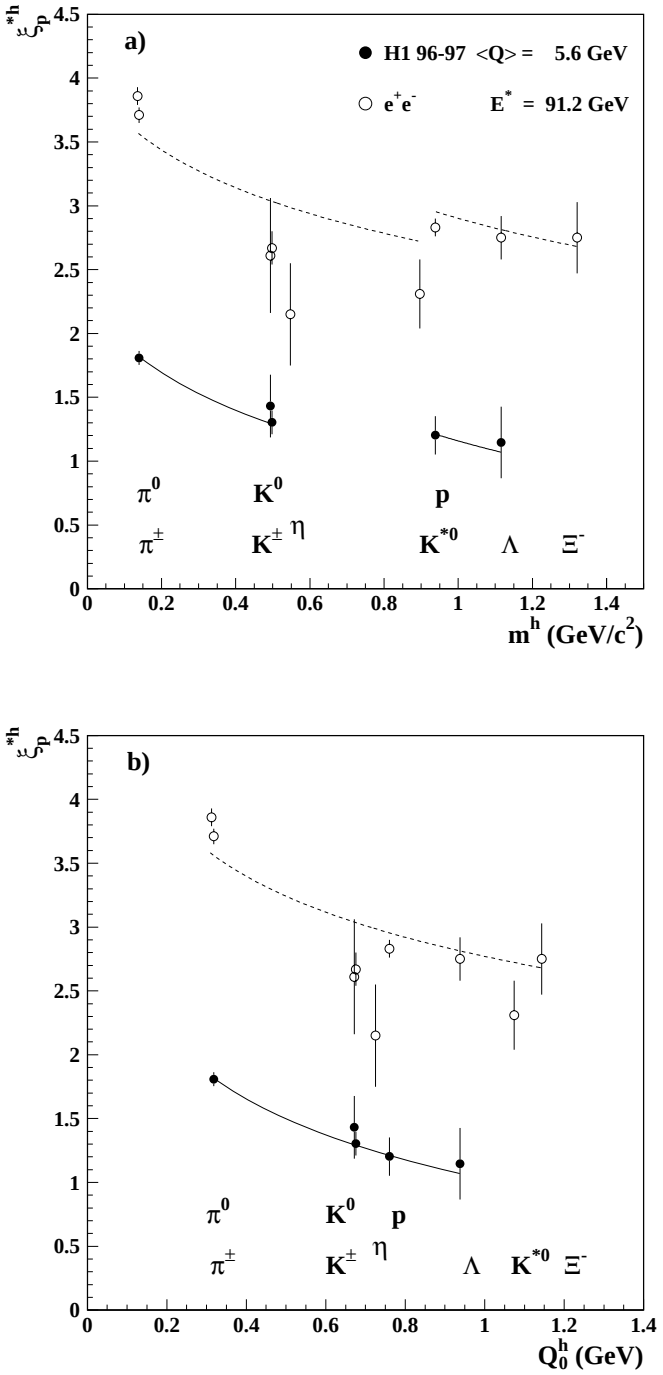


**Figure 8.10**: *Evolution of the peak position, $\xi_p^{*h}$, as a function of a) hadronic mass, $m^h$, and b) the parton shower cut-off parameter, $Q_0^h$. The solid line is a simultaneous fit to H1 data (closed circles) using a MLLA/LPHD calculation, together with equation 8.5, shown for $< Q >= 5.6$ GeV. The dashed line is the MLLA/LPHD prediction at $E^* = 91.2$ GeV using parameters from fitting H1 data.*

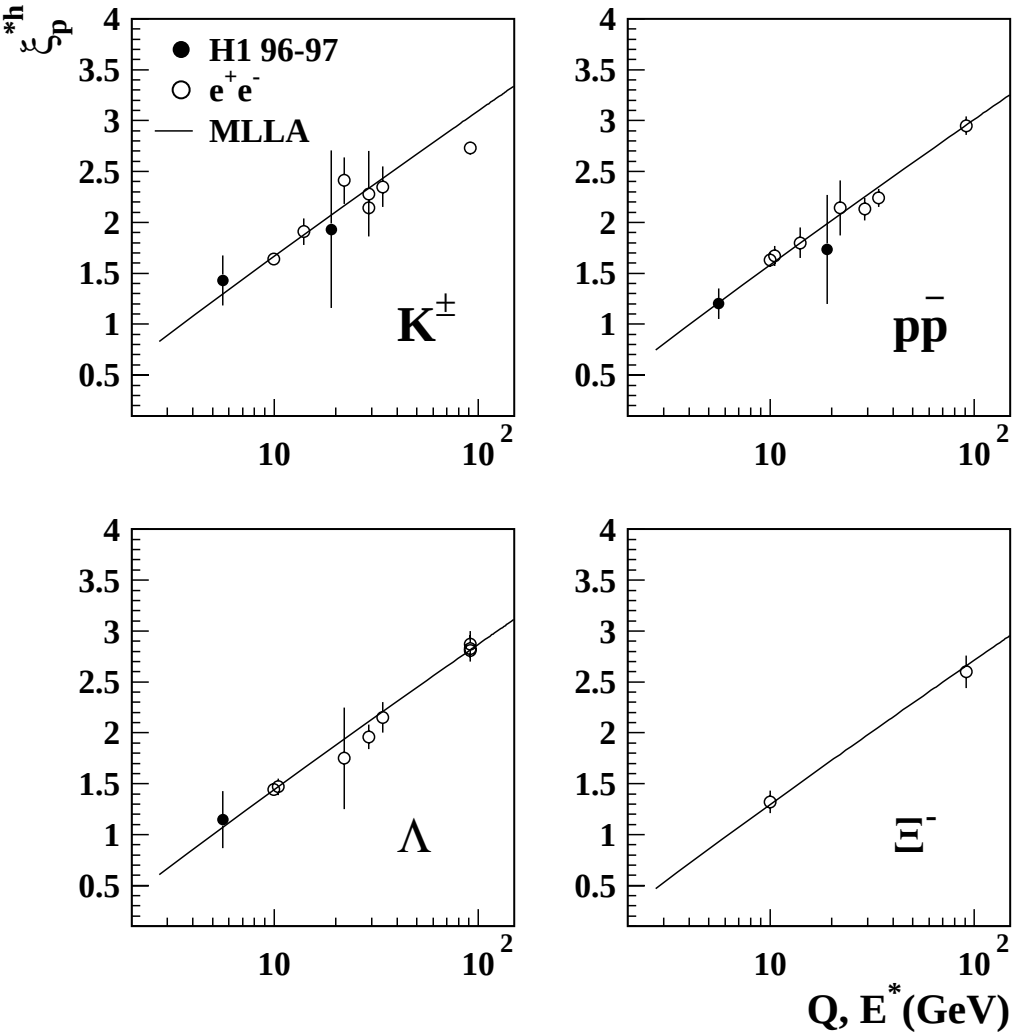


**Figure 8.11**: *Energy evolution of the peak position, $\xi_p^{*h}$, for a) $K^{\pm}$, b) protons, c) $\Lambda$, and d) $\Xi^-$ shown for H1 data (closed circles) and a selection of $e^+e^-$ data taken from [84]. The solid line is a MLLA/LPHD prediction for the evolution using parameters calculated from fitting H1 data, together with equation 8.5.*

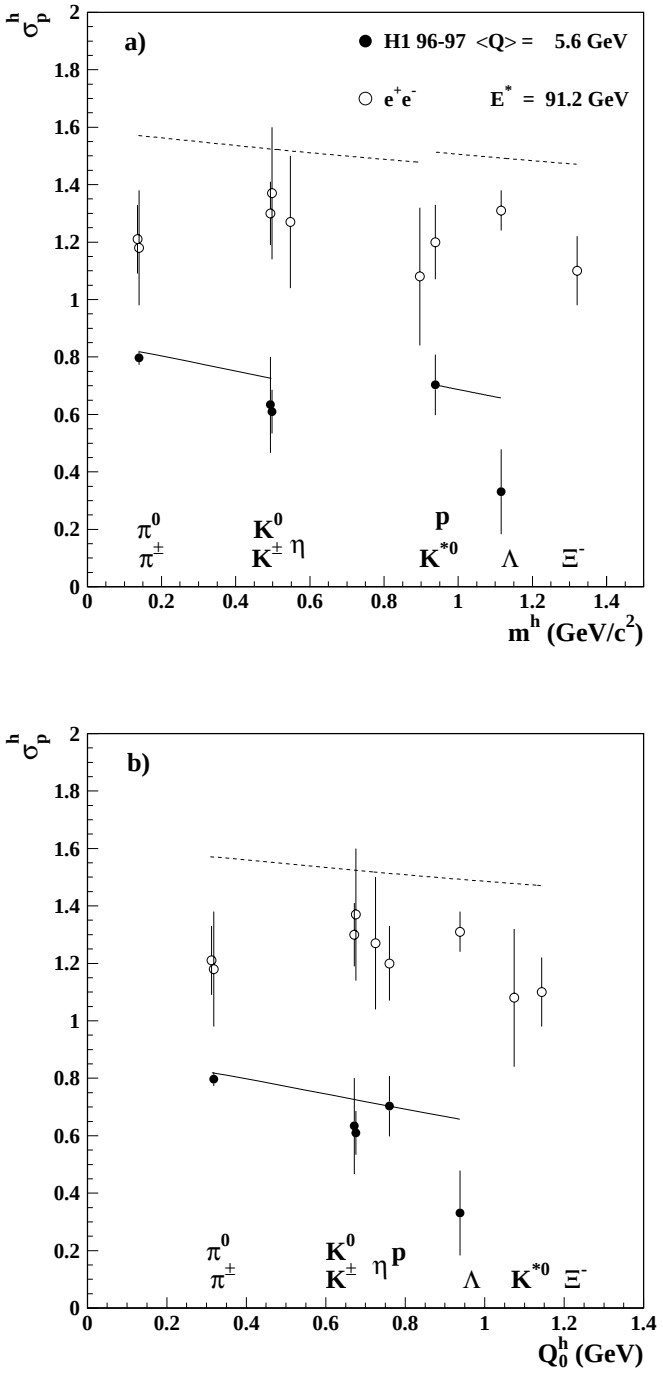


**Figure 8.12**: *Evolution of the width, $\sigma_p^h$, as a function of a) hadronic mass, $m^h$, and b) the parton shower cut-off parameter, $Q_0^h$. The solid line is a simultaneous fit to H1 data (closed circles) using a MLLA/LPHD calculation and equation 8.5, shown for $< Q >= 5.6$ GeV. The dashed line is the MLLA/LPHD prediction at $E^* = 91.2$ GeV using parameters calculated from fitting H1 data.*

| Particle | Model | Gradient | Intercept | $\chi^2/ndf$ |
|---|---|---|---|---|
| $\pi^{\pm}$ | MEAR | 0.686±0.002 | 0.62±0.01 | 7.0 |
| $\pi^{\pm}$ | MEPS | 0.693±0.002 | 0.64±0.01 | 8.3 |
| $K^0_S$ | MEAR | 0.42±0.01 | 0.63±0.02 | 17.5 |
| $K^0_S$ | MEPS | 0.52±0.01 | 0.53±0.02 | 1.3 |

**Table 8.10**: *Result of separate straight line fits to fragmentation function peak positions for $\pi^{\pm}$ and $K^0_S$ in generated MEAR and MEPS Monte Carlo.*

An application of a simple linear parameterisation of the energy evolution of $\xi_p^{*h}$ show the Monte Carlo models to follow the observed trends in data, but having higher statistics suggest an increased sensitivity to higher order terms necessary for its full description, as indicated by the large $\chi^2/ndf$ seen in Table 8.10.

Using MEAR Monte Carlo, a fit to the MLLA/LPHD formalism gives parameter values ($\Lambda_{eff} = 0.066 \pm 0.001$ GeV and $C = 0.175 \pm 0.001$ GeV) which are in very good agreement with those determined from data, but with an unacceptably high $\chi^2/ndf$ of 63. In comparison, MEPS Monte Carlo also produces a very high $\chi^2/ndf$ of 47, and the corresponding value of $\Lambda_{eff}$ ($\Lambda_{eff} = 0.090 \pm 0.001$ GeV) is significantly higher than that calculated using MEAR, but parameter $C$ ($C = 0.172 \pm 0.001$ GeV) is in very close agreement. Results are summarised in Table 8.11.

The high $\chi^2/ndf$ quoted above probably have their origin in Gaussian distortions. By narrowing the region over which the Gaussian function is applied to extract $\xi_p^{*h}$ and $\sigma_p^h$, a significant improvement in the fit quality can be achieved. However, the MEAR model favours a mass dependent gradient for the peak evolution, which is in disagreement with the MLLA/LPHD prediction of a universal gradient fixed by the parameter $\Lambda_{eff}$, and therefore suggests that with increased statistics the data may be sensitive to a breakdown of the MLLA/LPHD expectation.

| Model | Number of active flavours | | |
|---|---|---|---|
| | 3 | 4 | 5 |
| **MEAR** | | | |
| $\Lambda_{eff}$(GeV) | 0.074±0.001 | 0.066±0.001 | 0.052±0.001 |
| $C$ (GeV) | 0.170±0.001 | 0.175±0.001 | 0.182±0.001 |
| $\chi^2/ndf$ | 65 | 63 | 62 |
| **MEPS** | | | |
| $\Lambda_{eff}$(GeV) | 0.099±0.002 | 0.090±0.001 | 0.080±0.001 |
| $C$ (GeV) | 0.166±0.001 | 0.172±0.001 | 0.177±0.001 |
| $\chi^2/ndf$ | 51 | 47 | 44 |

**Table 8.11**: *Results of a simultaneous fit to the peak position, $\xi_p^{*h}$, and width, $\sigma_p^h$, using the MLLA/LPHD calculation defined in equations 8.3 and 8.4, together with equation 8.5, assuming three colours and three or more active quark flavours.*

## 8.6 Summary

This Chapter presented corrected exclusive fragmentation functions, $D^h(\xi_p)$, measured in the current hemisphere of the Breit frame for $\pi^{\pm}$, $K^{\pm}$, $K^0_S$, $p/\overline{p}$, and $\Lambda$ hadrons identified in merged 1996 and 1997 H1 data. A peak position, $\xi_p^{*h}$, and width, $\sigma_p^h$, are defined by fitting a simple Gaussian function in the turn-over region of $D^h(\xi_p)$. The sensitivity of $\xi_p^{*h}$ and $\sigma_p^h$ to a number of sources of systematic error has been investigated, with a dominant contribution attributed to the model dependence of the correction factors and the fitting interval, respectively.

Due to very large bin-by-bin correction factors, the $\xi_p^{*h}$ and $\sigma_p^h$ values measured from $K^{\pm}$ and $p/\overline{p}$ fragmentation functions are displayed only, and not included in any fitting.

The mass and energy evolution of $\xi_p^{*h}$ and $\sigma_p^h$ are successfully described within the MLLA/LPHD framework. A comparison made to exclusive $e^+e^-$ fragmentation data shows the evolution of $ep$ $\xi_p^{*h}$ and $\sigma_p^h$ values as a function of energy, hadronic mass, and $Q_0^h$ to follow that of $e^+e^-$ experiments, providing further evidence for

the universality of quark fragmentation. However, the MLLA/LPHD calculations are unable to describe the data fully, particularly the $e^+e^-$ $\sigma_p^h$ evolution with mass and $Q_0^h$ at fixed energy, and furthermore, the Monte Carlo models of the hadronic final state in DIS are incompatible with the detailed parameterisation of MLLA/LPHD.

# Chapter 9

# Conclusions

This thesis has studied the fragmentation properties of identified hadrons produced in $ep$ deep inelastic scattering (DIS), and compared results with those of $e^+e^-$ annihilation experiments.

By measuring the specific ionisation energy loss, $\mathrm{d}E/\mathrm{d}x$, of charged particles and calculating the invariant mass spectra of neutral secondary particles, it has been possible to identify samples of $\pi^{\pm}$, $K^{\pm}$, protons and antiprotons ($p/\overline{p}$), $K^0_S$, and $\Lambda$ hadrons. Exclusive current hemisphere fragmentation functions, $D^h(\xi_p)$, have been measured, but in determining $D^{K^{\pm}}(\xi_p)$ and $D^{p\overline{p}}(\xi_p)$ it has been necessary to apply very large correction factors in the fragmentation function turn-over region. This results from the restriction of unambiguous $K^{\pm}$ and $p/\overline{p}$ identification to a very narrow, low laboratory momentum interval. For this reason, the fragmentation properties of $K^{\pm}$ and $p/\overline{p}$ hadrons have been displayed only, and not included in any subsequent fitting for relevant parameterisations.

The exclusive fragmentation function properties have been summarised in terms of the peak position and width evolution as a function of hadronic mass, four-momentum transfer, $Q$, and parton cascade cut-off parameter, $Q^h_0$. The $ep$ data has been shown to follow closely that of $e^+e^-$ experiments, where the equivalent energy scale has been taken to be the centre-of-mass energy, $E^*$. This supports past observations that peak and width measurements, in contrast to average

charged particle multiplicities, are insensitive to leading order processes present in $ep$ collisions but absent in $e^+e^-$ annihilations, and are instead dependent upon hadronisation properties only.

The data is in agreement with the MLLA/LPHD expectation of a decreasing peak position and compatible with a narrowing width, as the mass increases. The $e^+e^-$ data on peak positions strongly suggests a different mass evolution for mesons and baryons, although the $ep$ results have less discriminating power and could also follow a universal evolution.

The data has been fitted simultaneously to a MLLA/LPHD expression describing the peak and width evolution with $Q/E^*$ and $Q_0^h$. The data is in agreement with the prediction of an effective QCD scale, $\Lambda_{eff}$, universal for all hadronic species. The data supports an empirically motivated relationship whereby the hadronic mass can be simply related to $Q_0^h$ by the addition (subtraction) of a constant, $C$, for mesons (baryons). Assuming four active quark flavours and three QCD colours, the fit to H1 data yields parameter values $\Lambda_{eff} = 0.060 \pm 0.008$ GeV and $C = 0.178 \pm 0.009$ GeV. However, with the $ep$-derived fit parameters substituted, the MLLA/LPHD calculation is unable to describe fully the $e^+e^-$-derived $\pi^\pm$ peak position evolution with energy, and the hadronic width evolution with mass and $Q_0^h$.

The fragmentation properties of identified hadrons produced from a struck quark scattering into the current hemisphere of the Breit frame in $ep$ DIS are found to be similar to those of hadrons formed via $e^+e^- \to q\overline{q}$ annihilations, thus providing further evidence for the universality of quark fragmentation.

# Appendix A

# Comparison of Data Samples

## A.1 Summary

Shown in Figures A.1 to A.17 is a comparison between 1996 and 1997 low and high $Q^2$ data samples for a selection of event variables, primary charged track and $V^0$ quality variables, and corrected identified hadron fragmentation functions.

For the Figures presented there is very good agreement between 1996 and 1997 data samples at both low and high $Q^2$, although at low $Q^2$ there is a small shift in the 1997 $z$-vertex distribution relative to that of 1996, and there are some differences in the $N_{\mathrm{d}E/\mathrm{d}x}$ distribution shape, particularly for $\pi^+$ and $\pi^-$ candidates.

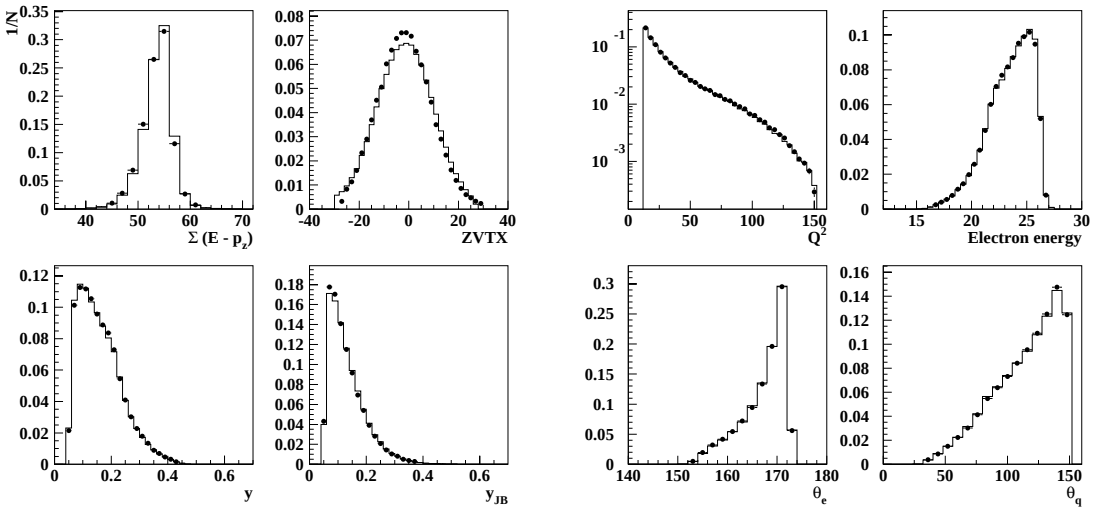


**Figure A.1**: *Event variables $\Sigma(E-p_z)$, event vertex z coordinate (ZVTX), $Q^2$, scattered electron energy and $\theta_e$, y calculated using two methods, and $\theta_q$, after event selection criteria have been applied, for 1996 (closed circles) and 1997 histograms) low $Q^2$ data.*

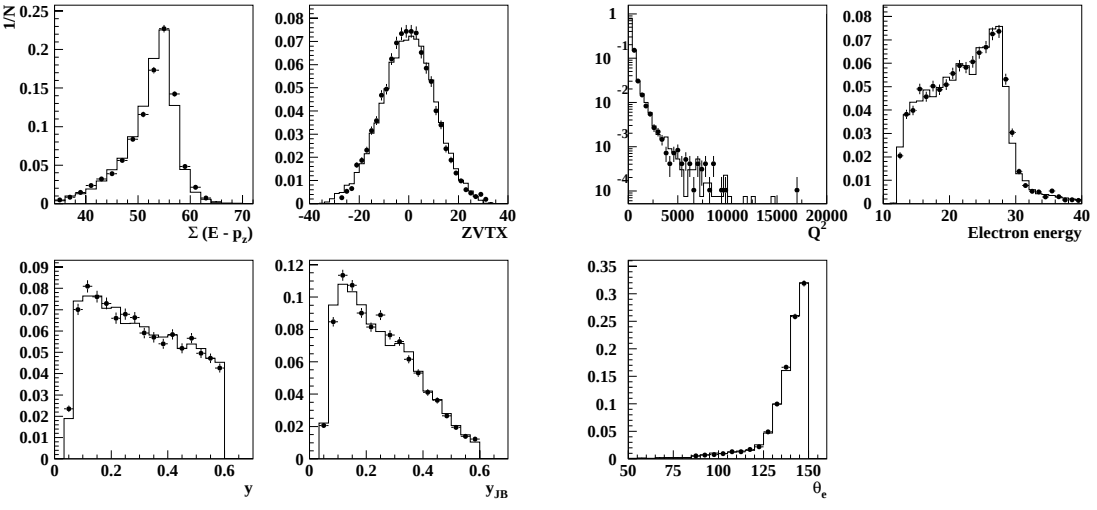


**Figure A.2**: *Event variables $\Sigma(E-p_z)$, event vertex z coordinate (ZVTX), $Q^2$, scattered electron energy and $\theta_e$, and y calculated using two methods, after event selection criteria have been applied, for 1996 (closed circles) and 1997 (histograms) high $Q^2$ data.*

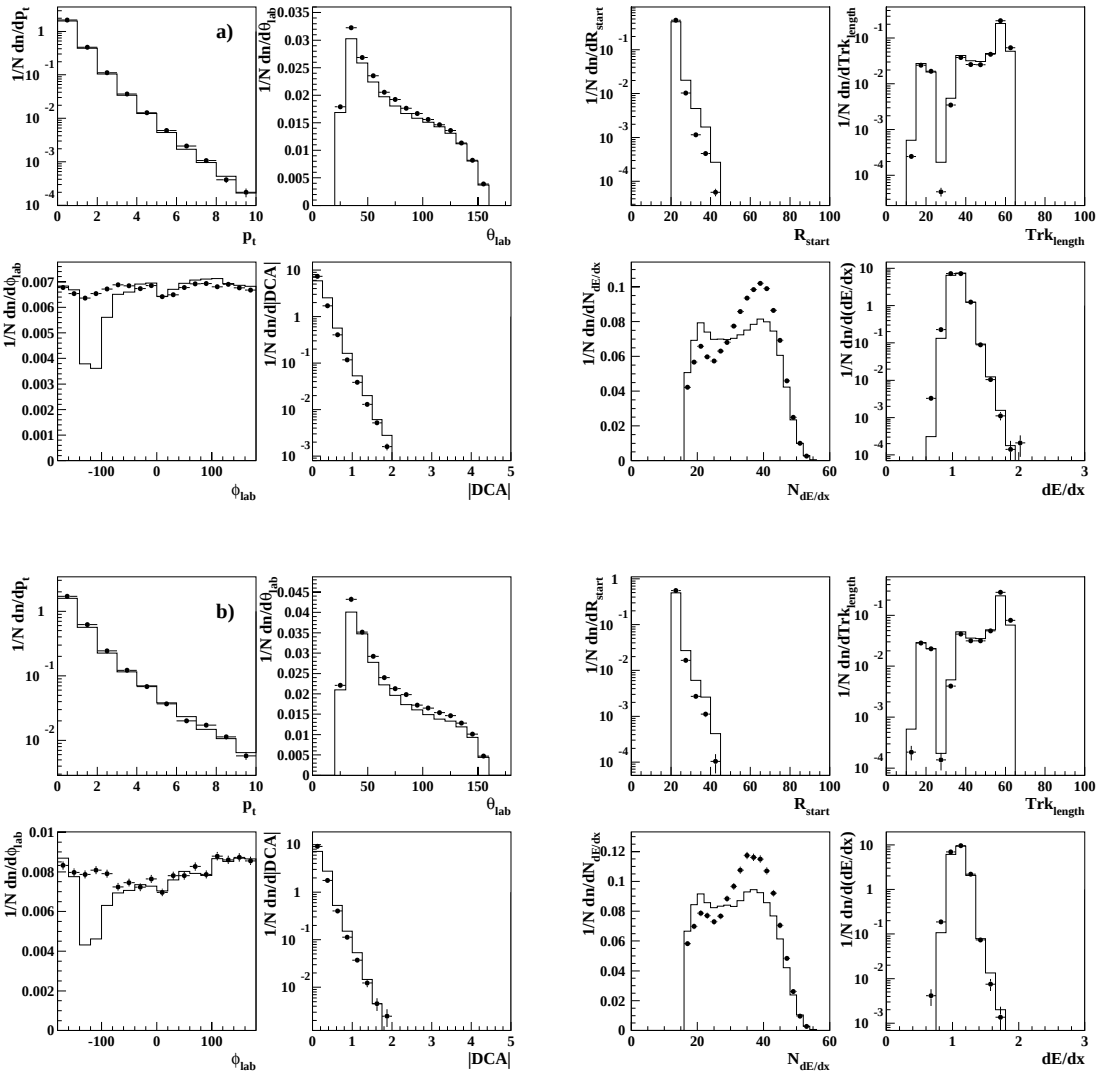


**Figure A.3**: *Selection of track quality variables shown for 1996 (closed circles) and 1997 (histogram) a) low $Q^2$ and b) high $Q^2$ data, for $\pi^+$ candidates identified using dE/dx information.*

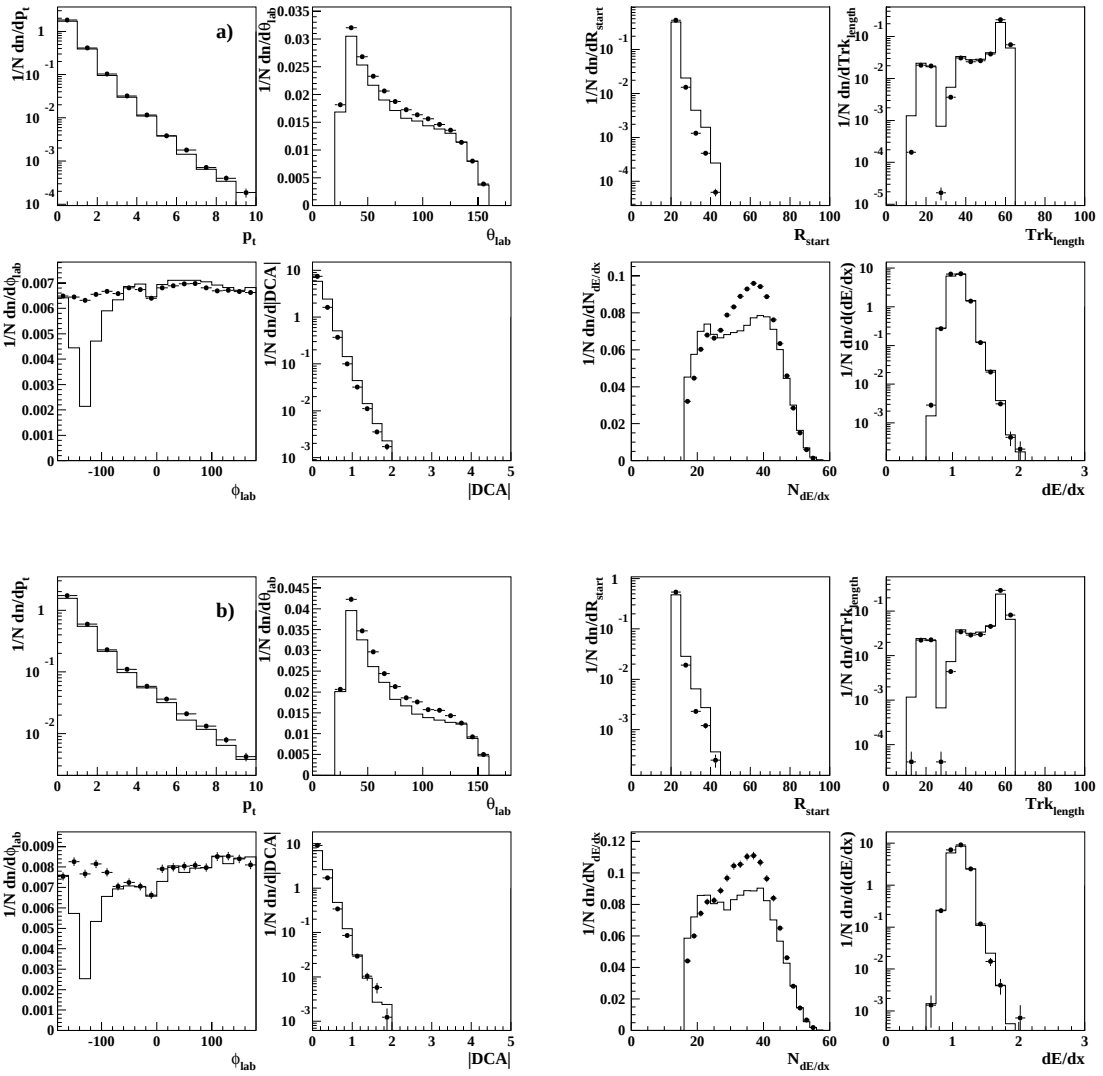


**Figure A.4**: *Selection of track quality variables shown for 1996 (closed circles) and 1997 (histogram) a) low $Q^2$ and b) high $Q^2$ data, for $\pi^-$ candidates identified using dE/dx information.*

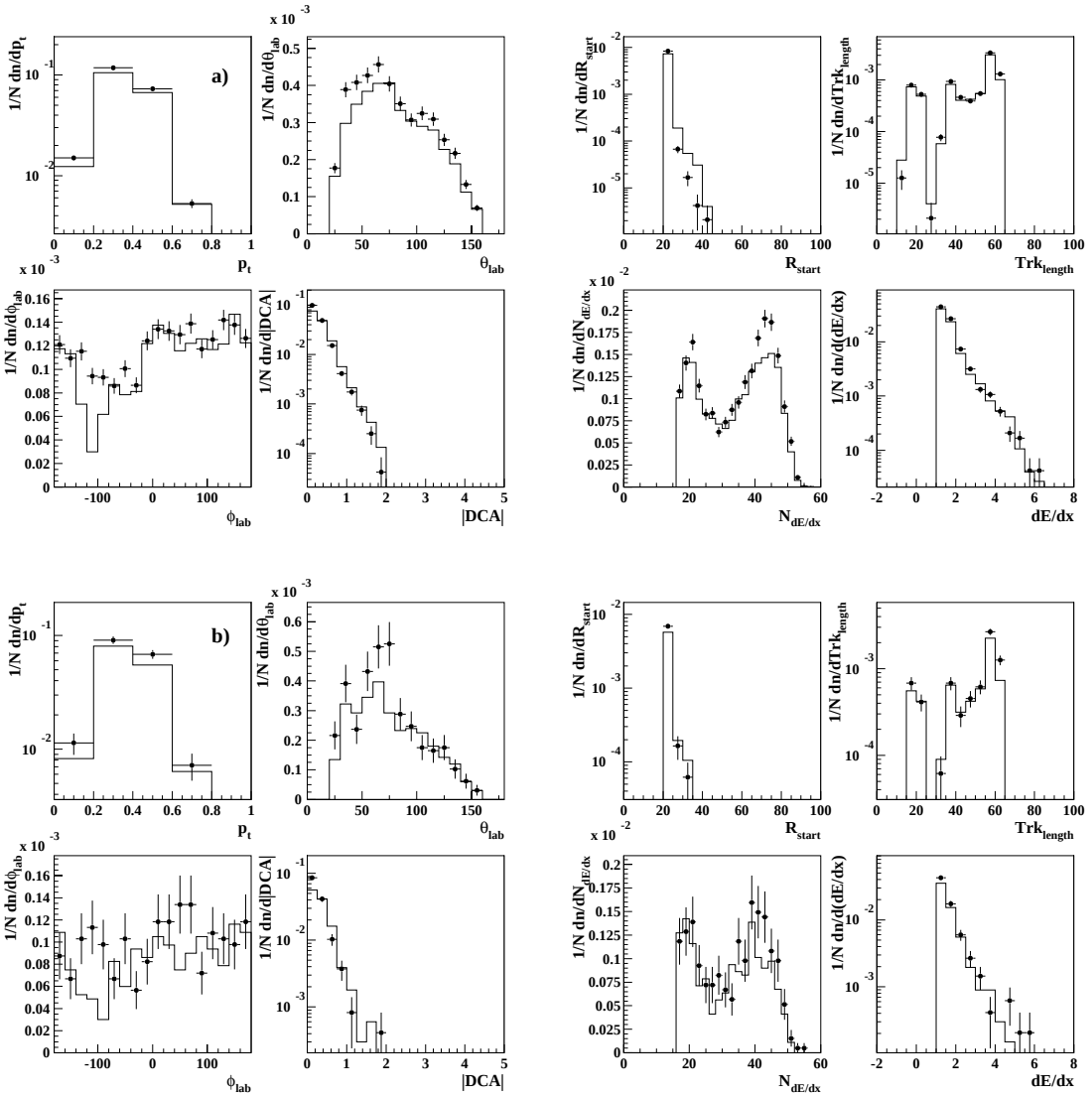


**Figure A.5**: *Selection of track quality variables shown for 1996 (closed circles) and 1997 (histogram) a) low $Q^2$ and b) high $Q^2$ data, for $K^+$ candidates identified using dE/dx information.*

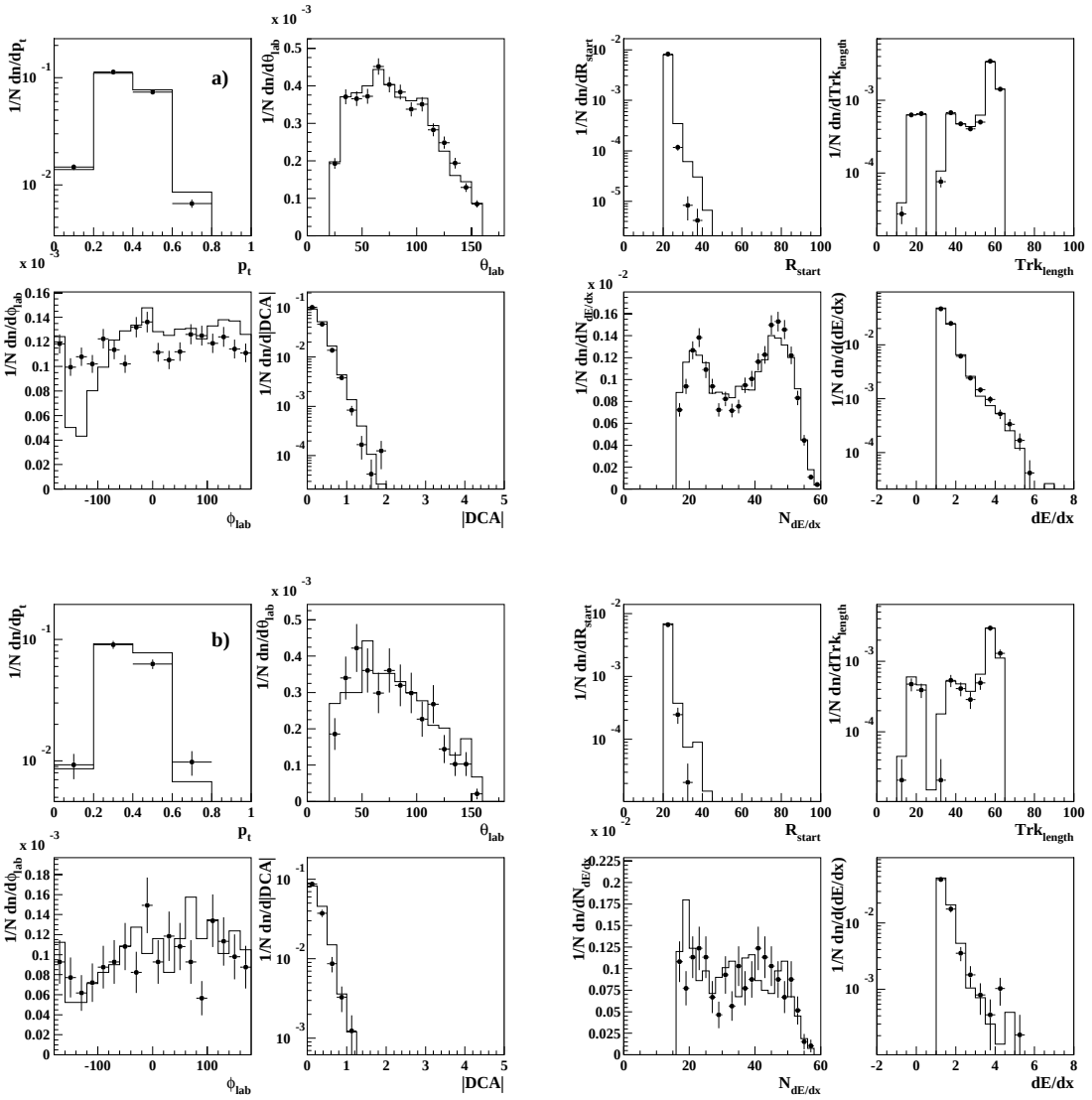


**Figure A.6**: *Selection of track quality variables shown for 1996 (closed circles) and 1997 (histogram) a) low $Q^2$ and b) high $Q^2$ data, for $K^-$ candidates identified using dE/dx information.*

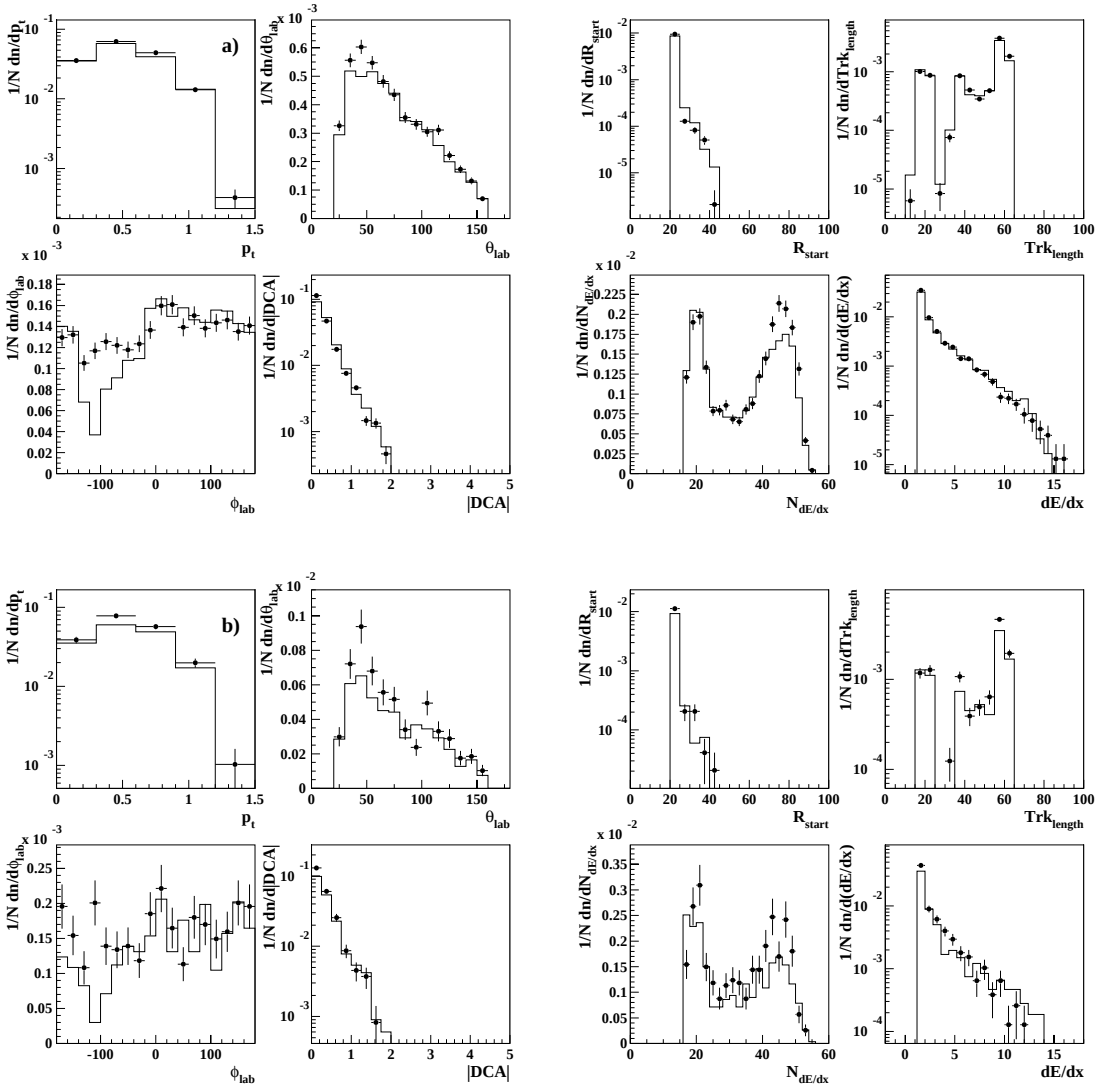


**Figure A.7**: *Selection of track quality variables shown for 1996 (closed circles) and 1997 (histogram) a) low $Q^2$ and b) high $Q^2$ data, for proton candidates identified using dE/dx information.*

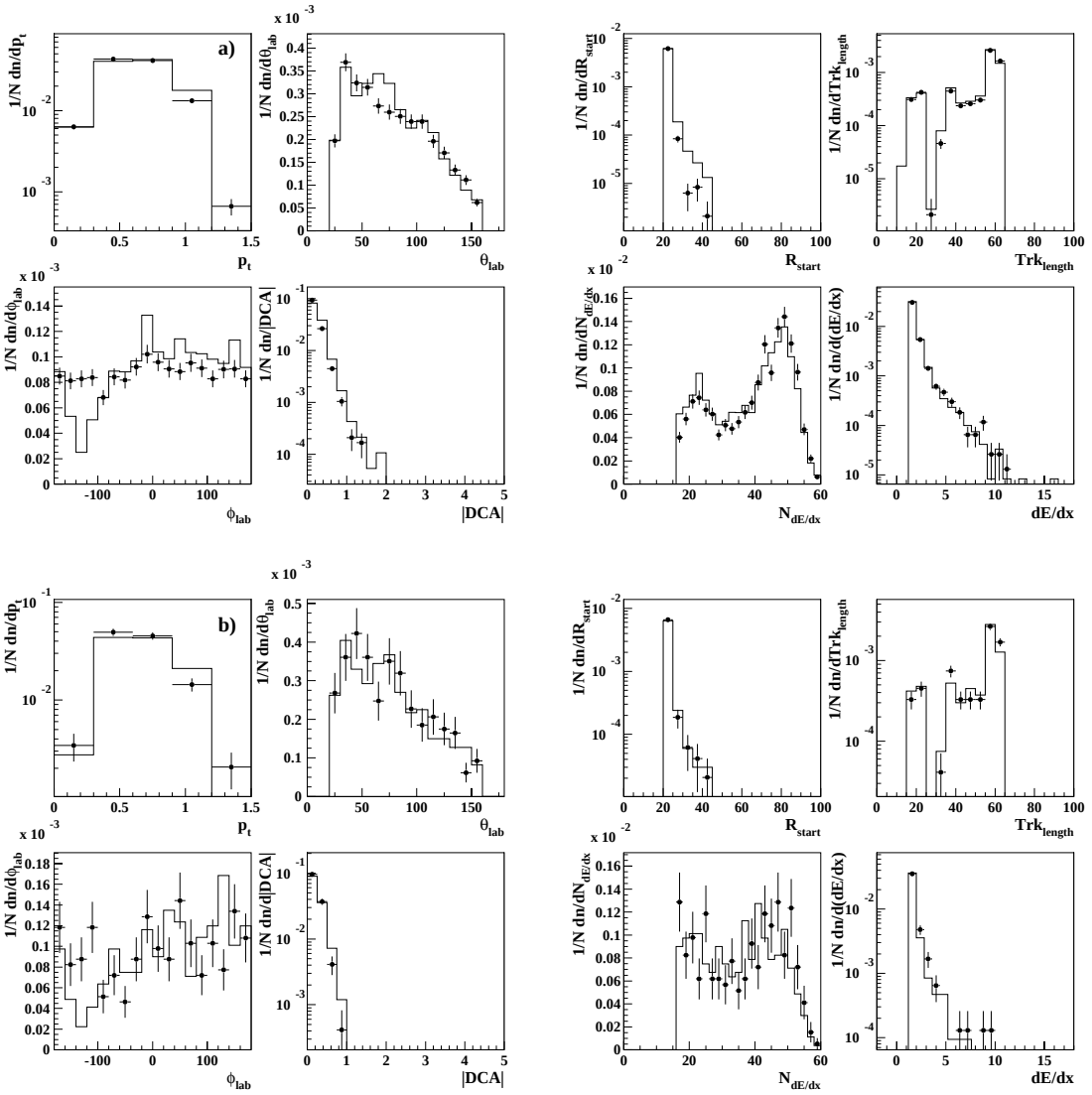


**Figure A.8**: *Selection of track quality variables shown for 1996 (closed circles) and 1997 (histogram) a) low $Q^2$ and b) high $Q^2$ data, for antiproton candidates identified using dE/dx information.*

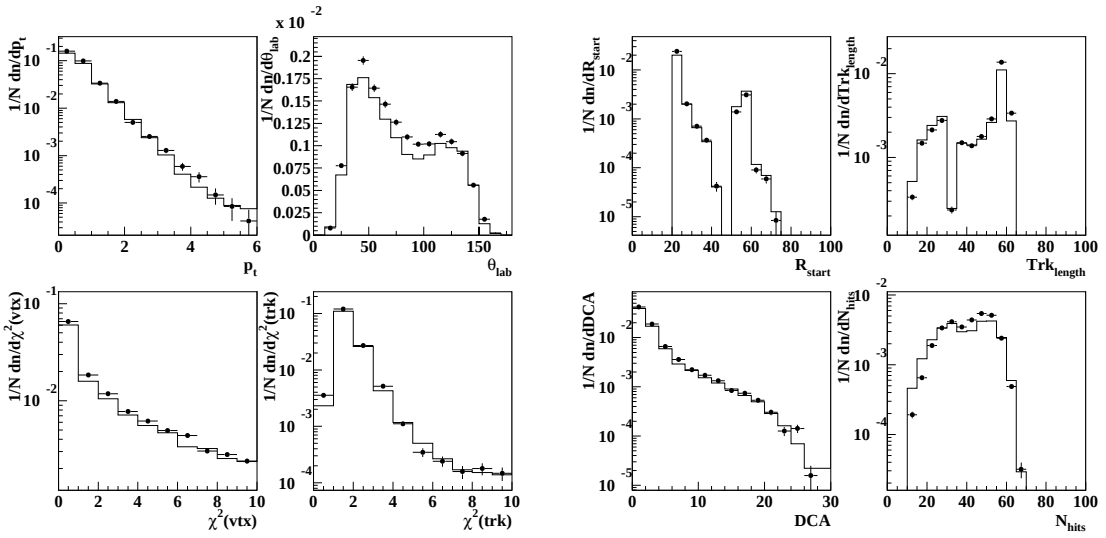


**Figure A.9**: *Selection of $V^0$ candidate daughter track quality variables for 1996 (closed circles) and 1997 (histogram) low $Q^2$ data.*

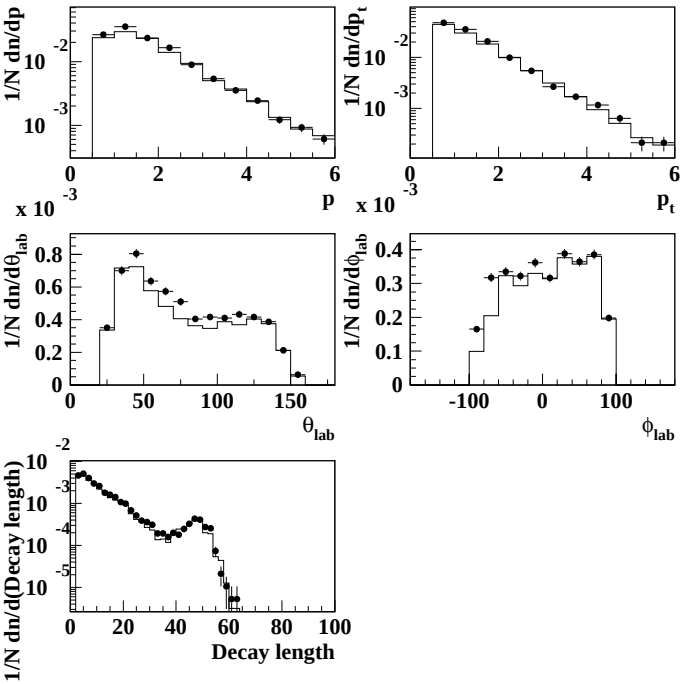


**Figure A.10**: *Selection of $V^0$ quality variables for 1996 (closed circles) and 1997 (histogram) low $Q^2$ data.*

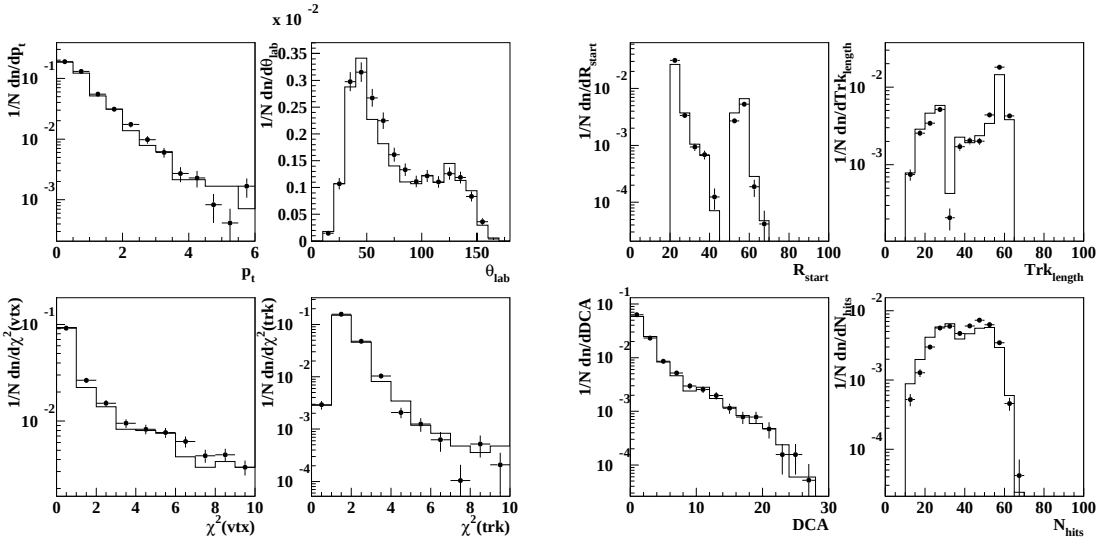


**Figure A.11**: *Selection of $V^0$ candidate daughter track quality variables for 1996 (closed circles) and 1997 (histogram) high $Q^2$ data.*

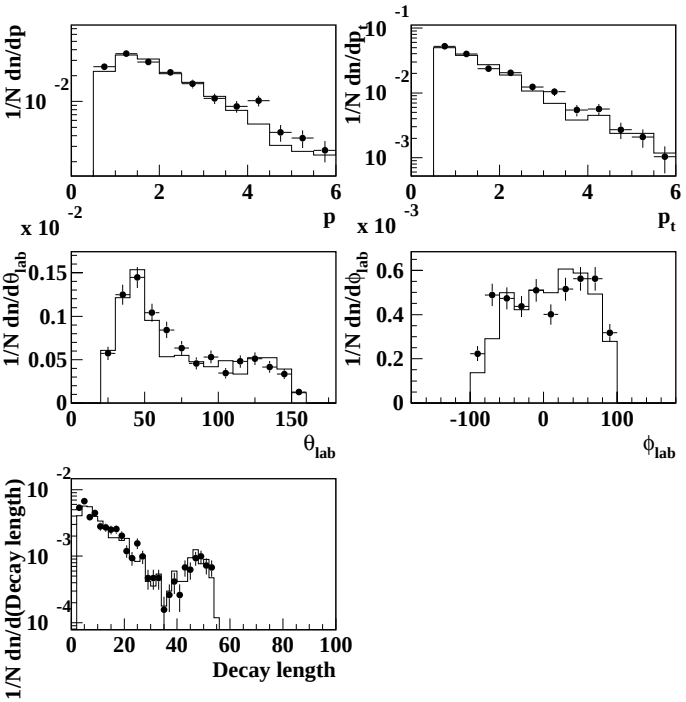


**Figure A.12**: *Selection of $V^0$ quality variables for 1996 (closed circles) and 1997 (histogram) high $Q^2$ data.*

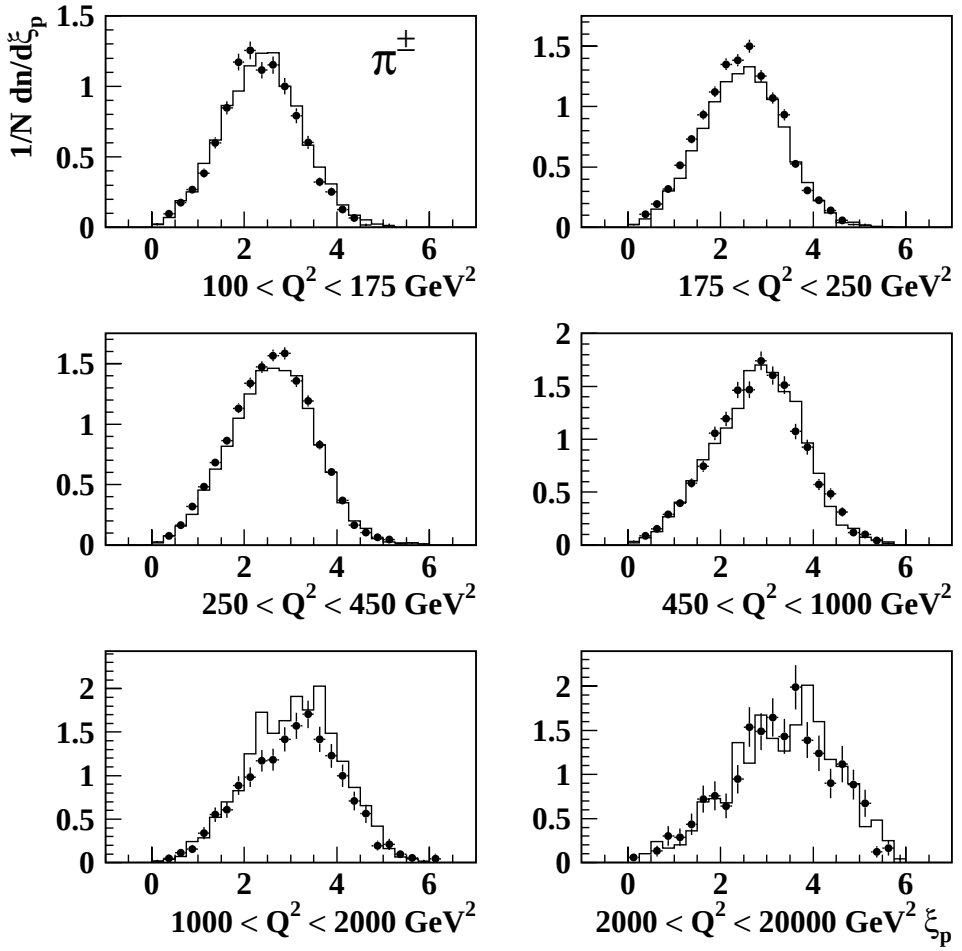


**Figure A.13**: *Corrected event normalised scaled momentum distributions of $\pi^{\pm}$ selected using dE/dx information, for low $Q^2$ 1996 (closed circles) and 1997 (histogram) data, subdivided into 7 $Q^2$ intervals.*

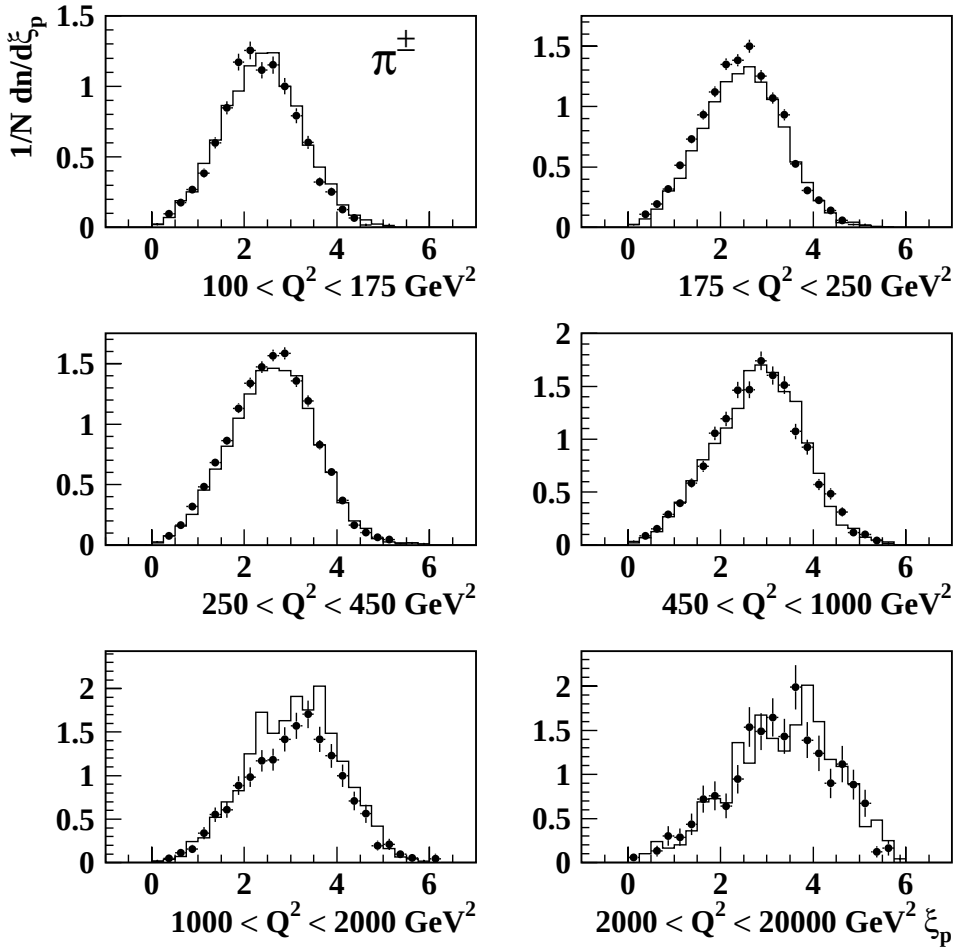


**Figure A.14**: *Corrected event normalised scaled momentum distributions of $\pi^{\pm}$ selected using dE/dx information, for high $Q^2$ 1996 (closed circles) and 1997 (histogram) data, subdivided into 6 $Q^2$ intervals.*

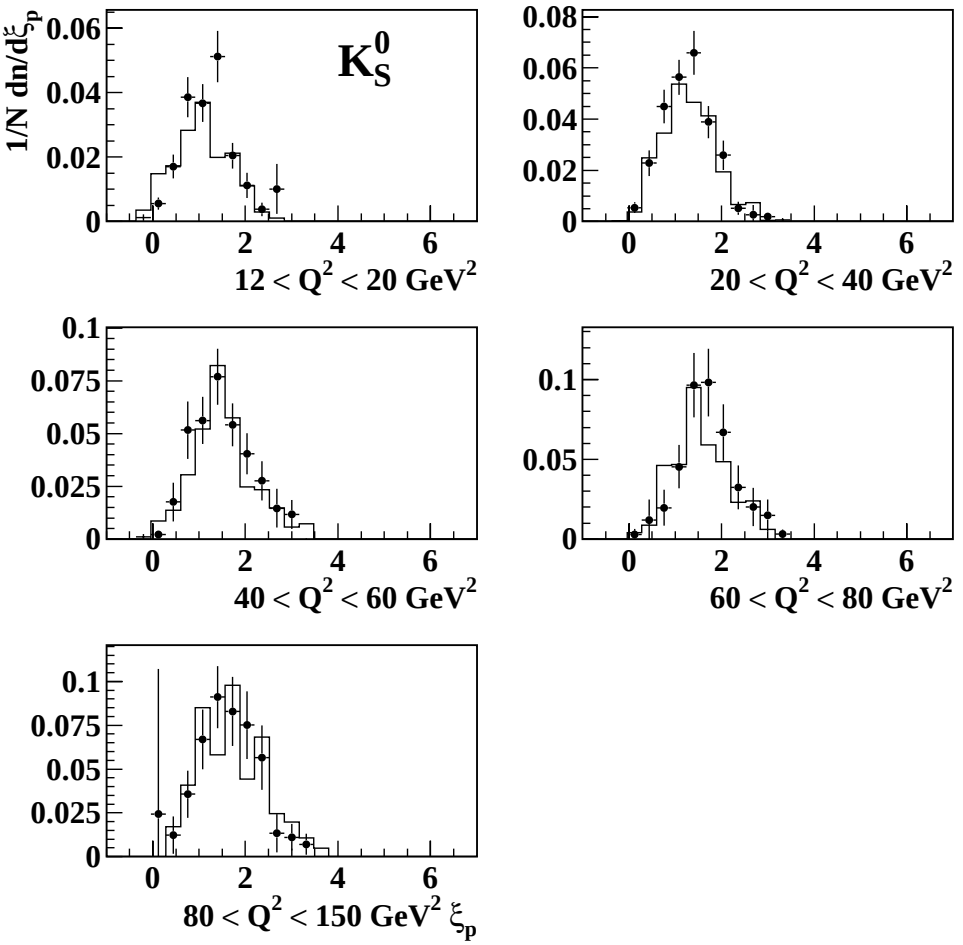


**Figure A.15**: *Corrected event normalised scaled momentum distributions of $K^0_S$ candidates, for low $Q^2$ 1996 (closed circles) and 1997 (histogram) data, subdivided into 5 $Q^2$ intervals.*

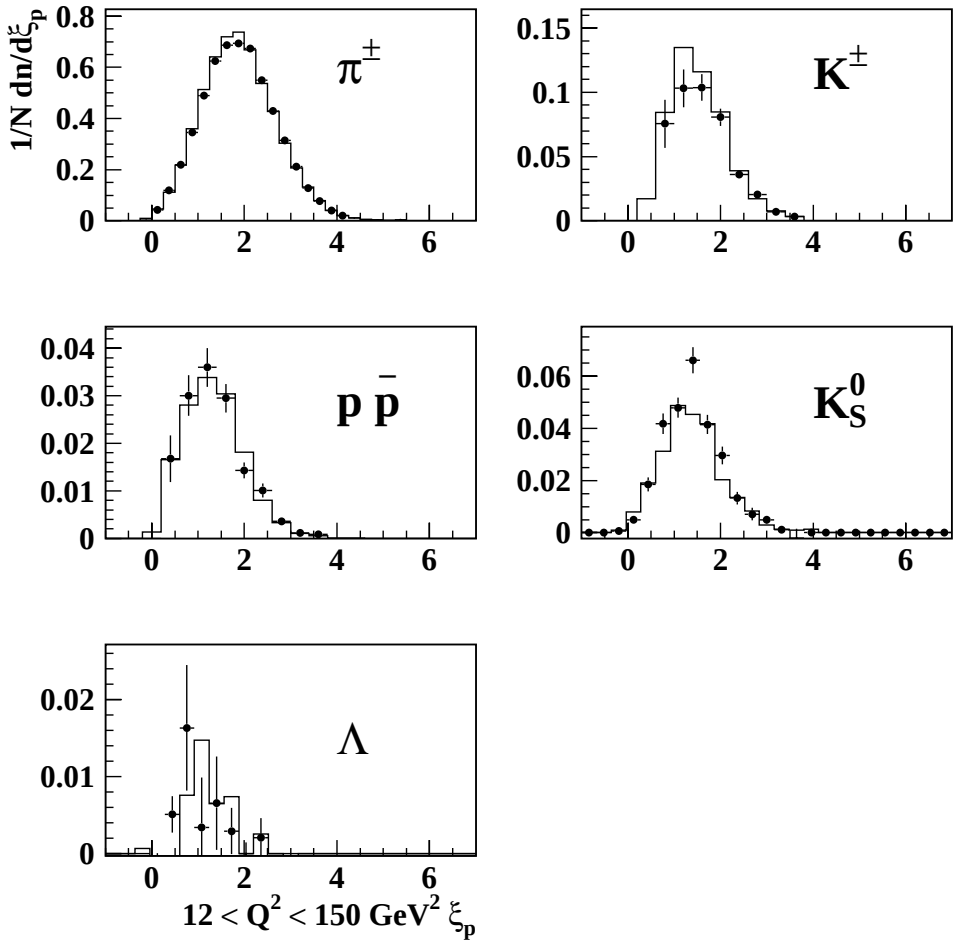


**Figure A.16**: *Corrected event normalised scaled momentum distributions of $\pi^{\pm}$, $K^{\pm}$, protons/antiprotons ($p\bar{p}$), $K^0_S$, and $\Lambda$, for low $Q^2$ 1996 (closed circles) and 1997 (histogram) data.*

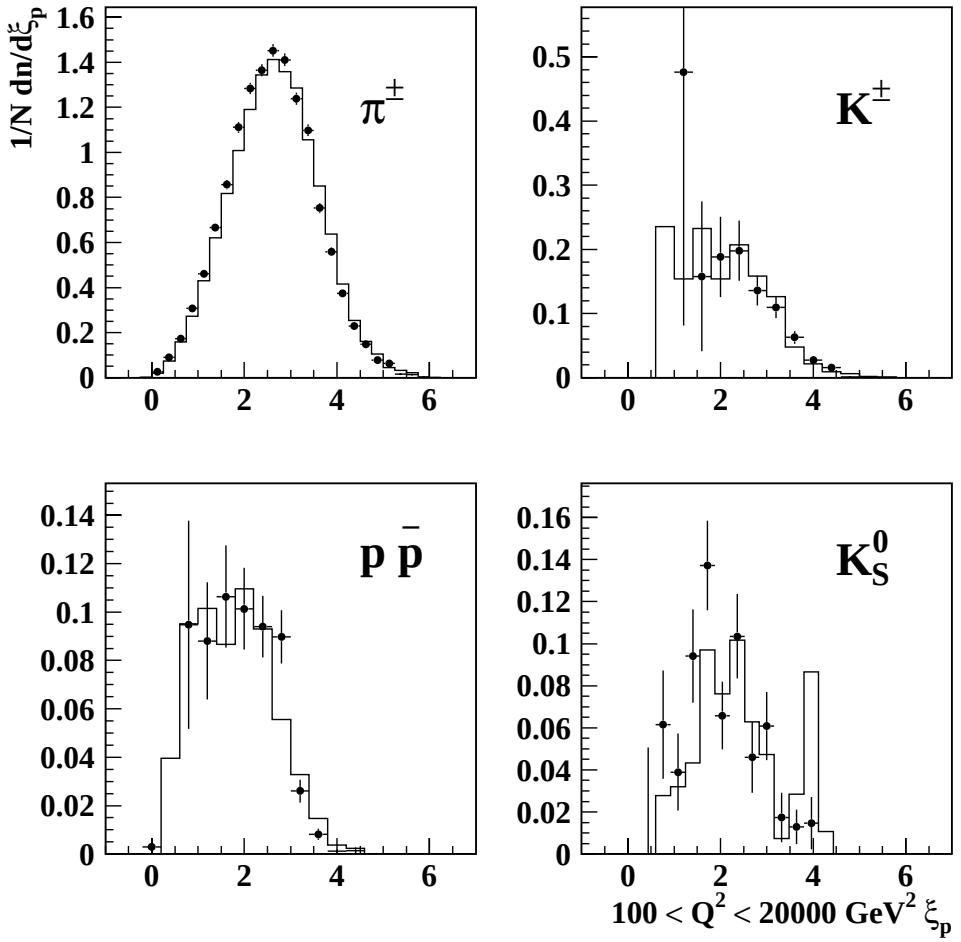


**Figure A.17**: *Corrected event normalised scaled momentum distributions of $\pi^{\pm}$, $K^{\pm}$, protons/antiprotons ($p\bar{p}$), and $K^0_S$, for high $Q^2$ 1996 (closed circles) and 1997 (histogram) data.*

# Bibliography


[1] G. Wolf (1994) DESY 94-022

[2] H1 Collaboration, Technical Proposal for the H1 Detector (1986); H1 Collaboration, I. Abt et al., Nucl. Instr. and Meth. **A386** (1997) 310, 348.

[3] ZEUS Collaboration, The Zeus Detector, Technical Proposal (1986).

[4] HERMES Collaboration, A proposal to measure the spin-dependent structure functions of the neutron and proton at HERA (1990).

[5] W. Hoffman, An Experiment to Study CP Violation in the $B$ System Using an Internal Target at the HERA Proton Ring, DESY-PRC 94/02 (1994).

[6] H. Bethe and W. Heitler, Proc. Roy. Soc. **A146** (1934) 83.

[7] Status of the BDC Analysis (and a proposal for future data treatment), H1 internal note, H1-08/98-550.

[8] H1 Collaboration, Technical Proposal to build Silicon Tracking Detectors for H1, DESY-PRC 92/01 (1992); W. Eick et al., Nucl. Instr. and Meth. **A386** (1997) 81.

[9] H1 Collaboration, C. Adloff et al., accepted by Eur. Phys. J. C (2000), DESY-00-181.

[10] H1 SPACAL Group, R.-D. Appuhn et al., Nucl. Instr. and Meth. **A386** (1997) 397.

[11] G. Bernadi et al., Guide to the Simulation Program H1SIM, H1 document.

[12] H. Albrecht et al., H1PHAN - H1 physics analysis program, H1 document (1991).

[13] S. Egli et al., Guide to the Simulation Program H1SIM, H1 document (1991).

[14] M.K. Gaillard, P.D. Grannis and F.J. Sciulli, Rev. Mod. Phys. vol. 71 No.2 (1999) S96.

[15] H1 Collaboration, T. Ahmed et al., Phys. Lett. **B299** (1993) 374.

[16] H1 Collaboration, C. Adloff et al., Eur. Phys. J. **C10** (1999) 363.

[17] M. Gell-Mann and F. Zachariasen, Phys. Rev. 124 (1961) 953; T.H. Bauer, R.D. Spital, D.R. Yennie, and F.M. Pipkin, Rev. Mod. Phys. 50 (1978), 261 (1978).

[18] P. Bate, *High Transverse Momentum 2-Jet and 3-Jet Cross Section Measurements in Photoproduction*, Ph.D. thesis, University of Manchester (1999).

[19] H1 Collaboration, C. Adloff et al., Eur. Phys. J. **C19** (2001) 269.

[20] H1 Collaboration, C. Adloff et al., Eur. Phys. J. **C13** (2000) 609.

[21] Yu.L. Dokshitzer, Sov. Phys. JETP 46 (1977) 641; V.N. Gribov and L.N. Lipatov, Sov. J. Nucl. Phys. 15 (1972) 438 and 675; G. Altarelli and G. Parisi, Nucl. Phys. **B126** (1977) 298.

[22] E.A. Kuraev, L.N. Lipatov and V.S. Fadin, Sov. Phys. JETP 45 (1972) 199; Y.Y. Balitsky and L.N. Lipatov, Sov. J. Nucl. Phys. 28 (1978) 282.

[23] B. Heinemann, *Measurement of Charged Current and Neutral Current Cross Sections in Positron-Proton Collisions at* $\sqrt{s}$ *= 300 GeV*, Ph.D. thesis, University of Hamburg (1999).

[24] H1 Collaboration, C. Adloff et al., Nucl. Phys. **B497** (1997) 3.

[25] H1 Collaboration, C. Adloff et al., Nucl. Phys. **B485** (1997) 3.

[26] H1 Collaboration, C. Adloff et al., Eur. Phys. J. **C12** (2000) 595.

[27] H1 Collaboration, C. Adloff et al., Nucl. Phys. **B462** (1999) 440.

[28] H1 Collaboration, T. Ahmed et al., Nucl. Phys. **B435** (1995) 3; C. Adloff et al., Z. Phys. **C76** (1997) 613; P. Newman, *A Study of the Dynamics of Diffractive Photoproduction at HERA*, Ph.D. thesis, University of Birmingham (1996).

[29] D.P. Traynor, *Hadronic Fragmentation Studies in Diffractive Deep Inelastic Scattering at HERA*, Ph.D. thesis, University of London (2001).

[30] H1 Collaboration, C. Adloff et al., Z. Phys. **C74** (1997) 191; N. Malden, *W Production in ep Collisions at HERA*, Ph.D. thesis, University of Manchester (2000); C. Diaconu, talk presented at DIS 2001, Bologna, April 2001.

[31] H1 Collaboration, H1 internal note, H1-10/97-531.

[32] E.D. Bloom et al., Phys. Rev. Lett **23** (1969) 930; M. Breitenbach et al., Phys. Rev. Lett. **23** (1969) 935.

[33] R.P. Feynman, Phys. Rev. **179** (1969) 1415.

[34] M. Gell-Mann, Phys. Lett. **8** (1964) 214.

[35] D.H. Perkins, Introduction to High Energy Physics, Addison-Wesley publishing Co. (1987).

[36] H1 Collaboration, I. Abt et al., Phys. Lett. **B321** (1994) 161.

[37] H1 Collaboration, C. Adloff et al., Nucl. Phys. **B504** (1997) 3.

[38] A.H. Mueller, Nucl. Phys. **B213** (1983) 85; erratum quoted ibid., **B241** (1984) 141.

[39] Yu.L. Dokshitzer, V.A. Khoze, A.H. Mueller and S.I. Troyan, Basics of Perturbative QCD, Editions Frontières, Gif-sur-Yvette (1991).

[40] V.A. Khoze and W. Ochs, Int. J. Mod. Phys. **A12** (1997) 2949.

[41] TASSO Collaboration, W. Braunschweig et al., Z. Phys. **C47** 187; H1 Collaboration, S. Aid et al., Nucl. Phys. **B445** (1995) 3.

[42] OPAL Collaboration, M.Z. Akrawy et al., Phys. Lett. **B247** (1990) 617.

[43] Ya.I. Azimov, Yu.L. Dokshitzer, V.A. Khoze and S.I. Troyan, Z. Phys. **C27** (1985) 65 and **C31** (1986) 213.

[44] G. Gustafson, Phys. Lett. **B175** (1986) 453; B. Andersson, G. Gustafson, L. Lönnblad and Ulf Petterson, Z. Phys. **C43** (1989) 625.

[45] OPAL Collaboration, M.Z. Akrawy et al., Z. Phys. **C47** (1990) 505.

[46] B.R. Webber, Lectures at Summer School on Hadronic Aspects of Collider Physics, Zuoz, Switzerland, August 1995, hep-ph/9411384.

[47] R.P. Feynman and R.D. Field, Nucl. Phys. **B136** (1978) 1.

[48] T. Meyer, Z. Phys. **C12** (1982) 77.

[49] P. Hoyer, P. Osland, H.G. Sander, T.F. Walsh, P.M. Zerwas, Nucl. Phys. **B161** (1979) 349; P. Biddulph and G. Thompson, Comp. Phys. Comm. 67 (1989) 13.

[50] B. Andersson et al., Phys. Rep. 97 (1983) 31.

[51] B.R. Webber, Nucl. Phys. **B238** (1984) 492.

[52] G. Ingleman, A. Edin, J. Rathsman, LEPTO 6.5 - A Monte Carlo Generator for Deep Inelastic Scattering, DESY 96-057 (1996).

[53] L. Lönnblad, Comp. Phys. Comm. 71 (1992) 15.

[54] M. Bengtsson and T. Sjöstrand, Z. Phys. **C37** (1988) 465.

[55] T. Sjöstrand, Comp. Phys. Comm. 82 (1994) 74.

[56] M. Seymour, Comp. Phys. Comm. 677 (1992) 465; G. Marchesini et al., Comp. Phys. Comm. 71 (1993) 465.

[57] D. Kant, private communication.

[58] N. Sahlmann, H1 internal note, H1-04/93-281; L. West, How to use the Heavy Flavour Working Group track, muon, and electron selection code H1PHAN VERSION $\geq$ 3.00/0.1, H1 document (2000).

[59] D. Kant and G. Thompson, H1 internal note, H1-00/12-589.

[60] G. Ingelman, Deep Inelastic Physics at HERA, DESY 87-144 (1987).

[61] D.P. Traynor, private communication.

[62] J. Steinhart, *Die Messung des totalen $c\overline{c}$-Photoproduktions-Wirkungsquerschnittes durch die Rekonstruktion von $\Lambda_c$-Baryonen unter Verwendung der verbesserten dE/dx-Teilchen-identifikation am H1 Experiment bei HERA*, Ph.D. thesis, University of Hamburg (1999).

[63] G. R. White, *Tests of Perturbative and Non-Perturbative QCD from Identified Proton, Kaon and Pion Studies in Deep Inelastic Scattering ep Interactions at HERA*, Ph.D. thesis, University of Lancaster (2000).

[64] The Particle Data Group, D.E. Groom et al., Eur. Phys. J. **C15** (2000) 1.

[65] G. Cowan, Statistical Data Analysis, Oxford University Press (1998).

[66] The H1 Detector at HERA, DESY 93-103 (1993).

[67] R.M. Sternheimer and R.F. Peierls, Phys. Rev. **B3** (1971) 3681.

[68] K.H. Streng, T.F. Walsh, and P.M. Zerwas, Z. Phys. **C2** (1979) 237.

[69] G. Thompson and D. Kant, H1 internal note, H1-08/95-452.

[70] P. Dixon, D. Kant, and G. Thompson, J. Phys. **G25** (1999) 1453; ZEUS Collaboration, J. Breitweg et al., Eur. Phys. J. **C11** (1999) 2.

[71] C.P. Fong and B.R. Webber, Phys. Lett. **B229** (1989) 289; Nucl. Phys. **B355** (1991) 54.

[72] D. Kant, *A Study of the Fragmentation of Quarks in $e^-p$ Collisions at HERA using the H1 Detector*, Ph.D. thesis, University of London (1996), RAL-TH-96-008.

[73] H1 Collaboration, C. Adloff et al., 29th International Conference on High Energy Physics ICHEP98, Vancouver, Canada, July 1998, No. 531.

[74] L3 Collaboration, B. Adeva et al., Phys. Lett. **B259** (1991) 199; D. Kant, Nucl. Phys. **B71** (1991) 31.

[75] H1 Collaboration, C. Adloff et al., Nucl. Phys. **B504** (1997) 3.

[76] CLEO Collaboration, S. Behrends et al., Phys. Rev. **D31** (1985) 2161;

[77] TASSO Collaboration, M. Altoff et al., Z. Phys. **C17** (1983) 5; R. Brandelik et al., Phys. Lett. **B94** (1980) 444; W. Braunschweig et al., Z. Phys. **C42** (1989) 189;

[78] TOPAZ Collaboration, R. Itoh et al., Phys. Lett. **B345** (1995) 335.

[79] ALEPH Collaboration, D. Buskulic et al., Z. Phys. **C64** (1994) 361; Z. Phys. **C66** (1995) 355.

[80] L3 Collaboration, M. Acciarri et al., Phys. Lett. **B328** (1994) 223.

[81] OPAL Collaboration, R. Akers et al., Z. Phys. **C68** (1995) 1; G. Alexander et al., Z. Phys. **C73** (1997) 569.

[82] Y.L. Dokshitzer, V.A. Khoze, and S.I. Troyan, J. Phys. **G17** (1991) 1481.

[83] DELPHI Collaboration, P. Abreu et al, Nucl. Phys. **B444** (1995) 3-26.

[84] N.C. Brümmer, Z. Phys. **C66** (1995) 367.

[85] Y.L. Dokshitzer, V.A. Khoze, and S.I. Troyan, Z. Phys. **C55** (1992) 107.